

AD-A039 507

MISSISSIPPI STATE UNIV MISSISSIPPI STATE ENGINEERING--ETC F/G 18/3  
A STUDY OF THE CHARGE AND CURRENT INDUCED ON AN AIRCRAFT IN AN --ETC(U)  
DEC 76 C D TAYLOR, K CHEN, T T CROW

UNCLASSIFIED

AFOSR-TR-77-0636

NL

1 OF 2  
AD  
A039 507



AD A 039507

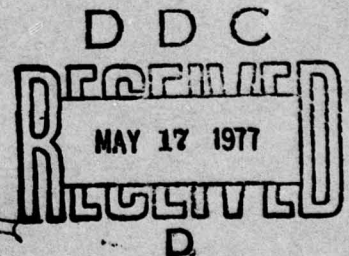


DEPARTMENT  
OF  
ELECTRICAL ENGINEERING

COPY AVAILABLE TO DDC DOES NOT  
PERMIT FULLY LEGIBLE PRODUCTION

A STUDY OF THE CHARGE AND CURRENT INDUCED  
ON AN AIRCRAFT IN AN EMP SIMULATOR FACILITY,  
PART I: THE FORMULATION  
PART II: THE SINGULARITY EXPANSION METHOD  
PART III: THE NUMERICAL RESULTS

ENGINEERING AND  
INDUSTRIAL RESEARCH STATION



MISSISSIPPI STATE UNIVERSITY  
STATE COLLEGE, MISSISSIPPI

DISTRIBUTION STATEMENT A

Approved for public release;  
Distribution Unlimited

AD No. \_\_\_\_\_  
DDC FILE COPY



AIR FORCE OFFICE OF SCIENTIFIC RESEARCH (AFSC)  
NOTICE OF TRANSMITTAL TO DDC  
This technical report has been reviewed and is  
approved for public release IAW AFR 190-12 (7b).  
Distribution is unlimited.  
A. D. BLOSE  
Technical Information Officer

ACCESSION for	
NTIS	White Section <input checked="" type="checkbox"/>
DDC	Dark Section <input type="checkbox"/>
UNANNOUNCED <input type="checkbox"/>	
JUSTIFICATION	
DISTRIBUTION/AVAILABILITY CODES	
AVAIL. AND/OR SPECIAL	
A	23

9

Final rept.

6

A STUDY OF THE CHARGE AND CURRENT INDUCED ON  
AN AIRCRAFT IN AN EMP SIMULATOR FACILITY.

PART I. THE FORMULATION.

Part II. The Singularity Expansion Method.

Part III. The Numerical Results.

by

10

Clayborne D. Taylor  
Keh-Tong Chen  
Terry T. Crow  
Murali Kumbale

12

131 p.

11

Dec 76

15

AF - AFOSR - 2961 - 76

18

AFOSR

19

TR-77-636

16

9751

17

05

Prepared for  
Air Force Office of Scientific Research  
Bolling Air Force Base  
Washington, D. C. 20332

December 1976

DDC  
RECEIVED  
MAY 17 1977  
D

The research reported in this document was  
sponsored under Grant number AFOSR-76-2961

DISTRIBUTION STATEMENT A

Approved for public release;  
Distribution Unlimited

390 182

## TABLE OF CONTENTS

	Page
Abstract	1
1. Introduction	2
2. Analysis	5
a. Theoretical Model	5
b. Surface Current and Charge Densities	6
c. Simulator Field Computations	10
d. Ground Plane Considerations	11
e. Time Domain Analysis	12
3. Conclusion	13
4. References	14



A STUDY OF THE CHARGE AND CURRENT INDUCED ON  
AN AIRCRAFT IN AN EMP SIMULATOR FACILITY,

PART I: THE FORMULATION

A study of the aircraft skin current and charge is made for an aircraft under the illumination of the electromagnetic field produced by a nuclear EMP simulator. This work is motivated by the need to relate the response of an aircraft in the EMP simulator to the response of an aircraft under actual EMP illumination. The analysis is directed toward a specific EMP simulator at Kirtland AFB, New Mexico, however, the methodology presented is applicable to other types of simulator facilities.

- 1 -

## 1. Introduction

An electromagnetic pulse such as the nuclear EMP (electromagnetic pulse) incident on an aircraft will induce current and charge densities on its surface. These distributions represent the electromagnetic fields external to the aircraft. Since the interior fields are related in a linear fashion to the exterior fields, acquiring a knowledge of the external fields is the first step in determining the currents and voltages induced in the electrical system of the aircraft. Transfer functions, either theoretical or experimental, are used to relate the voltage and/or current at a particular location to the most significant point or points of entry for the electromagnetic energy.

The simulation of the nuclear EMP requires the radiation of energy over an extremely broad frequency band. At present there are three classes of EMP simulators: the bounded wave simulator or transmission line, the open radiator and the hybrid simulator.<sup>1</sup> The bounded wave simulator provides the best simulation of the EMP in terms of frequency spectrum and field uniformity. However, for the illumination of very large objects such as aircraft the construction costs and the time required for construction become serious problems. Because of the low frequency content of the EMP, the dimensions of the open radiator type of simulator become inordinately large and present operational difficulties. The hybrid simulator may be the most cost effective of the simulator facilities. At high frequency the hybrid simulator behaves as an open radiator and at low frequency the near field of the simulator antenna are utilized. However there may be a tremendous point-to-

point variation in the field components produced by this simulator, at least to the extent that the response of an illuminated object may depend upon the orientation of the object as well as its location in the facility.

The Air Force Weapons Laboratory located at the Kirtland Air Force Base uses various hybrid type simulation facilities to test the response of an aircraft to the nuclear EMP.<sup>1</sup> In each of the existing facilities the aircraft must rest on a concrete pad which eliminates the possibility of testing directly the inflight mode response. Also the electromagnetic field components produced in the facilities generally have a spacial variation that is considerably different from those associated with the actual nuclear EMP. Thus a theoretical model is required for the interpretation of test data as well as for the extrapolation of the test data to predict the inflight mode response.

This paper presents a theoretical-numerical formulation for determining the current and charge distributions induced on an aircraft with low frequency illumination, i.e., for wavelengths that are large in terms of the wing or fuselage diameters. The analysis considers an electromagnetic model for the aircraft formed with axial segments of bodies of revolution, where the cross section radii and segment lengths are chosen both for convenience and for the most accurate physical representation of the aircraft (see figure 1). Details of the formulation are given in an earlier report.<sup>2</sup>

The foregoing formulation yields only the total axial current on the axial segments of the bodies of revolution. Assuming a uniform circumferential distribution can lead to significant errors.<sup>3</sup> With the assumption of electrically thin segments the quasi state distribution of current and charge may be utilized to predict the circumferential



distributions. This is accomplished using the results from the analysis of the infinitely long cylinder.

In order to determine the solution for the aircraft skin current and charge distributions the electromagnetic field illuminating the aircraft must be known as a function of frequency. Experimental field map data could be used. Two specific illuminations are considered incident on the aircraft. First a plane wave propagating normal to the wings and fuselage is considered. Second the electromagnetic field produced by the ATHAMAS (also called HPD) simulator of the Air Force Weapons Laboratory is considered (see figure 2).<sup>1,4</sup> The later field strengths are computed according to the analysis of Blackburn and Taylor.<sup>5</sup>

Verification of the theoretical model is accomplished by extensive comparisons with measured data that are obtained using scale models of aircraft and measurements conducted on the EC-135 aircraft in the ATHAMAS simulator. These will be presented in a subsequent report (PART III: Numerical Results).

## 2. Analysis

### a. Theoretical Model

In solving for the induced current and charge densities on an aircraft the principal features of the aircraft--wings, fuselage, stabilizers, etc.--are represented using axial segments of bodies of revolution. For an aircraft such as the EC-135 a convenient body of revolution model is shown in figure 1. Here the bodies of revolution are either cylinders or prolate spheroids. An alternative model (to be discussed subsequently) could be constructed from segments of cylinders. The lengths of the principal features of the aircraft are matched with the model while the radii of the circular cross sections are chosen as suggested by King.<sup>6</sup> The choice of the radii is not a crucial factor.

For convenience the induced current and charge densities the diameters of the principal elements or features of the aircraft are considered small in terms of wave length so that the axial current on the elements dominates the rotational current that may be excited. Therefore, the solution technique is necessarily limited to low frequency. To determine the current induced, the elements of the aircraft structure are divided into electrically short increments with an assumed sinusoidal axial current, i.e., for the nth segment of the jth element with end currents  $I_j(s_{jn})$  and  $I_j(s_{j,n+1})$ ,

$$I_j(s_j) = \frac{I_j(s_{j,n+1})\sin k(s_j - s_{jn}) + I_j(s_{jn})\sin k(s_{j,n+1} - s_j)}{\sin k(s_{j,n+1} - s_{jn})} \quad (1)$$

is the induced axial current distribution. The unknown end currents of the aforementioned electrically short current segments may be obtained

by using the so-called extended boundary condition to develop a complex system of linear equations and then using standard numerical solution techniques to solve the system of linear equations.<sup>2,7</sup>

The foregoing solution technique is numerically stable and is most efficient for aircraft-like dimension. However, it would be totally unsuitable for treating thin wire configurations due to the convergence problems that would occur.<sup>8</sup>

#### b. Surface Current and Charge Densities

In comparing the results of the body of revolution formulation with experimental data the axial current that is obtained from the formulation must be related to the induced surface current density. Since the axial segments of the bodies of revolution are required to be electrically thin it is assumed that the circumferential variation of the current is related to the axial current as on the infinitely long cylinder.

Accordingly consider the circumferential variation of the axial surface current density (or circumferential magnetic field). At a particular cross section of an element of the aircraft structure the magnetic field may be expanded in a Fourier series as

$$H_{\theta}^{\text{tot}}(s_j, \theta) = \frac{I(s_j)}{2\pi a_j(s_j)} + f(s_j, \theta) \quad (2)$$

where

$$f(s_j, \theta) = \sum_{n=1}^{\infty} [A_n(s_j) \cos n\theta + B_n(s_j) \sin n\theta] \quad (3)$$

Evidently the function  $f(s_j, \theta)$  represents the asymmetrical portion of the magnetic field that cannot be determined from the body of revolution



formulation as discussed in the foregoing.

In order to obtain an approximation to the function  $f(s_j, \theta)$  the infinitely long cylindrical scattered is considered. With an incident plane wave propagating normal to the cylinder and with the electric field directed parallel to the cylinder, the total magnetic field at the surface of the cylinder is<sup>9</sup>

$$H_{\theta}^{\text{tot}}(s_j, \theta) = \frac{I}{2\pi a} + \frac{4 H^{\text{inc}}}{\pi ka} \sum_{n=1}^{\infty} \frac{j^{-n} \cos n\theta}{H_n^{(2)}(ka)} \quad (4)$$

where  $I$  is the total axial current,  $H_n^{(2)}(ka)$  is the Hankel function of the second kind, and  $H^{\text{inc}}$  is directed in the  $\theta = 3\pi/2$  direction. Therefore an approximation to the asymmetrical portion of the magnetic field for a finite length cylinder is

$$f(s_j, \theta) \approx \frac{4H^{\text{inc}}}{\pi ka} \sum_{n=1}^{\infty} \frac{j^{-n} \cos n\theta}{H_n^{(2)}(ka)} \quad (5)$$

For electrically thin cylinders, i.e.,  $(ka)^2 \ll 1$ , (5) yields the magnetostatic current distribution<sup>3</sup>

$$f(s_j, \theta) \approx 2\hat{\theta} \cdot \bar{H}^{\text{inc}} \quad (6)$$

where the unit vector  $\hat{\theta}$  is defined in the right hand sense with respect to the direction of positive current. Using (6) in (2) yields the total circumferential component of the surface magnetic field for the infinitely long cylinder is

$$H_{\theta}^{\text{tot}}(s_j, \theta) \approx \frac{I}{2\pi a} + 2\hat{\theta} \cdot \bar{H}^{\text{inc}} \quad (7)$$

where the corresponding current density is

$$J_z(s_j, \theta) = H_\theta^{\text{tot}}(s_j, \theta) \quad (8)$$

The axial component of the magnetic field (corresponding to a circumferential current) also can be obtained from the infinitely long cylinder formulation. Again consider broadside incidence but with the electric field now directed perpendicular to the axis of the cylinder. The axial component of the magnetic field at the surface of the cylinder is<sup>9</sup>

$$H_z^{\text{tot}}(s_j, \theta) = -J_\theta(s_j, \theta) \approx H_z^{\text{inc}}[1 - j2ka \cos \theta] \quad (9)$$

provided  $(ka)^2 \ll 1$ , for the quasistatic result.

For a plane wave of arbitrary polarization incident from the broadside on an infinite cylinder, the wave is first decomposed into parallel and perpendicular polarized components then (7) and (9) applied directly for the corresponding polarizations. These results may also be applied to the aircraft problem provided the elements of the structure are electrically thin. It should be noted however that for the aircraft problem  $\bar{H}^{\text{inc}}$  should also include the magnetic fields scattered from all the elements of the aircraft. But these generally can be neglected and accurate results still be obtained. Therefore, the aircraft surface current distribution is approximately, on the  $j$ th element

$$\begin{aligned} \bar{J}_s(s_j, \theta) \approx & \left[ \frac{I_j(s_j)}{2\pi a_j(s_j)} + 2\hat{\theta} \cdot \bar{H}^{\text{inc}} \right] \hat{z} \\ & - \hat{z} \cdot \bar{H}^{\text{inc}} [1 - j2ka \cos \theta] \hat{\theta} \end{aligned} \quad (10)$$

The modes of current oscillation associated with the terms of (10) may be readily identified. The term

$$\frac{I_j(s_j)}{2\pi a_j(s_j)}$$

represents an electric dipole oscillation of the axial current. The term

$$2\hat{\theta} \cdot \vec{H}^{inc}$$

represents a magnetic dipole oscillation, a circulation of current about the element axis. For the circumferential current the term

$$\hat{z} \cdot \vec{H}^{inc}$$

also represents a circulation of current but here it is about the circumference of the element cross section. And finally the term

$$j \hat{z} \cdot \vec{H}^{inc} 2ka \cos \theta$$

represents an electric dipole oscillation.

For a body of revolution (10) becomes

$$\begin{aligned} \vec{J}_s(s_j, \theta) \approx & \left[ \frac{I_j(s_j)}{2\pi a_j(s_j)} + 2 \hat{\theta} \cdot \vec{H}^{inc} \right] \hat{t} \\ & - \hat{z} \cdot \vec{H}^{inc} [1 - j 2ka \cos \theta] \hat{\theta} \end{aligned} \quad (11)$$

where  $\hat{t}$  is the unit vector tangential to the surface of the body yet perpendicular to  $\hat{\theta}$ .<sup>10</sup> The foregoing is used to predict the surface current density using the axial currents obtained from the numerical solution.

The surface charge density is obtained via the equation of continuity. It is



$$\rho_s(s_j, \theta) = \frac{j}{\omega} \operatorname{div} \bar{J}_s$$

For a body of revolution

$$\operatorname{div} \bar{J}_s = \frac{1}{a_j(s_j)} \left\{ \frac{\partial}{\partial \theta} \hat{\theta} \cdot \bar{J}_s + \cos \theta(s_j) \frac{\partial}{\partial s_j} [a_j(s_j) \hat{t} \cdot \bar{J}_s(s_j, \theta)] \right\}$$

Hence

$$\rho_s(s_j, \theta) = \frac{j}{\omega a_j(s_j)} \left\{ \frac{\partial}{\partial \theta} \hat{\theta} \cdot \bar{J}_s(s_j, \theta) + \cos \theta(s_j) \frac{\partial}{\partial s_j} [a_j(s_j) \hat{t} \cdot \bar{J}_s(s_j, \theta)] \right\}$$

predicts the charge density associated with the surface current density.

#### c. Simulator Field Computations

For an aircraft in a nuclear EMP simulation facility such as the HPD facility at the Kirtland AFB, New Mexico, a very complicated spacial variation of the field incident on the aircraft occurs. The numerical solution, however, requires only that the axial component of the illuminating electric field be specified at a discrete set of points over the aircraft configuration. Hence the solution for the induced axial current may be effected in a straight forward manner. Then the evaluation of the surface current density is accomplished with a knowledge of the illuminating magnetic field components as discussed in the foregoing.

One advantage of using the body of revolution formulation is that the illuminating field values needed may be obtained experimentally and/or theoretically since recently Blackburn and Taylor<sup>4</sup> developed a formulation for calculating the electromagnetic fields produced by a hybrid type of EMP simulator such as the HPD simulator. Their results compare quite favorably with measured data. In any event the theoretical results could

be used to supplement measured data. Only the time domain fields were measured directly.<sup>4</sup> The Fourier transform or frequency data were obtained by digitizing the time domain results and applying the Fourier transform numerically.

d. Ground Plane Considerations

For an aircraft in proximity to a ground plane the procedure for determining the total surface magnetic field is further complicated by the interaction with the ground plane. Due to this interaction the current and charge densities tend to be greater on the side of the aircraft near the ground plane. According to the static solution for the circumferential variation of the axial current on an infinitely long cylinder parallel to a perfectly conducting ground, the distribution of current normalized to a unit axial current is<sup>11</sup>

$$f_I(s_j, \theta) = \frac{\sqrt{1 - [a_j(s_j)/h]^2}}{1 + [a_j(s_j)/h] \cos \theta}$$

where  $h$  is the height of the center of the cross section above the ground plane, and  $\theta = 0$  locates the section of the cylinder nearest the ground plane. The incident magnetic field contribution to the current density should remain the same for a cylinder over the ground plane as for the cylinder in free space, except that the ground reflected wave must be included as part of the incident magnetic field. Thus the circumferential magnetic field component becomes

$$H_{\theta}^{\text{tot}}(s_j, \theta) \approx \frac{I(s_j) f_I(s_j, \theta)}{2 \pi a_j(s_j)} + 2 \hat{\theta} \cdot (\bar{H}^{\text{inc}} + \bar{H}^{\text{ref}})$$

where  $\vec{H}^{\text{ref}}$  is the magnetic field of the ground reflected wave. The foregoing expression is then used to compute the axial current density on an aircraft in the ground alert mode.

To compute the corresponding charge density induced on an aircraft in the ground alert mode the equation of continuity is applied as mentioned in the foregoing.

e. Time Domain Analysis

The time domain induced skin current and charge will be calculated for the aircraft in the HPD facility and for the aircraft inflight illuminated by a plane wave EMP. The body of revolution formulation that is used involves a numerical solution for the axial current over the entire aircraft for a given excitation frequency. To obtain the currents under pulse excitation, the aircraft currents are calculated for the frequency band of the incident pulse and then Fourier superimposed. An alternative approach that is more advantageous under certain conditions is the use of the singularity expansion method<sup>6</sup>. Both procedures are to be considered. The surface charge density on the aircraft can be obtained similarly.

Since the excitation of the aircraft skin current is considerably different for the two cases considered--simulator environment and the inflight environment--the current and charge at certain locations will be calculated and compared as a function of frequency. Then corresponding comparisons will be made for the time domain currents and charges.

## 1. Conclusion

A theoretical-numerical analysis has been developed to determine the low frequency skin current and charge densities induced on an aircraft illuminated by an incident electromagnetic field. The theoretical model has been verified by comparison of the results with data that are obtained from scale model measurements. Along the principle features of the aircraft the theoretical data is generally within 6 db of the measured data.

Pulse excitation can also be treated by use of the Fourier transform. To illustrate the theoretical technique an aircraft is considered illuminated by a unit step incident pulse.

An important application of the analysis, at the present, is in the interpretation of skin current and charge data obtained in an EMP simulator facility.



## 4. References

1. Baum, C. E., "EMP Simulators for Various Types of Nuclear EMP Environments: An Interim Categorization," Sensor and Simulation Note 151, Air Force Weapons Laboratory, Kirtland AFB, New Mexico, July 1972.
2. Taylor, C. C., Chen, K. T., and Crow, T. T., "An Improvement on Wire Modeling for Determining the EMP Interaction with Aircraft," Air Force Weapons Laboratory Technical Report AFWL-TR-74-317, Kirtland AFB, N.M., October 1974.
3. Saucer, M. I., Latham, R. W. and Varvatis, A. D., "Relationship Between Total Currents and Surface Current Densities Induced on Aircraft and Cylinders," Air Force Weapons Laboratory Interaction Note 194, Kirtland AFB, N.W., August 1974.
4. Dana, T. A., Bumgardner, M. K., and Skogmo, P. J., "Horizontally Polarized Dipole Facility Evaluation," Report No. AL-144, EG and G, Inc., Albuquerque, New Mexico, January 1975.
5. Blackburn, R. F. and Taylor, C. D., "On the Electromagnetic Fields from a Hybrid Type of EMP Simulator," Air Force Weapons Laboratory Sensor and Simulation Note 211, Kirtland AFB, N.M., November 1975.
6. King, R. W. P., Theory of Linear Antennas, Harvard University Press, Cambridge, Mass., 1957, Chapter 1, Section 7, pp. 14-20.
7. Crow, T. T. Graves, B. D., and Taylor, C. D., "The Singularity Expansion Method as Applied to Perpendicular Crossed Wires," IEEE Trans. Ant. Prop., Vol. AP-23, pp. 540-546, July 1975.
8. Butler, C. M. and Wilton, D. R., "Analysis of Various Numerical Techniques Applied to Thin-Wire Scatterers," IEEE Trans. Ant. Prop., Vol. AP-23, pp. 534-540, July 1975.
9. Harrington, R. F., Time Harmonic Electromagnetic Fields, McGraw-Hill, New York, 1961, p. 233.
10. Taylor, . D. and Wilton, D. R., "The Extended Boundary Condition Solution of the Dipole Antenna of Revolution," IEEE Trans. on Antennas and Propagation, Vol. AP-20, No. 6, pp. 772-776.
11. Taylor, C. D., "On the Circumferential Current and Charge Distributions on Circular Cylinders Near a Ground Plane," Interaction Note 138, Air Force Weapons Laboratory, March 1973.

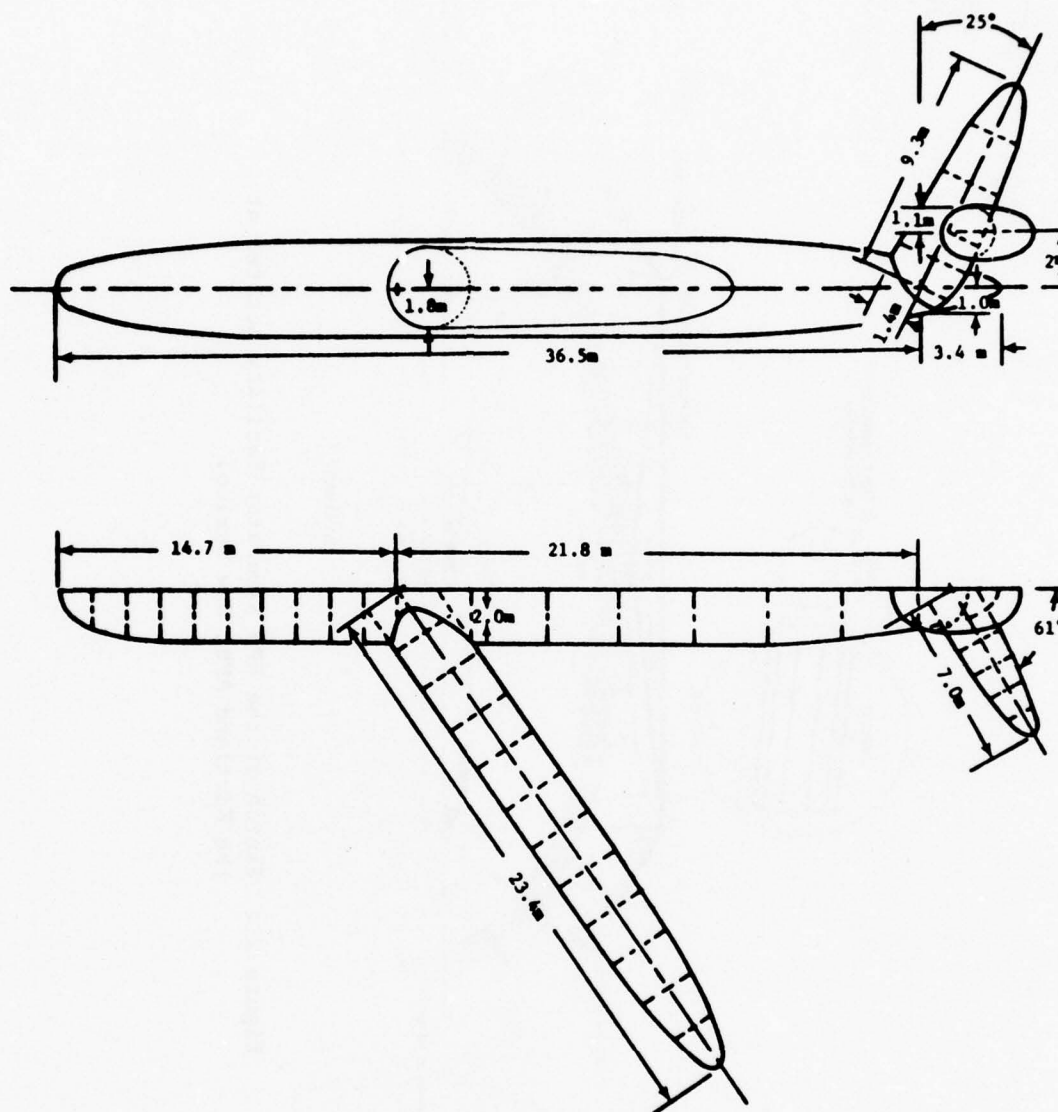


Figure 1: Body of Revolution Model of the EC-135 Aircraft.  
Current Zones are Indicated with Dotted Lines.

BEST AVAILABLE COPY

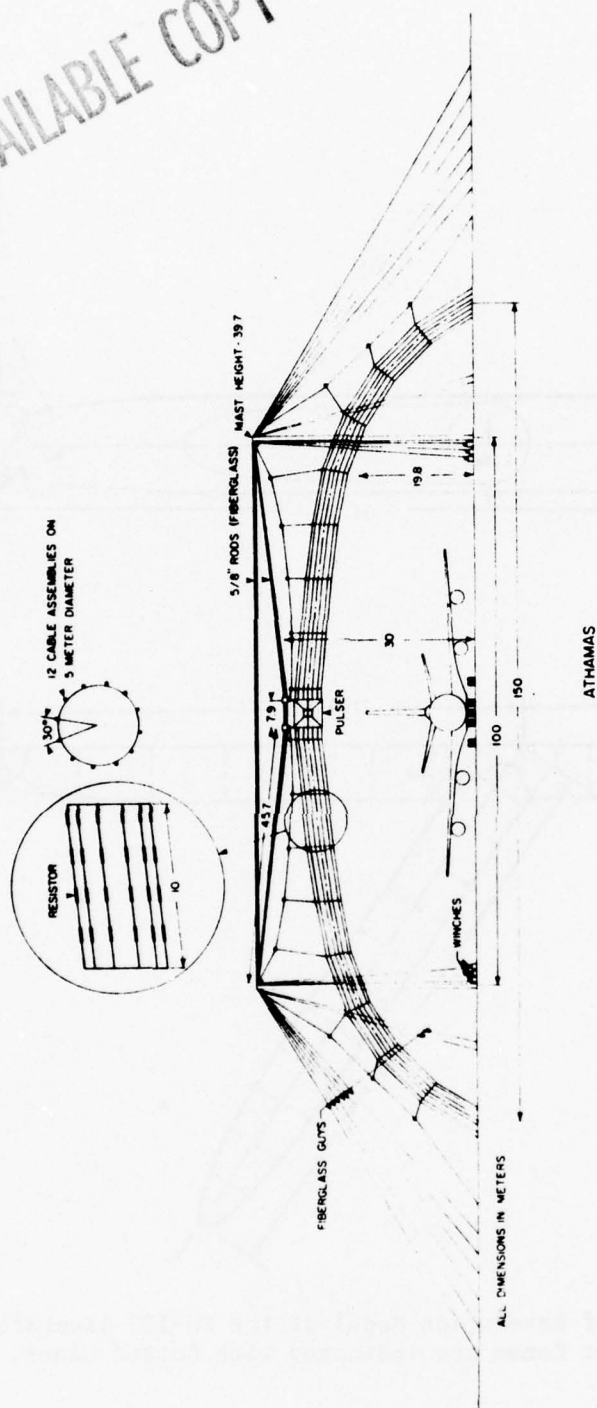


Figure 2 : Sketch of the HPD Simulator Facility Located at the Kirtland AFB, New Mexico.

A STUDY OF THE CHARGE AND CURRENT INDUCED ON  
AN AIRCRAFT IN AN EMP SIMULATOR FACILITY,  
PART II: THE SINGULARITY EXPANSION METHOD

by

Terry T. Crow  
Murali Kumbale  
Clayborne D. Taylor

Prepared for  
Air Force Office of Scientific Research  
Bolling Air Force Base  
Washington, D. C. 20332

December 1976

The research reported in this document was  
sponsored under Grant number AFOSR-76-2961



## TABLE OF CONTENTS

	Page
Abstract	1
1. Introduction	2
2. Formulation	3
3. Numerical Results	4
4. Conclusion	11
5. References	12

A STUDY OF THE CHARGE AND CURRENT INDUCED ON  
AN AIRCRAFT IN AN EMP SIMULATOR FACILITY,  
PART II: THE SINGULARITY EXPANSION METHOD

For an aircraft under the illumination of the electromagnetic field produced by a nuclear EMP simulator the natural resonant frequencies are significantly affected by the presence of the concrete pad supporting the aircraft. In order to determine this effect the singularity expansion method has been applied to a system consisting of two perpendicular crossed conducting thin cylinders oriented parallel to a perfectly conducting ground plane.

## 1. Introduction

Using the singularity expansion method (SEM) it is possible to determine the time domain scattering from a conducting object in terms of a summation of damped sinusoids.<sup>1</sup> In the evaluation of the SEM solution the resonant or natural frequencies of the scattering object are also obtained. In this report SEM is applied to two perpendicular crossed conducting thin cylinders located above a perfectly conducting ground plane. This configuration may be viewed as a crude model of an aircraft. And the SEM solution technique can provide insight into interaction of the aircraft with the ground plane.

A few numerical results are presented. In particular the natural frequencies are determined as geometrical parameters of the wires are varied.

## 2. Formulation

As described in earlier work the formulation is based on the exact field expression about a current filament with a sinusoidal current.<sup>2,3</sup> The axial field component is<sup>4</sup>

$$\hat{r}_{21} \cdot \bar{E}(\bar{r}) = \frac{1}{4\pi\epsilon s} \left\{ I'(\bar{r}_1) \frac{e^{-s|\bar{r}-\bar{r}_1|/c}}{|\bar{r}-\bar{r}_1|} - I'(\bar{r}_2) \frac{e^{-s|\bar{r}-\bar{r}_2|/c}}{|\bar{r}-\bar{r}_2|} \right\} \quad (1)$$

for the complex Laplace frequency  $s = \sigma + j\omega$ , the filament extends from  $\bar{r} = \bar{r}_1$  to  $\bar{r} = \bar{r}_2$ ,  $I'$  is the axial derivative of the current and

$$\hat{r}_{21} = \frac{\bar{r}_2 - \bar{r}_1}{|\bar{r}_2 - \bar{r}_1|}$$

The radial component of the field is

$$\begin{aligned} \hat{\rho}_{21} \cdot \bar{E}(\bar{r}) = \frac{1}{4\pi\epsilon s \rho_{21}} \left\{ \hat{r}_{21} \cdot \left[ (\bar{r}-\bar{r}_2) I'(\bar{r}_2) \frac{e^{-s|\bar{r}-\bar{r}_2|/c}}{|\bar{r}-\bar{r}_2|} \right. \right. \\ \left. \left. - (\bar{r}-\bar{r}_1) I'(\bar{r}_1) \frac{e^{-s|\bar{r}-\bar{r}_1|/c}}{|\bar{r}-\bar{r}_1|} \right. \right. \\ \left. \left. - \frac{s}{c} I(\bar{r}_2) e^{-s|\bar{r}-\bar{r}_2|/c} - I(\bar{r}_1) e^{-s|\bar{r}-\bar{r}_1|/c} \right] \right\} \quad (2) \end{aligned}$$

where  $\rho_{21}$  is the radial variable corresponding to the radial variable in a cylindrical coordinate system with the  $z$  axis coincident with the axis of the current filament.

The system of algebraic equations for the current distribution is derived by dividing the wires into segments and expressing the current on the  $k$ th segment of the  $m$ th wire as



$$I_{mk}(x) = \frac{\alpha_k \sinh[s(x_{k+1} - x)/c] + \alpha_{k+1} \sinh[s(x - x_k)/c]}{\sinh[s(x_{k+1} - x_k)/c]} \quad (3)$$

$$x_k \leq x \leq x_{k+1}$$

At this point one must modify (1) and (2) which are free space equations to account for contributions due to the image currents. Image currents are assumed to have the same magnitude as the object currents. For object currents parallel to the ground plane, image currents are antiparallel to the object currents; for object currents perpendicular to the ground plane, image currents are parallel to the object currents. The scattered field components about the crossed wires are determined as functions of the  $\alpha_k$ 's by substituting (3) into the modified forms of (1) and (2). The crossed wires are assumed to be illuminated by an incident field whose electric field is directed parallel to the y-axis (Fig. 1). Again one must account for the ground reflected wave, and the total electric field illuminating the aircraft is

$$\vec{E}_{total}^{inc} = \vec{E}^{inc} + \vec{E}^{reflected}$$

The total electric field ( $\vec{E}_{total}^{inc} + \vec{E}^{scat}$ ) is required to satisfy the boundary condition that its component tangent to the wire axis be zero. Requiring that these equations be satisfied at a discrete set of match points, one finds a linear set of equations for the  $\alpha_k$ 's. The match points are taken to be the end points of the current segments referred to in (3). Three comments are in order: 1) the King-Wu charge boundary conditions<sup>5</sup> replace three of the above equations for  $\alpha_k$ 's; 2) the Kirchhoff current law replaces a fourth equation; 3) the current at the second match point on each segment is assumed to be the average of that on the first

and third match points--the first match point on each segment is at the junction of the four wires. The current is assumed zero at the end of each wire.

The resulting system of linear equations for the current can be written as

$$\bar{\bar{Z}}(s) \bar{J}(s) = \bar{E}(s) \quad (4)$$

where  $\bar{\bar{Z}}(s)$  is the square system matrix,  $\bar{J}(s)$  is a column matrix whose elements are the  $\alpha_k$ 's, and  $\bar{E}(s)$  is a column matrix whose elements are the incident field components evaluated at the match points. Certain elements in the  $\bar{E}(s)$  matrix are set equal to zero as a result of the boundary conditions and averaging discussed in the previous paragraph. SEM results assert that the current vector may be written as

$$\bar{J}(s) = \sum_{\alpha} \eta_{\alpha} \frac{1}{s - s_{\alpha}} E_0(s) \bar{v}_{\alpha} \quad (5)$$

$E_0(s)$  is the Laplace transform of the incident waveform, and the  $s_{\alpha}$ 's are the complex natural frequencies defined as the zeros of the determinant of the system matrix

$$\det[\bar{\bar{Z}}(s_{\alpha})] = 0 \quad (6)$$

the  $\bar{v}_{\alpha}$ 's are the natural modes defined by

$$\bar{\bar{Z}}(s_{\alpha}) \bar{v}_{\alpha} = 0 \quad (7)$$

and the  $\eta_{\alpha}$ 's are the coupling coefficients defined as<sup>6</sup>

$$\eta_{\alpha} = \frac{\langle \bar{\mu}_{\alpha}, \bar{E} \rangle}{\langle \bar{\mu}_{\alpha}, \bar{K}_{\alpha}, \bar{v}_{\alpha} \rangle} \frac{1}{E_0(s)} \quad (8)$$

the  $\bar{\mu}_\alpha$ 's are solutions of

$$\bar{Z}(s_\alpha)^T \bar{\mu}_\alpha = 0 \quad (9)$$

where  $\langle \bar{a}, \bar{b} \rangle = \int_{\text{wires}} \bar{a} \cdot \bar{b} \, d\ell$

and

$$\bar{\kappa}_{\alpha 1} = \left. \frac{\partial \bar{Z}(s)}{\partial s} \right|_{s=s_\alpha}.$$

The details of such calculations have been discussed in various reports.<sup>7,8</sup>

It is of interest to report that the  $s_\alpha$ 's tabulated later in this report were located using subroutine SEARCH<sup>9</sup> based on the Cauchy integral theorem and verified using a Muller iteration method.<sup>7</sup>

For a step pulse incident on the wires,

$$E_o(s) = \frac{E_o}{s} \quad (10)$$

The time domain current becomes

$$\bar{J}(t) = u(t) \sum_{\alpha} \eta_{\alpha} \frac{E_o}{s_{\alpha}} e^{s_{\alpha} t} \bar{v}_{\alpha} \quad (11)$$

where  $u(t)$  is the unit Heaviside step function.

### 3. Numerical Results

Geometrical parameters for the crossed cylinder configuration are illustrated and defined in figure 1. A limited parametrical study is presented to establish the feasibility of the method and to determine trends. In table 1 the complex natural frequencies are given for crossed cylinders with aircraft-like dimensions in free space. These form a reference set to compare with corresponding data for crossed cylinders located over a ground plane. Data for a few configurations are given in Table 2.

When  $\ell'_1 = \ell_1$  the crossed cylinder interaction is decoupled, i.e. the axial currents induced on the cylinders are the same as would exist on a single cylinder. But in general the natural modes induced on the crossed cylinder configuration may be separated into two types--coupled cylinder modes and isolated cylinder modes. The isolated cylinder modes are those that would occur on an isolated cylinder over a ground plane. Hence these modes are independent of  $\ell'_1/\ell_1$ . From the data in Table 2, the  $\alpha = 2, 6, \dots$  modes are the isolated cylinder modes while all the other modes are the coupled cylinder modes. But as  $\ell'_1 \rightarrow \ell_1$  the coupled modes vanish.

Note that as  $h$  is decreased by  $1/2$  the real parts of  $s_\alpha$  decrease almost proportionally while the imaginary parts of  $s_\alpha$  change less than 10%. The decrease in the real parts of  $s_\alpha$  correspond to an increased  $Q$  and the structure's decreased capacity to reradiate electromagnetic energy. If the ground plane were lossy then the real parts of  $s_\alpha$  should reflect the loss of energy into the ground plane. Experimental data



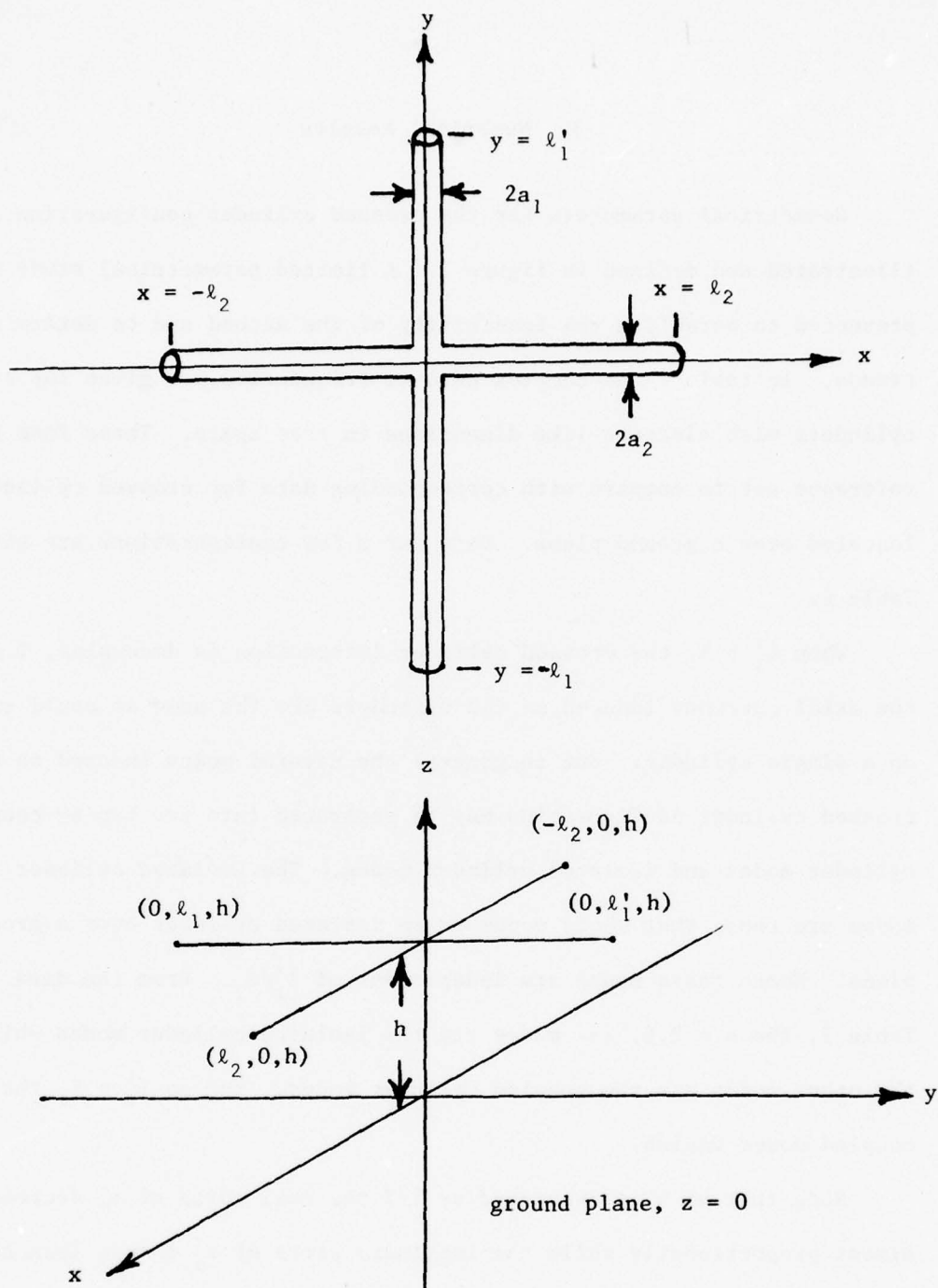


Figure 1: Two perpendicular crossed cylinders oriented parallel to a perfect ground plane.

indicates that even for a concrete pad the real parts of  $s_\alpha$  should not be as large as the free space values. This will be discussed in Part III: Numerical Results.

Table 1: Complex Natural Frequencies for Crossed Cylinder Configurations in Free Space  
 $(\ell_1' + \ell_1 = L = 2\ell_2, L/a_2 = 20., a_1 = a_2, \ell_1'/\ell_1 = 0.50)$

---

$\alpha$	$s_\alpha L/c$
1	-0.2935 + j 2.2922
2	-0.4203 + j 2.5082
3	-0.3346 + j 3.8392
4	-0.6609 + j 6.0656
5	-1.0065 + j 8.1563
6	-0.9528 + j 8.2939
7	-1.1143 + j 11.0767

Table 2: Complex Natural Frequencies for Crossed  
Cylinder Configurations Over a Ground Plane  
( $\ell_1' + \ell_1 = L = 2\ell_2$ ,  $L/a_2 = 20.$ ,  $a_1 = a_2$ )

$\alpha$	$s_\alpha L/c$	
	$\ell_1'/\ell_1 = 0.25, h = 0.1L$	$\ell_1'/\ell_1 = 0.50, h = 0.1L$
1	-0.0130 + j 2.1788	-0.0202 + j 2.4525
2	-0.0426 + j 2.7605	-0.0426 + j 2.7605
3	-0.0864 + j 4.7561	-0.0470 + j 3.9166
4	-0.1872 + j 5.6984	-0.1775 + j 5.9389
5	-0.3299 + j 8.2189	-0.3015 + j 7.7876
6	-0.3289 + j 8.3861	-0.3289 + j 8.3861
7	-0.3167 + j 9.5512	-0.5359 + j 10.7325
$\alpha$	$s_\alpha L/c$	
	$\ell_1'/\ell_1 = 0.25, h = 0.2L$	$\ell_1'/\ell_1 = 0.50, h = 0.2L$
1	-0.0342 + j 2.1190	-0.0513 + j 2.3606
2	-0.0898 + j 2.5918	-0.0898 + j 2.5918
3	-0.2122 + j 4.6285	-0.1021 + j 3.7688
4	-0.3591 + j 5.3673	-0.3909 + j 5.7399
5	-0.7195 + j 7.9511	-0.6691 + j 7.5812
6	-0.6478 + j 8.0338	-0.6478 + j 8.0338
7	-0.6609 + j 9.3583	-1.2847 + j 11.0712

#### 4. Conclusion

With the limited parametric study that is presented it has been shown that SEM applied to perpendicular crossed cylinders does provide insight into the aircraft-ground plane interaction. This interaction is particularly significant in understanding the response of an aircraft to the nuclear EMP. However, the study presented is not complete and is reserved for future investigation.



## 5. References

1. C. E. Baum, The Singularity Expansion Method, Topics in Applied Physics, Vol. 10. (Edited by L. B. Felson), Springer Verlag. 1976.
2. T. T. Crow, B. D. Graves, and C. D. Taylor, "The Singularity Expansion Method as Applied to Perpendicular Crossed Cylinders in Free Space," Air Force Weapons Laboratory Interaction Note 161, Oct. 1973.
3. Terry T. Crow, Billy D. Graves, and Clayborne D. Taylor, "The Singularity Expansion Method as Applied to Perpendicular Crossed Wires," IEEE Trans. Antennas Propagat., Vol. AP-23, pp. 540-546, July 1975.
4. S. A. Schelkunoff and H. T. Friis, Antennas: Theory and Practice, New York; Wiley, 1952, p. 370.
5. T. T. Wu and R. W. P. King, "The Tapered Antenna and Its Application to the Junction Problem for Thin Wires," IEEE Trans. Antennas Propagat., Vol. AP-24, pp. 42-46, Jan. 1976.
6. C. E. Baum, "On the Singularity Expansion Method for the Solution of Electro-magnetic Interaction Problems, AFWL Interaction Note 88, Dec. 1971.
7. T. T. Crow, B. D. Graves, and C. D. Taylor, "Numerical Techniques Useful in the Singularity Expansion Method as Applied to Electro-magnetic Interaction Problems, AFWL MaN 27, Dec. 1972.
8. F. M. Tesche, "On the Singularity Expansion Method as Applied to Electromagnetic Scattering from Thin-Wires, AFWL Interaction Note 102, Apr. 1972.
9. B. K. Singaraju, D. V. Giri, and C. E. Baum, "Further Developments in the Evaluation of the Zeros of Analytic Functions and Relevant Computer Programs," AFWL MaN 42, Mar. 1976.

MEMORANDUM TO FILE

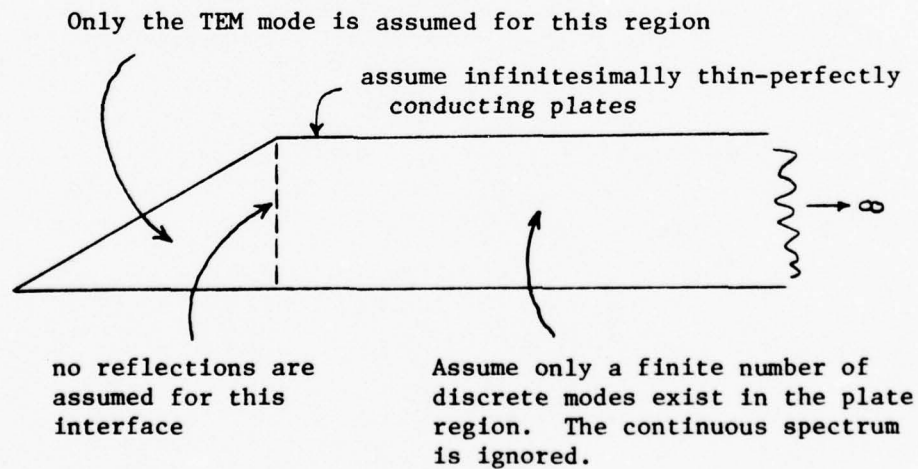
18 March 1977

To: Capt. L. Roberts, ELA

From: Clayborne D. Taylor, Consultant

Re: Preposal entitled, "Excitation of Modal Fields in Parallel-Plate Transmission Line"

1. The work being proposed should be supported. Having been involved in strip line studies for many years, the Electromagnetics Laboratory at the University of Illinois is eminently qualified to do the work.
2. Obtaining the modal expansion for the electromagnetic field within a finite width parallel-plate waveguide is a very useful result. However, the study proposed does employ a number of judicious approximations of which you should be aware. The illustration below identifies the principle approximations



Also the propagation constants for the discrete modes are obtained via a ray-optical approximation.

3. The foregoing approximations notwithstanding, the proposed work is a very meaningful study. Moreover it can be accomplished with the level of effort that is proposed. It will provide the most accurate estimate to date for the high order mode contribution to the fields between the parallel plates.
4. It would be quite helpful if the accuracy of the approximations used in the proposed work were estimated and included in the proposal.

MEMORANDUM TO FILE

18 March 1977

To: Lt. Col. A. G. Cupka, ELA

From: Clayborne D. Taylor, Consultant

Re: Report of TDY Activities, 7-11 March 1977

1. The subject work activities are reported without reference to the date since many of the activities involved work completed over several days.
2. A meeting called by Col Wheeler of NTO was attended where the executive summary of the EC-135 assessment was discussed.
3. Several days were spent in the study of the relationship between individual wire currents and the bulk current induced on a multi-conductor cable.
4. A meeting called by ELP was attended where the multiconductor cable measurements being performed by MRC were reported. Their work is directed primarily toward verifying the theoretical model being developed by SAI. It was suggested that MRC also investigate typical cable lays and routing for measurement purposes.
5. Proposals for studies of simulator-test object interaction were discussed with Capt. Roberts. Reviews of the proposals are in preparation.



MEMORANDUM TO FILE

18 March 1977

To: Capt. L. Roberts, ELA

From: Clayborne D. Taylor, Consultant

Re: Proposal entitled: Currents and Charges on Cylinders in a  
Parallel-Plate Transmission Line

1. Most of the work being proposed should be supported. In particular, the proposed measurements should be supported since Professor King of Harvard University is the world's authority on that type of research.
2. The measurements proposed for the crossed cylinders in a parallel-plate transmission line facility should be quite useful in providing an additional means of evaluating test data collected at the EMP simulator facilities utilizing parallel-plate transmission lines. In particular, the results are necessary for interpreting test data for very large test objects.
3. In addition to the aforementioned measurements analytical studies are proposed for a wire cross within a wire rhombic structure and within a parallel wire loop structure. It is stated that these studies may be necessary for interpreting the transmission line measured data. But these structures although amenable to analysis are considerably different from the transmission line problem and the fields produced are very much more complex. It is doubtful that the proposed analytic results would be of more than superficial value.

4. It is very interesting that the proposed research could not possibly be performed with the level of effort that is proposed. For example Profs. King & Wu would spend only 3.5 man months, technicians would spend about 18 man months, a secretary would spend  $3/4$  man month, and a programmer would spend about  $1\ 1/2$  weeks. And that is the total proposed effort. However, Prof. King would probably spend more time than is proposed and he probably will have students available to help.

A STUDY OF THE CHARGE AND CURRENT INDUCED ON  
AN AIRCRAFT IN AN EMP SIMULATOR FACILITY,  
PART III: NUMERICAL RESULTS

by

Clayborne D. Taylor  
Keh-Tong Chen  
Terry T. Crow

prepared for

Air Force Office of Scientific Research  
Bolling Air Force Base  
Washington, D. C. 20332

December 1976

The research reported in this document was  
sponsored under Grant number AFOSR-76-2961

## TABLE OF CONTENTS

	Page
Abstract	1
1. Introduction	2
2. Numerical Results	4
a. Intersecting cylinder Aircraft Model	4
b. B-1 Scale Model Data	5
c. EC-135 Scale Model Data	6
d. Ground Plane Coupling Data	7
e. Measured Data from HPD Simulator	7
f. Computed Results for HPD Simulator Facility	9
g. Computed Results for Inflight Mode	10
h. Extrapolation to Free Space	11
3. Conclusion	13
4. References	14



A STUDY OF THE CHARGE AND CURRENT INDUCED ON  
AN AIRCRAFT IN AN EMP SIMULATOR FACILITY,  
PART III: NUMERICAL RESULTS

ABSTRACT

A theoretical-numerical solution technique is used to determine the current and charge densities induced on an aircraft by an electromagnetic pulse. To represent the aircraft the formulation uses an electromagnetic model formed with axial segments of bodies of revolution. Verification of the theoretical model is accomplished by extensive comparisons with measured data obtained by using scale models.

Measured and calculated data are also presented for an EC-135 aircraft in the ATHAMAS I (also called HPD) simulator at Kirtland AFB, New Mexico. In addition the EC-135 is considered to be illuminated in flight by a typical estimate of the nuclear EMP. Comparison of the in flight data with corresponding simulator data is made to investigate the possibility of general trends.

## 1. Introduction

This report as the sequel to parts I and II presents the numerical results obtained using a theoretical-numerical formulation for determining the current and charge distributions induced on aircraft an electromagnetic pulse generated to simulate the nuclear EMP (electromagnetic pulse) emitted by the detonation of a nuclear weapon.<sup>1,2</sup> The analysis considers an electromagnetic model for the aircraft formed with axial segments of bodies of revolution, where the cross section radii and segment lengths are chosen both for convenience and for the most accurate physical representation of the aircraft. Details of the formulation are given in the earlier reports.

Two specific illuminations are considered incident on the aircraft. First a plane wave pulse propagating normal to the wings and fuselage is considered for an aircraft in flight. Second the electromagnetic pulse produced by the ATHAMAS (also called HPD) EMP simulator of the Air Force Weapons Laboratory, Kirtland AFB is considered. The later field strengths are computed according to the analysis of Blackburn and Taylor.<sup>3</sup> For both the in flight and simulator results two polarizations of the electric field are considered incident on the aircraft.

An explicit contribution from the incident magnetic field must be included to obtain accurate results for the surface current density. This is accomplished by combining the axial current contribution to the magnetic field with the incident magnetic field following the result for the infinitely long circular cylinder. Both the current and charge density calculations are made and presented for the frequency regime in

which the analysis is valid. And Fourier transform theory is used to obtain the corresponding time domain behavior.

Verification of the theoretical model is accomplished by extensive comparisons with measured data. There are comparisons with a limited amount of data obtained for the EC-135 aircraft in the ATHAMAS facility. But most of the measured data were obtained using scale models of the B-1 and the EC-135 aircraft and a physical reproduction of a cylinder model of an aircraft. The details of the measurements are given in other reports.<sup>4-6</sup> In addition to these comparisons an extensive amount of data is presented for the EC-135 inflight and in the ATHAMAS facility.

## 2. Numerical Results

Before an extensive amount of data is presented, a verification of the theoretical model is made. First comparisons are made with data obtained from a physical reproduction of a cylinder model of an aircraft.

For the calculated charge density data to be presented only the axial current density is considered and the equation of continuity applied. The procedure used to obtain the surface current density is described in Part I.<sup>1</sup>

### a. Intersecting Cylinder Aircraft Model

In figure 1 a model of the B-1 aircraft is formed by using intersecting sections of wires or circular cylinders. In order to ascertain the accuracy of the presented formulation a scale model of the cylinder model of B-1 aircraft was constructed and the surface current density measured at various locations as a function of frequency for topside incidence. If the theoretical-numerical data and the measured data were precise for the cylinder (or wire model) then there should be exact agreement. In figures 2, 3 and 4 measured and calculated data is compared. Also shown on the figures are data obtained from the body of revolution model (see figure 5). Here the station number on the fuselage is the linear distance from the nose of the aircraft. Current density measurements are made on the shadowed as well as the illuminated side of the aircraft model.

From figures 2, 3 and 4 the following observations can be made.

(i) The current density on the shadow side is completely different from the current density on the illuminated side for frequencies above the fundamental resonance of the aircraft.



- (ii) The shadowing effect is adequately treated in the analysis.
- (iii) The formulation yields accurate predictions of the fuselage current density for frequencies up to about 20 MHz for the B-1 model.
- (iv) The body of revolution model predicts lower peak currents and higher resonant frequencies than occur for the wire model.
- (v) Because of the substantial difference in the current densities on the wire and body of revolution models, the body of revolution model should be a considerable improvement on the wire model of an aircraft. This occurs primarily because the body of revolution model of an aircraft is a better physical representation of an aircraft.

It has been demonstrated that the theoretical-numerical formulation adequately predicts the surface current density induced on a crossed cylinder configuration that resembles an aircraft. The next step in the verification is to show that the currents and charges induced on a body of revolution model are an approximation to those induced on an actual aircraft. To that end comparisons are made with data obtained from measurements obtained using scale models of the EC-135 and B-1 aircraft.

#### b. B-1 Scale Model Data

In figures 6 and 14 the fuselage and wing current densities induced on a B-1 aircraft are presented for a few frequencies. Both the wings forward and wings swept configurations are shown. In the wings swept configuration the B-1 is almost a delta wing aircraft. From these figures the following conclusions are possible.

- (i) Although the theoretical model does not include many of the structural details of the aircraft the fuselage and wing current densities can be predicted within about 6 db over virtually the entire aircraft for frequencies up to about 20 MHz.

(ii) Since the distribution of current is accurate then the charge distribution should also be reasonably accurate.

c. EC-135 Scale Model Data

The EC-135 aircraft is shown in figures 15 and 16, and the appropriate body of revolution model is shown in figure 5. It is obvious that the physical appearance of this aircraft is more amenable to modeling by the body of revolution model than the B-1.

Current density and charge density data are presented for the EC-135 aircraft in figures 17 through 20. In order to cover the entire frequency range with the available instrumentation different size scale models were used.<sup>6</sup> These models were various versions of the Boeing 707 aircraft and did not have exactly the same relative shapes. This accounts, in part, for the differences in the data acquired in overlapping frequency regimes for different scale models. On the basis of the data presented in figures 17 through 20 the following observations are made.

(i) The body of revolution model accurately predicts the fundamental resonances of the aircraft.

(ii) As a function of frequency the predictions for current and charge from the body of revolution model are within about 6 db of measured results.

(iii) For the fundamental resonance the body of revolution model predicts a lower resonant frequency (less than 10% difference) than is observed.

(iv) For the higher order resonances the body of revolution model predicts a higher resonant frequency (about 25% difference) than is observed.

(v) The difference in current densities from the illuminated to shadowed sides of the aircraft are accurately predicted.

#### d. Ground Plane Coupling Data

When an aircraft is in the ground alert mode it is resting on a concrete pad and it may be grounded by means of one or two ground straps attached at convenient locations. In the analysis of the aircraft in this mode the ground straps are not considered for convenience. However, the addition of ground straps in the formulation is a minor modification.

Orienting a cylinder parallel to a perfectly conducting ground plane forms a two wire transmission line, the second wire is the image of the cylinder. This represents a very high Q configuration. And a configuration of cylinders or cylinder-like objects parallel to a perfectly conducting ground plane must be expected to exhibit the same behavior. Hence an aircraft in the ground alert mode over a perfectly conducting ground should exhibit very high Q resonances.

In figure 21 the resonant frequency versus aircraft height above a perfectly conducting ground is shown. For the typical aircraft height the variation is greatest. Both measured and computed data are shown for the intersecting cylinder model of an aircraft. In figure 22 the peak resonant current density versus aircraft height is shown. These data indicate that current density predictions are comparable in accuracy to the inflight predictions. However, the resonant frequency predictions will be more in error than corresponding inflight predictions.

At this point the ground coupling effect on an aircraft for an imperfect ground can only be surmised.

#### e. Measured Data from HPD Simulator Facility

For an aircraft in a nuclear EMP simulation facility such as the HPD facility at the Kirtland AFB, New Mexico, a very complicated spacial

variation of the field incident on the aircraft occurs. The numerical solution, however, requires only the axial component of the illuminating electric field be specified at a discrete set of points over the aircraft configuration. Hence the solution for the induced axial current may be effected in a straight forward manner. Then the evaluation of the surface current density is accomplished with a knowledge of the illuminating magnetic field component perpendicular to the respective aircraft elements.

The HPD facility at the Kirtland AFB is illustrated in figure 23. Two aircraft orientations are considered; first, the aircraft fuselage is located in the plane of the loop with the wing-fuselage junction directly beneath the pulser, and second the aircraft fuselage is oriented perpendicular to the plane of the loop with the wing-fuselage junction directly beneath the pulser.

In figures 24 through 27 the time domain axial current densities measured at a few locations on the aircraft are shown for the EC-135 in the aforementioned parallel orientation. Also shown are calculated results obtained by considering two separate approximations. First the ground beneath the aircraft is assumed to be perfectly conducting (with image) and second the ground beneath the aircraft is assumed to be free space (without image). The illuminating field—with ground bounce—is considered to be the same in both cases. At the HPD facility the aircraft is supported by a concrete pad about 3 feet thick with no steel reinforcement. The constitutive electrical properties of the concrete are estimated to be,<sup>8</sup> conductivity  $\sim .008\Omega/\text{m}$  and dielectric constant  $\sim 20$  at 5 MHz. Thus it is expected that the measured data fall somewhere



between (within  $\sim 6$  db) the calculated data for the perfect ground and the no-ground approximations. A more satisfactory theoretical treatment including a lossy ground is currently being pursued by the authors.

From figures 24 through 27 three principle observations are readily made. First, the measured peaks are roughly a factor of two greater than the calculated peaks. Second, for the very early time behavior the perfect ground and no-ground data essentially coincide for the points on top of the fuselage. And third, the late time oscillation of the measured currents are more attenuated than the perfect ground results and less attenuated than the no-ground results.

The Fourier transforms of the time domain measurements are presented in figures 28 through 31. Theoretical data for the perfect ground and no-ground situations are also included. In general the magnitude of the Fourier transforms of the measured data are less than the calculated transforms by about a factor of two. This is due in part to the inaccuracy of the Blackburn-Taylor prediction of the simulator field components. Also it is noted that the no-ground results are more similar in shape to the Fourier transform of the measured data. But most important the calculated resonant peaks occur at frequencies lower than corresponding resonances in the measured data. This also has been observed in the comparisons with scale model data.

#### f. Computed Results for HPD Simulator Facility

Comparisons with measured data in the preceding section indicate the accuracy of the calculated results. In this section the axial current densities at a number of locations over the aircraft structure is presented. Figures 32 through 35 exhibit the simulator magnetic field at a few points on the aircraft structure in a perpendicular



orientation (see the figures for an illustration). In figures 36 through 43 the magnitude of the Fourier transform of the axial current density is presented. The point at which the current is evaluated is illustrated by the aircraft figure. Both the perfectly conducting ground (with image) and the no-ground (without image) results are presented. Figures 44 through 47 exhibit the time domain results corresponding to the aforementioned Fourier transform data.

Charge density data for the EC-135 in the HPD simulator is presented in figures 48 through 56. Here, as before, the aircraft is in the perpendicular orientation. It should be mentioned that for the aircraft in the perpendicular orientation there is no axial current induced on the fuselage and the vertical stabilizer. That is the reason for no current and charge density data being presented for these elements.

In preparation for the presentation of current and charge density data on the aircraft in the parallel orientation, the HPD magnetic field components are shown for a few locations along the aircraft structure. Figures 61 through 93 present current density data at points over the aircraft structure for both the perfect ground and no-ground approximations. Again the position of the current evaluation is indicated in the aircraft figure. Figures 94 through 129 present corresponding charge density data.

#### g. Computed Results for Inflight Mode

As mentioned in the foregoing the current and charge density induced on an aircraft in a simulator facility must be related to the corresponding densities on an aircraft inflight. To that end the theoretical model is considered to be illuminated by the typical estimate of the

nuclear EMP when the aircraft is in the inflight mode. Accordingly the nuclear EMP is approximated by a plane wave pulse with electric field,<sup>9</sup>

$$E(t) = E_0(e^{-\alpha t} - e^{-\beta t})$$

where

$$E_0 = 5.2 \times 10^4 \text{ V/m}$$

$$\alpha = 1.5 \times 10^6 \text{ s}^{-1}$$

$$\beta = 2.6 \times 10^8 \text{ s}^{-1}$$

And the accompanying magnetic field is

$$H(t) = \frac{1}{\zeta} E(t)$$

where  $\zeta \approx 120\pi$  ohms.

First current and charge density data are presented for the electric field polarized parallel to the fuselage (corresponding to the parallel orientation of the aircraft in the HPD simulator facility). These data are presented in figures 130 through 175. Second, the current and charge density are presented for the electric field polarized perpendicular orientation of the aircraft in the HPD simulator facility. As before the location of the current and charge evaluation is illustrated in the figure. Also the illumination is from the topside of the aircraft.

#### h. Extrapolation to Free Space

The peak electric and magnetic fields for the inflight mode illumination is roughly a factor of 3 greater than the peak field strengths produced by HPD. Hence the peak currents and charge densities are expected to differ by corresponding amounts. For example, on the forward fuselage section at the wing-fuselage junction the peak current

density on top of the fuselage in the simulator is  $\sim 150$  A/m at  $t \sim 0.1 \mu\text{s}$  from figure 89. And from figure 146 the corresponding peak current density for the inflight mode is  $\sim 640$  A/m at  $t \sim 0.05 \mu\text{s}$ . For another example, the current density midway and on top of the wing is from figure 91 is  $\sim 60$  A/m at  $t \sim 0.1 \mu\text{s}$ . And from figure 151 the corresponding peak current density is  $\sim 280$  A/m at  $t \sim 0.025 \mu\text{s}$ .

A comparison of the charge densities for the aircraft inflight and in the HPD simulator is made in a similar fashion to that for the current densities. From figure 125 the peak charge density at the wing tip for an aircraft in the HPD facility is  $\sim .04 \times 10^{-4}$  c/m<sup>2</sup> at  $t \sim .4 \mu\text{s}$ . And the corresponding charge density for the inflight response from figure 172 is  $\sim .13 \times 10^{-4}$  c/m<sup>2</sup> at  $t \sim .4 \mu\text{s}$ .

### 3. Conclusion

A theoretical-numerical analysis has been developed to determine the low frequency skin current and charge densities induced on an aircraft illuminated by an incident electromagnetic field. The theoretical model has been verified by comparison of the results with an extensive amount of measured data. In general, along the principle features of the aircraft the theoretical data is within 6 db of the measured data.

An important application of the analysis, at the present, is in the interpretation of skin current and charge data obtained in an EMP simulator facility. Typical results are presented for the HPD facility at the Kirtland AFB, New Mexico.

#### REFERENCES

1. Taylor, C. D., Chen, K. T. and Crow, T. T., "A Study of the Charge and Current Induced on an Aircraft in an EMP Simulator Facility, Part I: The Formulation," Final Report Grant No. AFOSR-76-2961, submitted to Air Force Office of Scientific Research, December 1976.
2. Crow, T. T., Kumbale, M. and Taylor, C. D., "A Study of the Charge and Current Induced on an Aircraft in an EMP Simulator Facility, Part II: The Singularity Expansion Method," Final Report Grant No. AFOSR-76-2961, submitted to Air Force Office of Scientific Research, December 1976.
3. Blackburn, R. F. and Taylor, C. D., "On the Electromagnetic Fields from a Hybrid Type of EMP Simulator," Air Force Weapons Laboratory Sensor and Simulation Note 211, Kirtland AFB, N. M., November 1975.
4. Knott, E. F., "Surface Field Measurements," Air Force Weapons Laboratory Interaction Application Memo 5, Kirtland AFB, N.M., September 1974.
5. Liepa, V. V., "Sweep Frequency Surface Field Measurements," Air Force Weapons Laboratory Technical Report, AFWL-TR-75-217, Kirtland AFB, N.M., July 1975.
6. Liepa, V. V., and Dusette, D.L., "Free Space EC-135 Scale Model Measurements," to be published as an Air Force Weapons Laboratory Technical Report.
7. Dana, T. A., Bumgardner, M. K., and Skogmo, J. P., "Horizontally Polarized Dipole Facility Evaluation," Report No. AL-144, EG and G, Inc., Albuquerque, N.M., January 1975.
8. Castillo, J. P., "Effects of Wave Reflection on Objects Near a Plane Ground," Air Force Weapons Laboratory ATHAMAS MEMO No. 8, Kirtland AFB, N. M., May 1975.
9. Barnes, P. R., "The Effects of Electromagnetic Pulse (EMP) on State and Local Radio Communications," Oak Ridge National Laboratory Report No. ORNL-4873, Oak Ridge, TN, October 1973.



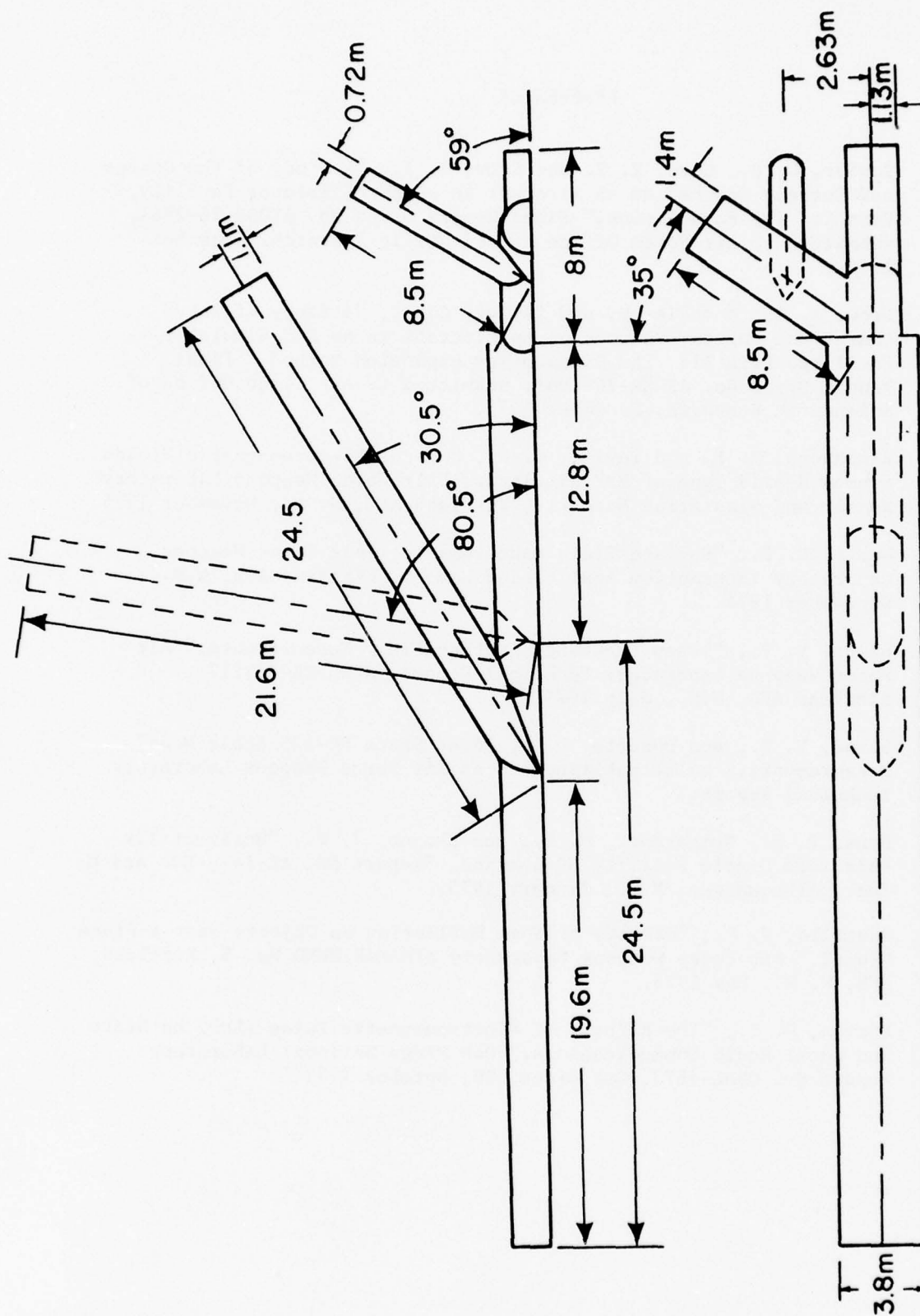


**Figure 1: Intersecting Cylinder (Wire) Model of the B-1 Aircraft with the Wings Forward and Wings Swept Positions.**

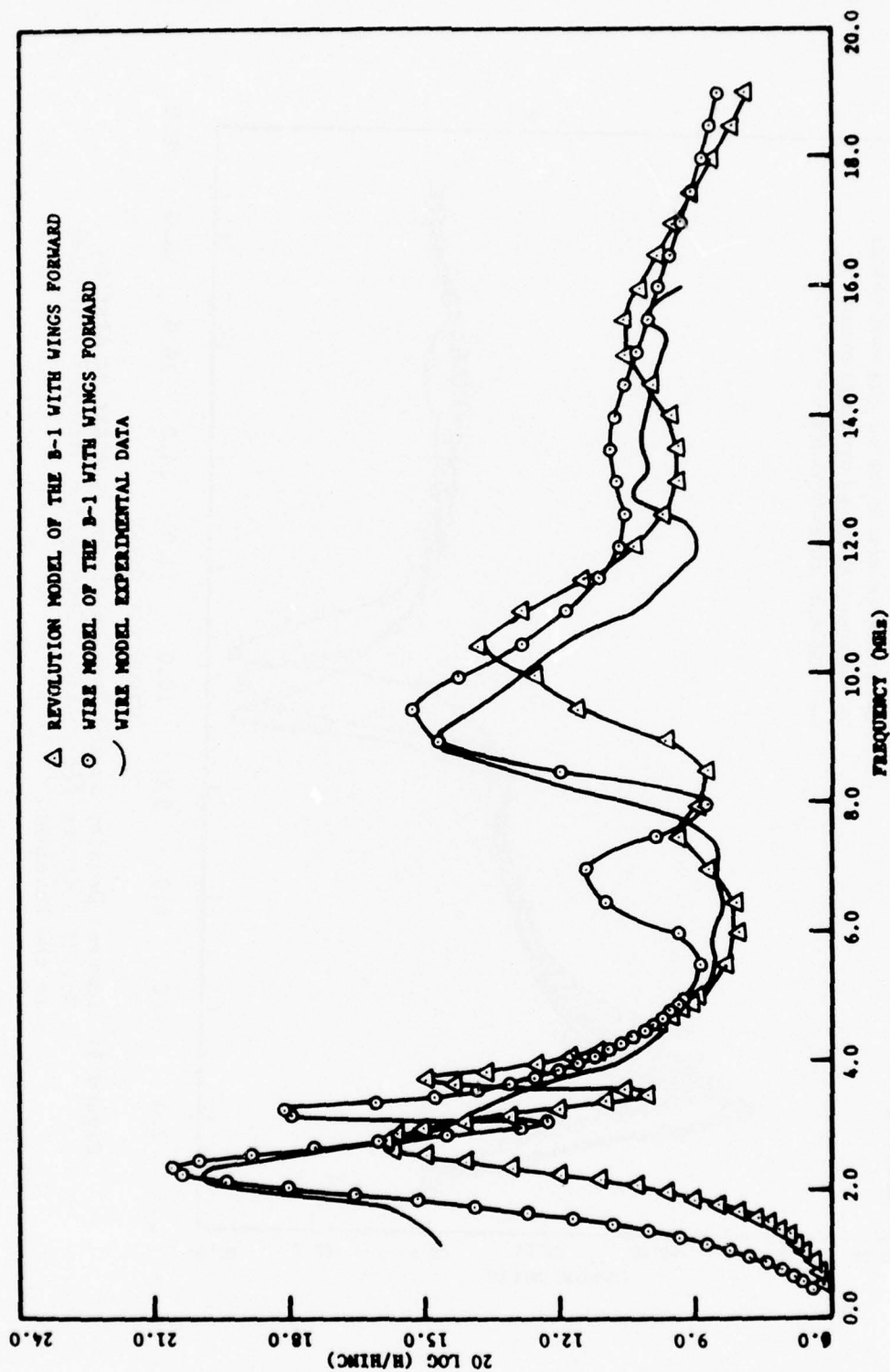


Figure 2: Current Density on the Topside of the Fuselage at  
 Station No. 5.0 meters for Topside Illumination  
 with Einc Parallel to the Fuselage.

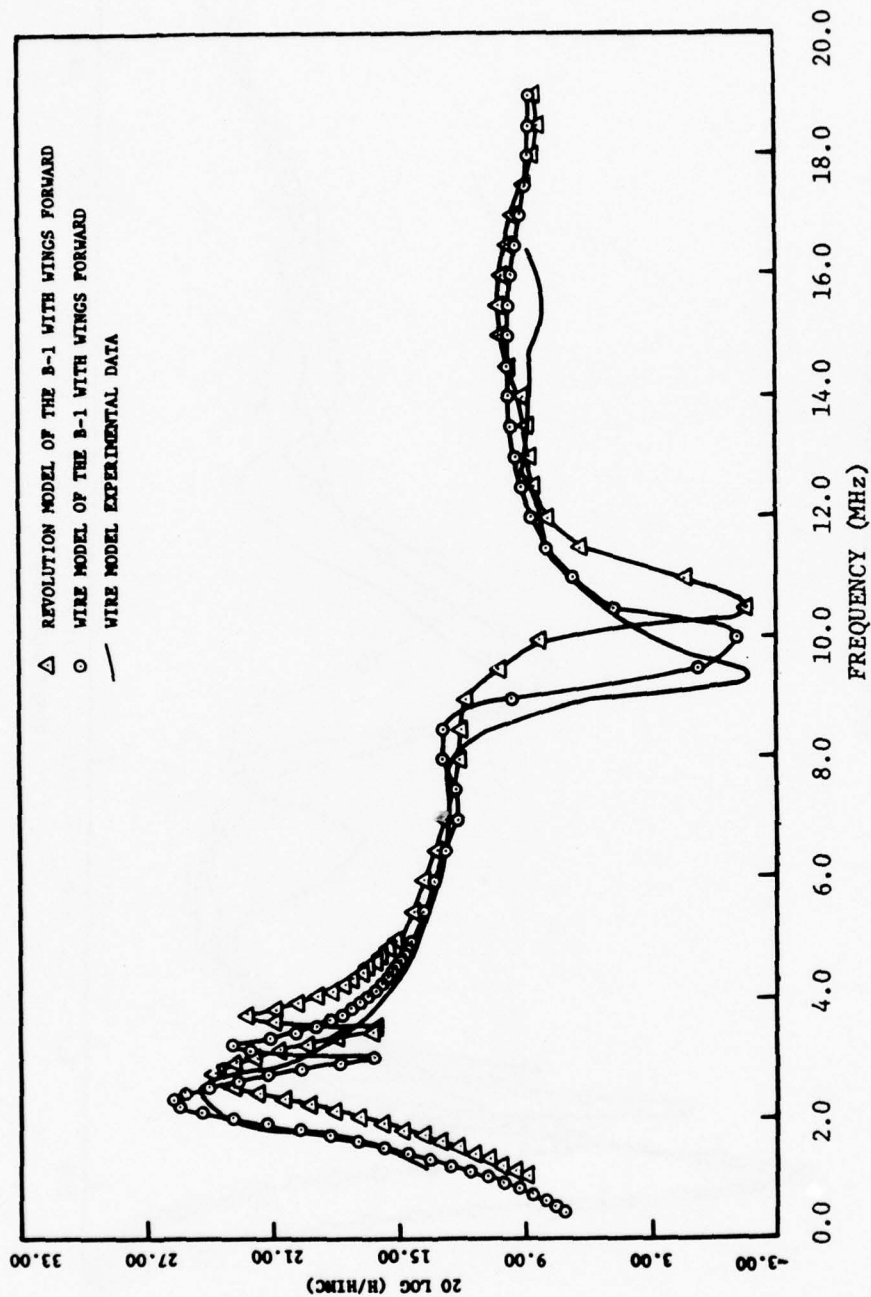


Figure 3: Current Density on the Topside of the Fuselage at Atation No. 22.5 meters for Topside Illumination with Einc Parallel to the Fuselage.

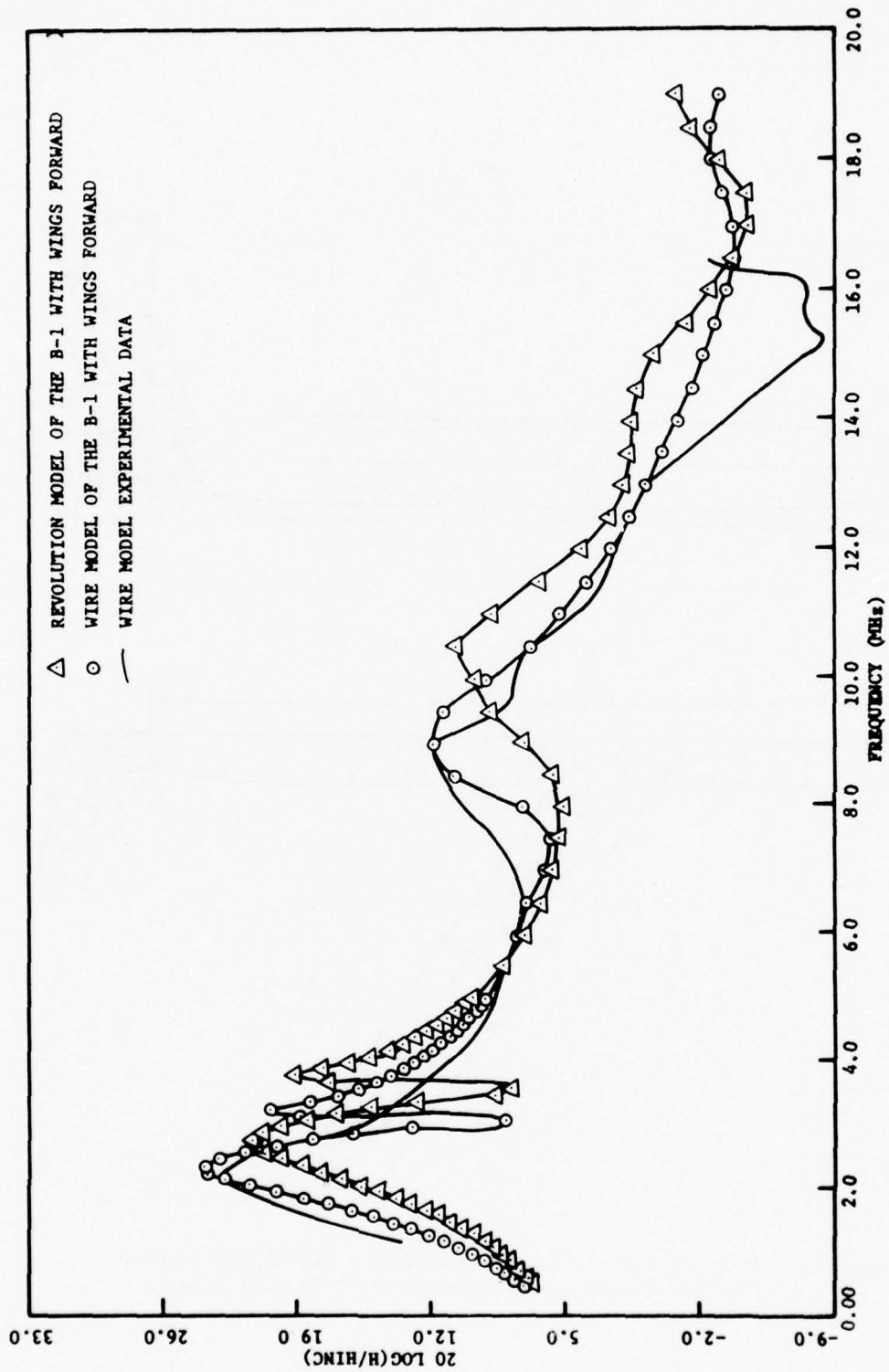


Figure 4: Current Density on the Bottom of the Fuselage at Station No. 22.5 meters for Topside Illumination with Einc Parallel to the Fuselage.

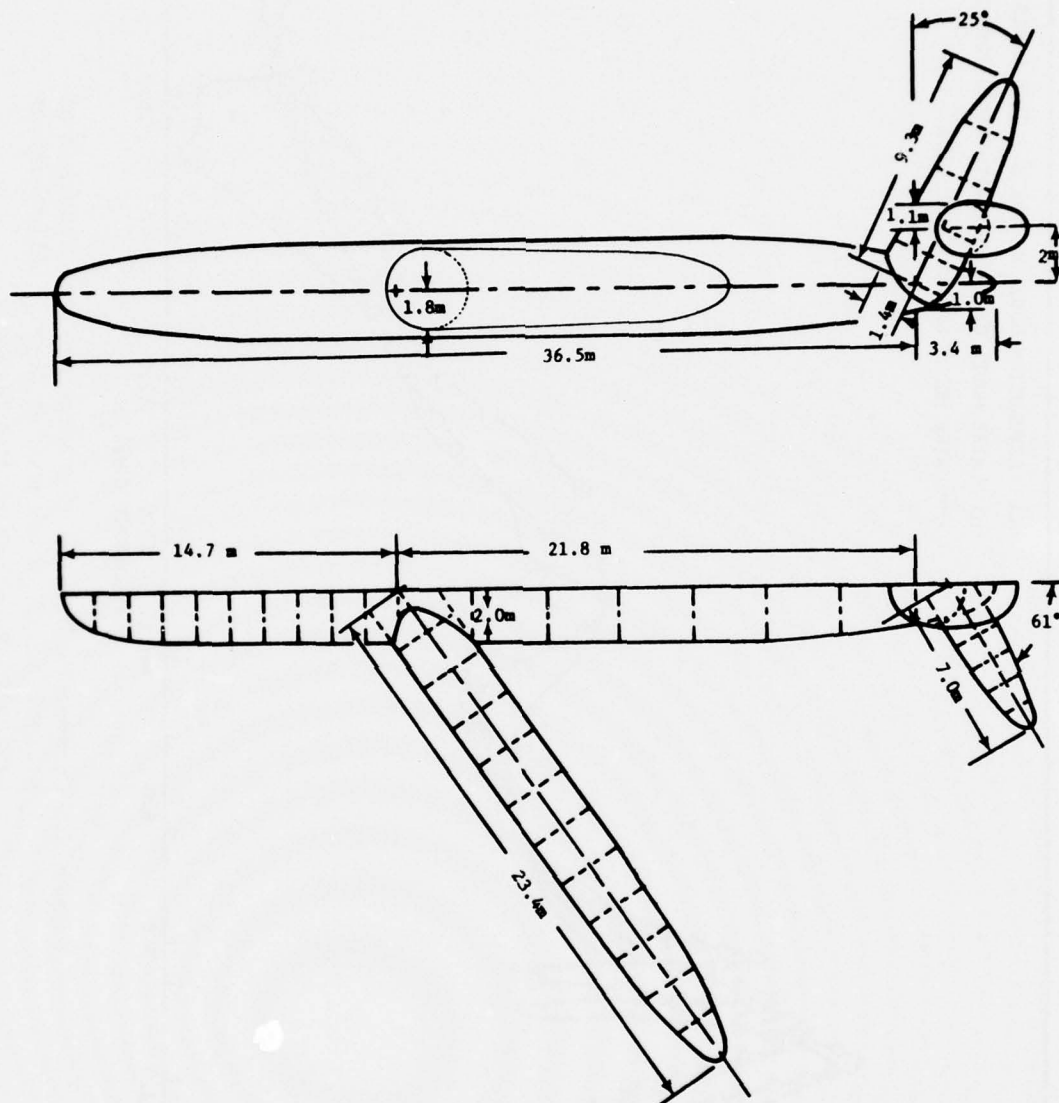


Figure 5: Body of Revolution Model of the EC-135 Aircraft.  
Current Zones are Indicated with Dotted Lines.



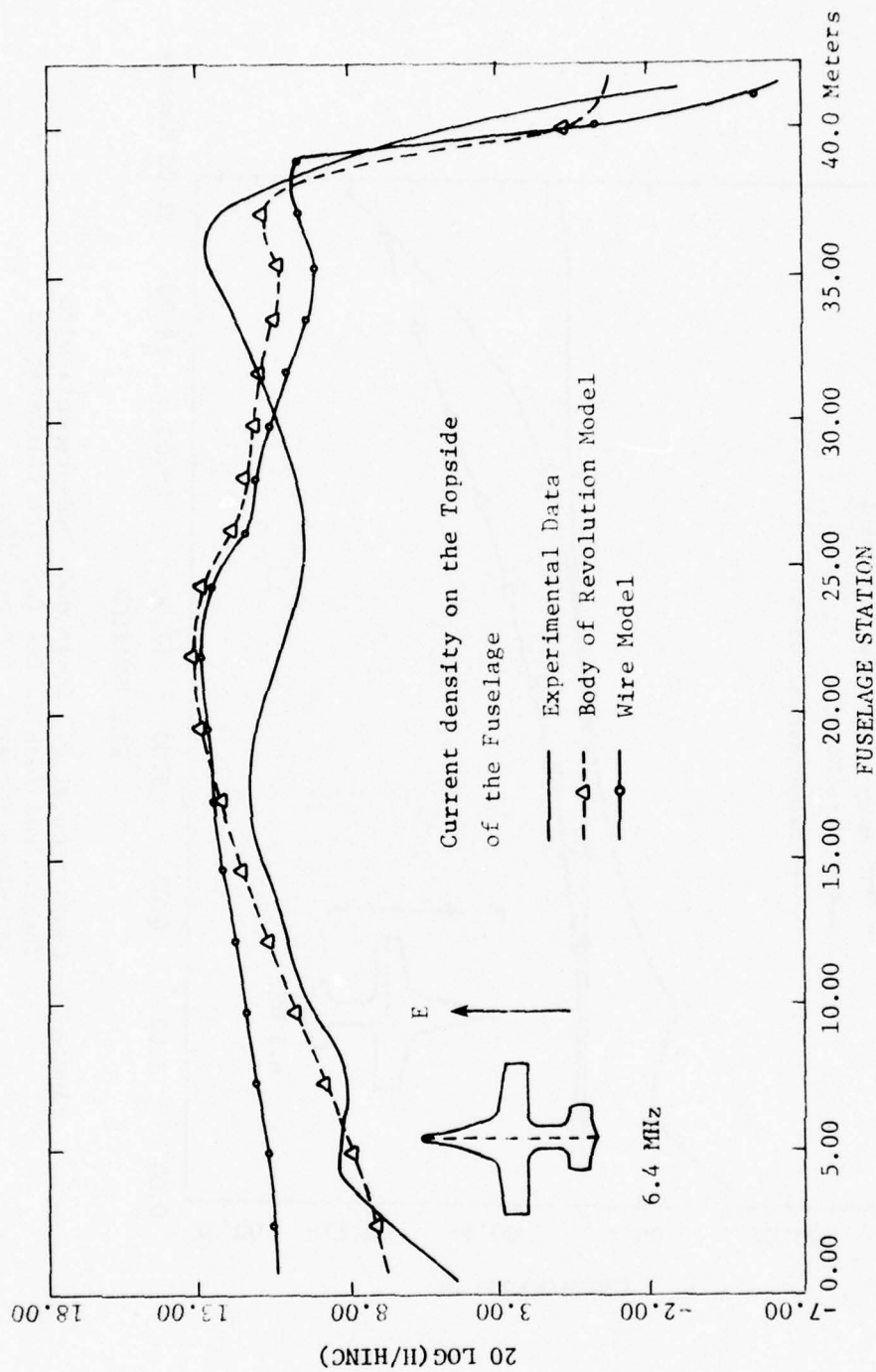


Figure 6: Comparison of B-1 Scale Model Measurements with Theoretical Results for Top Side Illumination and Wings Forward.  
 $f = 6.4 \text{ MHz}$ .

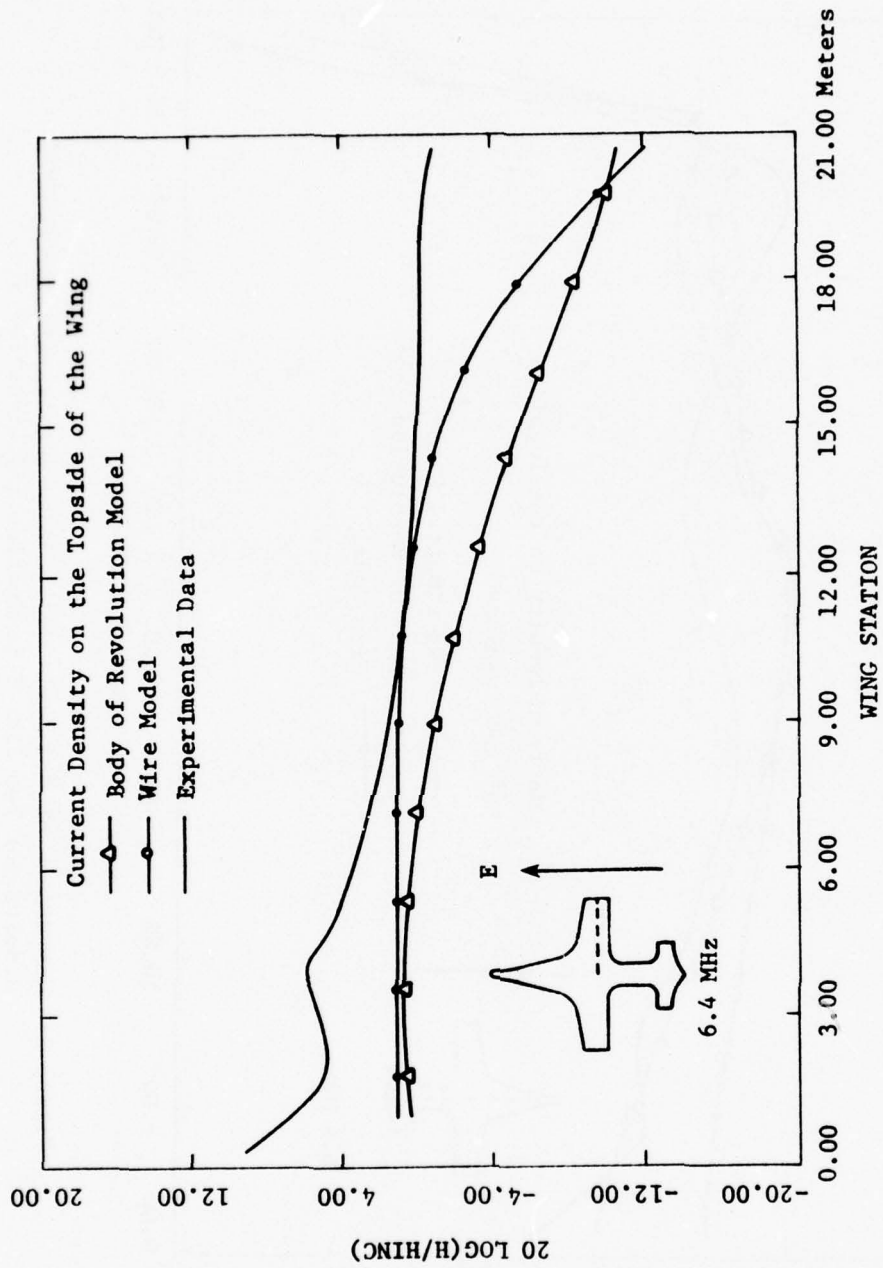


Figure 7: Comparison of B-1 Scale Mode Measurements with Theoretical Results for Top Side Illumination and Wings Forward.  $f = 6.4$  MHz.

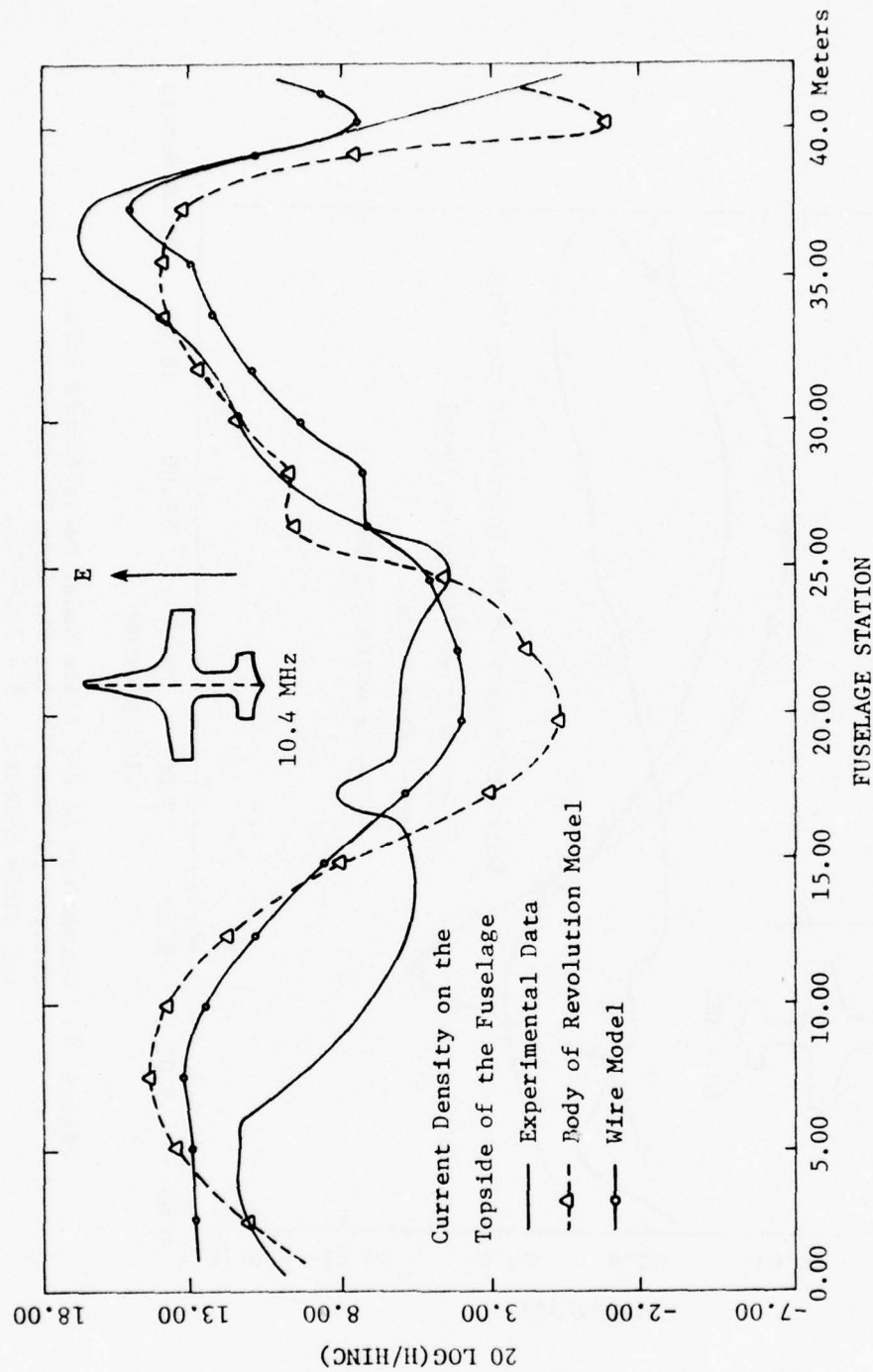


Figure 8: Comparison of B-1 Scale Model Measurements with Theoretical Results for Top Side Illumination and Wings Forward.  
 $f = 10.4$  MHz.

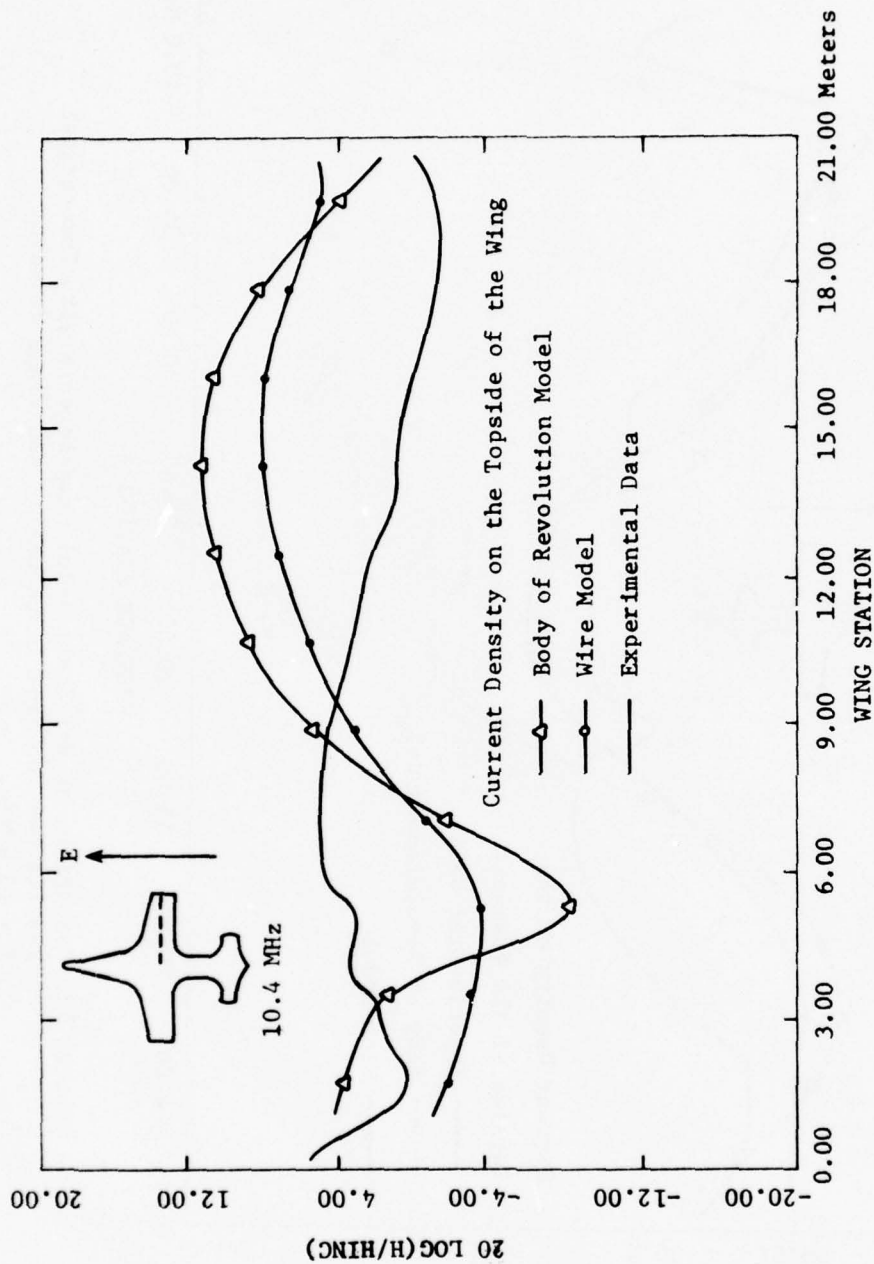


Figure 9: Comparison of B-1 Scale Model Measurements with Theoretical Results for Top Side Illumination and Wings Forward.  $f \approx 10.4$  MHz.

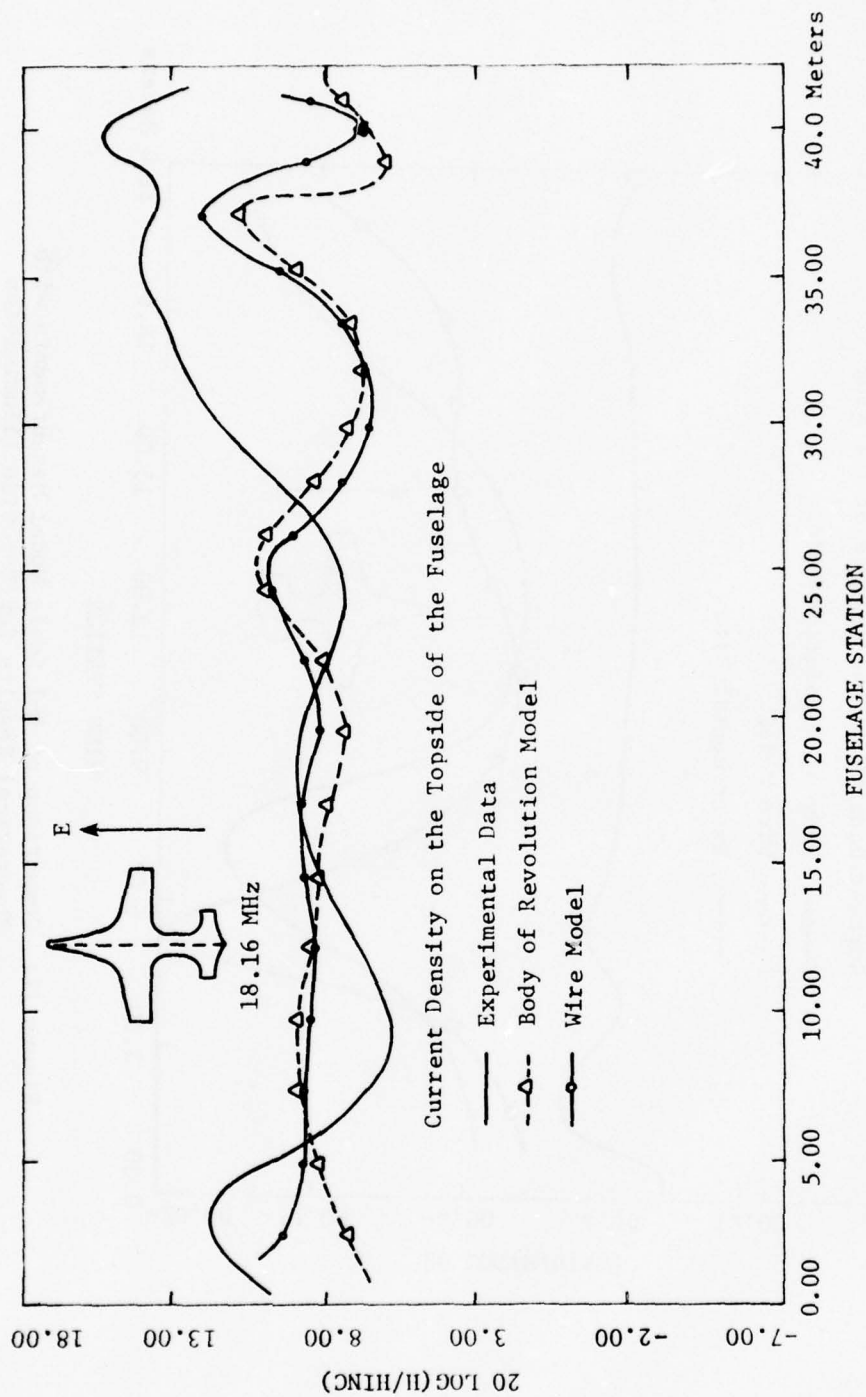
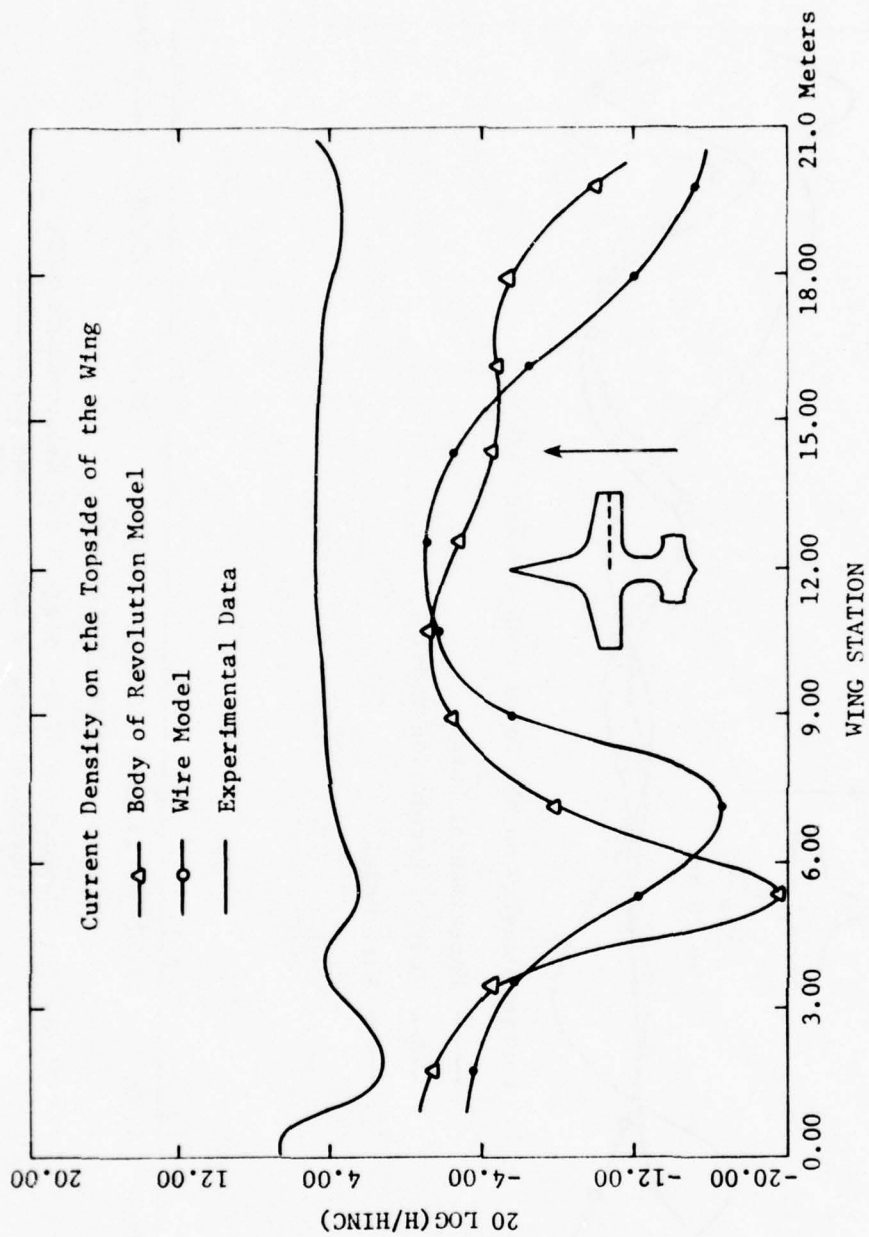


Figure 10: Comparison of B-1 Scale Model Measurements with Theoretical Results for Top Side Illumination and Wings Forward.  $f = 18.16$  MHz.





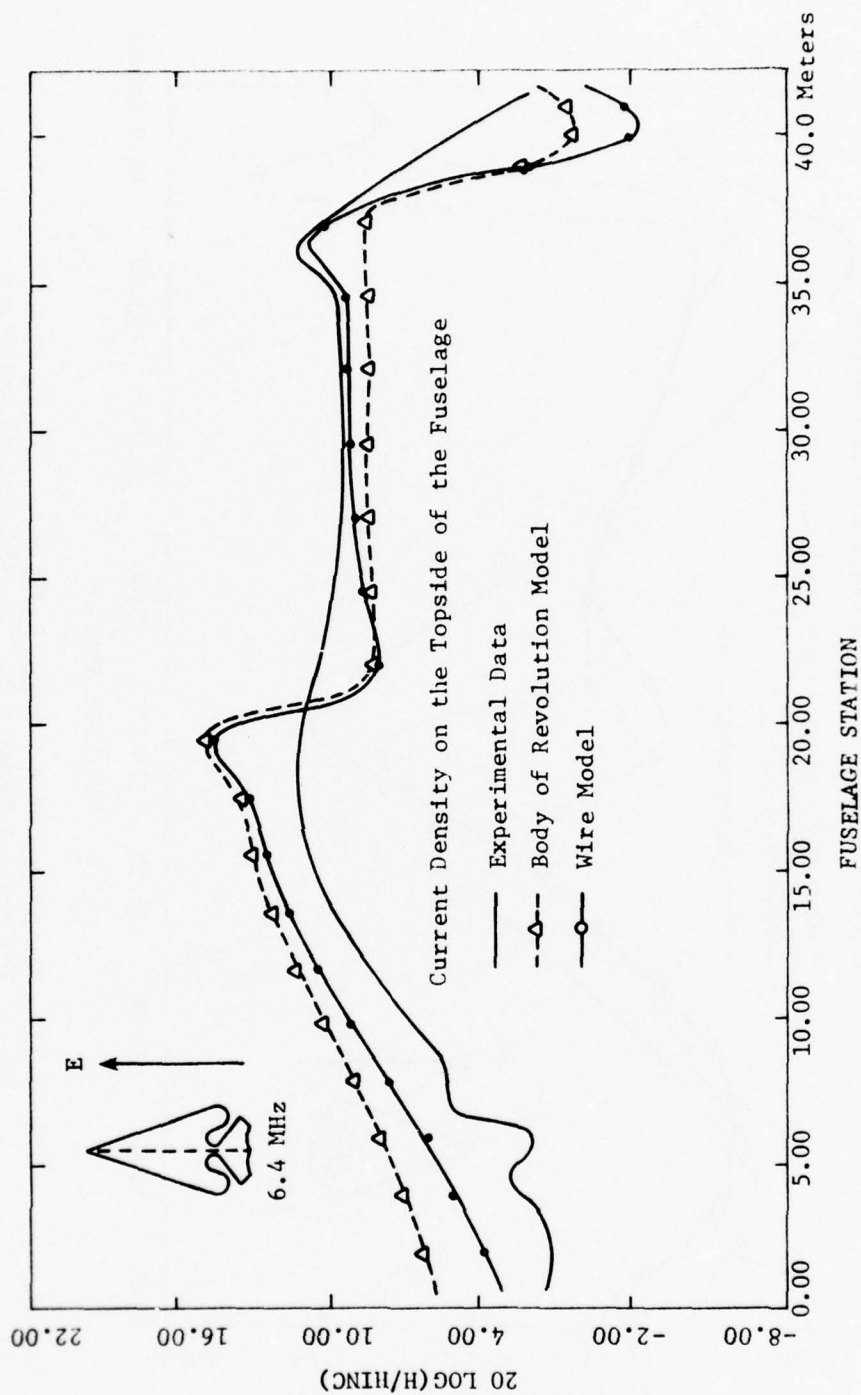


Figure 12: Comparison of B-1 Scale Model Measurements with Theoretical Results for Top Side Illumination and Wings Swept.  $f = 6.4 \text{ MHz}$ .

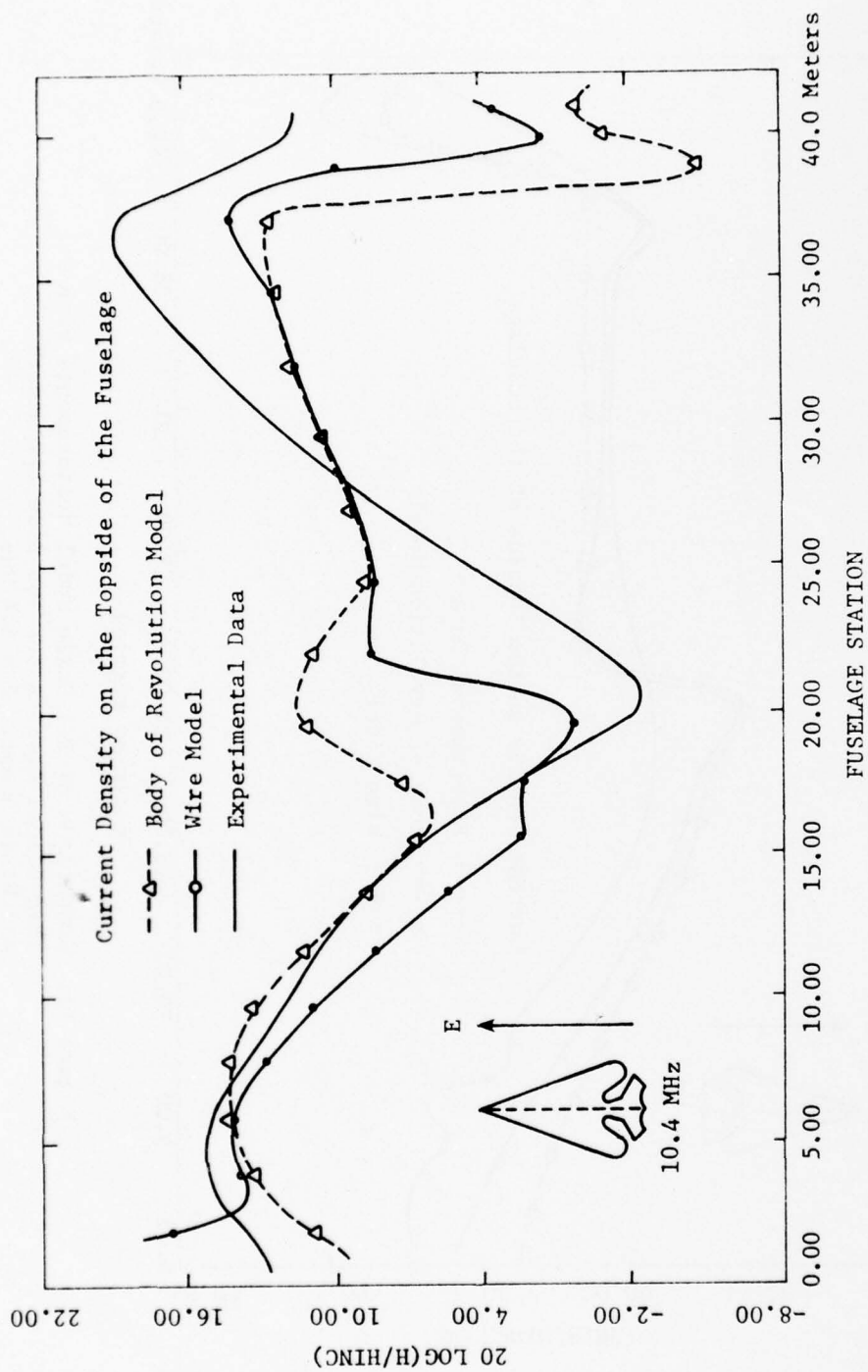


Figure 13: Comparison of B-1 Scale Model Measurements with Theoretical Results for Top Side Illumination and Wings Swept.  $f = 10.4$  MHz.

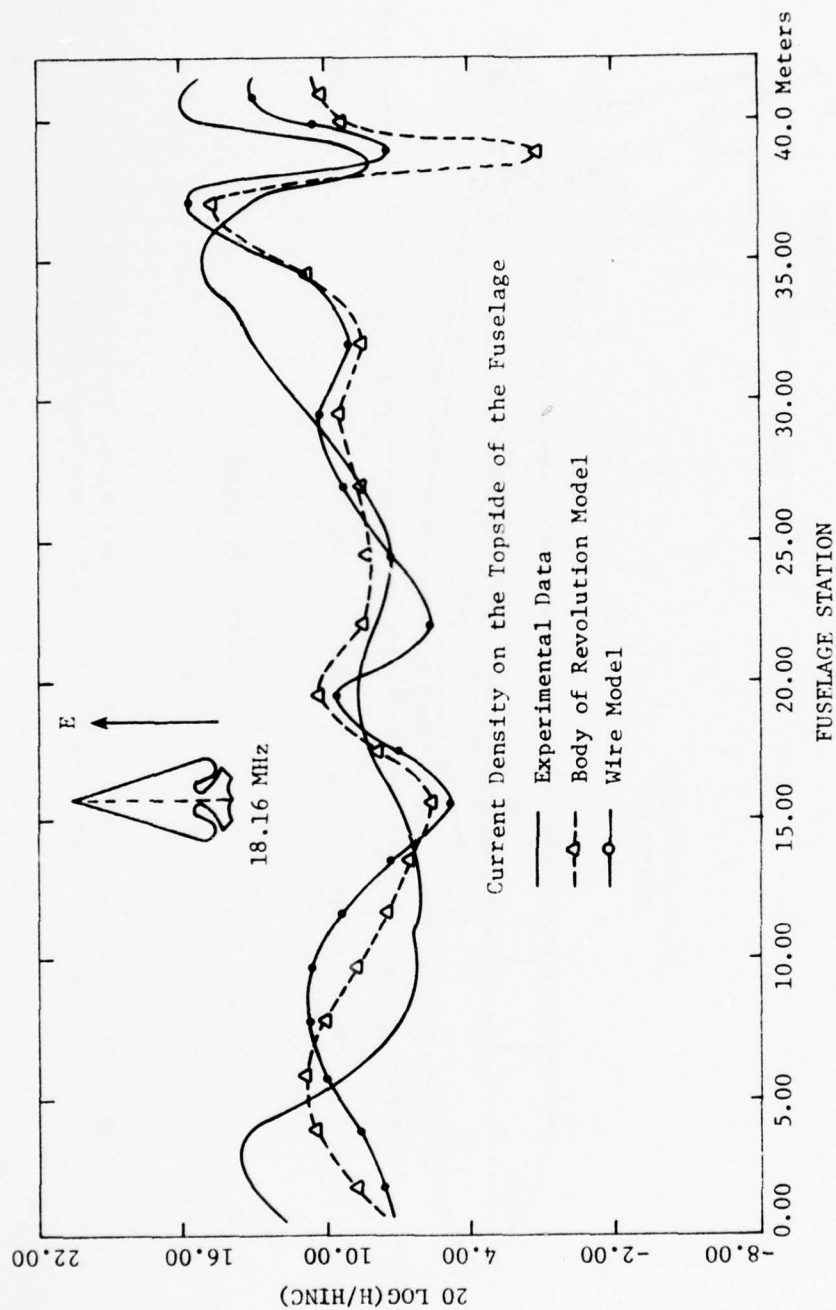


Figure 14: Comparison of B-1 Scale Model Measurements with Theoretical Results for Top Side Illumination and Wings Swept.  $f = 18.16$  MHz.

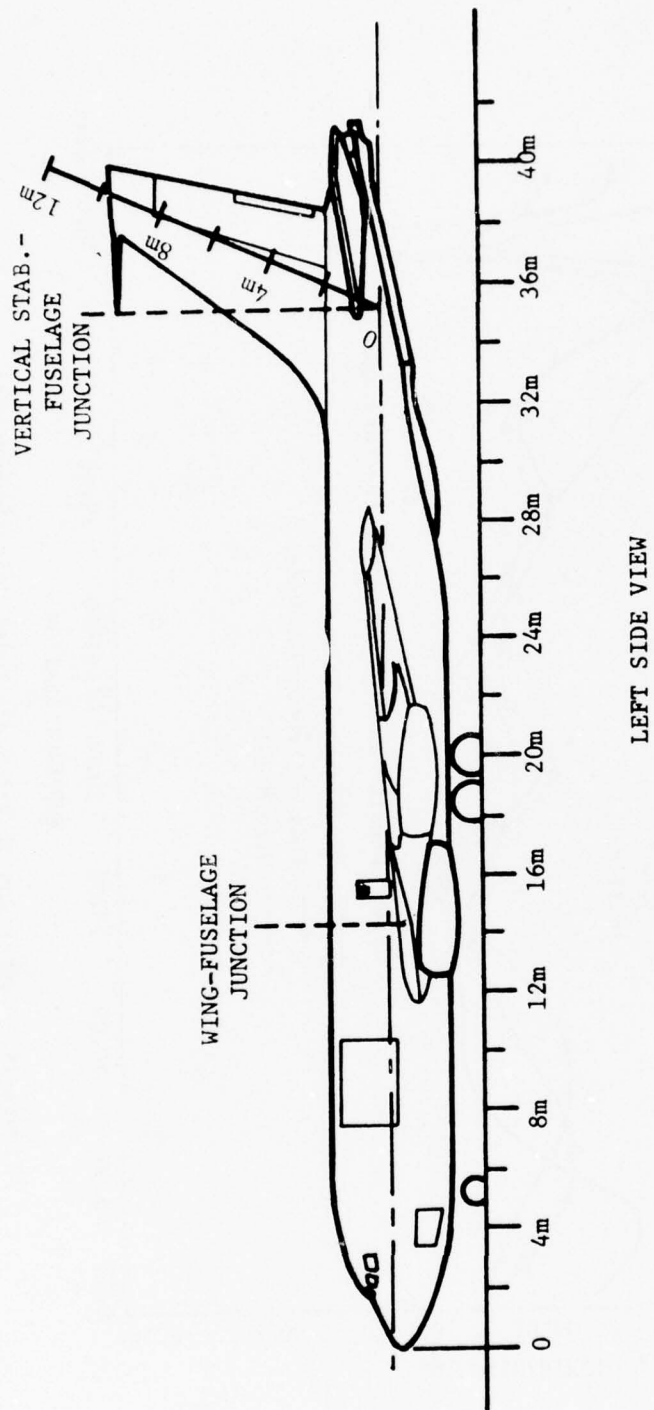


Figure 15: EC-135 Aircraft in the Ground Alert Mode. Fuselage and Vertical Stabilizer Station Numbers are Shown in Meters.



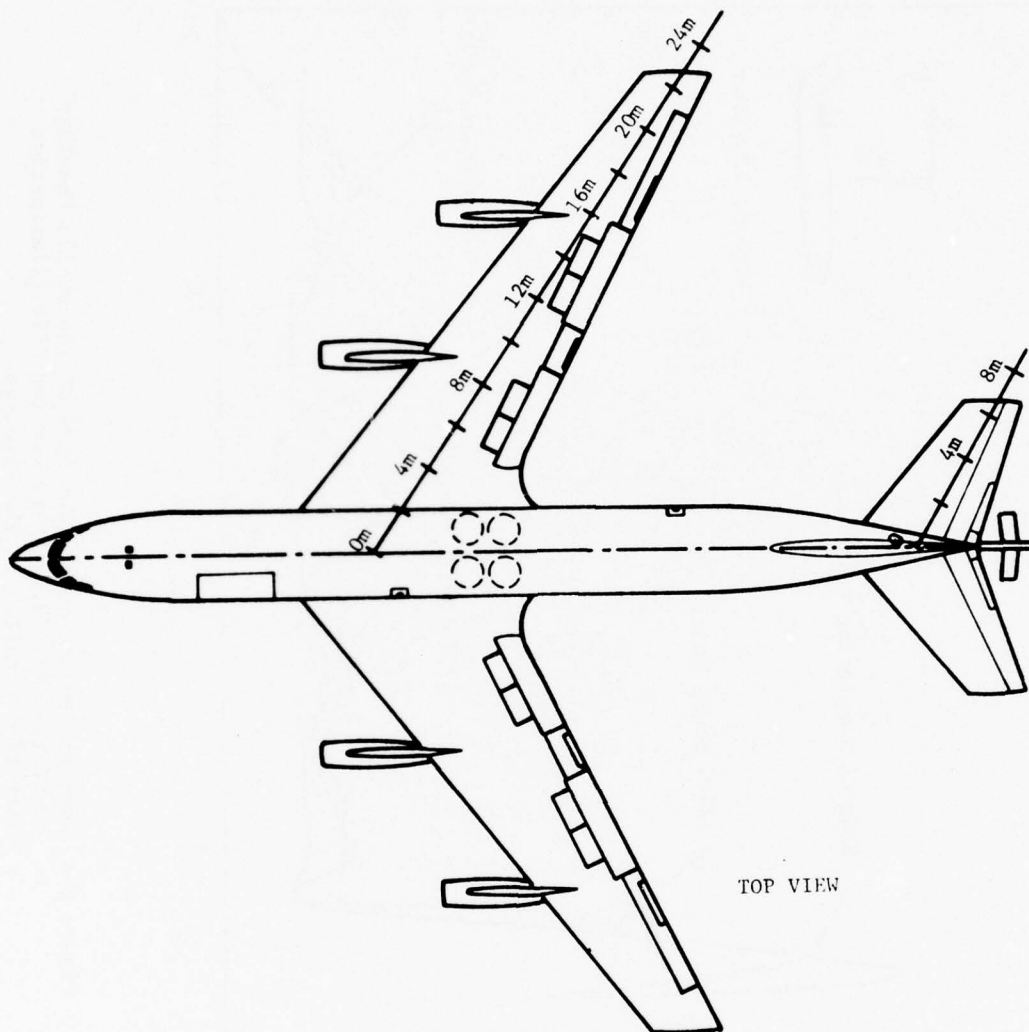


Figure 16: EC-135 Aircraft in the Inflight Mode. Wing and Horizontal Stabilizer Station Numbers are Shown in Meters.

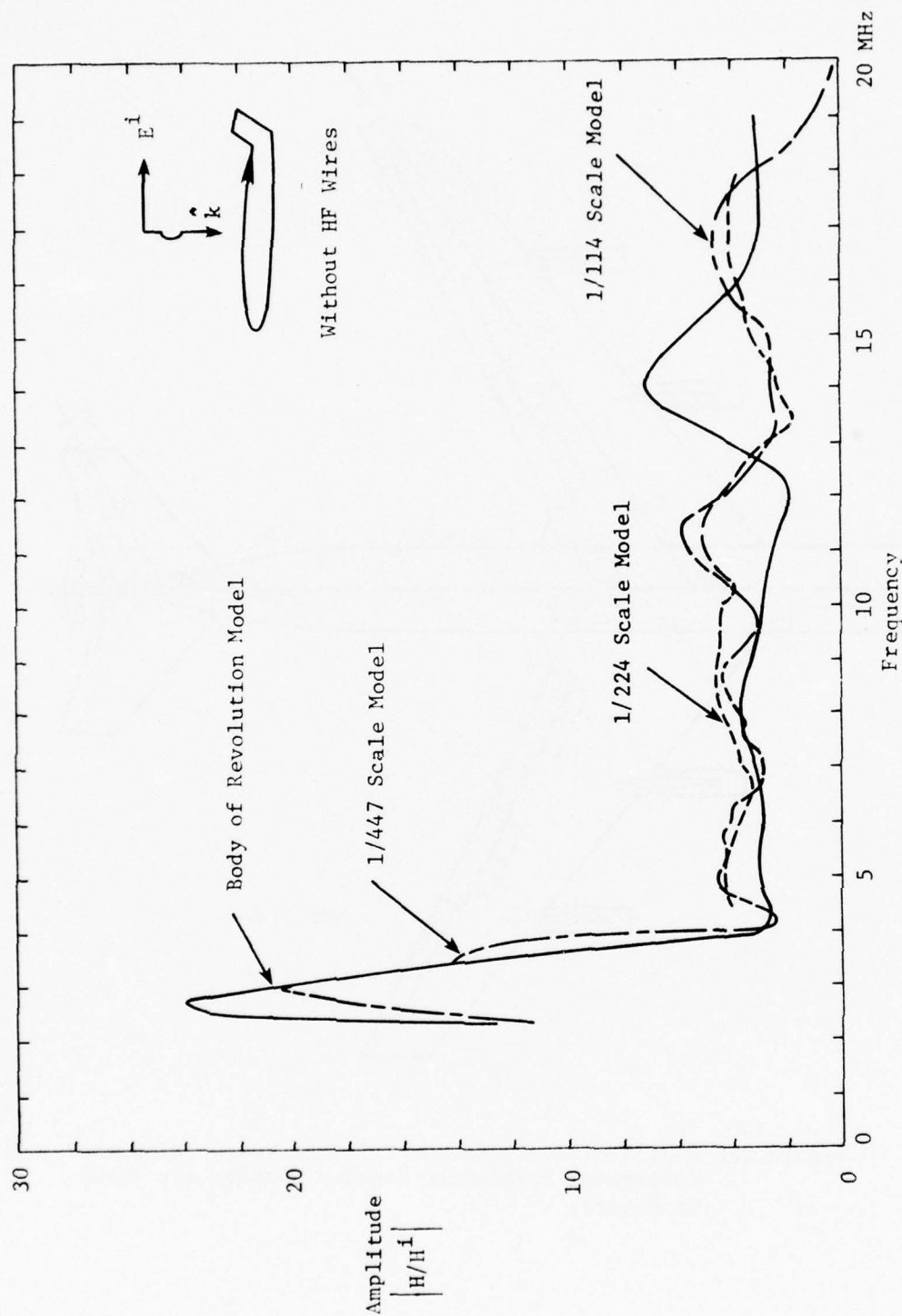


Figure 17: Current Density on the Top Side of the EC-135 Fuselage at Station No. 22.5 meters for Top Side Illumination with  $E_{inc}$  Parallel to the Fuselage.

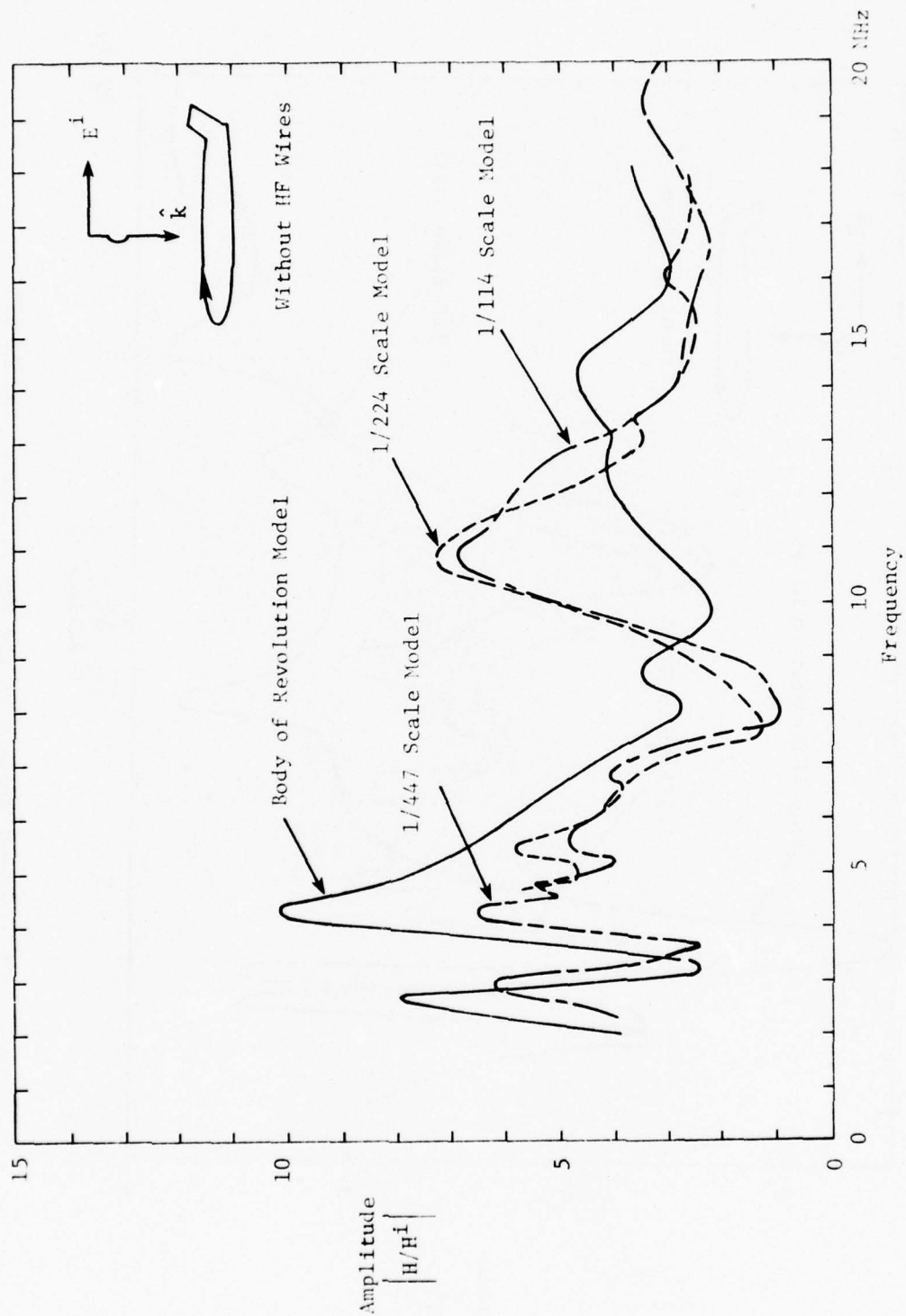


Figure 18: Current Density on the Top Side of the EC-135 Fuselage at Station No. 5.0 meters for Top Side Illumination with Einc Parallel to the Fuselage.

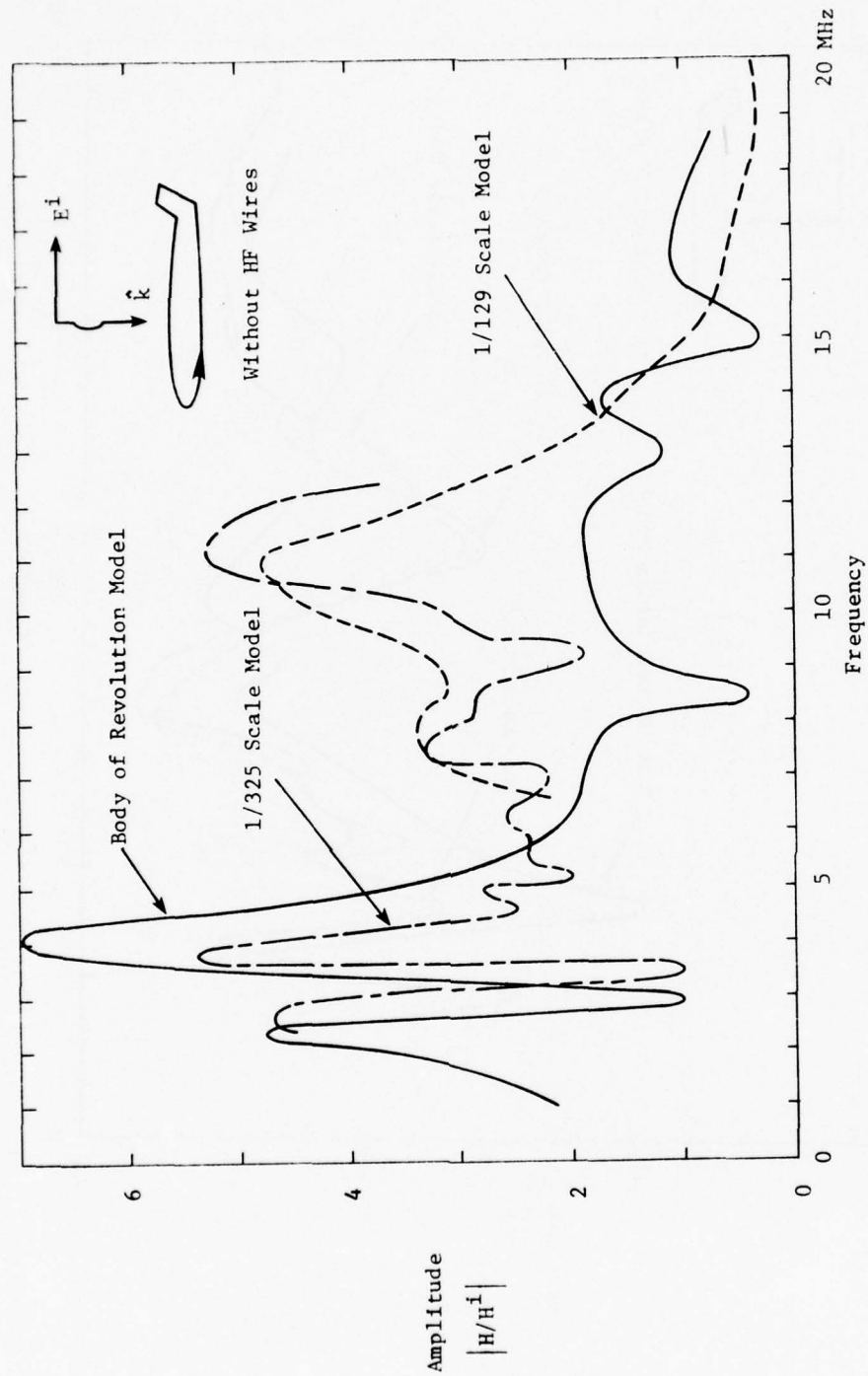


Figure 19: Current Density on the Bottom Side of the EC-135 Fuselage at Station No. 5.0 meters for Top Side Illumination with Einc Parallel to the Fuselage.

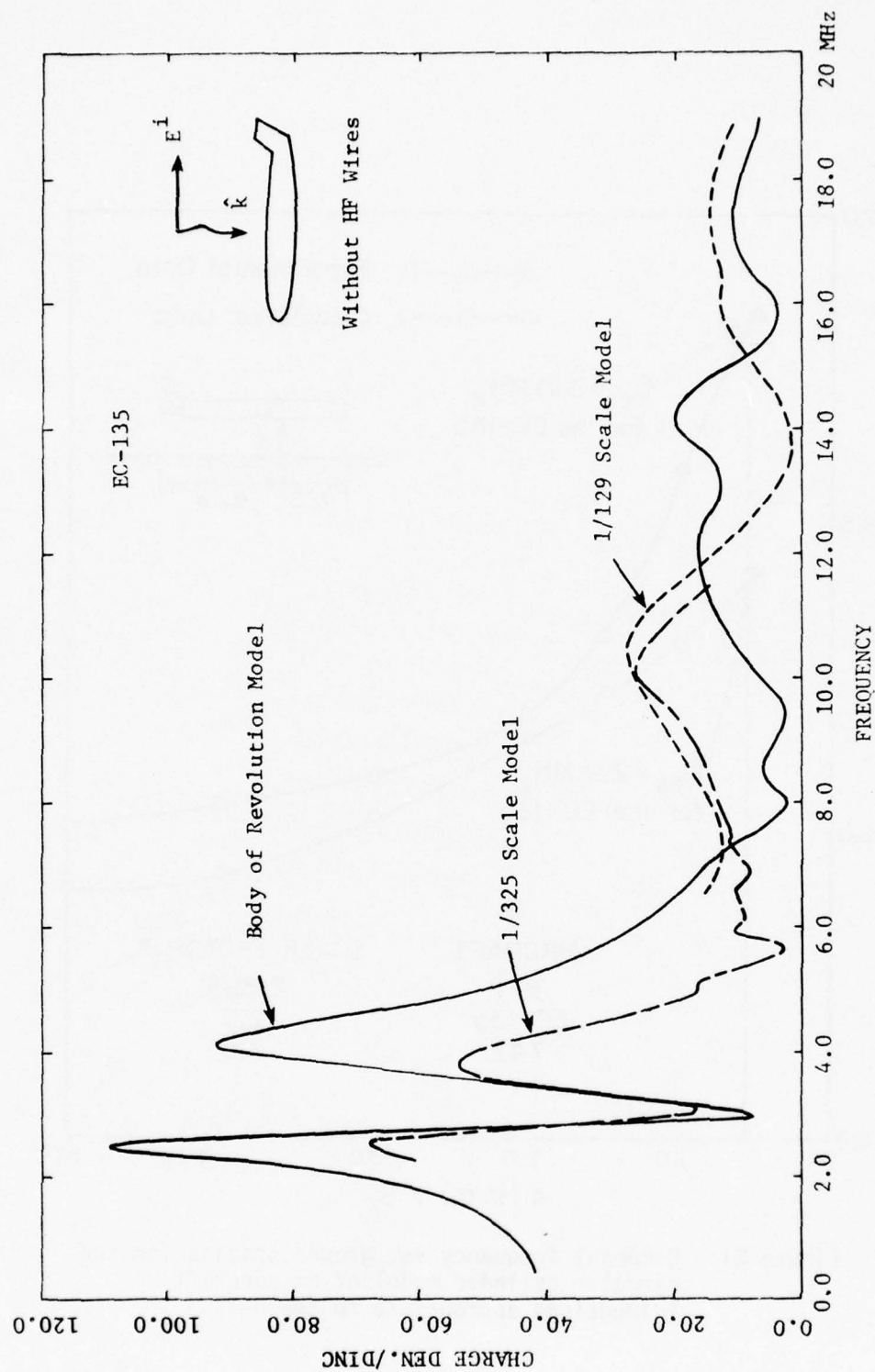


Figure 20: Charge Density on the Nose of the EC-135 Aircraft for Top Side Illumination with Einc Parallel to the Fuselage.



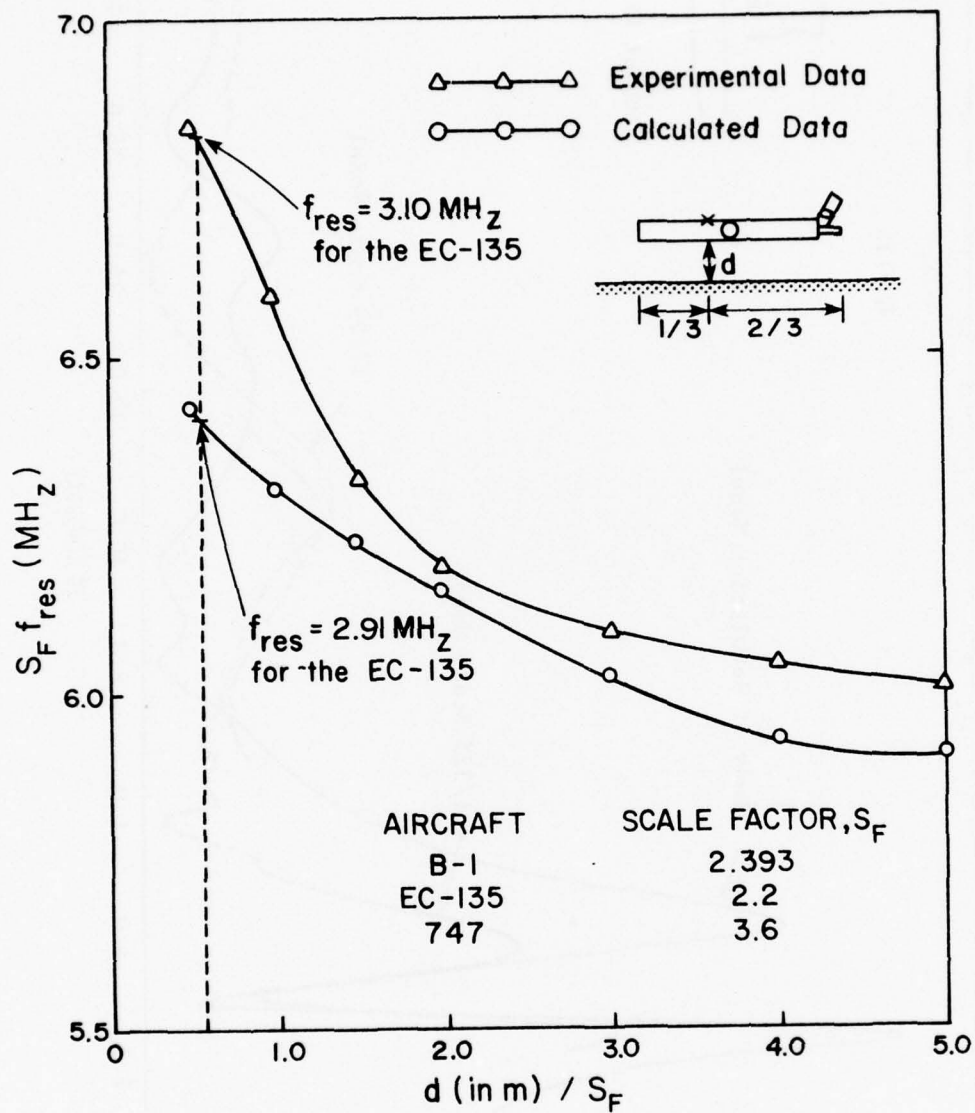


Figure 21: Resonant frequency vs. ground spacing for the circular cylinder model of an aircraft (dimensions appropriate to the B-1).

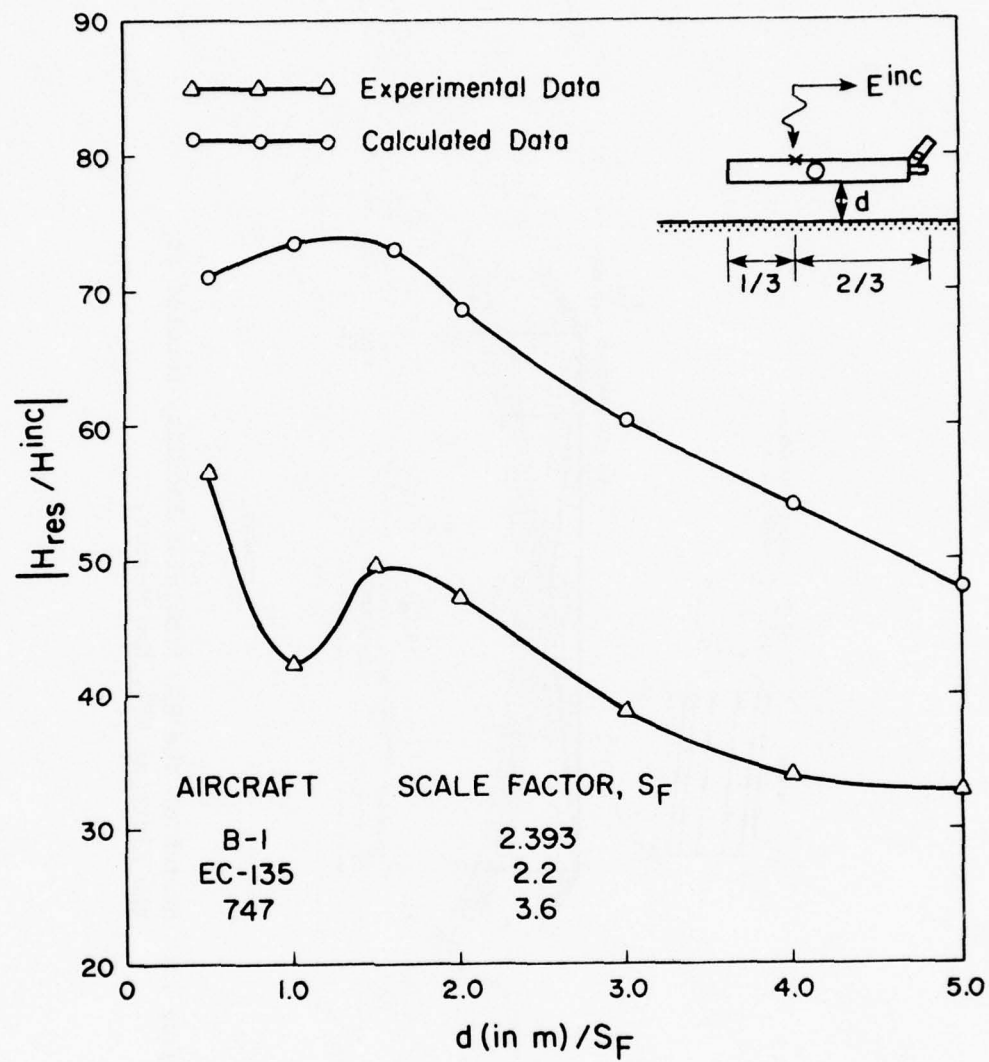


Figure 22: Surface current density at resonance vs. ground spacing for the circular cylinder model of an aircraft with dimensions appropriate to the B-1.

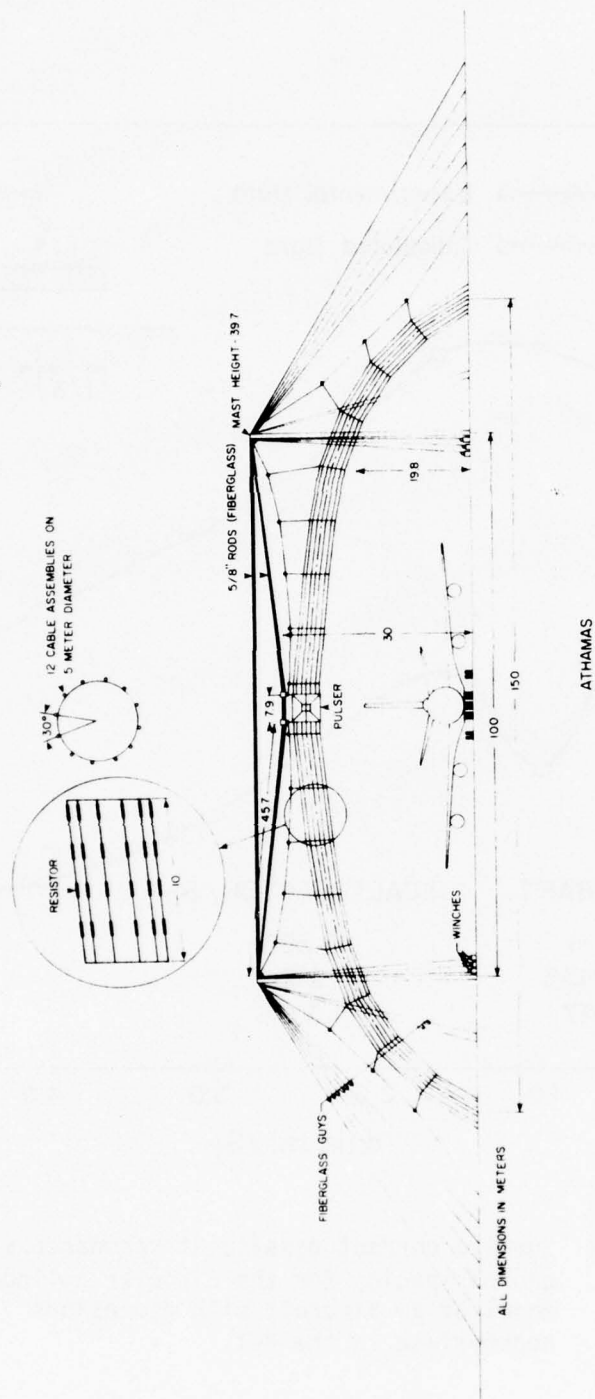


Figure 23: Sketch of the HPD Simulator Facility Located at the Kirtland AFB, New Mexico.

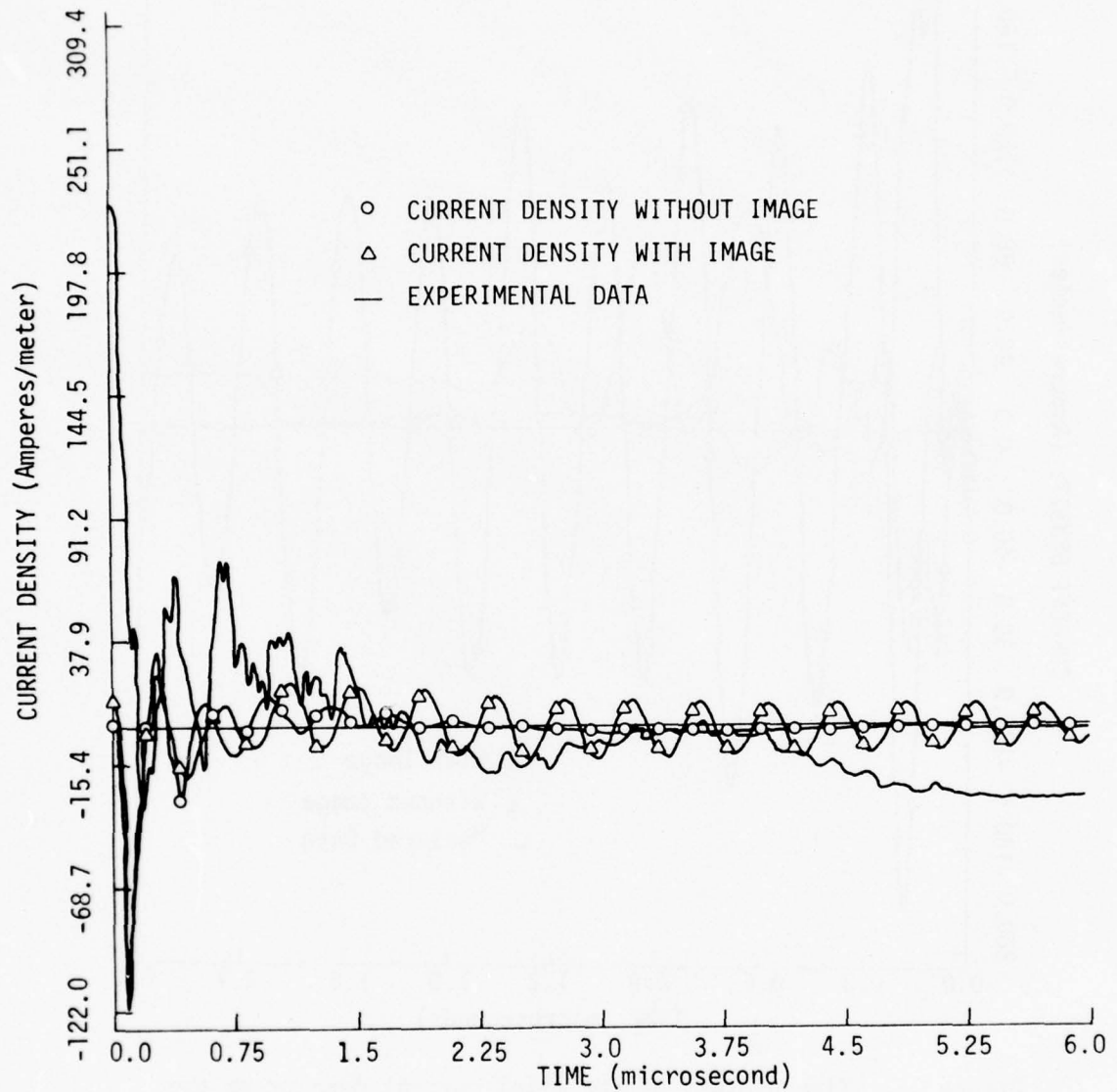


Figure 24: Time history of the axial current density on top of the fuselage (28 meters from the nose) for the EC-135 aircraft in the HPD simulator facility.

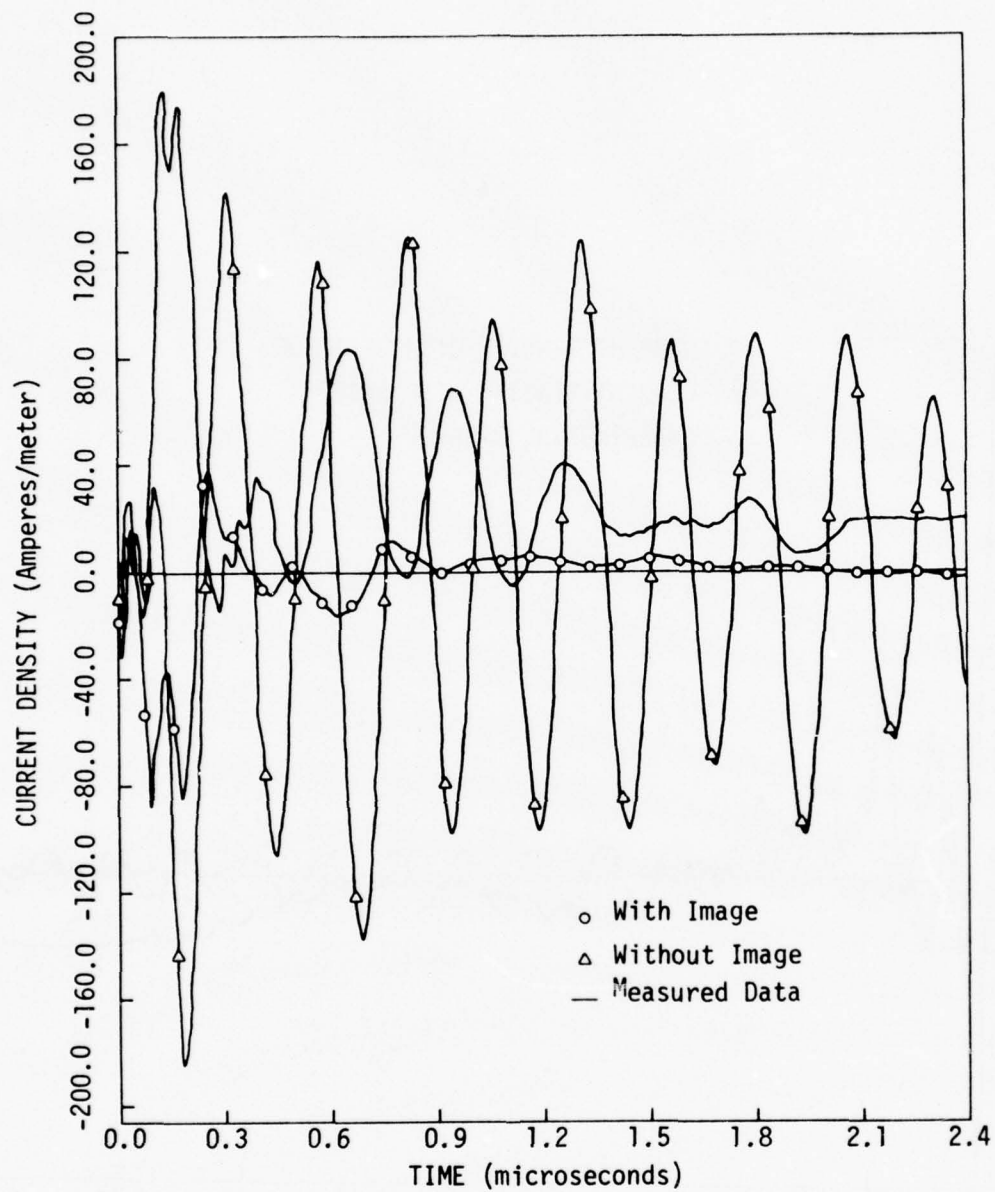


Figure 25: Time history of the axial current density on the bottom of the fuselage (13.5 meters from the nose) for the EC-135 aircraft in the HPD simulator facility.



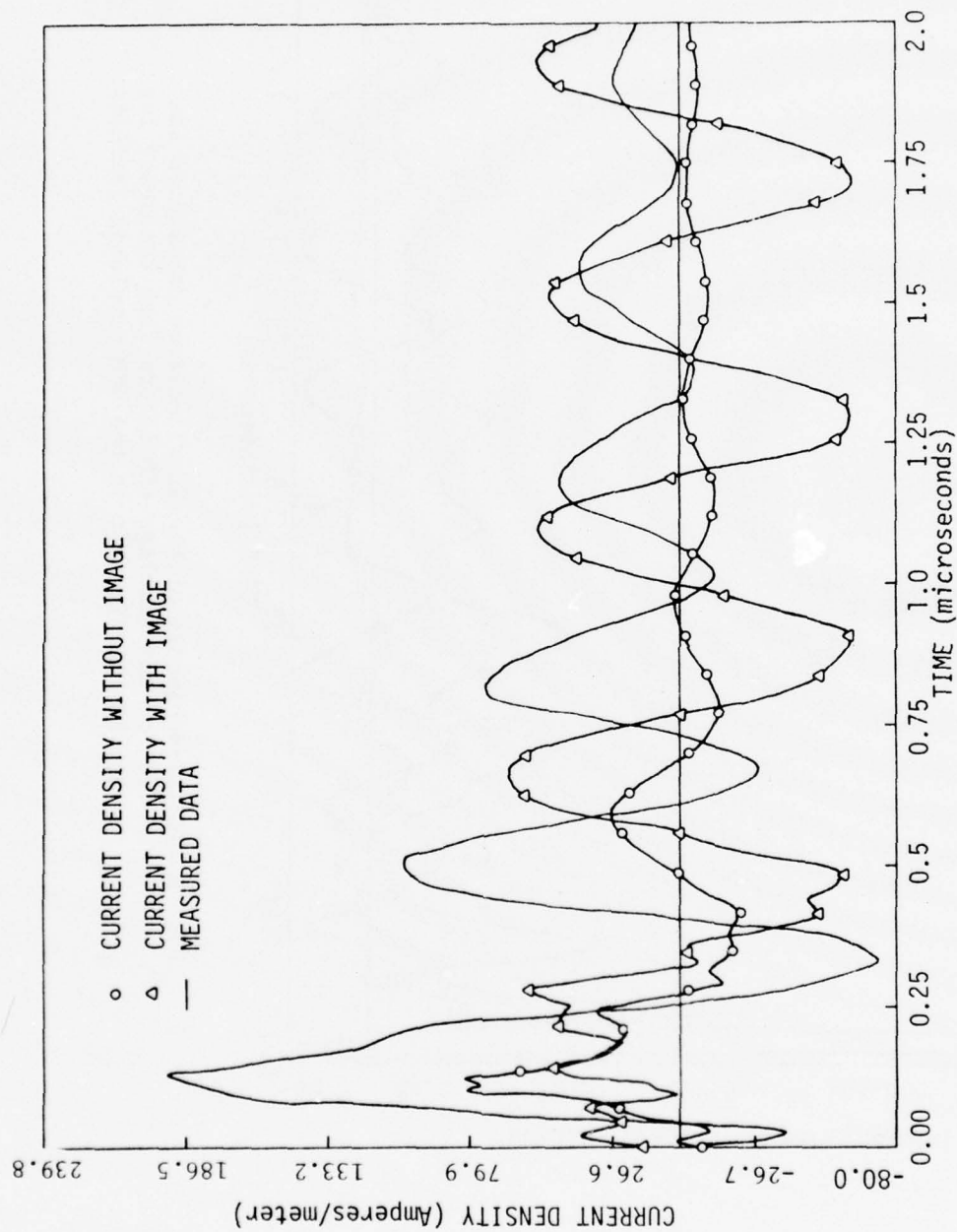


Figure 26: Time history of the axial current density on the bottom of the fuselage (28 meters from the nose) for the EC-135 aircraft in the HPD simulator facility.

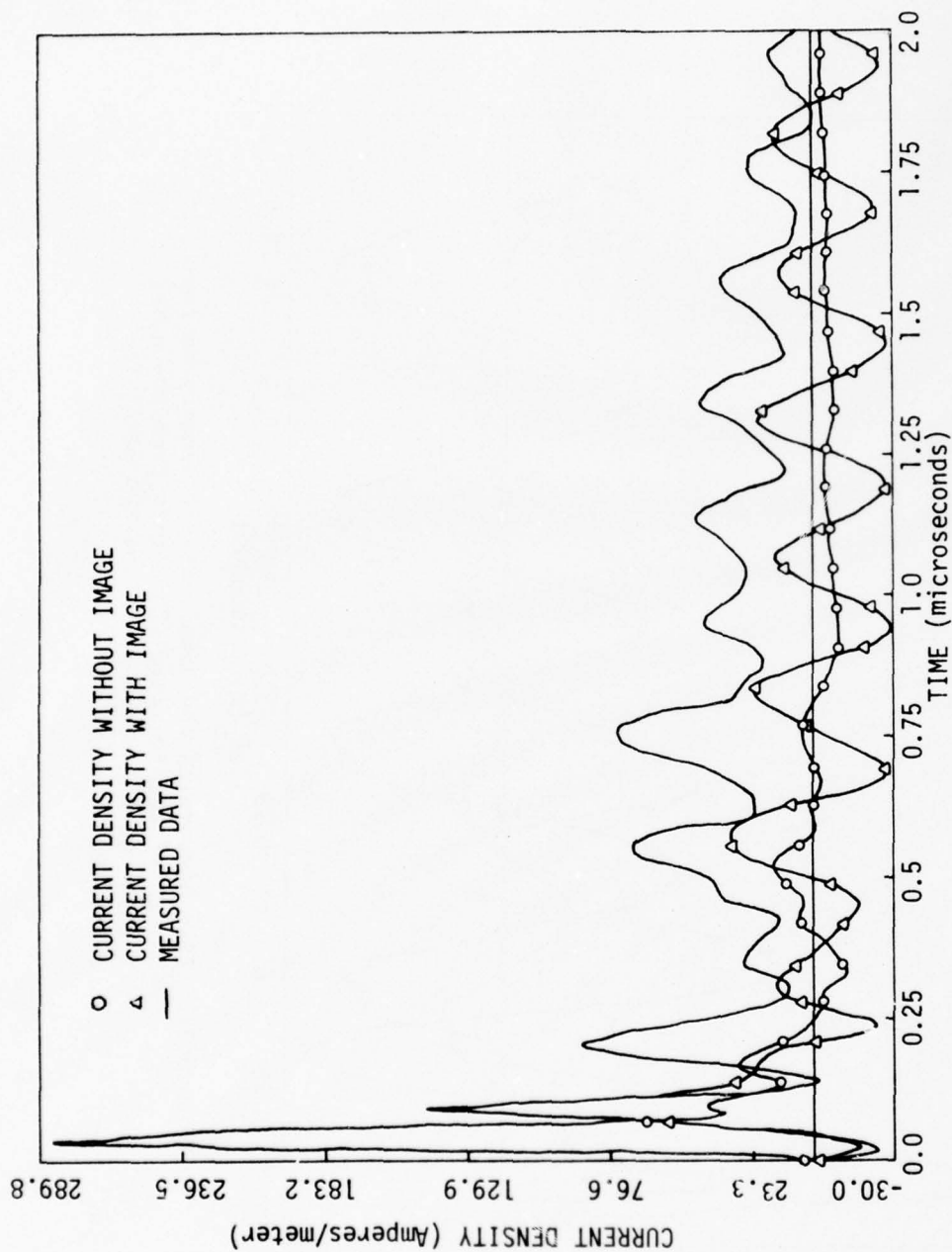


Figure 27: Time history of the axial current density on the top of the fuselage (10 meters from the nose) for the EC-135 aircraft in the HPD simulator facility.

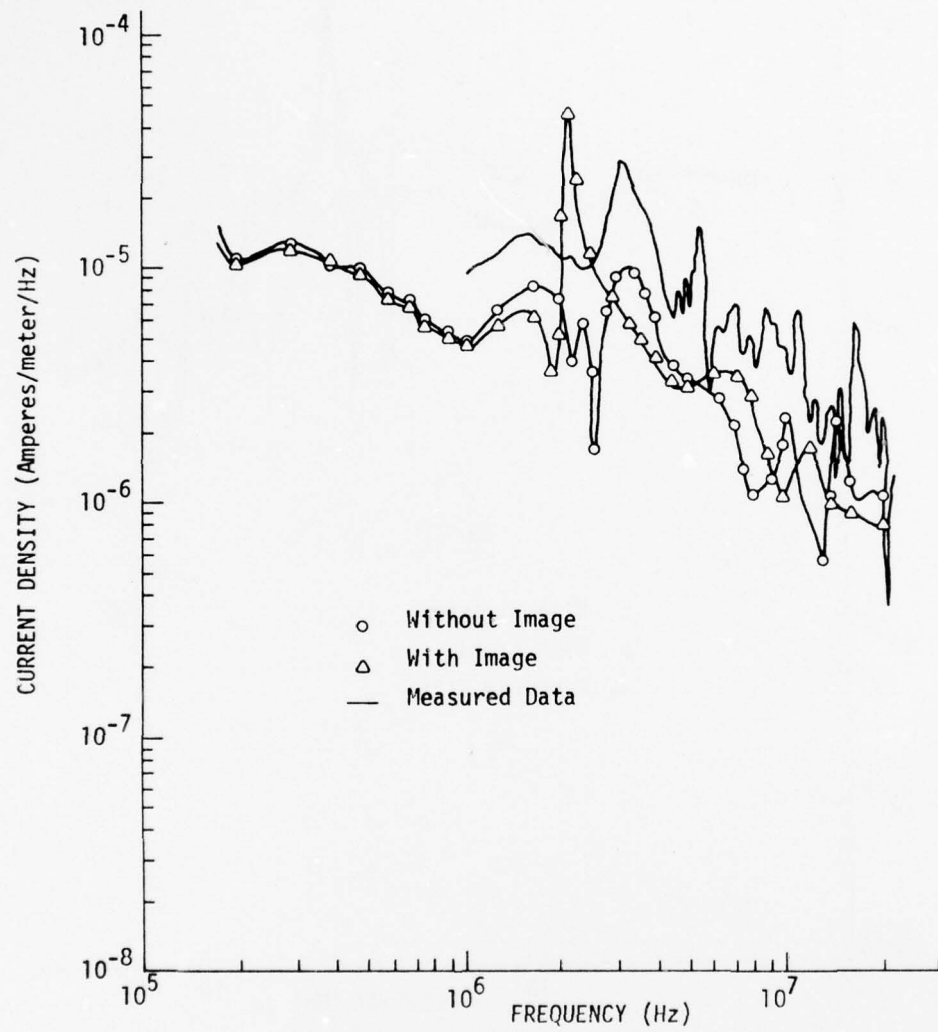


Figure 28: Fourier transform of the axial current density on top of the fuselage (28 meters from the nose) for the EC-135 aircraft in the HPD simulator facility.

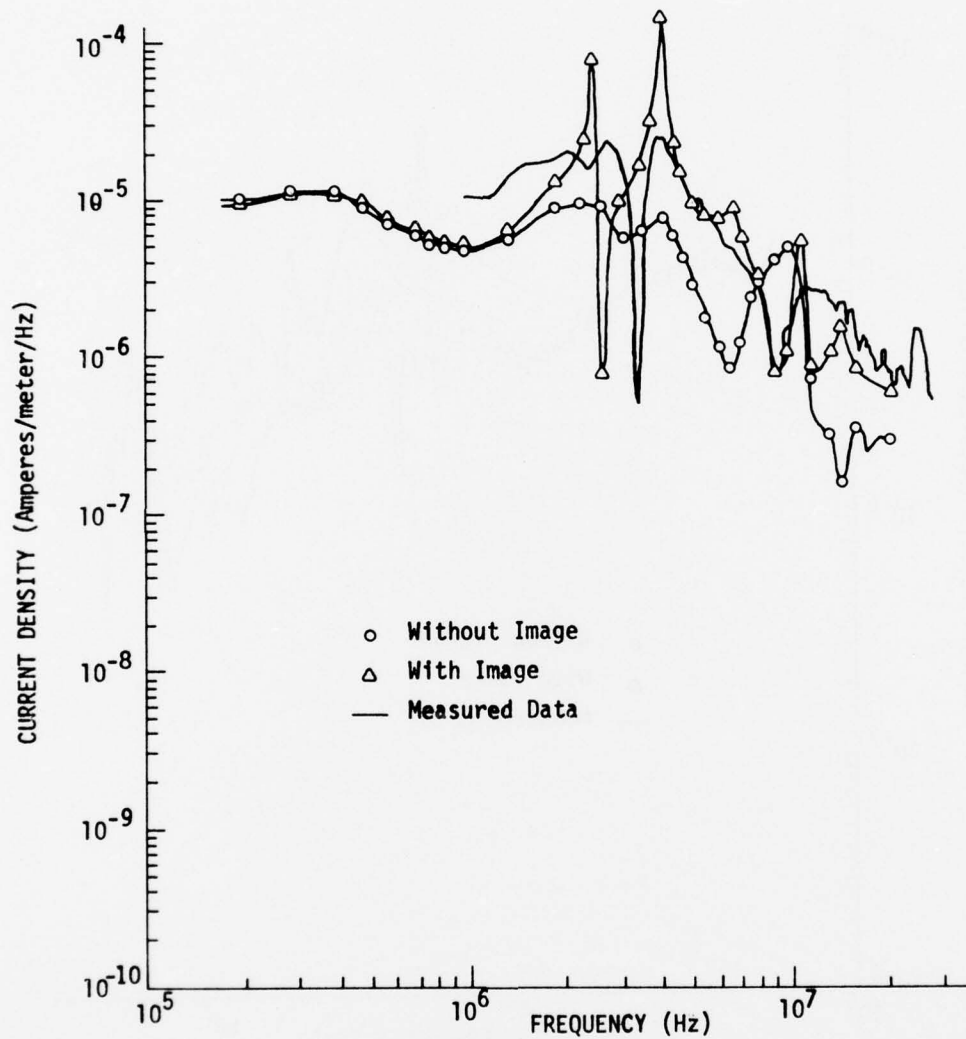


Figure 29: Fourier transform of the axial current density on the bottom of the fuselage (13.5 meters from the nose) for the EC-135 aircraft in the HPD simulator facility.

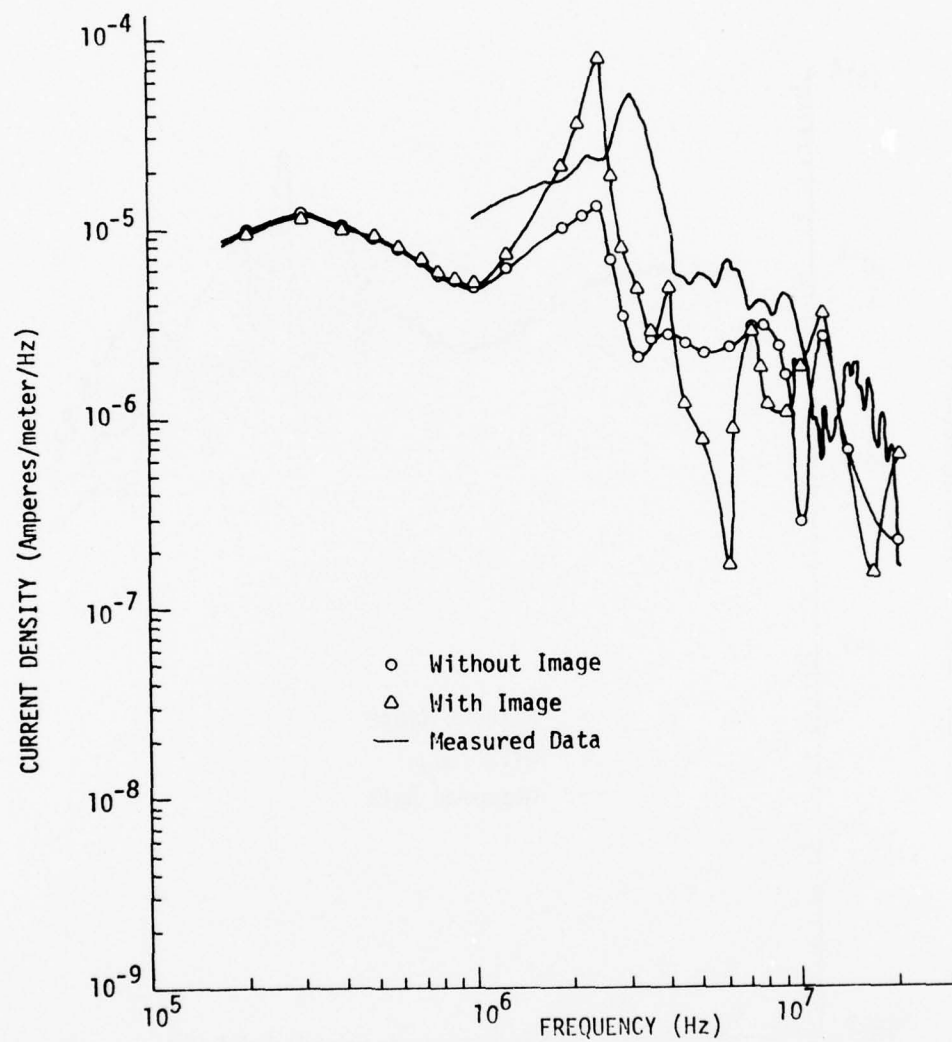


Figure 30: Fourier transform of the axial current density on the bottom of the fuselage (28 meters from the nose) for the EC-135 aircraft in the HPD simulator facility.



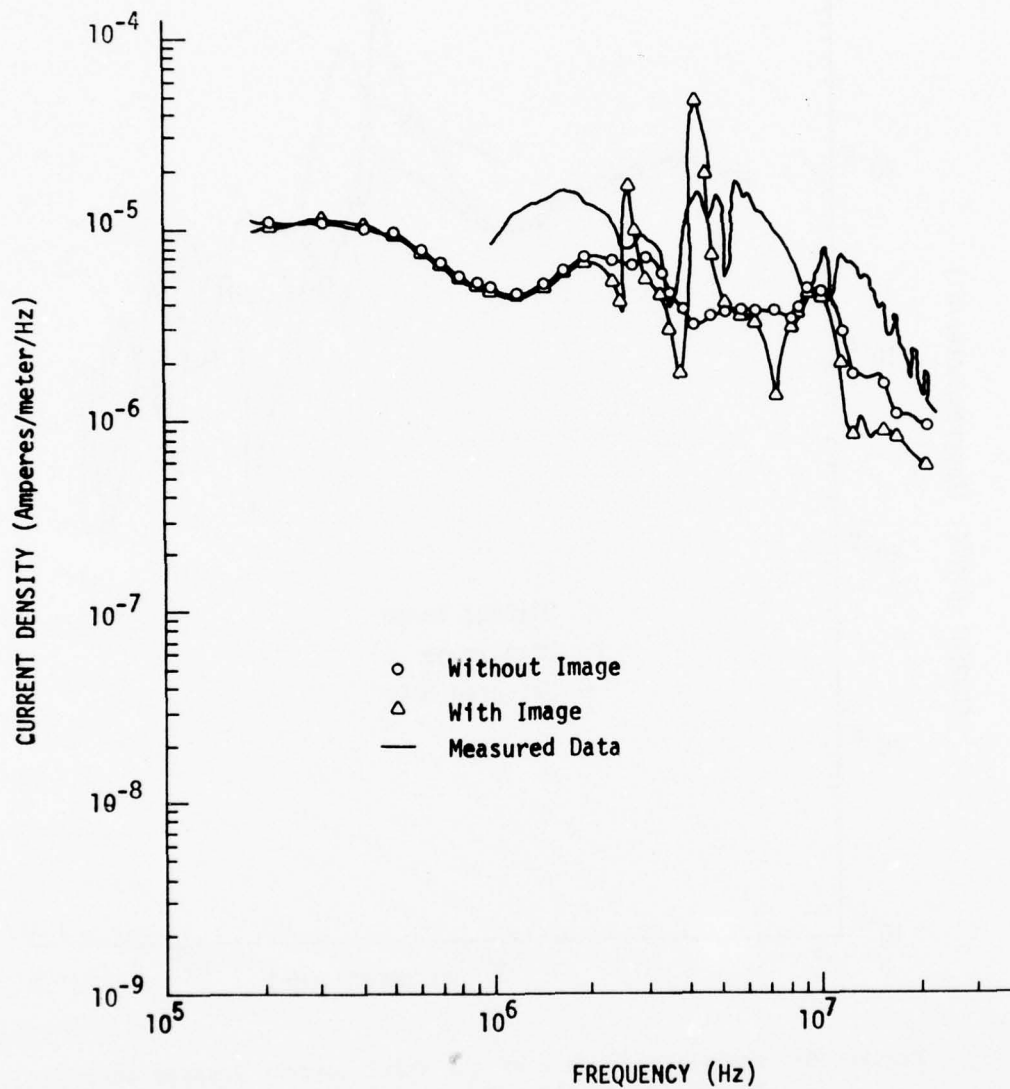


Figure 31: Fourier transform of the axial current density on top of the fuselage (10 meters from the nose) for the EC-135 aircraft in the HPD simulator facility.

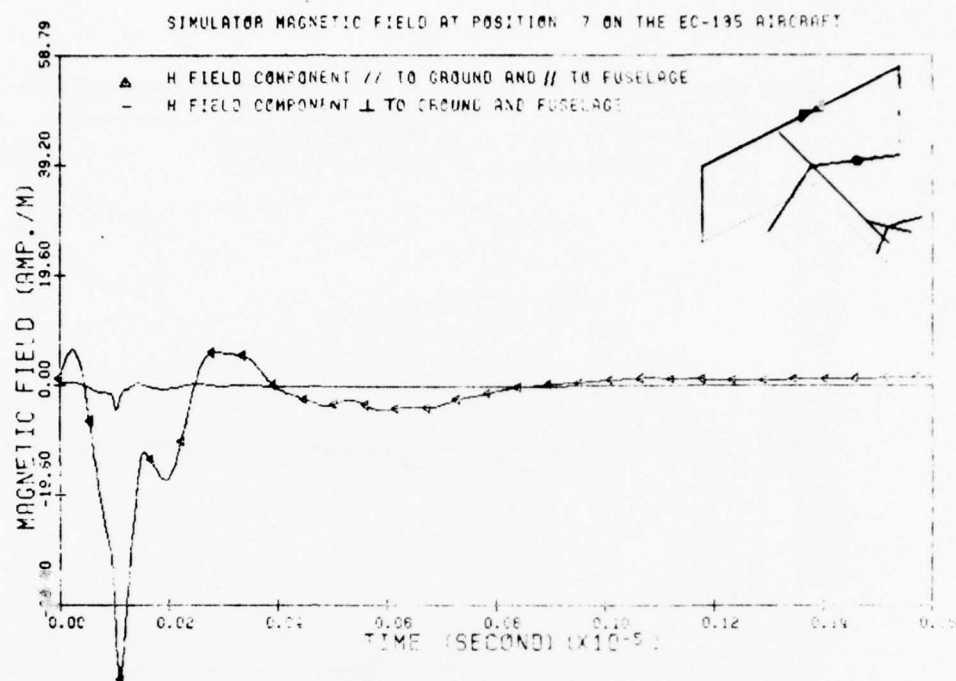


Figure 32:

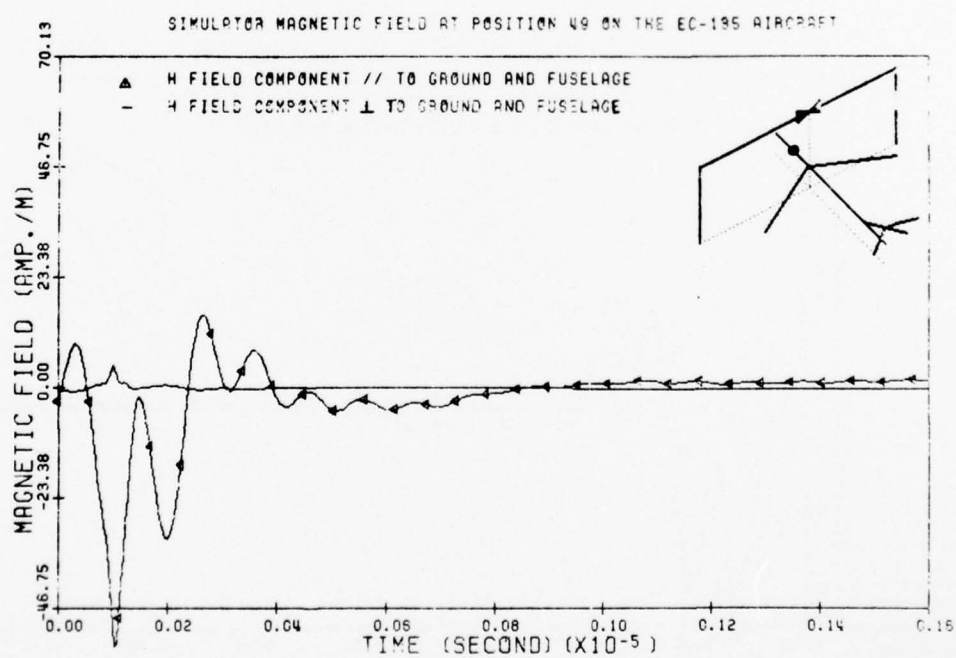


Figure 33:

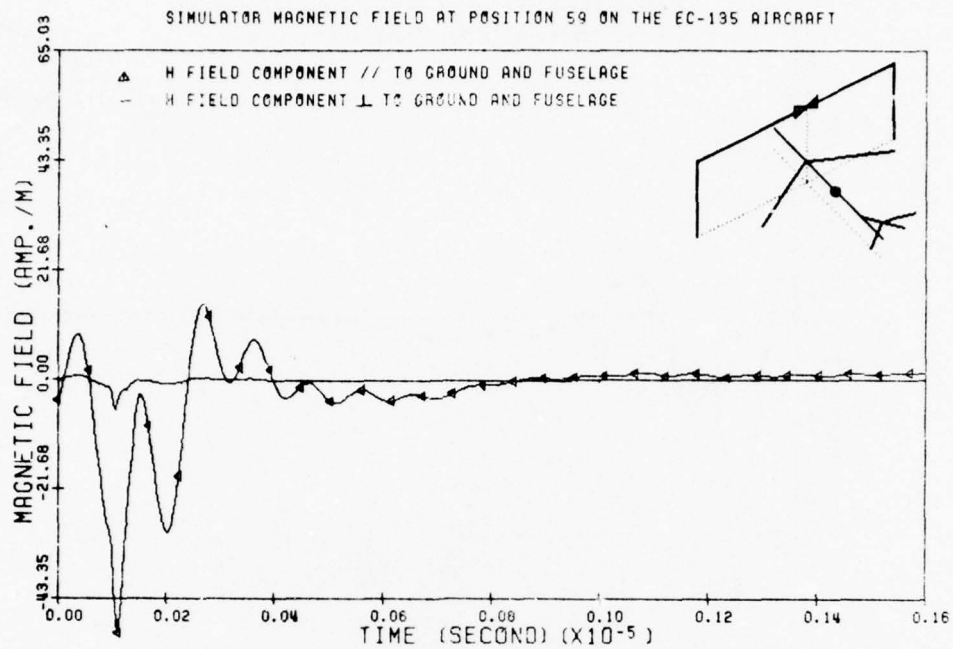


Figure 34:

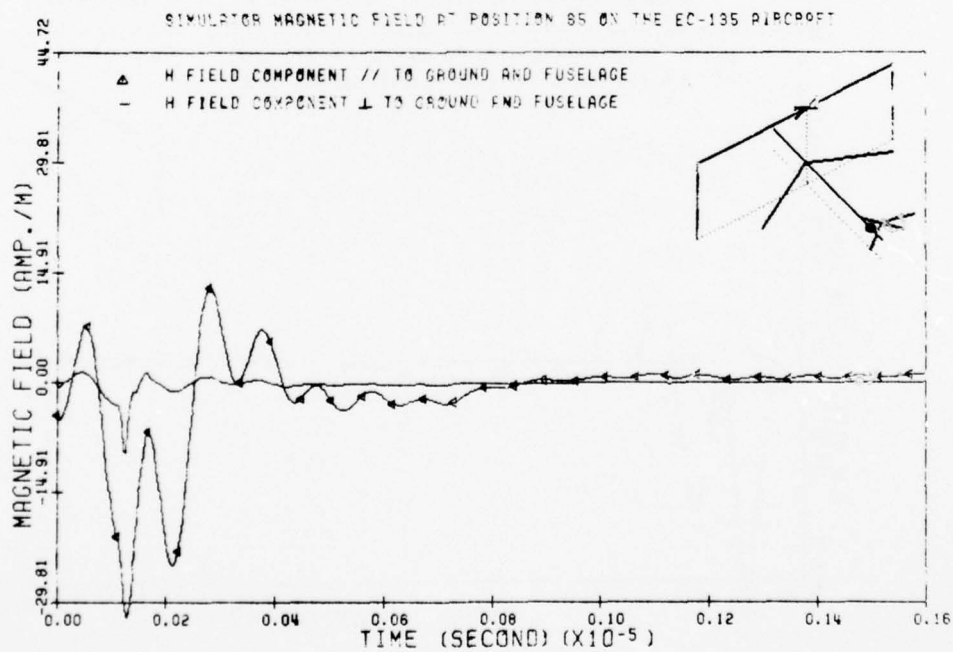


Figure 35:

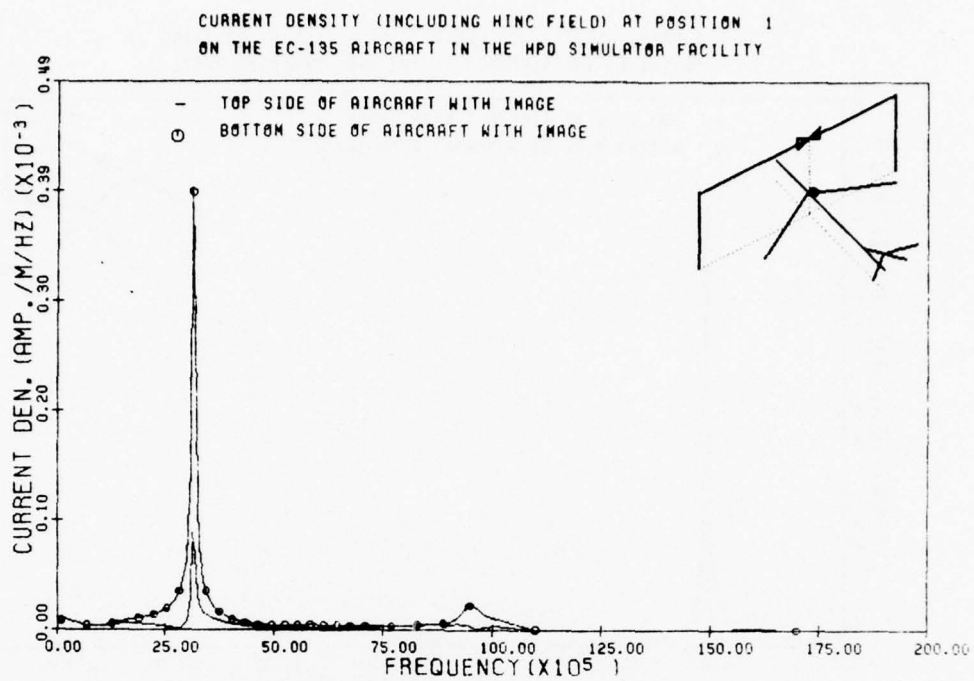


Figure 36:

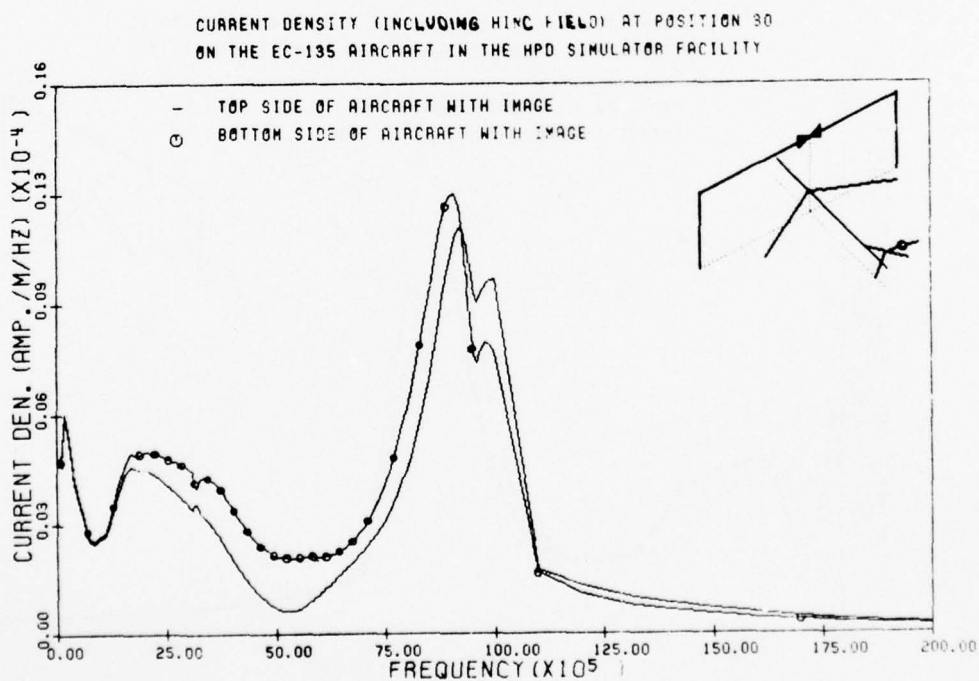


Figure 37:

CURRENT DENSITY (INCLUDING HINC FIELD) AT POSITION 7  
ON THE EC-135 AIRCRAFT IN THE HPD SIMULATOR FACILITY

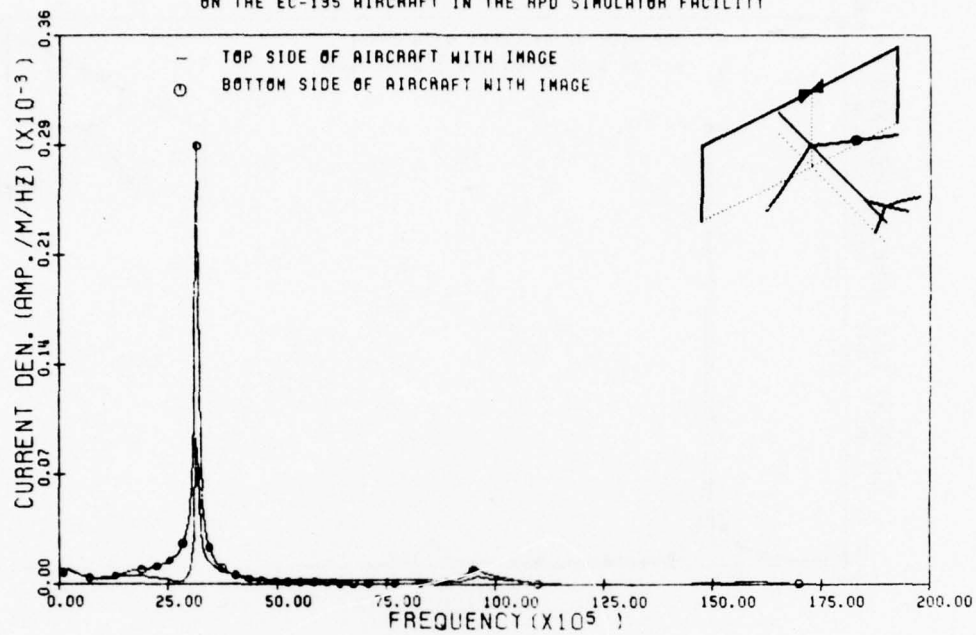


Figure 38:

CURRENT DENSITY (INCLUDING HINC FIELD) AT POSITION 27  
ON THE EC-135 AIRCRAFT IN THE HPD SIMULATOR FACILITY

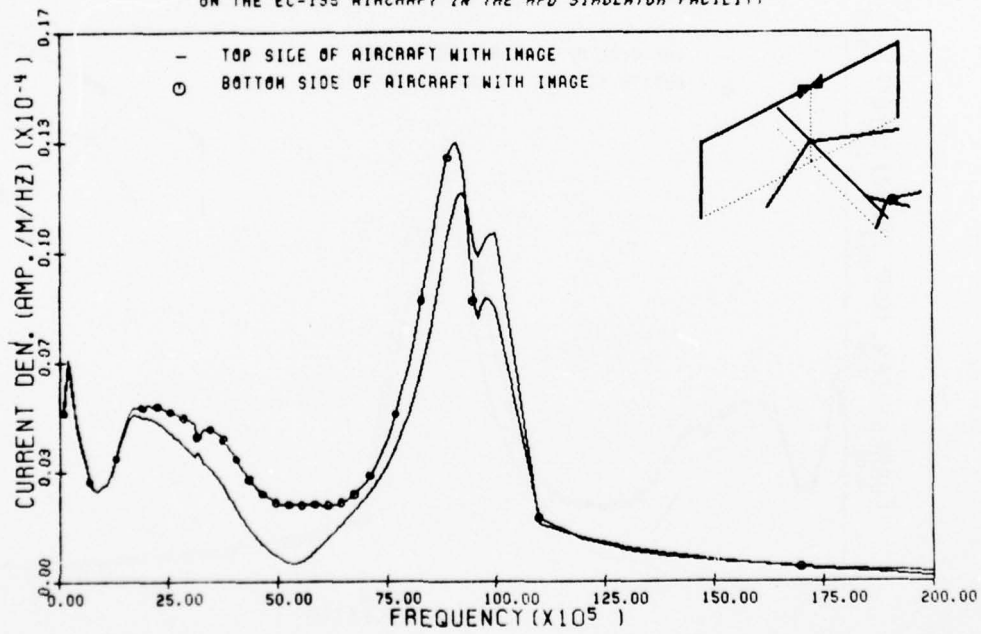


Figure 39:



# BEST AVAILABLE COPY

CURRENT DENSITY (INCLUDING HINC FIELD) AT POSITION 27  
ON THE EC-135 AIRCRAFT IN THE HPD SIMULATOR FACILITY

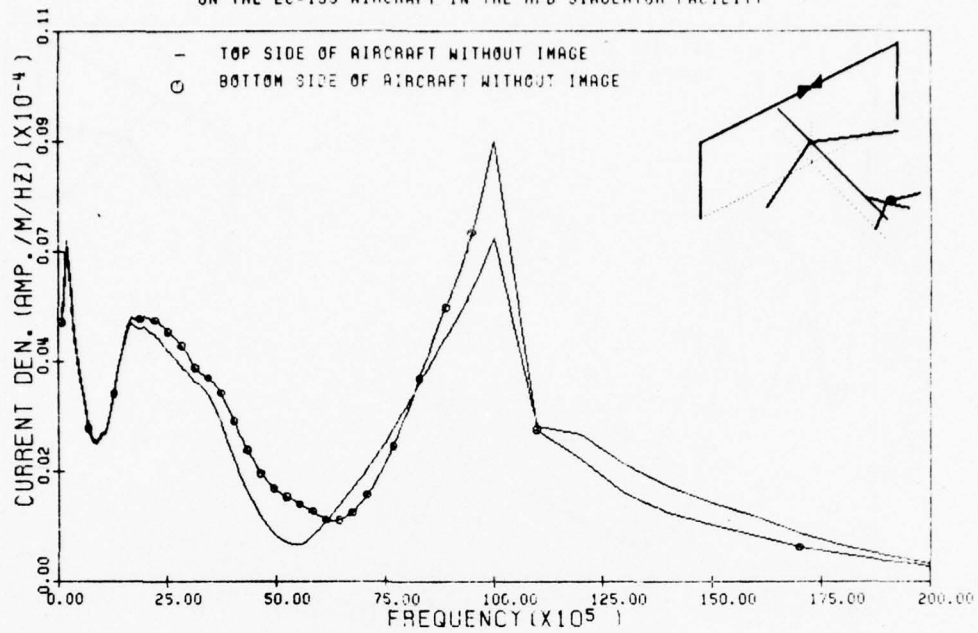


Figure 40:

CURRENT DENSITY (INCLUDING HINC FIELD) AT POSITION 30  
ON THE EC-135 AIRCRAFT IN THE HPD SIMULATOR FACILITY

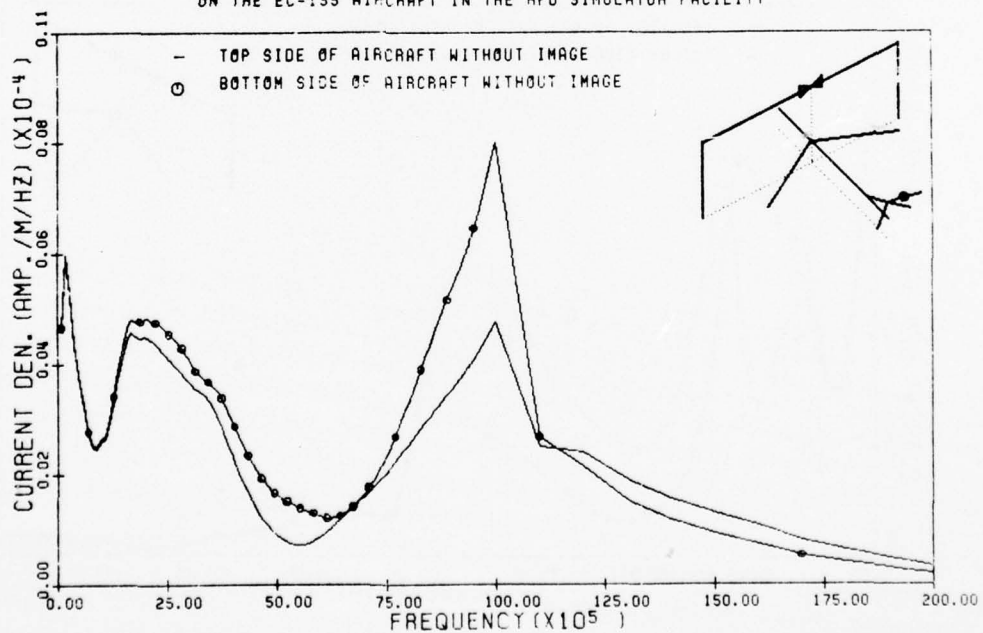


Figure 41:

BEST AVAILABLE COPY

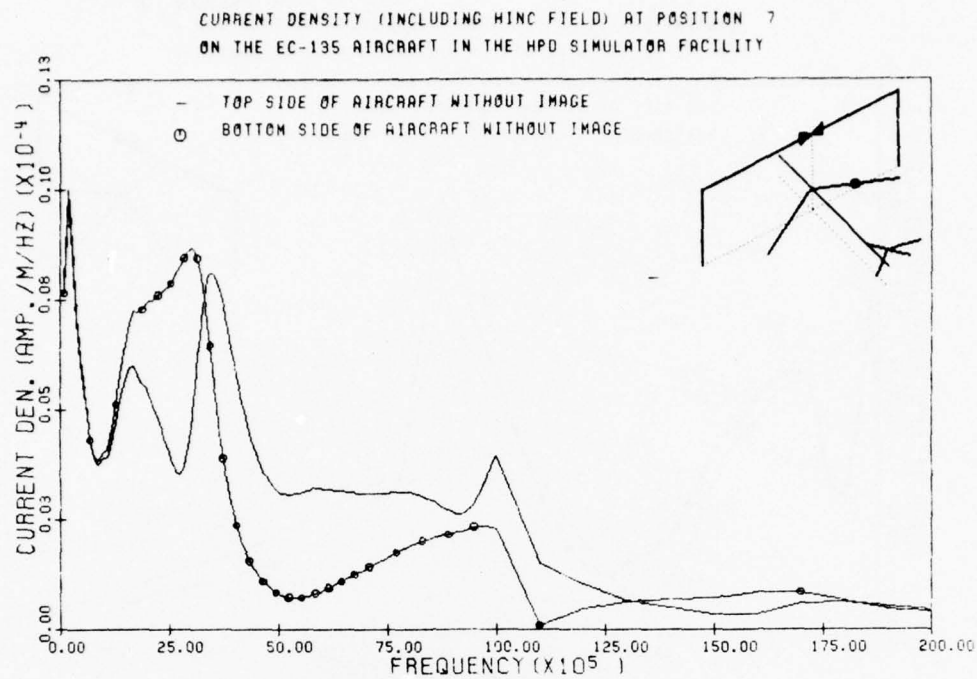


Figure 42:

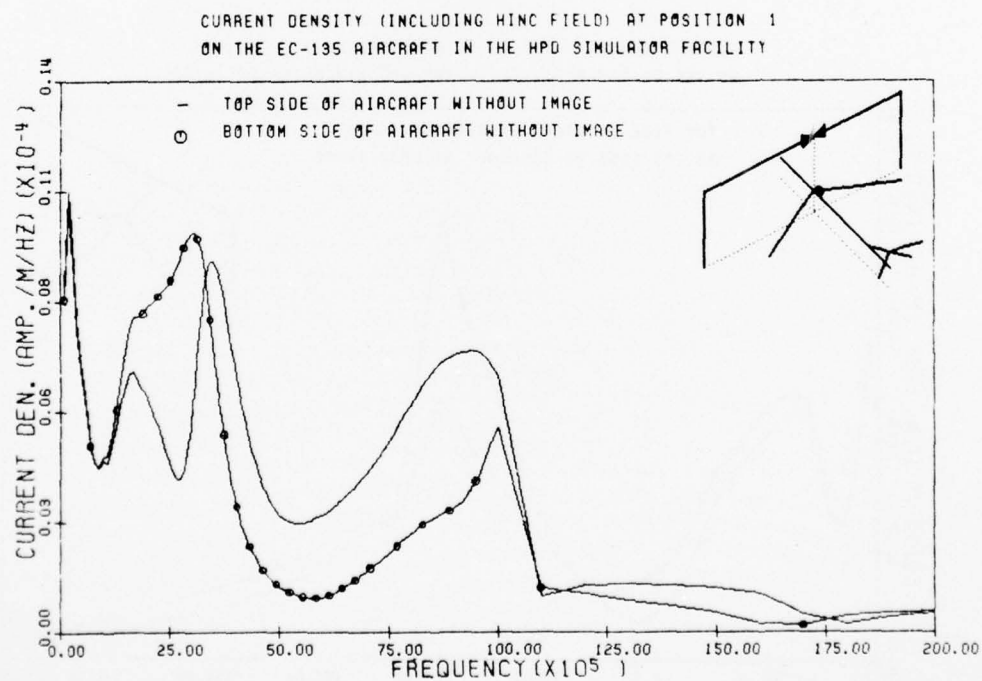


Figure 43:

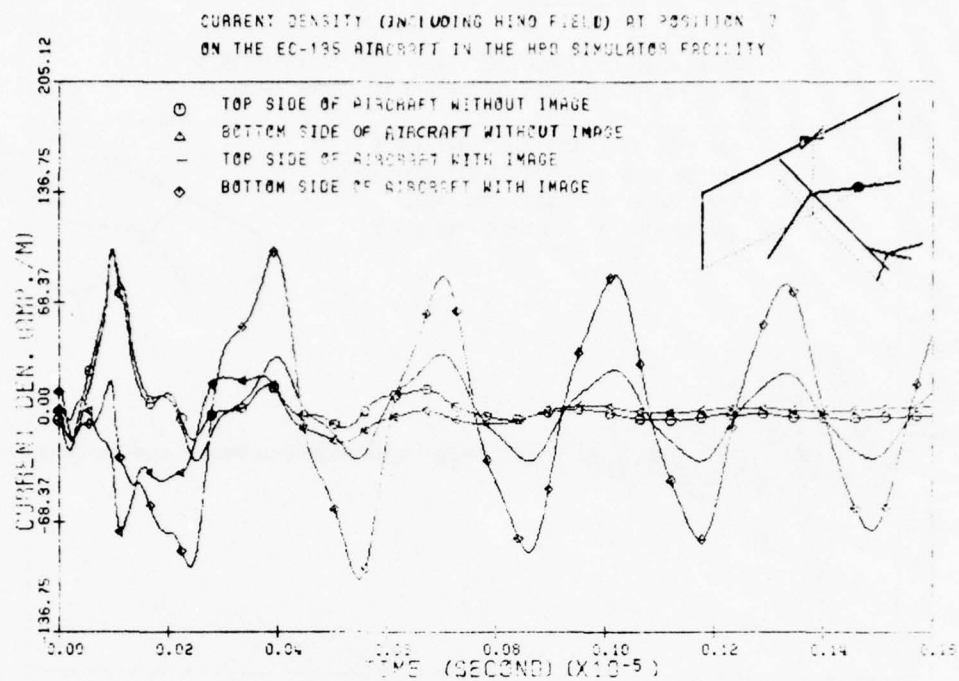


Figure 44:

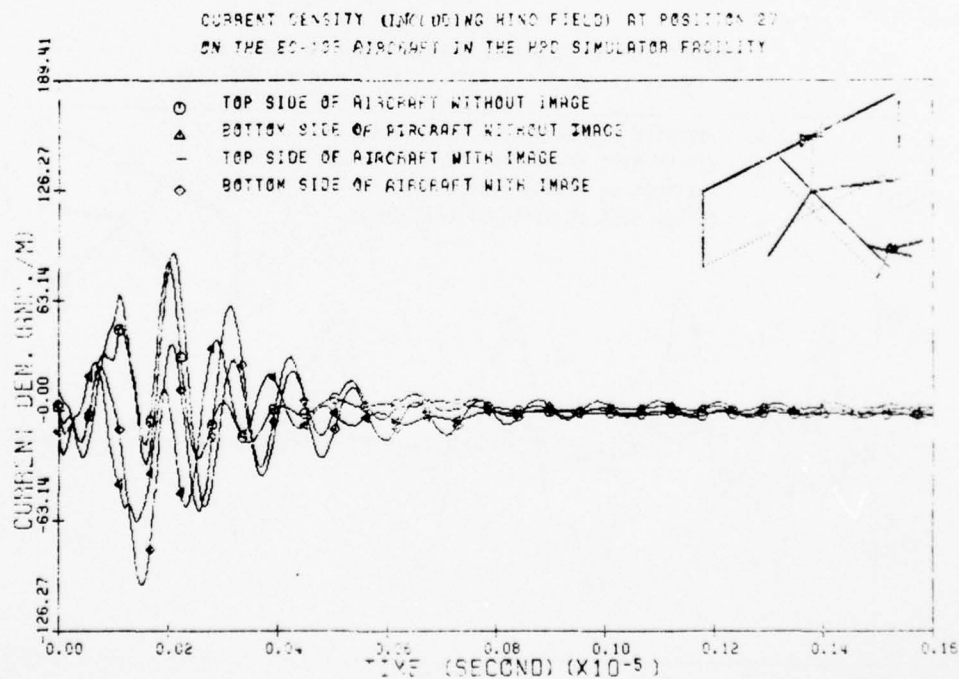


Figure 45:

BEST AVAILABLE COPY

CURRENT DENSITY (INCLUDING HING FIELD) AT POSITION 30  
ON THE EC-135 AIRCRAFT IN THE HPD SIMULATOR FACILITY

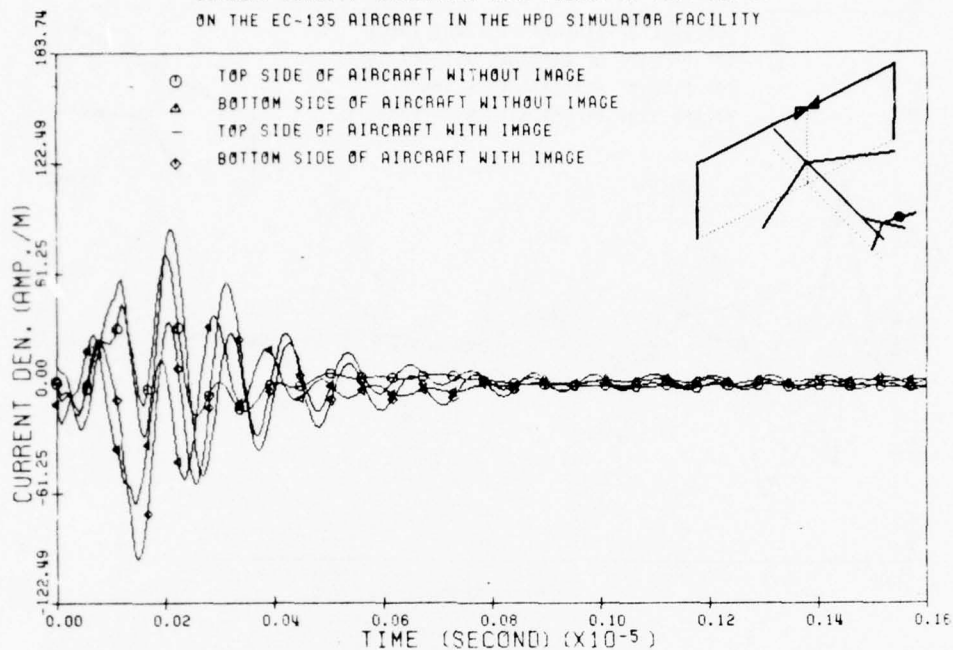


Figure 46:

CURRENT DENSITY (INCLUDING HING FIELD) AT POSITION 1  
ON THE EC-135 AIRCRAFT IN THE HPD SIMULATOR FACILITY

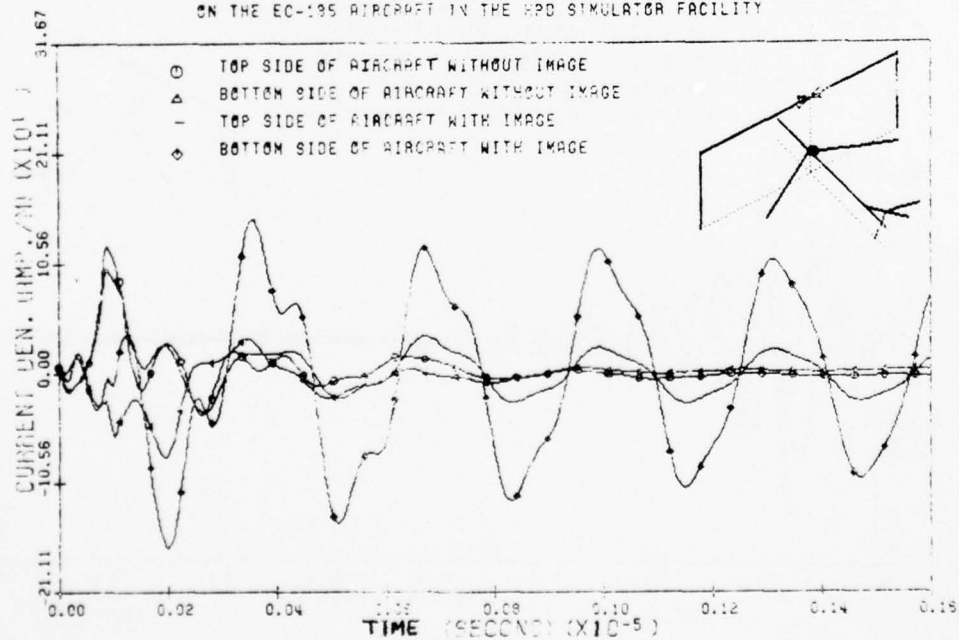


Figure 47:

CHARGE DENSITY AT POSITION 7 ON THE EC-135  
AIRCRAFT IN THE HPD SIMULATOR FACILITY

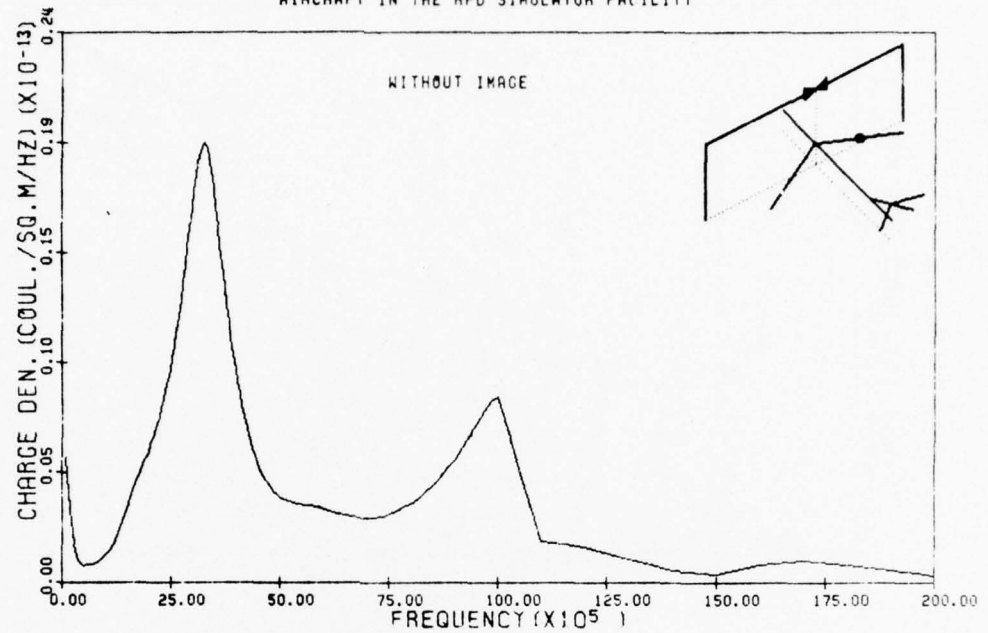


Figure 48:

CHARGE DENSITY AT POSITION 13 ON THE EC-135  
AIRCRAFT IN THE HPD SIMULATOR FACILITY

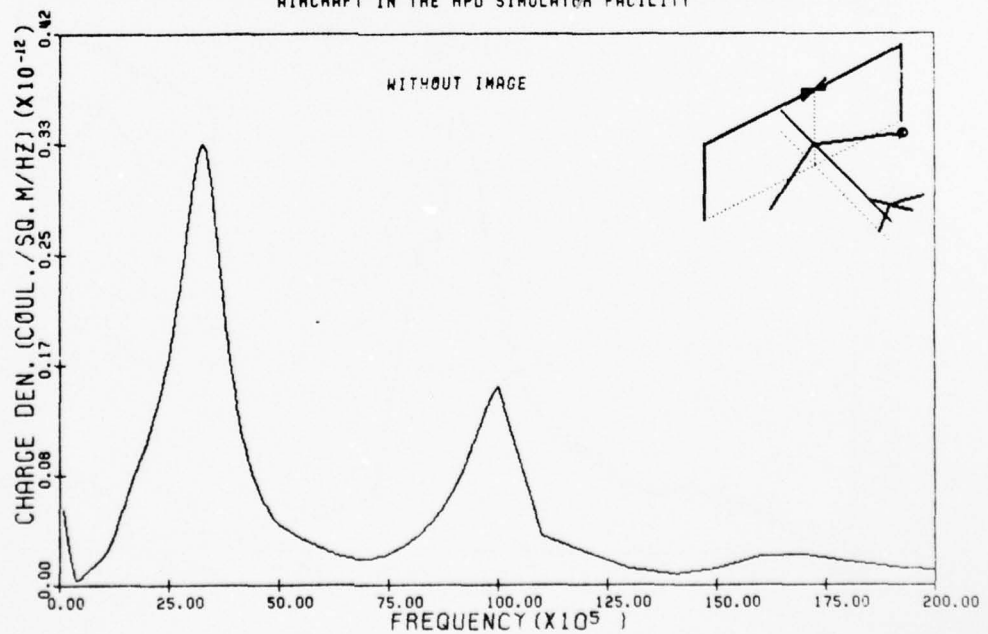


Figure 49:



CHARGE DENSITY AT POSITION 12 ON THE EC-135  
AIRCRAFT IN THE HPD SIMULATOR FACILITY

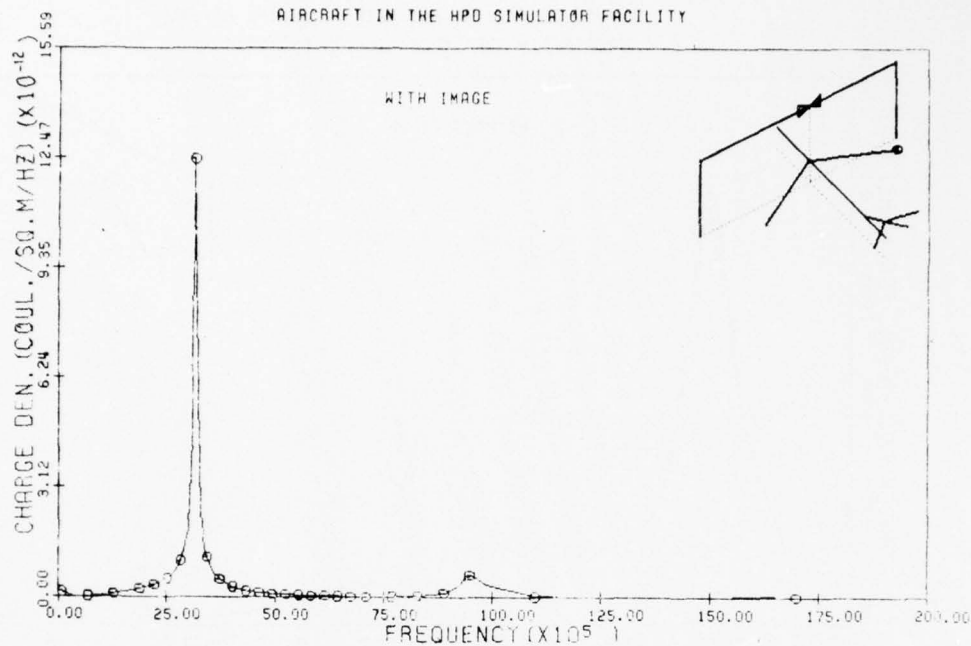


Figure 50:

CHARGE DENSITY AT POSITION 33 ON THE EC-135  
AIRCRAFT IN THE HPD SIMULATOR FACILITY

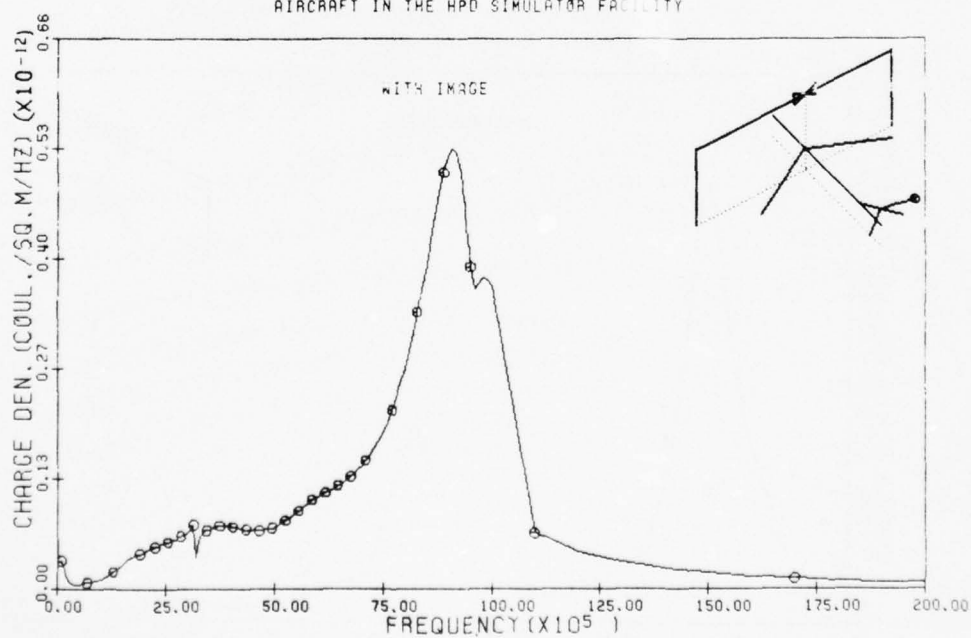


Figure 51:

AD-A039 507

MISSISSIPPI STATE UNIV MISSISSIPPI STATE ENGINEERING--ETC F/G 18/3  
A STUDY OF THE CHARGE AND CURRENT INDUCED ON AN AIRCRAFT IN AN --ETC(U)  
DEC 76 C D TAYLOR, K CHEN, T T CROW

AF-AFOSR-2961-76

UNCLASSIFIED

AFOSR-TR-77-0636

NL

2 OF 2  
AD  
A039507



END

DATE  
FILMED  
6-77

CHARGE DENSITY AT POSITION 7 ON THE EC-135  
AIRCRAFT IN THE HPD SIMULATOR FACILITY

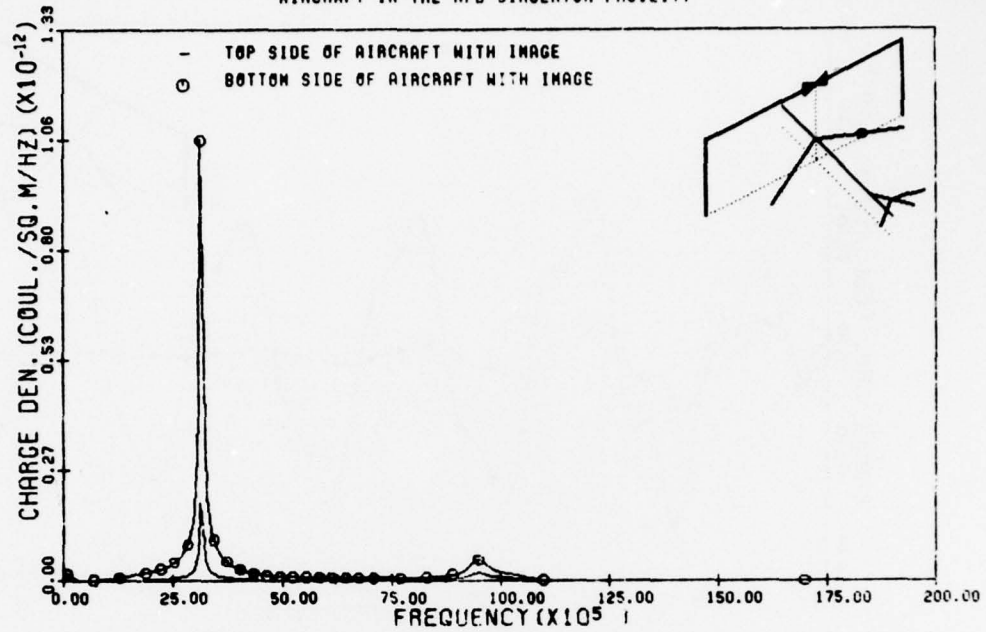


Figure 52:

CHARGE DENSITY AT POSITION 99 ON THE EC-135  
AIRCRAFT IN THE HPD SIMULATOR FACILITY

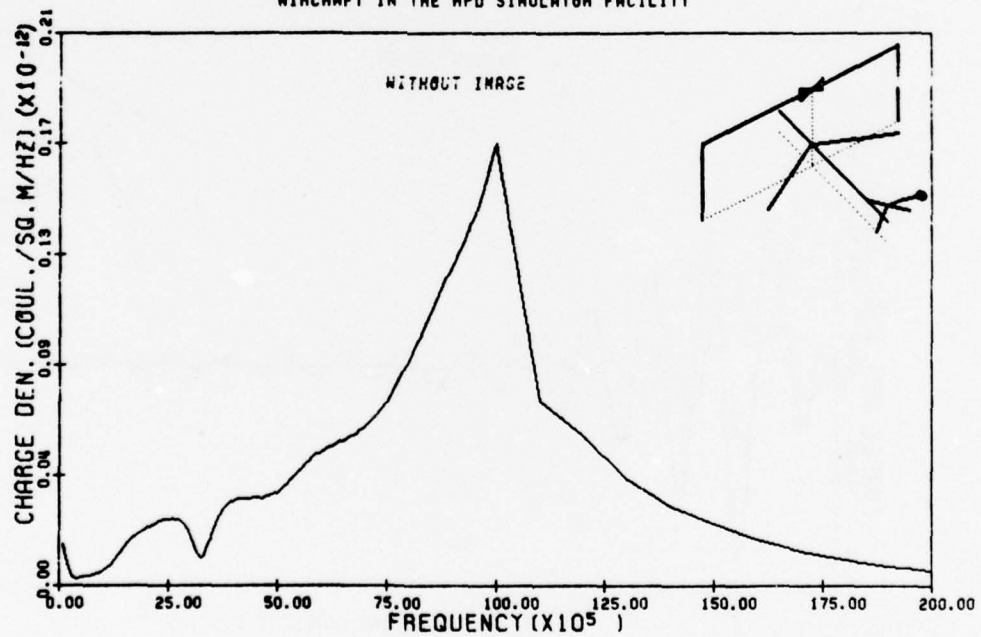


Figure 53:

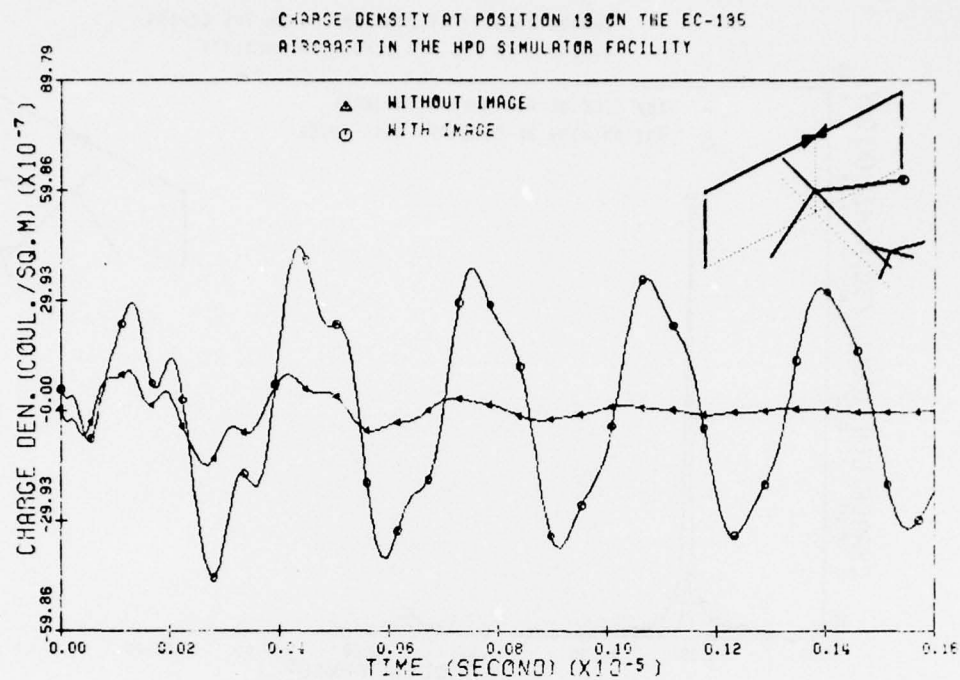


Figure 54:

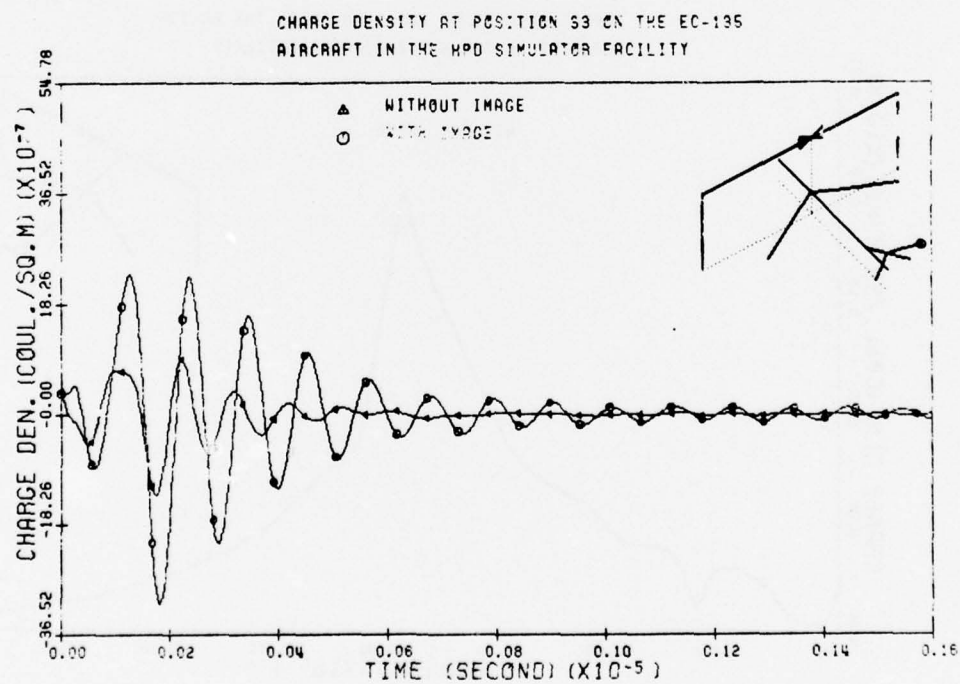


Figure 55:

CHARGE DENSITY AT POSITION 7 ON THE EC-135  
AIRCRAFT IN THE HPD SIMULATOR FACILITY

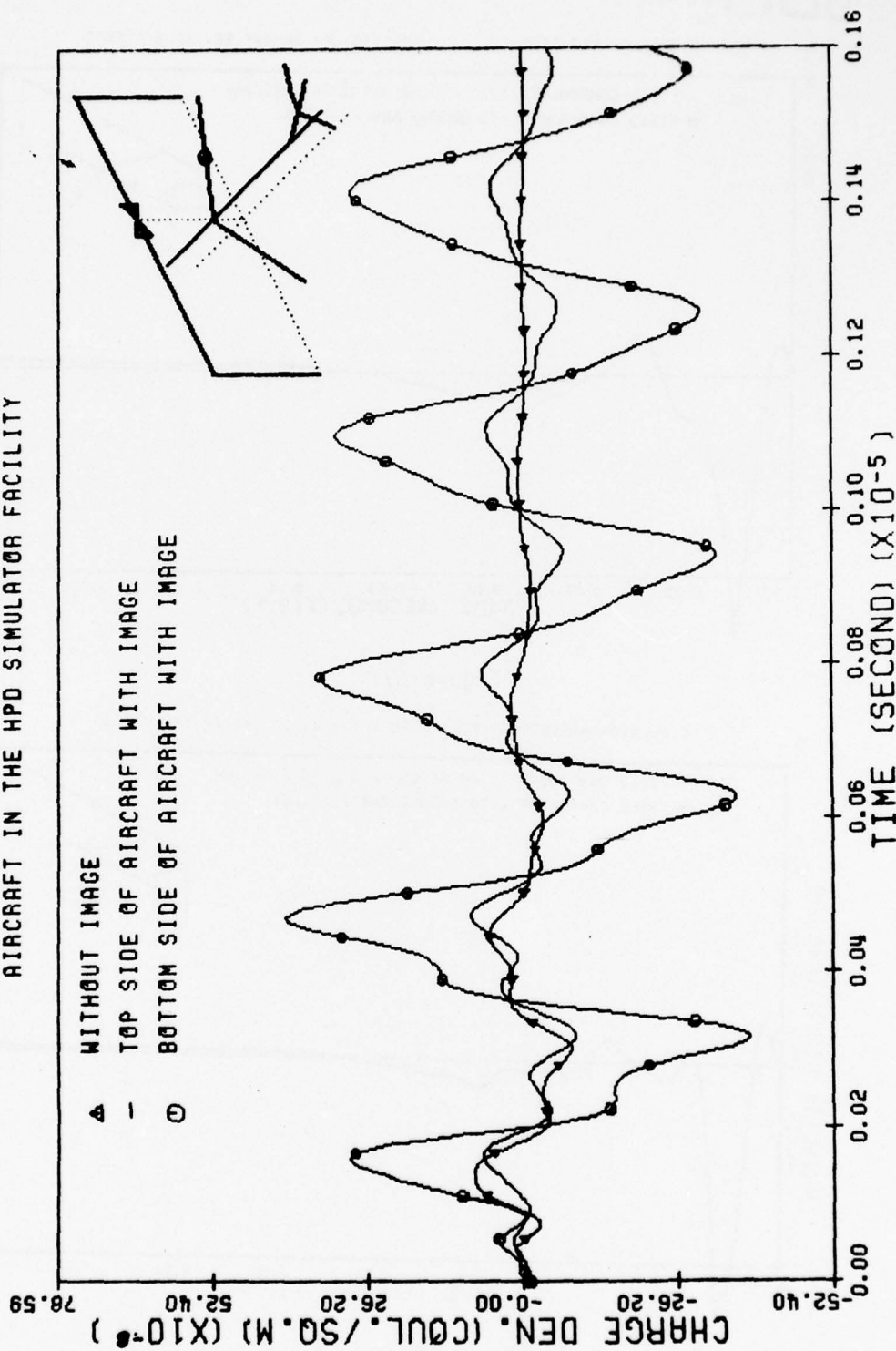


Figure 56:



BEST AVAILABLE COPY

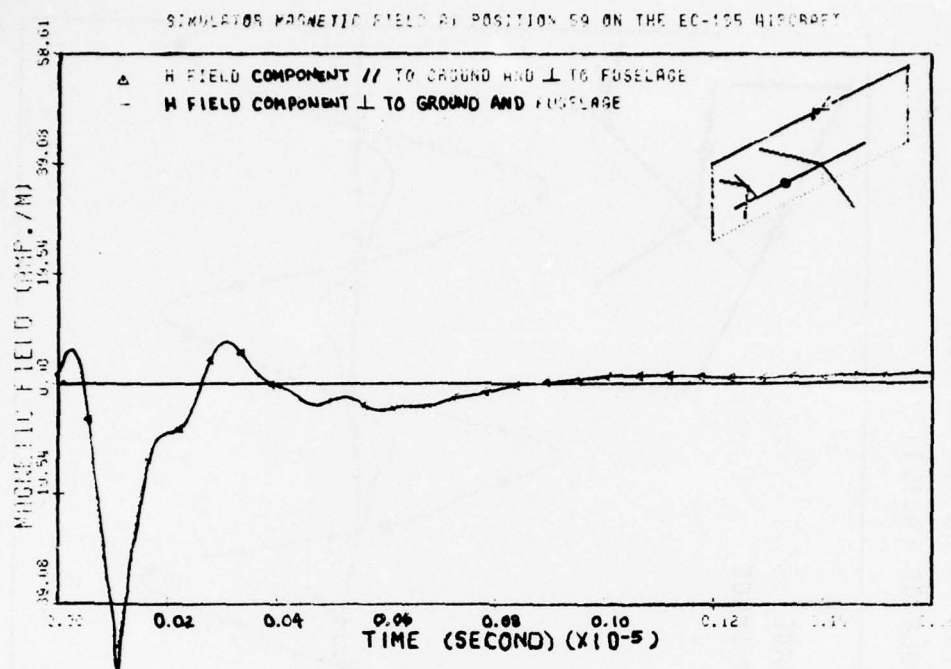


Figure 57:

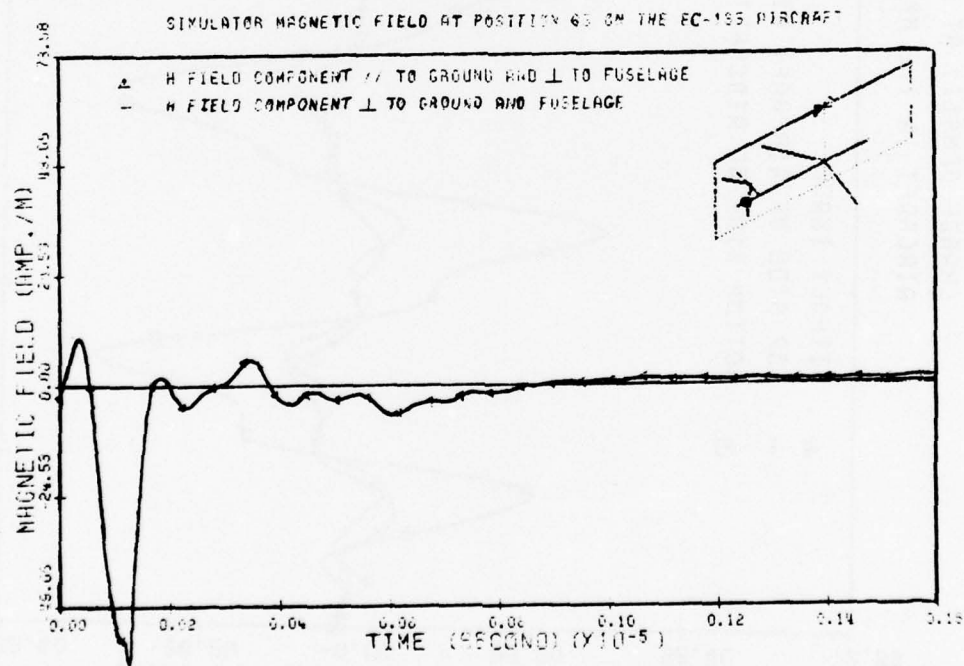


Figure 58:

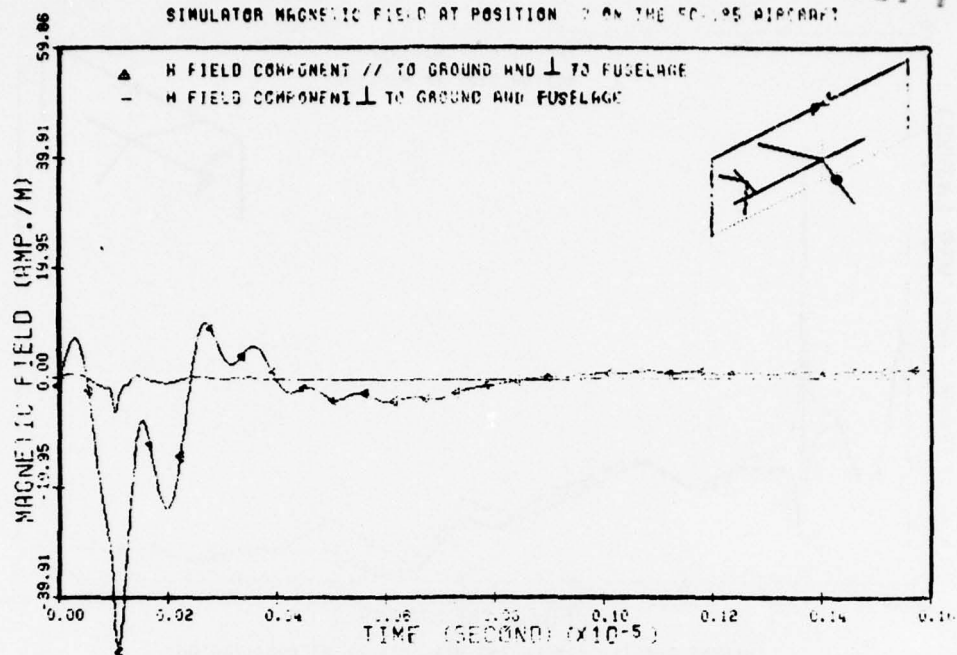


Figure 59:

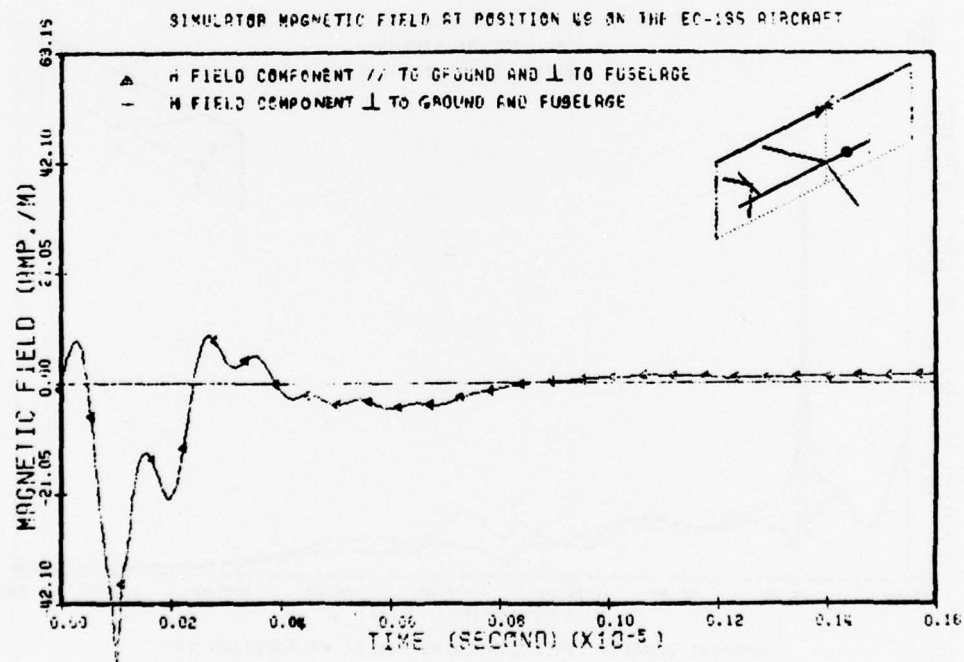


Figure 60:

BEST AVAILABLE COPY

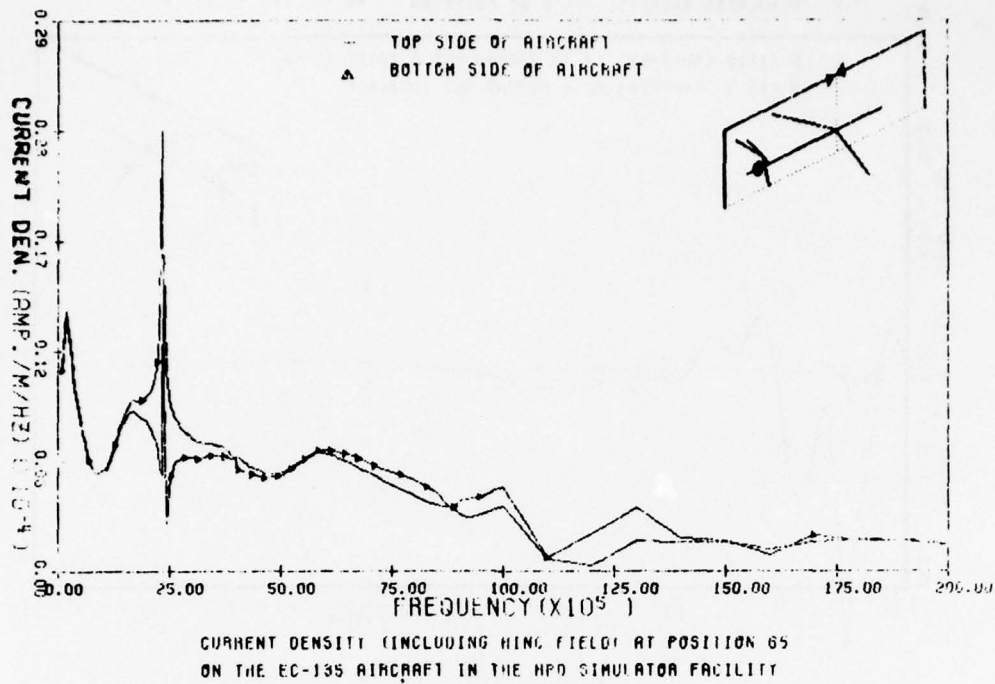


Figure 61:

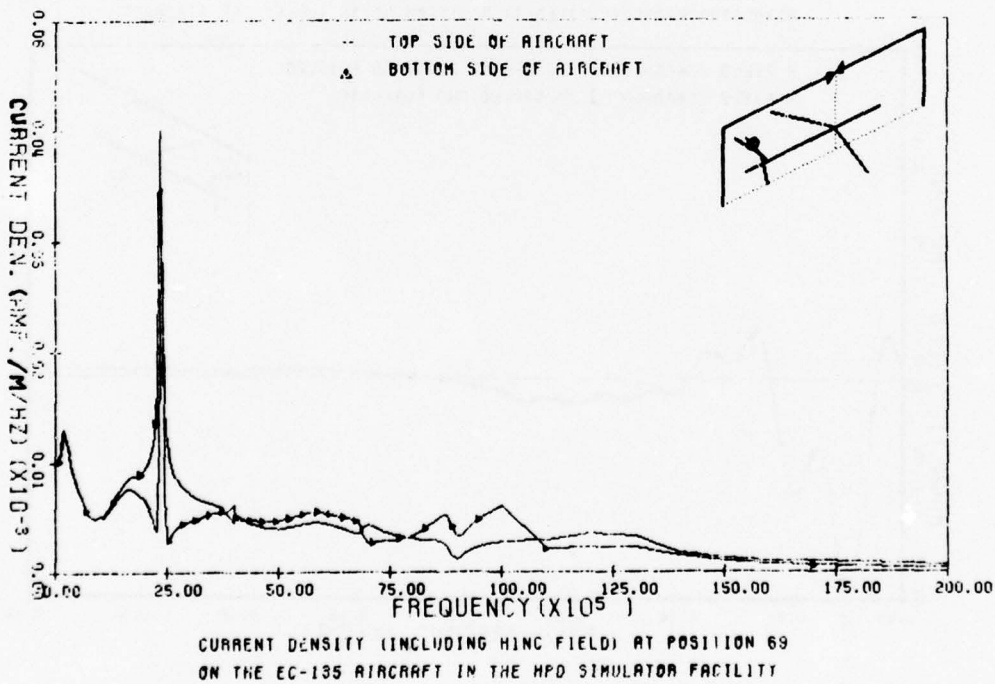


Figure 62:

BEST AVAILABLE COPY

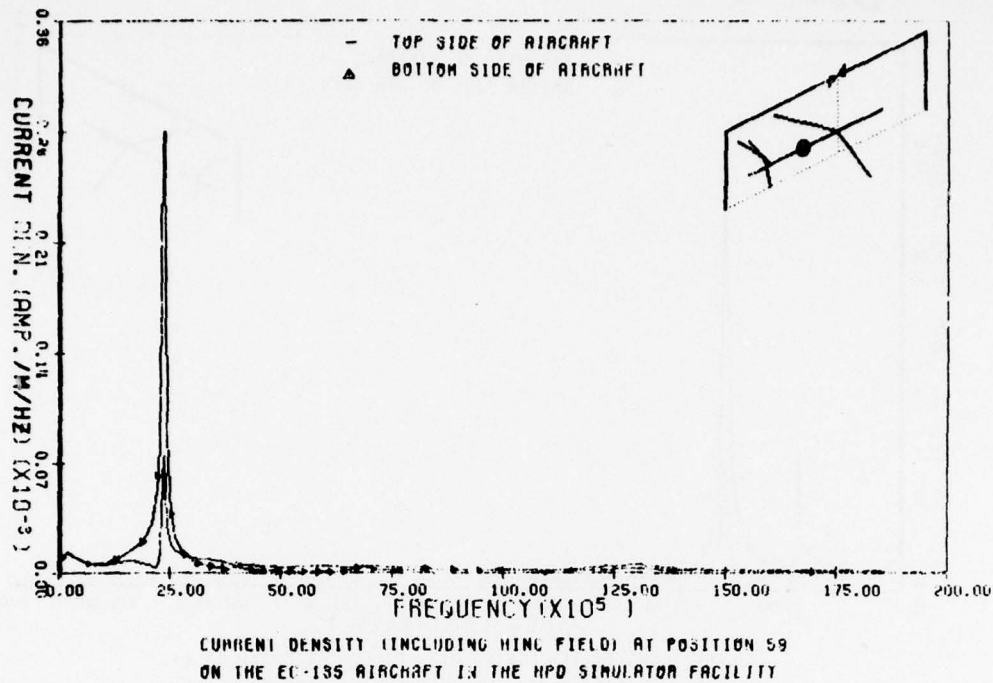


Figure 63:

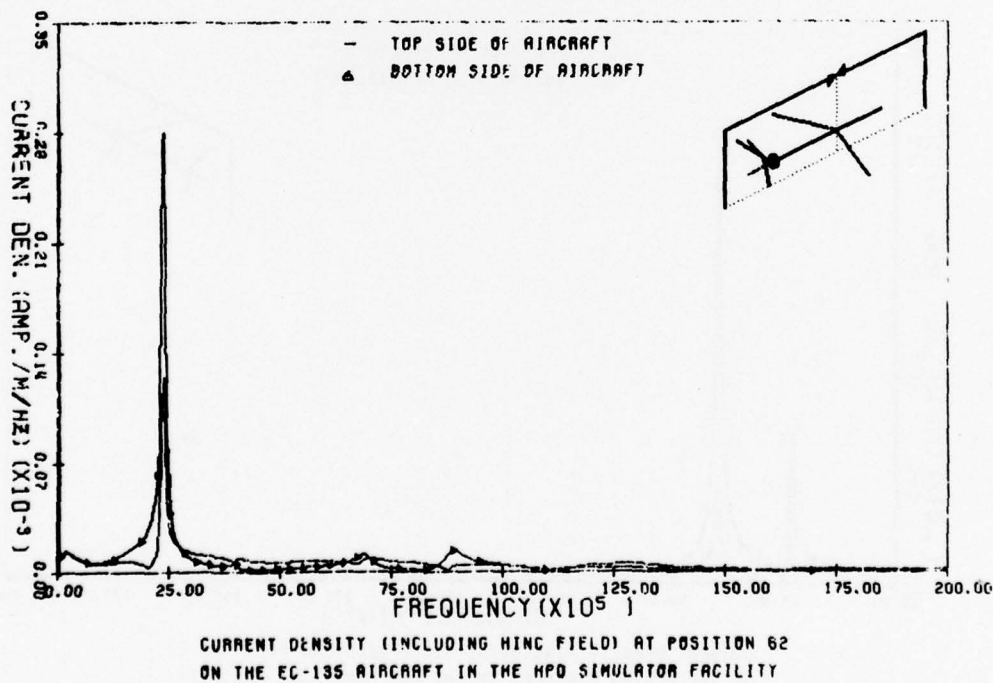


Figure 64:

BEST AVAILABLE COPY

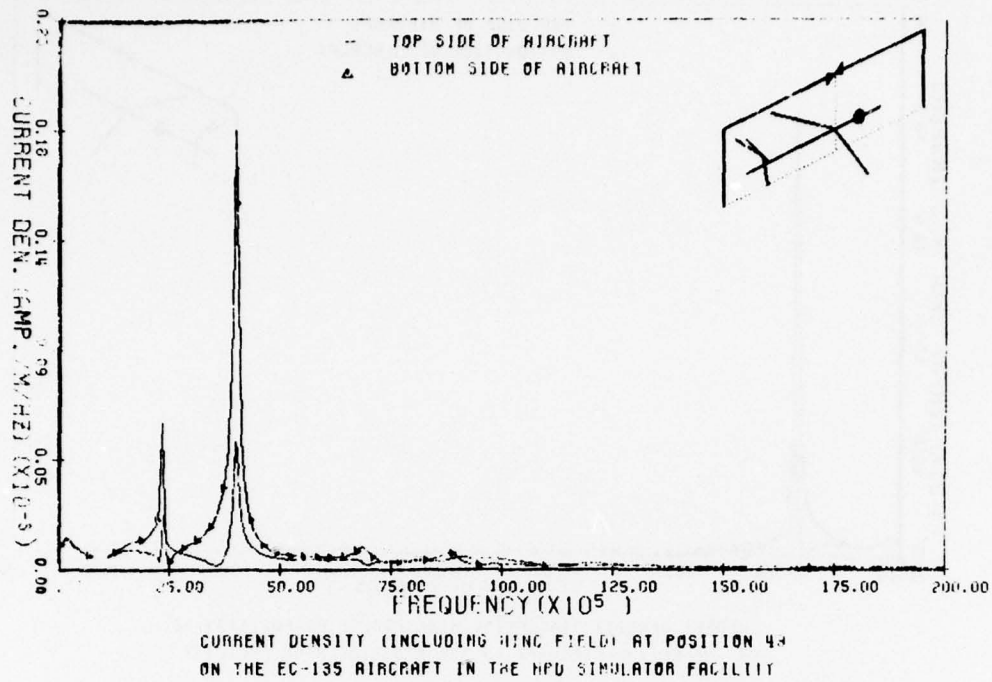


Figure 65:

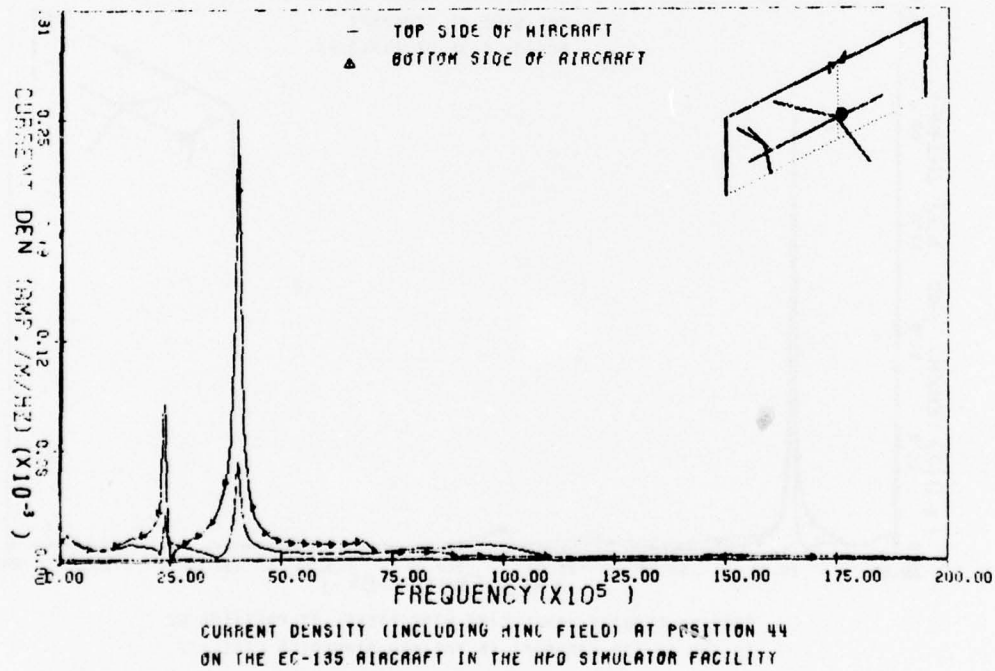
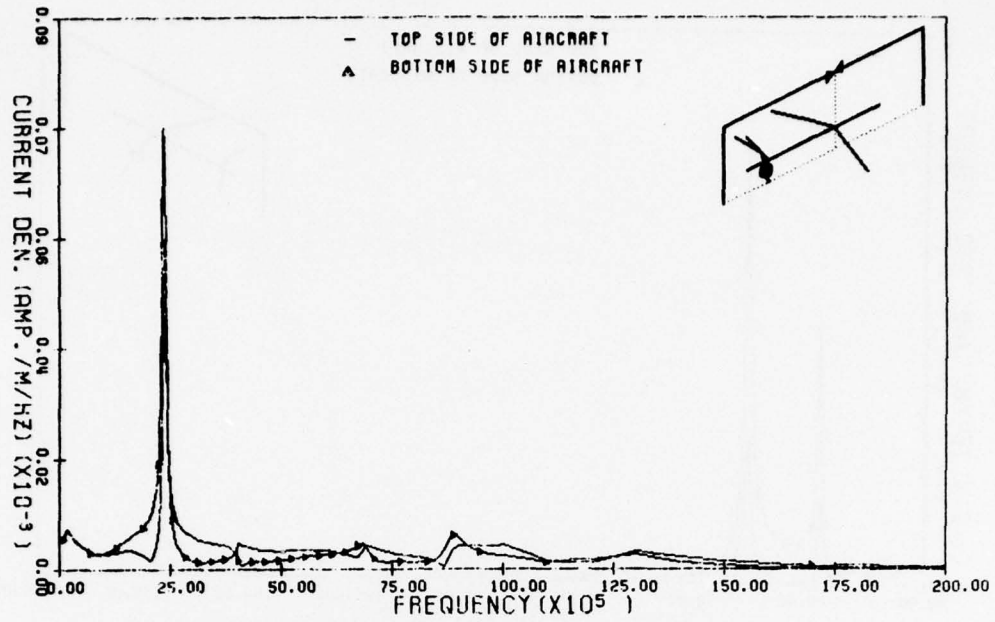


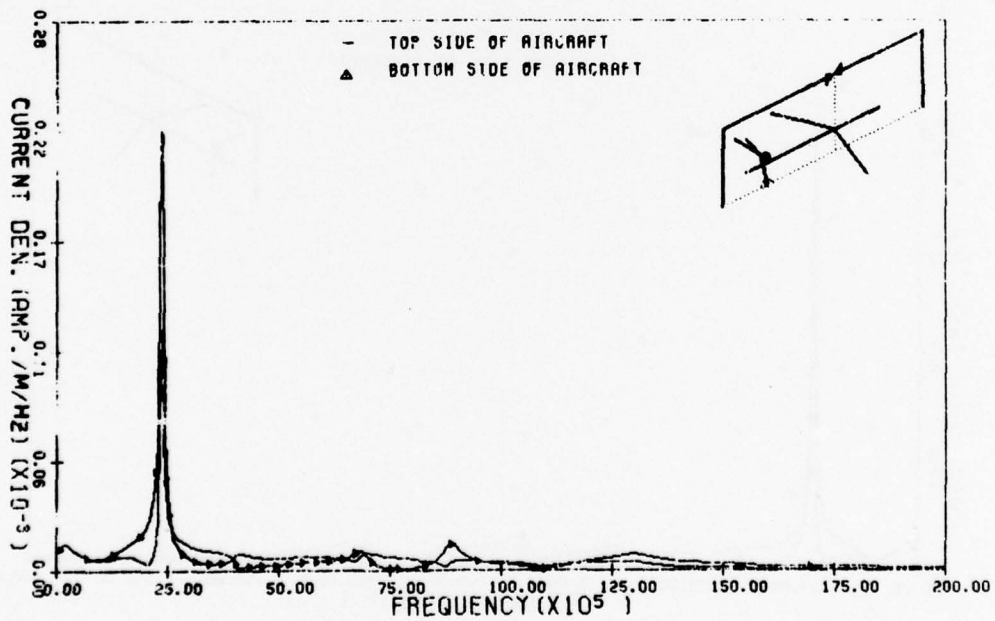
Figure 66:





CURRENT DENSITY (INCLUDING HING FIELD) AT POSITION 30  
ON THE EC-135 AIRCRAFT IN THE HPD SIMULATOR FACILITY

Figure 67:



CURRENT DENSITY (INCLUDING HING FIELD) AT POSITION 42  
ON THE EC-135 AIRCRAFT IN THE HPD SIMULATOR FACILITY

Figure 68:

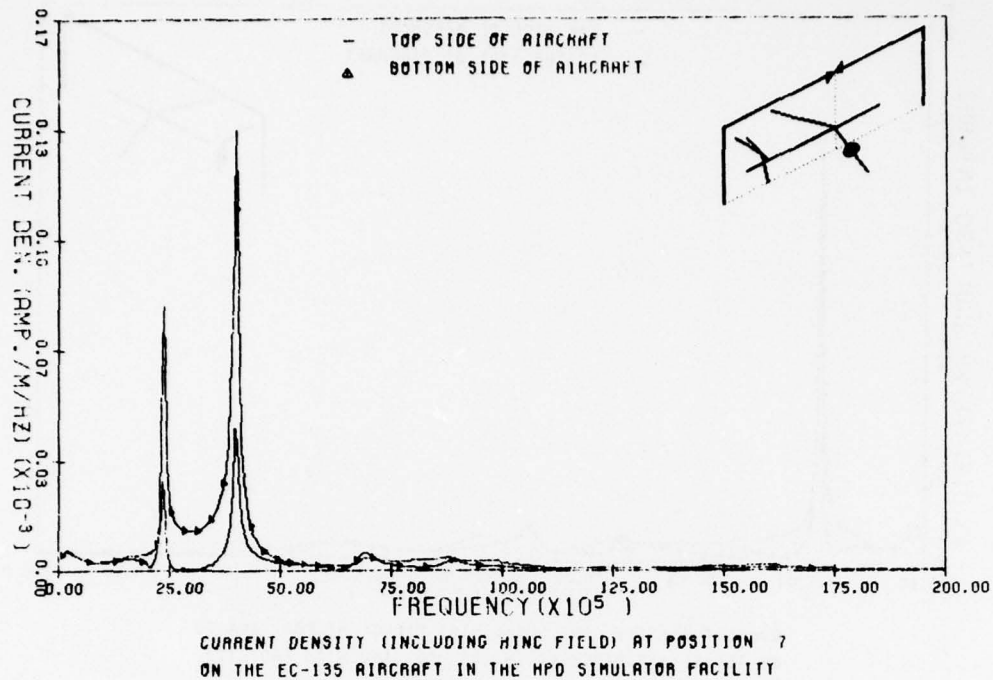


Figure 69:

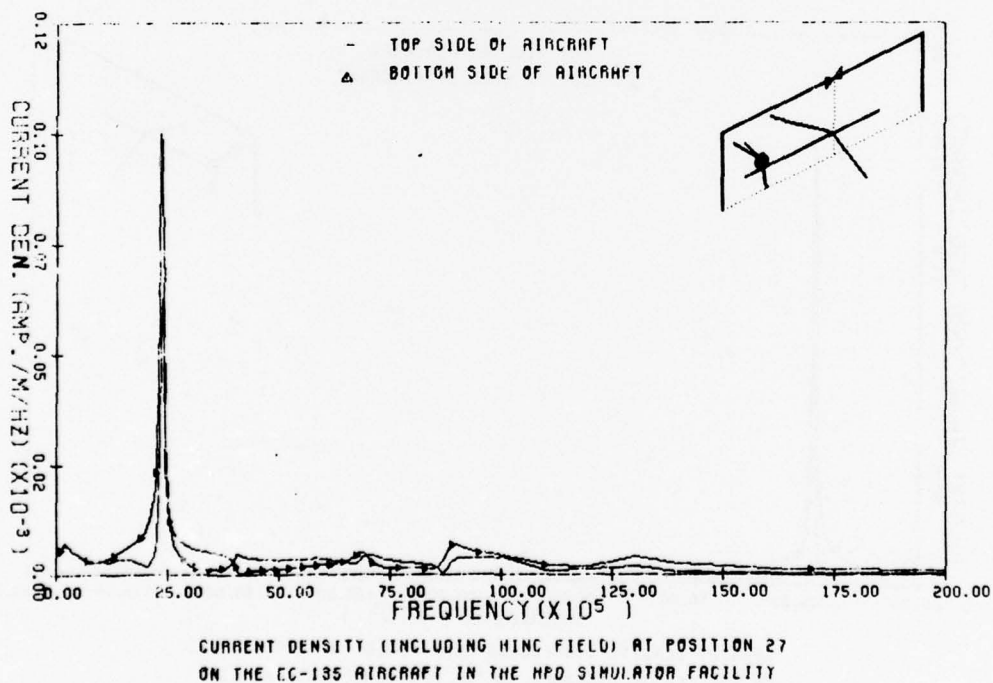
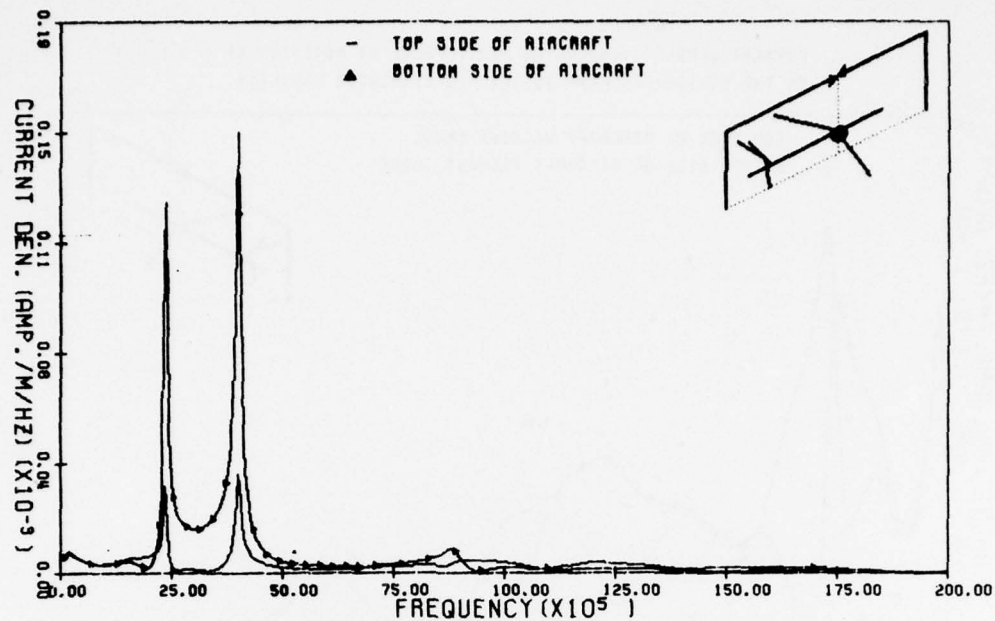


Figure 70:



CURRENT DENSITY (INCLUDING HINC FIELD) AT POSITION 1  
ON THE EC-135 AIRCRAFT IN THE HPD SIMULATOR FACILITY

Figure 71:

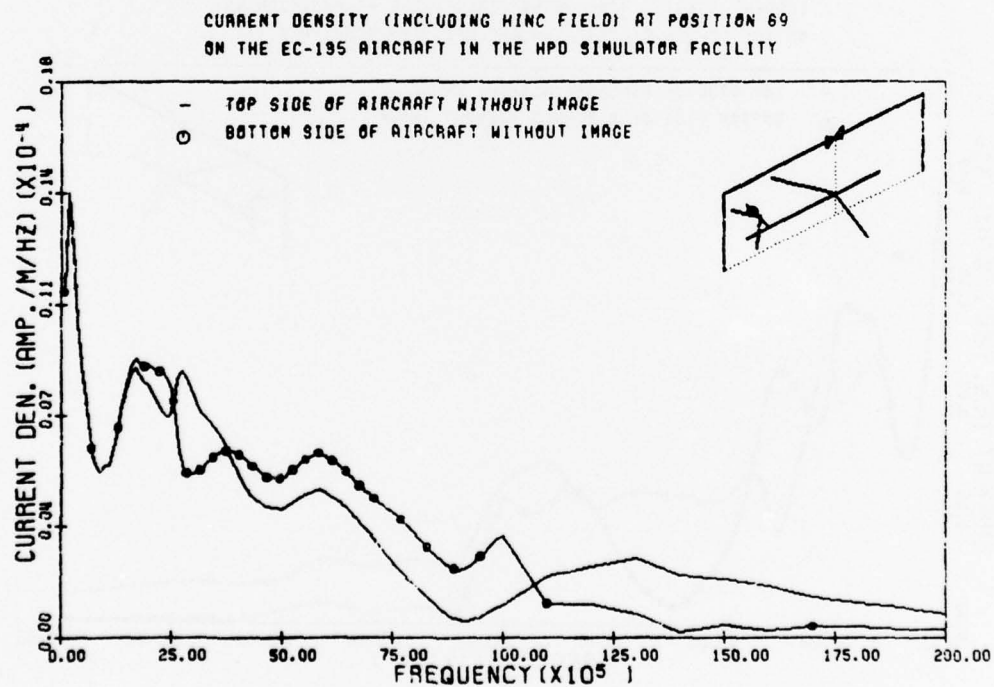


Figure 72:

CURRENT DENSITY (INCLUDING HING FIELD) AT POSITION 42  
ON THE EC-135 AIRCRAFT IN THE HPD SIMULATOR FACILITY

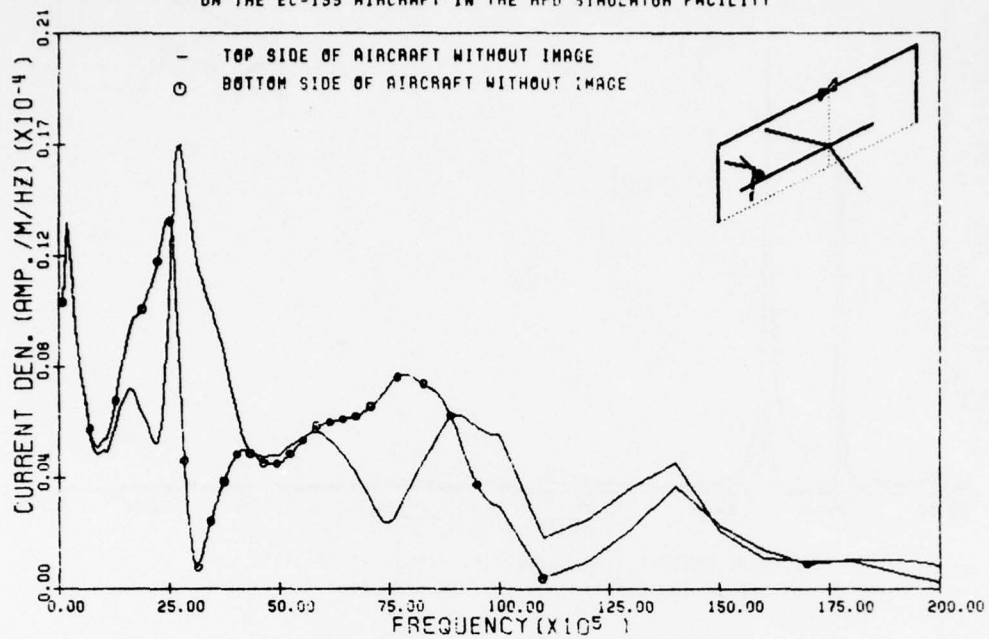


Figure 73:

CURRENT DENSITY (INCLUDING HING FIELD) AT POSITION 49  
ON THE EC-135 AIRCRAFT IN THE HPD SIMULATOR FACILITY

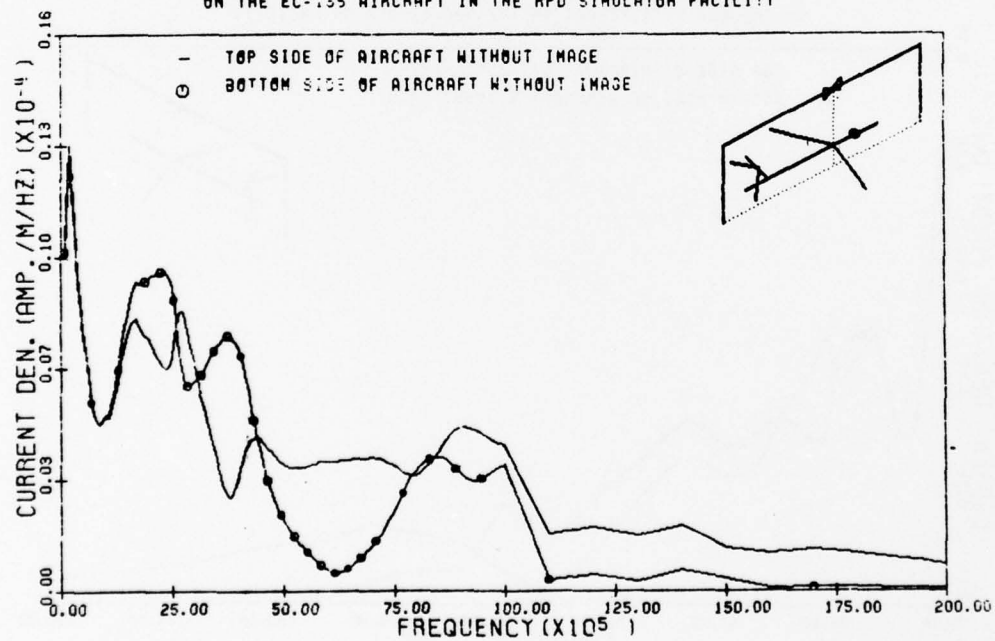


Figure 74:

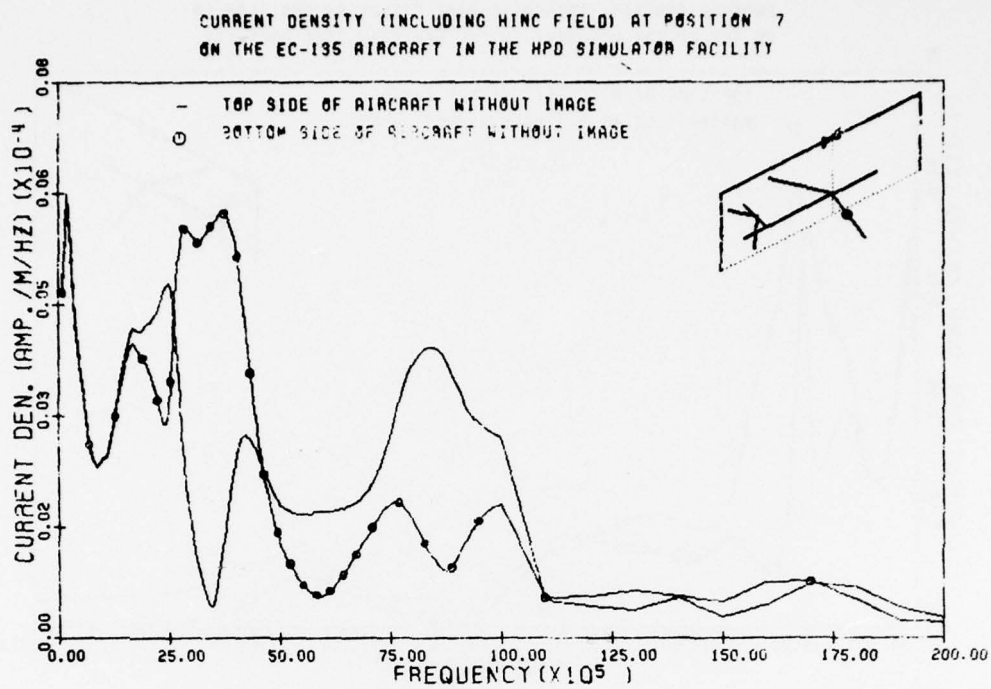


Figure 75:

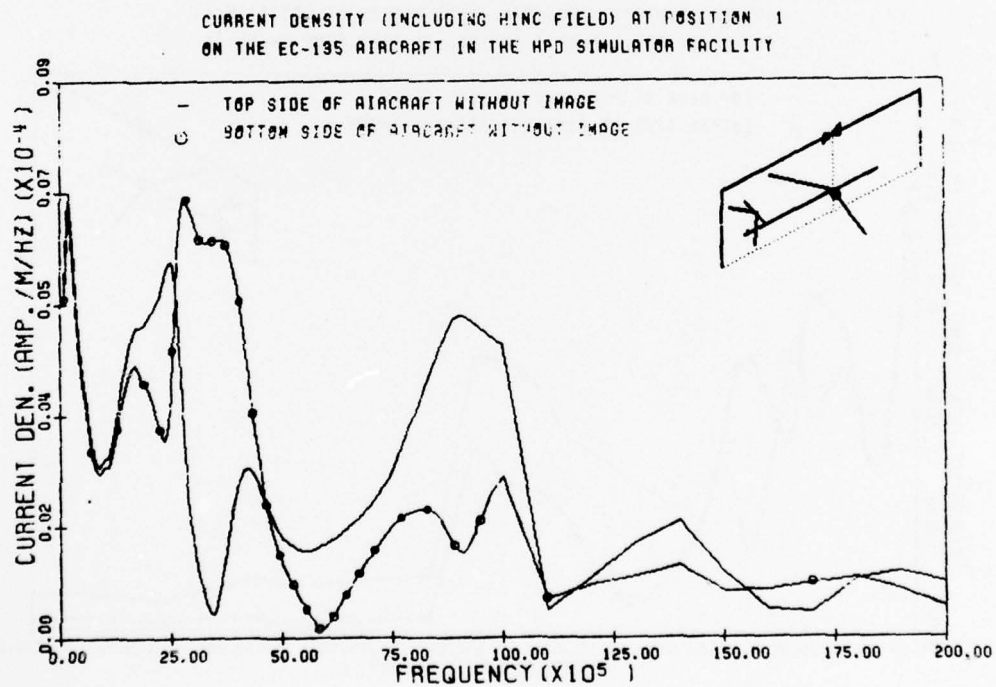


Figure 76:



BEST AVAILABLE COPY

CURRENT DENSITY (INCLUDING HINC FIELD) AT POSITION 59  
ON THE EC-135 AIRCRAFT IN THE HPD SIMULATOR FACILITY

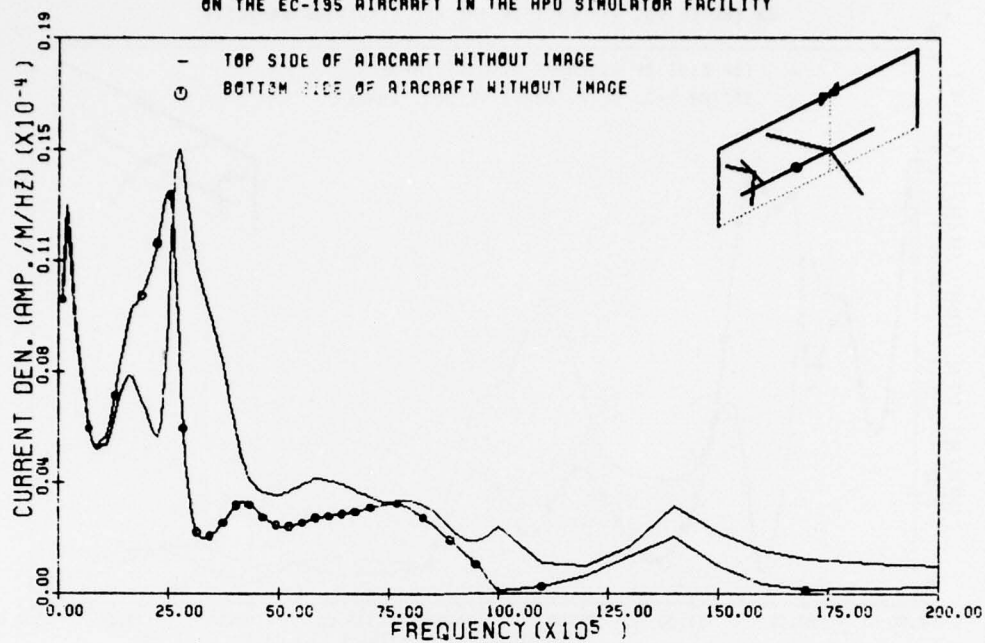


Figure 77:

CURRENT DENSITY (INCLUDING HINC FIELD) AT POSITION 44  
ON THE EC-135 AIRCRAFT IN THE HPD SIMULATOR FACILITY

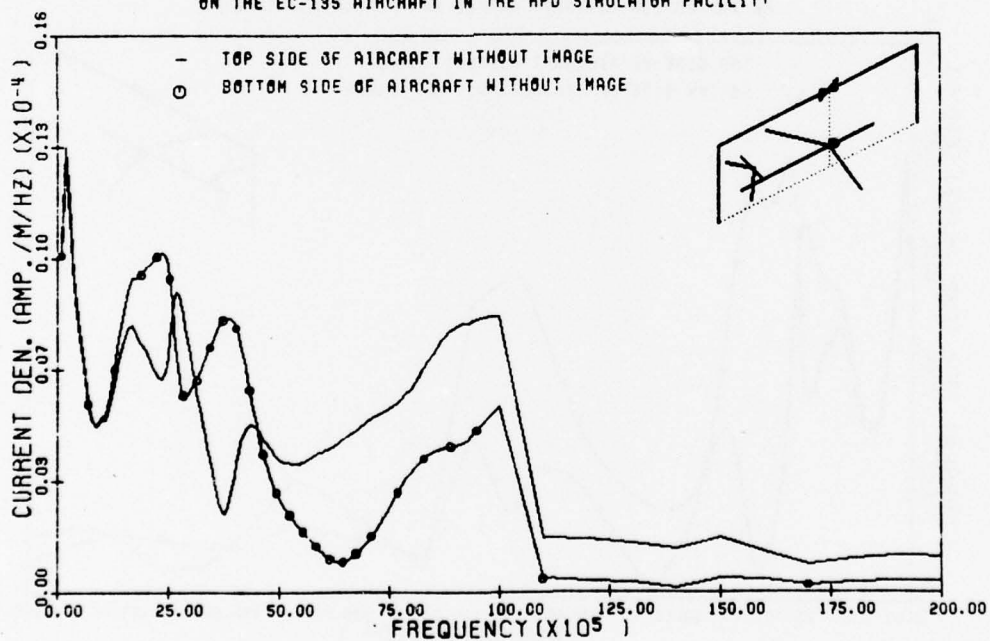


Figure 78

CURRENT DENSITY (INCLUDING HIND FIELD) AT POSITION 27  
ON THE EC-135 AIRCRAFT IN THE HPD SIMULATOR FACILITY

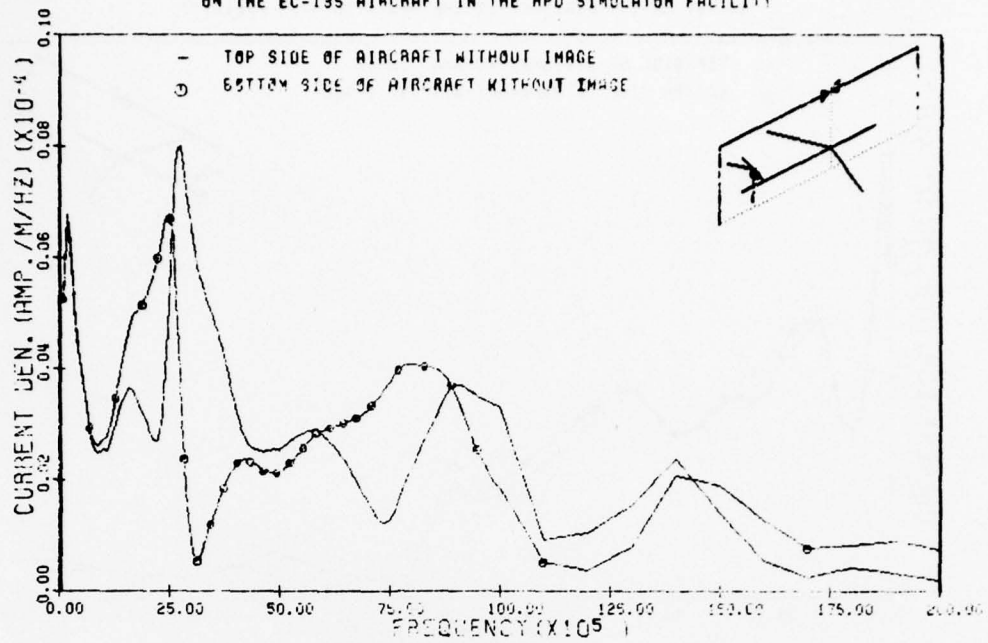


Figure 79:

CURRENT DENSITY (INCLUDING HIND FIELD) AT POSITION 40  
ON THE EC-135 AIRCRAFT IN THE HPD SIMULATOR FACILITY

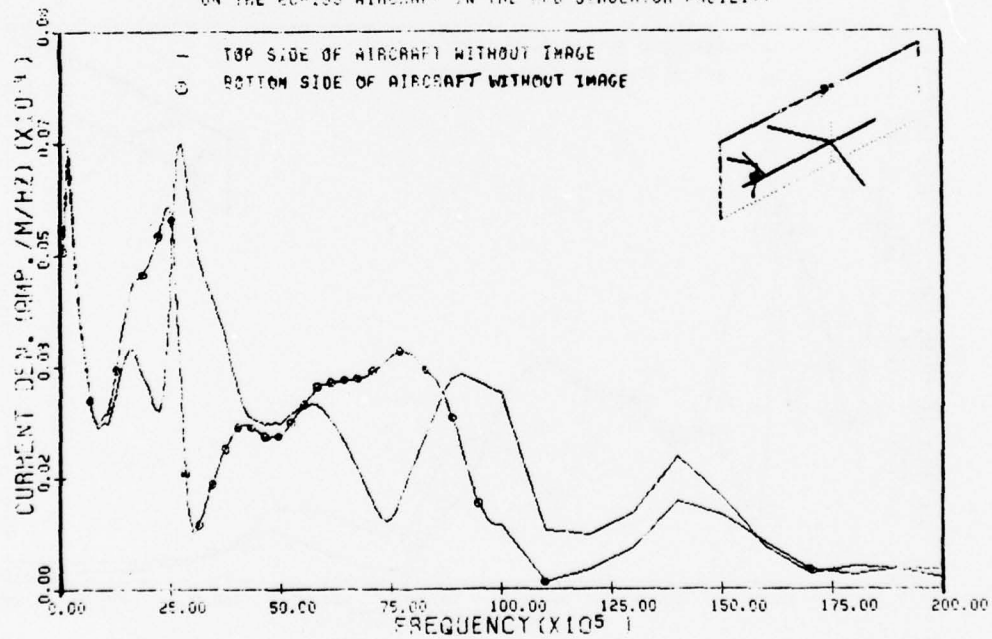


Figure 80:

BEST AVAILABLE COPY

CURRENT DENSITY (INCLUDING HING FIELD) AT POSITION 55  
ON THE EC-135 AIRCRAFT IN THE HPD SIMULATOR FACILITY

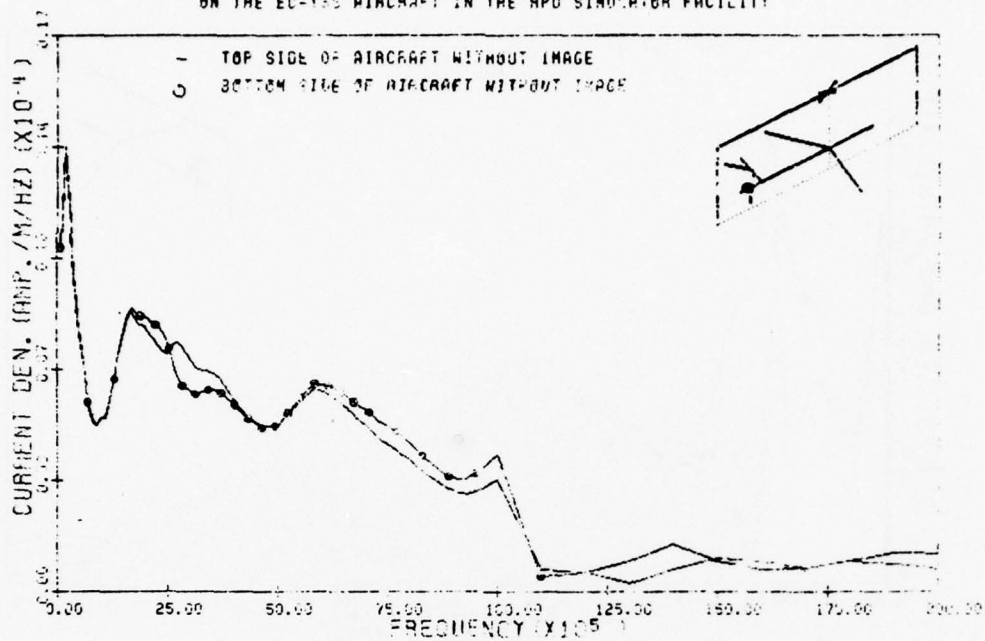


Figure 81:

CURRENT DENSITY (INCLUDING HING FIELD) AT POSITION 62  
ON THE EC-135 AIRCRAFT IN THE HPD SIMULATOR FACILITY

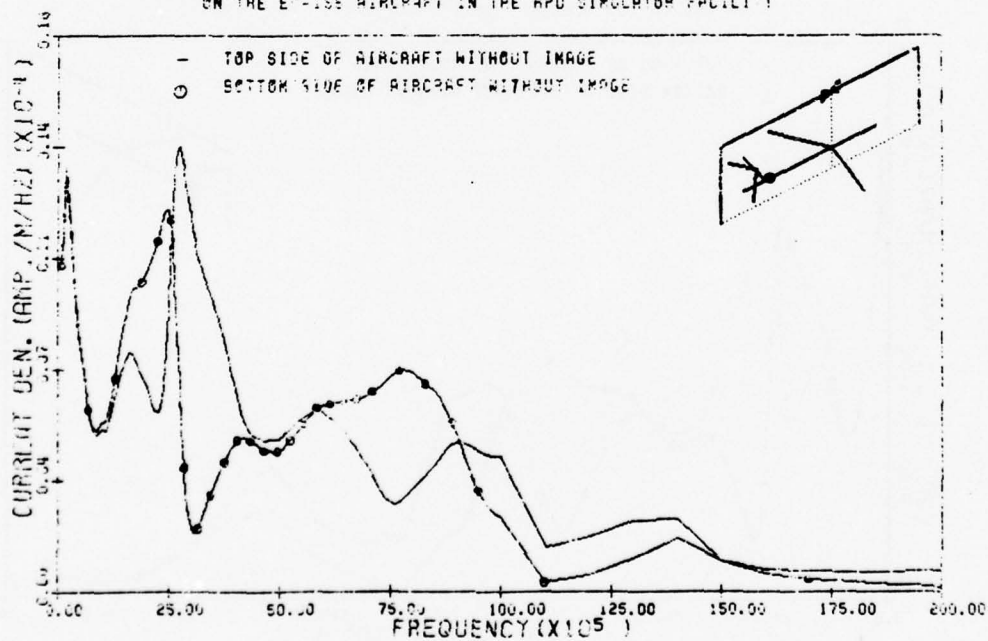


Figure 82:

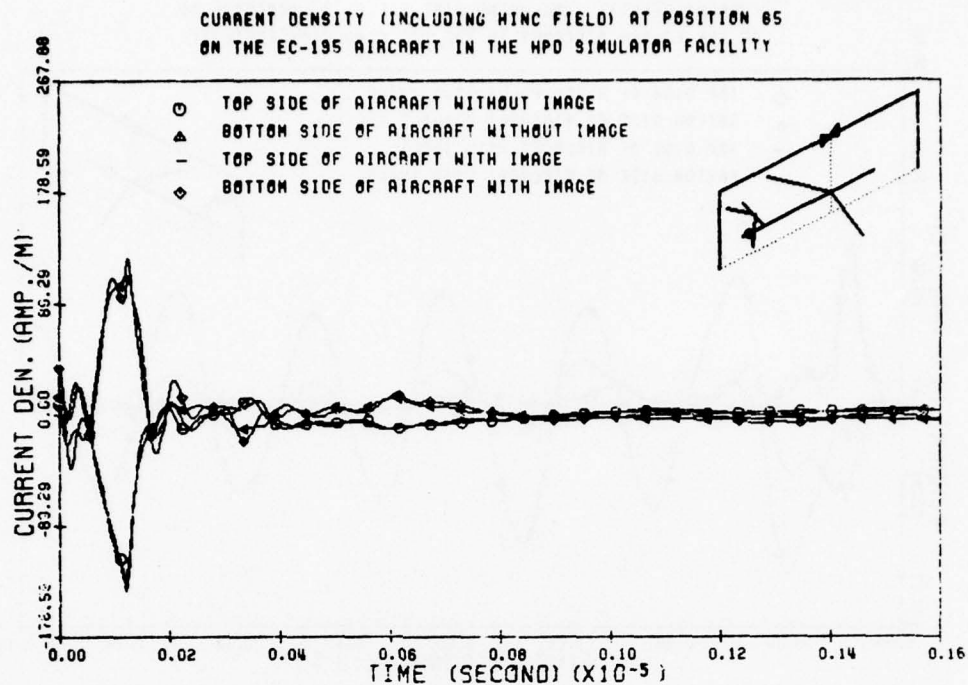


Figure 83:

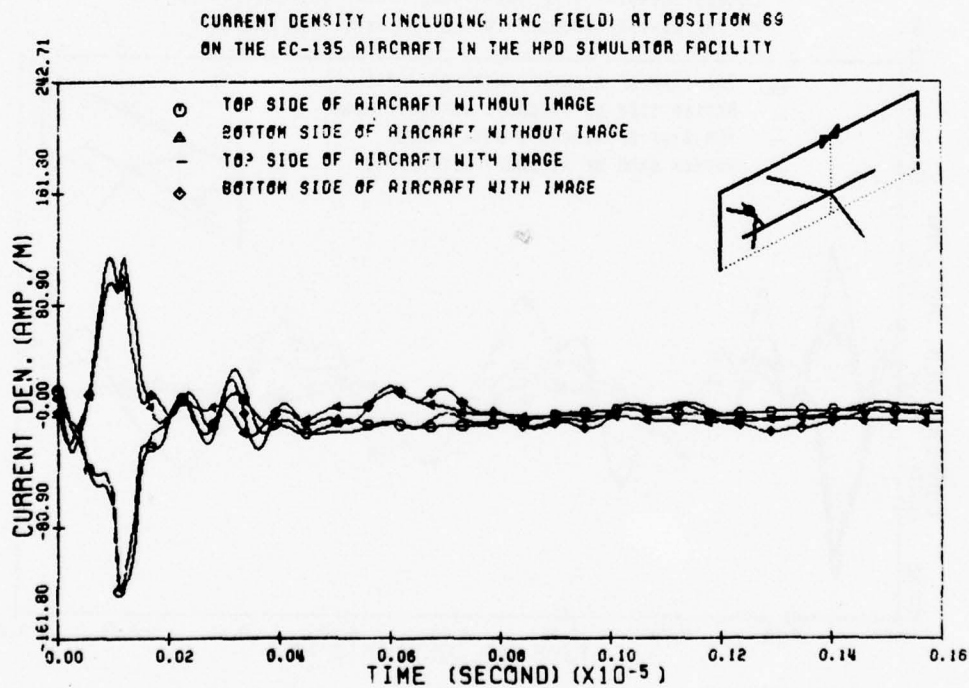


Figure 84:

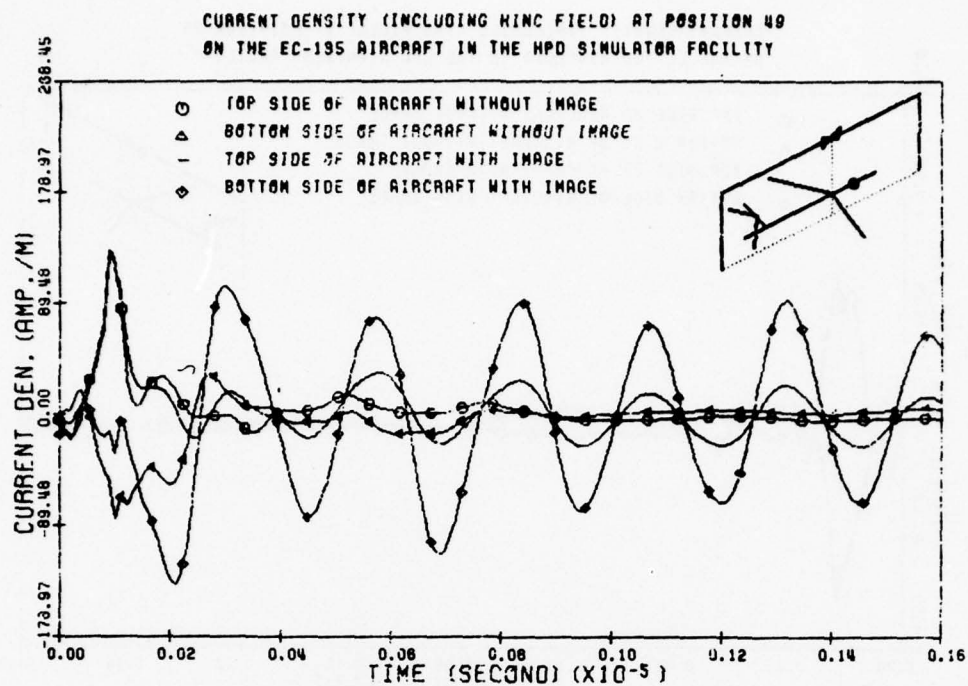


Figure 85:

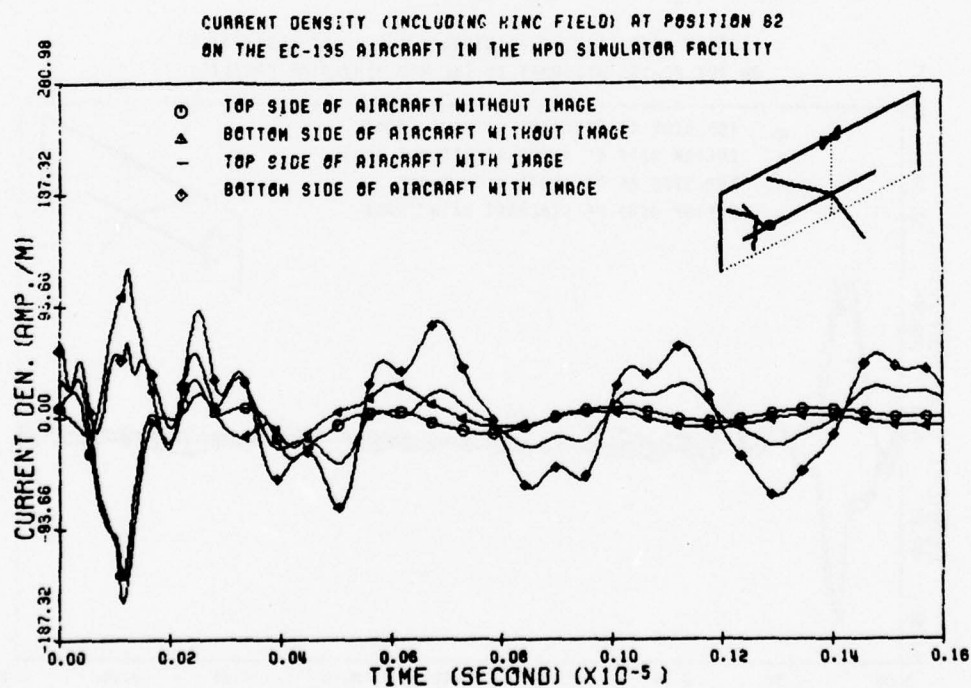


Figure 86:



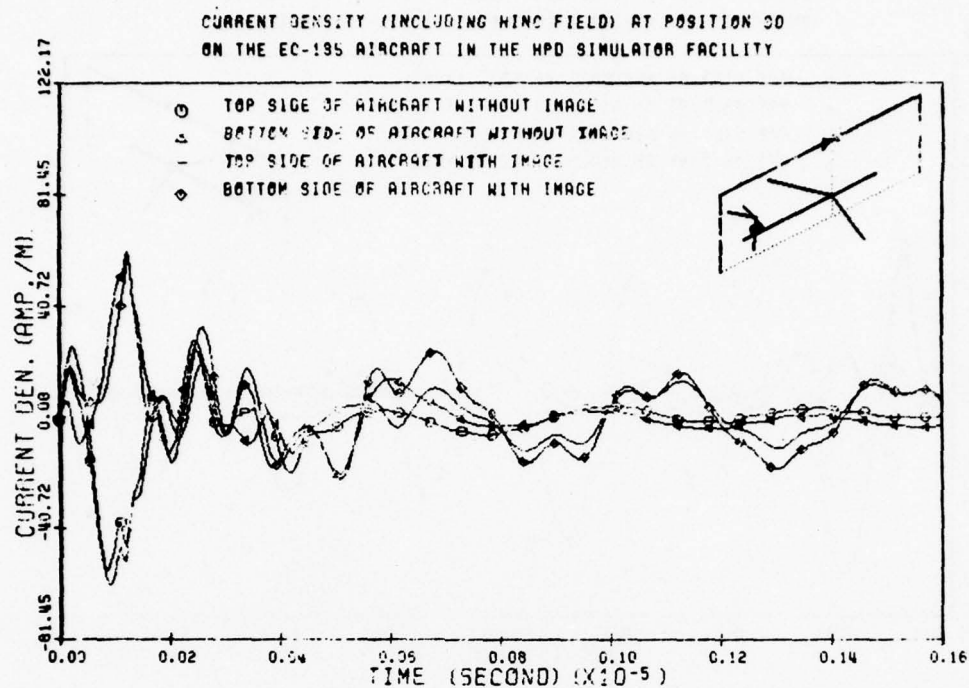


Figure 87:

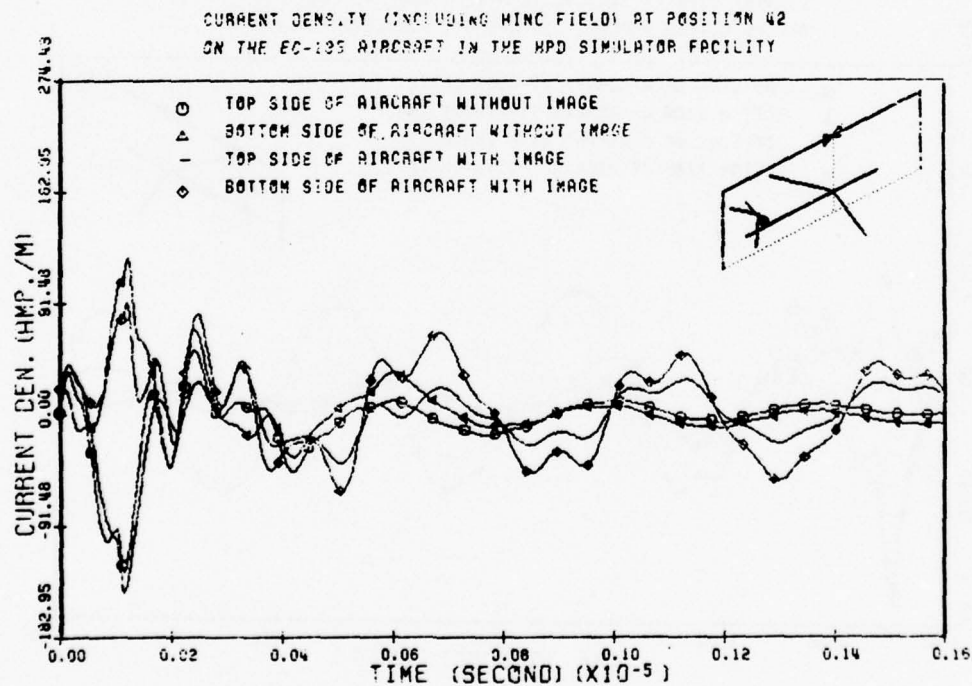


Figure 88:

CURRENT DENSITY (INCLUDING MIND FIELD) AT POSITION 40  
ON THE EC-135 AIRCRAFT IN THE HPD SIMULATOR FACILITY

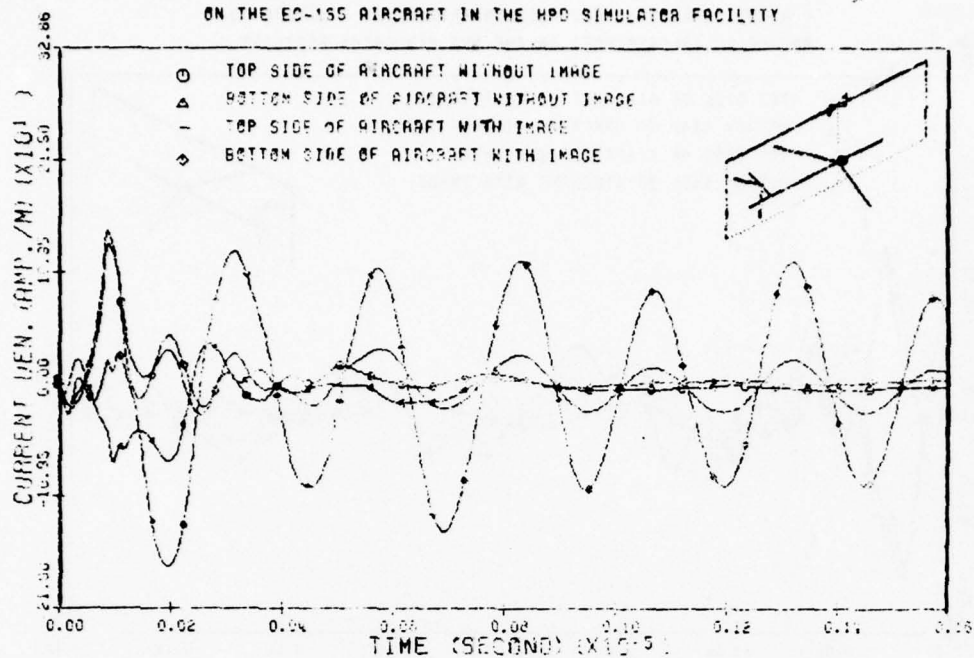


Figure 89:

CURRENT DENSITY (INCLUDING MIND FIELD) AT POSITION 55  
ON THE EC-135 AIRCRAFT IN THE HPD SIMULATOR FACILITY

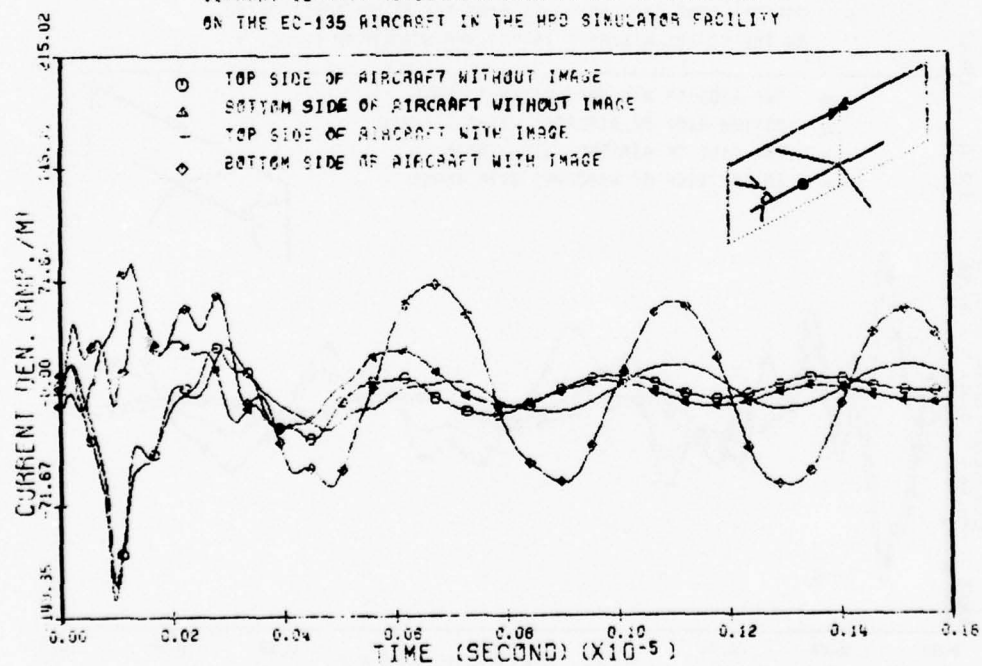


Figure 90:

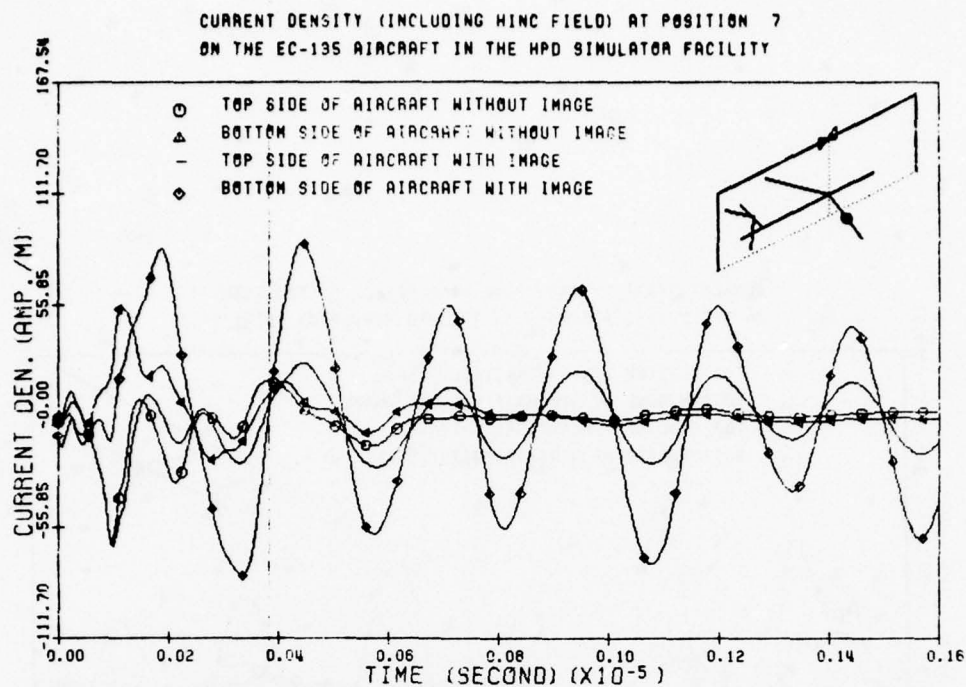


Figure 91:

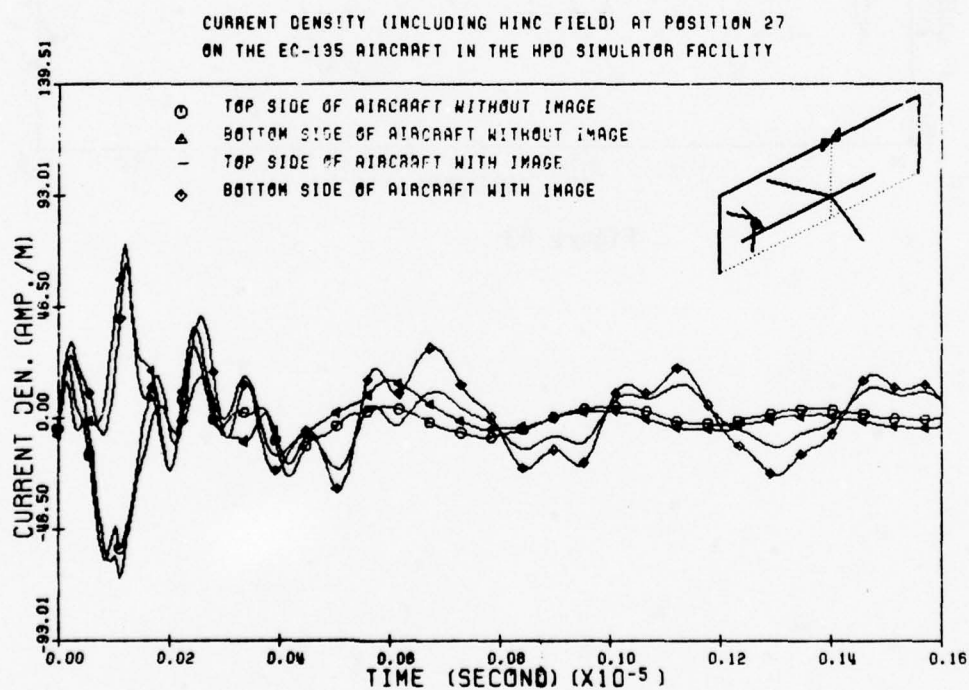


Figure 92:

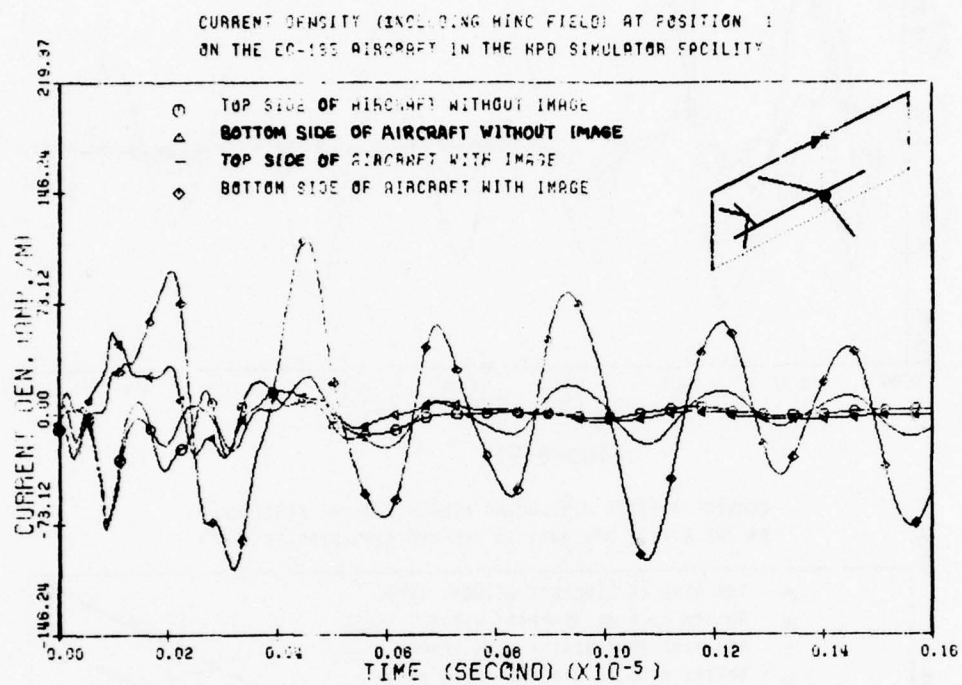


Figure 93:

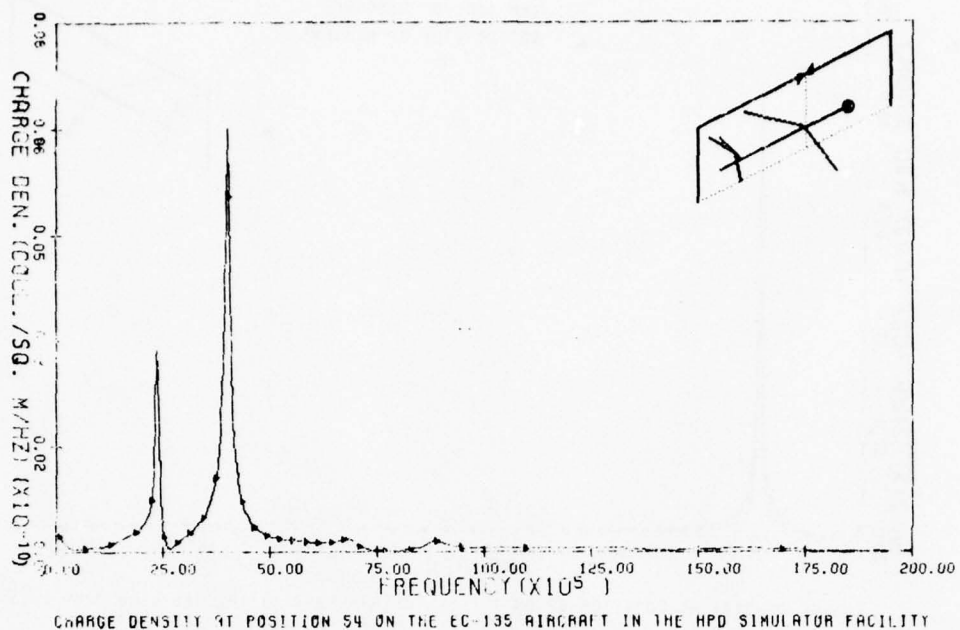


Figure 94:

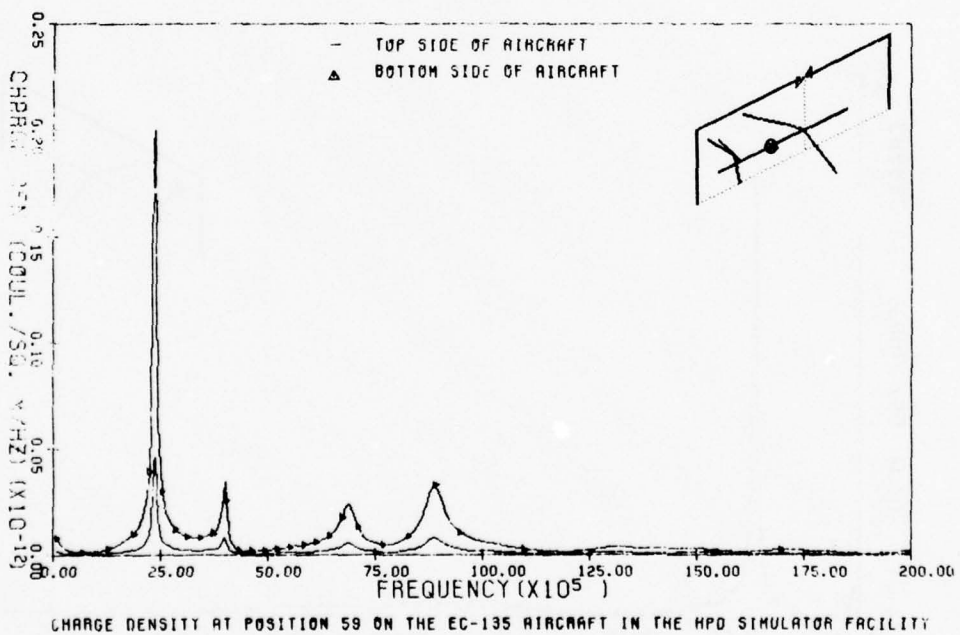


Figure 95:



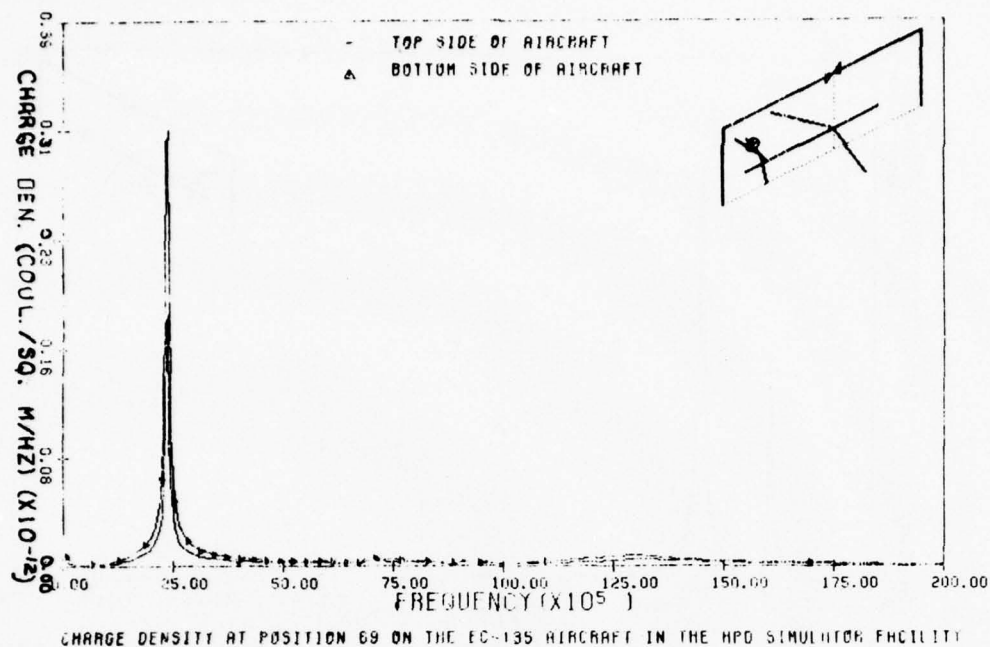


Figure 96:

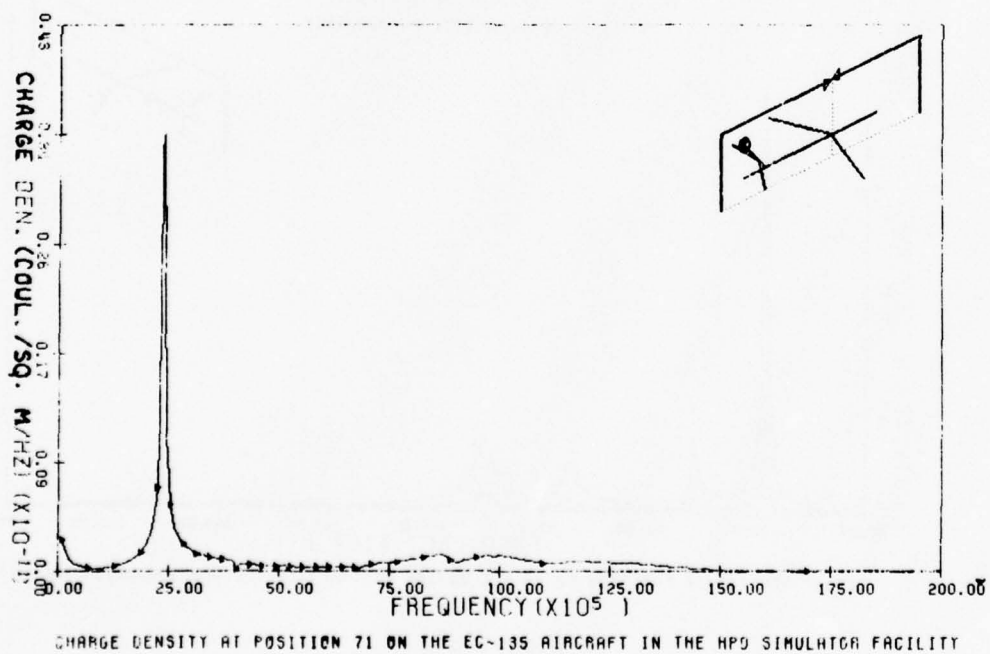


Figure 97:

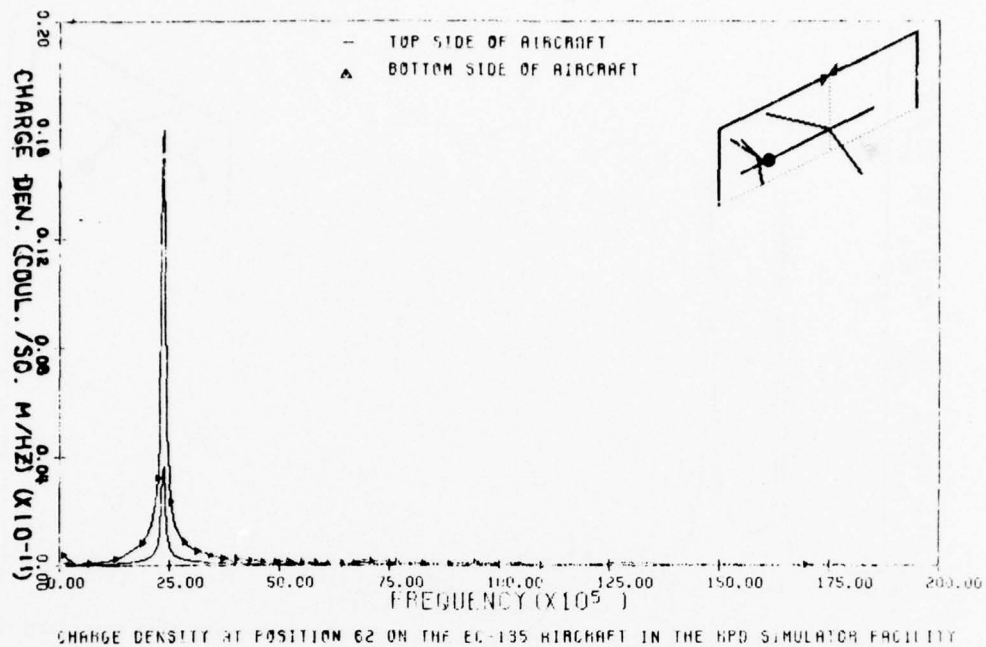


Figure 98:

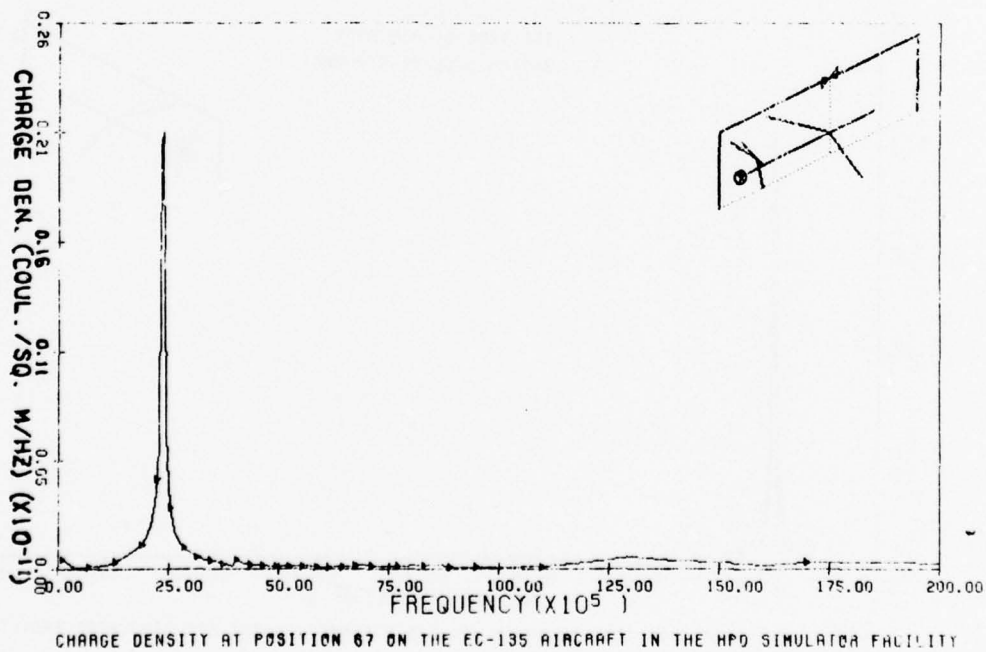
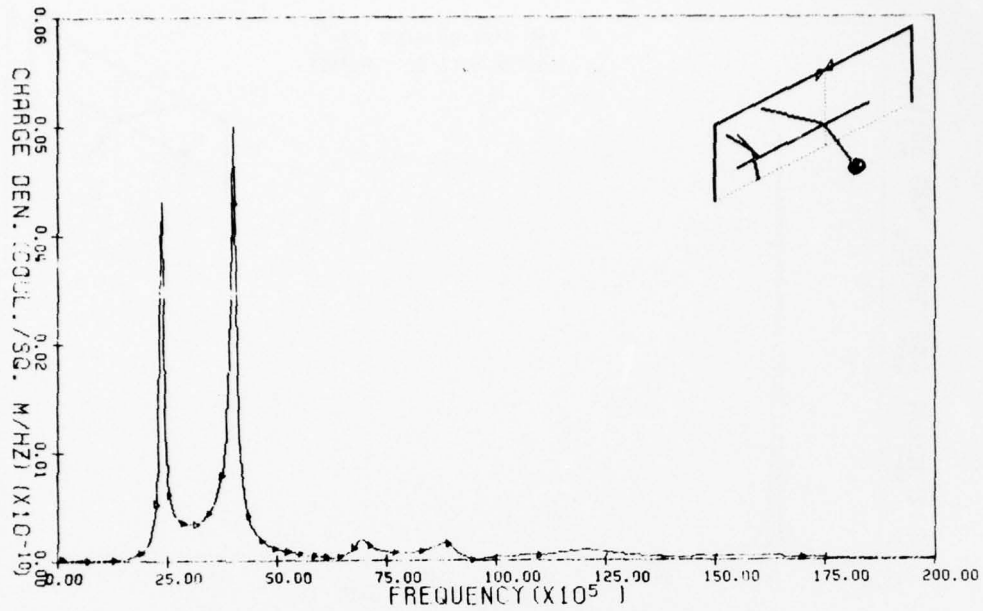
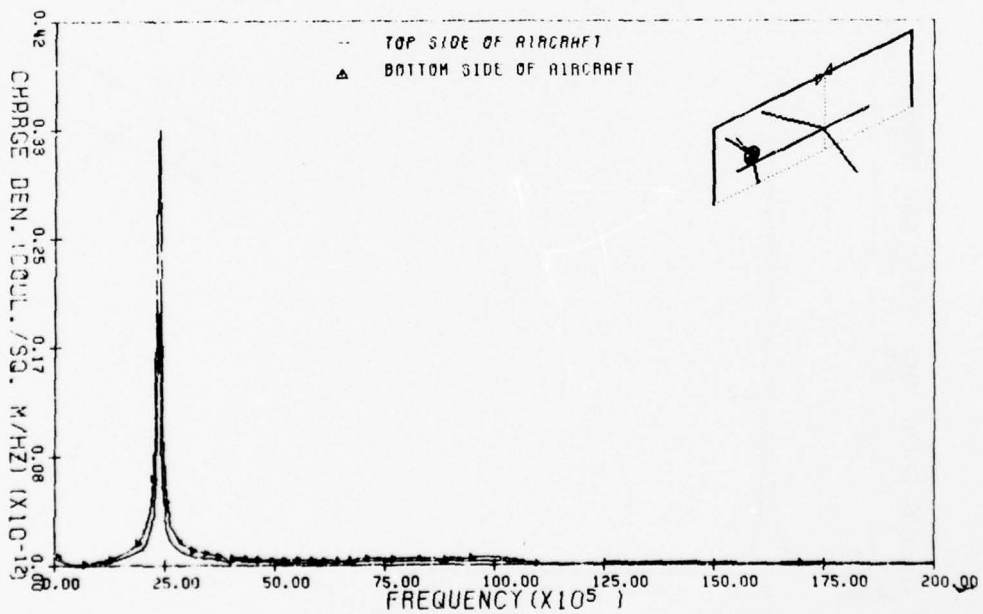


Figure 99:



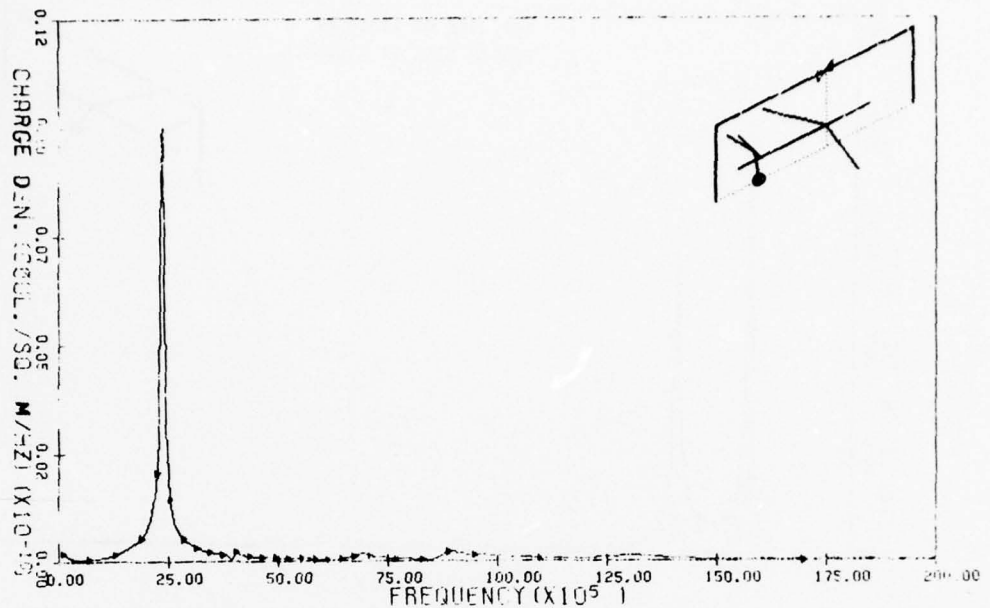
CHARGE DENSITY AT POSITION 13 ON THE EC-135 AIRCRAFT IN THE HPD SIMULATOR FACILITY

Figure 100:



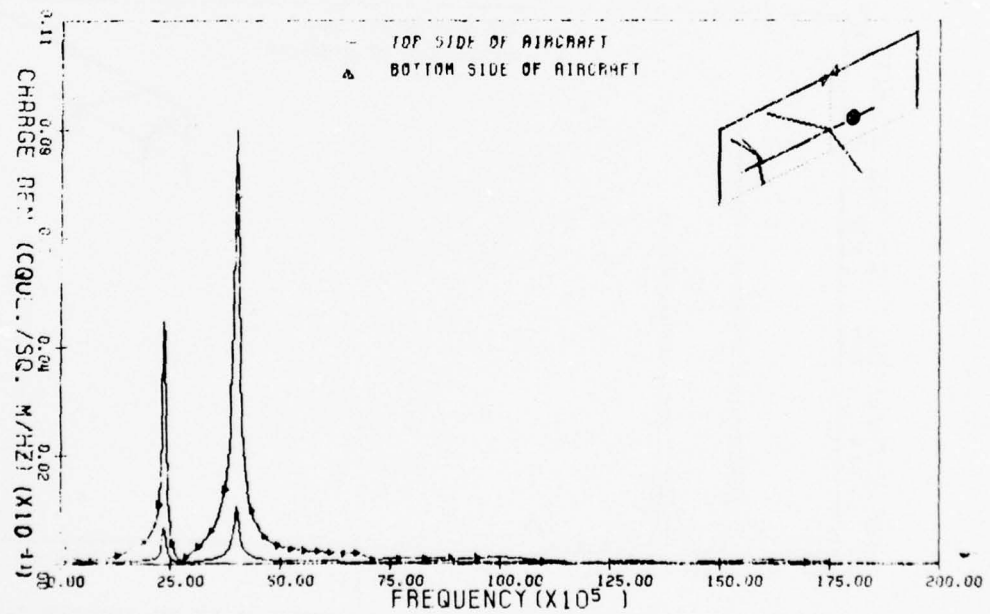
CHARGE DENSITY AT POSITION 27 ON THE EC-135 AIRCRAFT IN THE HPD SIMULATOR FACILITY

Figure 101:



CHARGE DENSITY AT POSITION 33 ON THE EC-135 AIRCRAFT IN THE HPD SIMULATOR FACILITY

Figure 102:



CHARGE DENSITY AT POSITION 49 ON THE EC-135 AIRCRAFT IN THE HPD SIMULATOR FACILITY

113

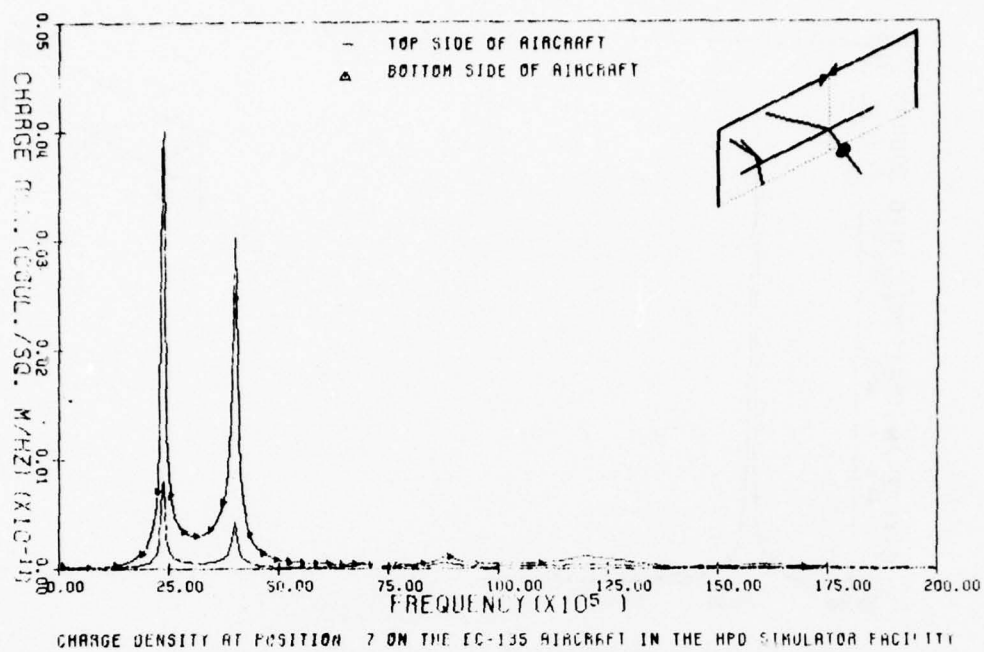


Figure 104:

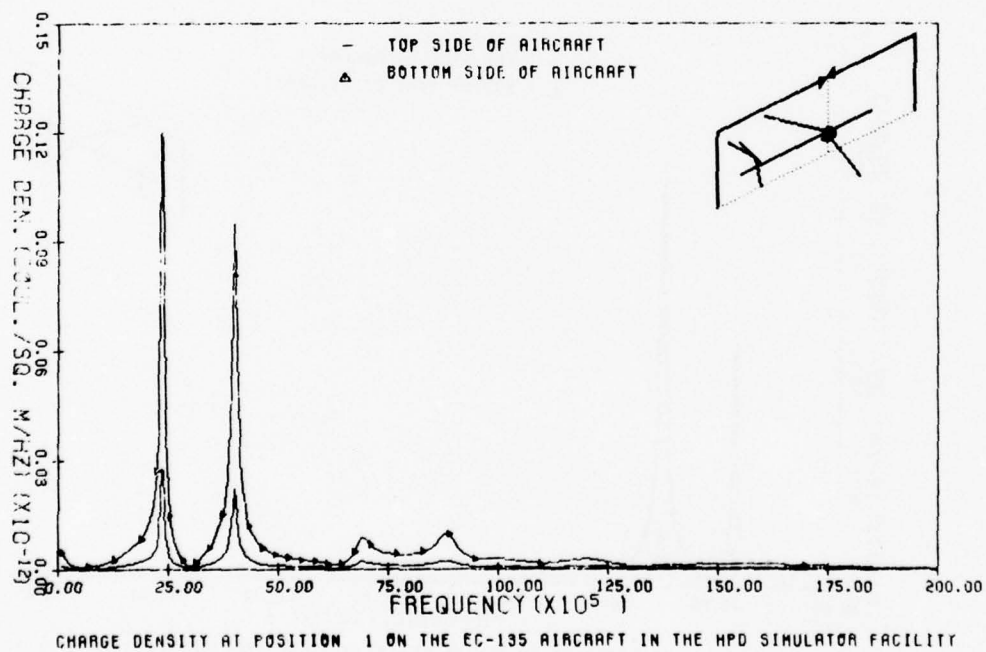


Figure 105:



CHARGE DENSITY AT POSITION 71 ON THE EC-135  
AIRCRAFT IN THE HPD SIMULATOR FACILITY

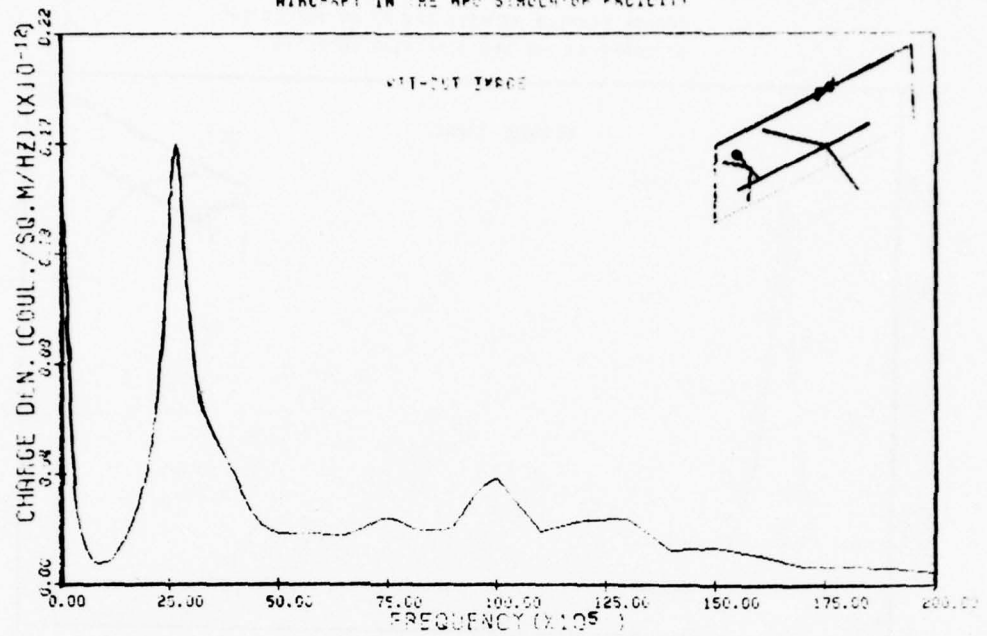


Figure 106:

CHARGE DENSITY AT POSITION 66 ON THE EC-135  
AIRCRAFT IN THE HPD SIMULATOR FACILITY

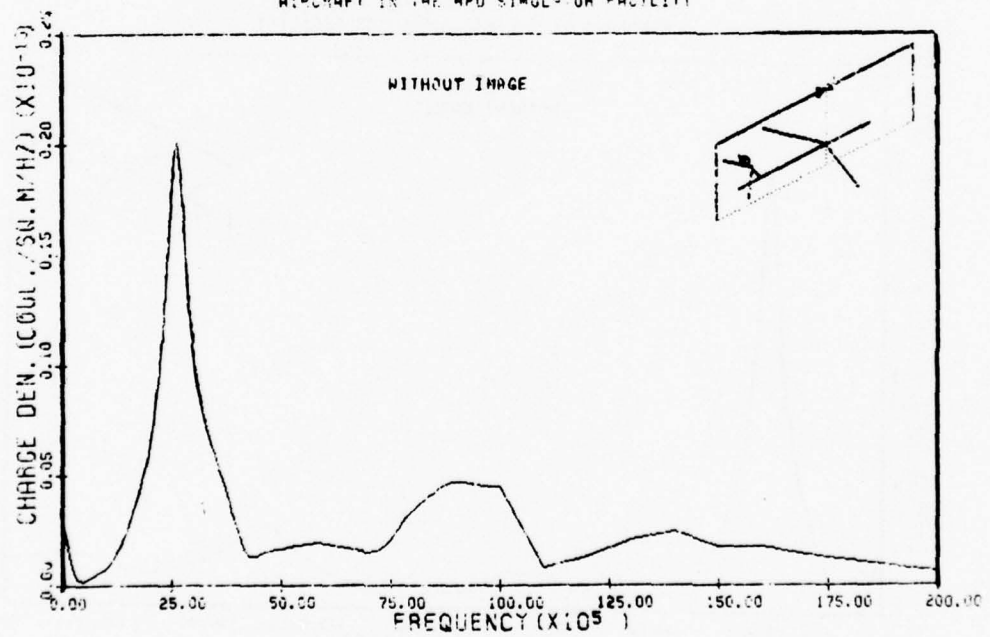


Figure 107:

CHARGE DENSITY AT POSITION 69 ON THE EC-135  
AIRCRAFT IN THE HPD SIMULATOR FACILITY

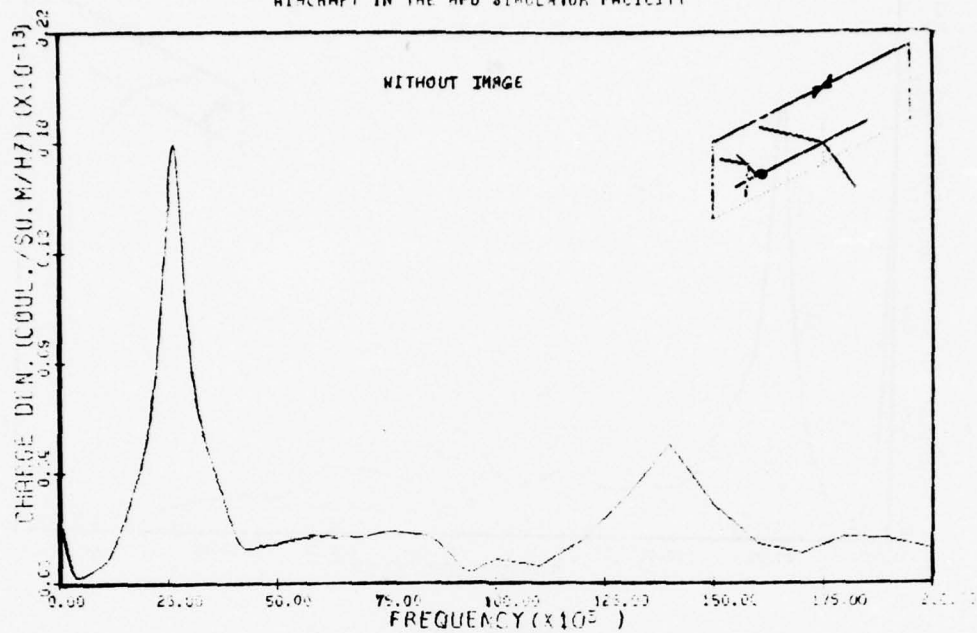


Figure 108:

CHARGE DENSITY AT POSITION 67 ON THE EC-135  
AIRCRAFT IN THE HPD SIMULATOR FACILITY

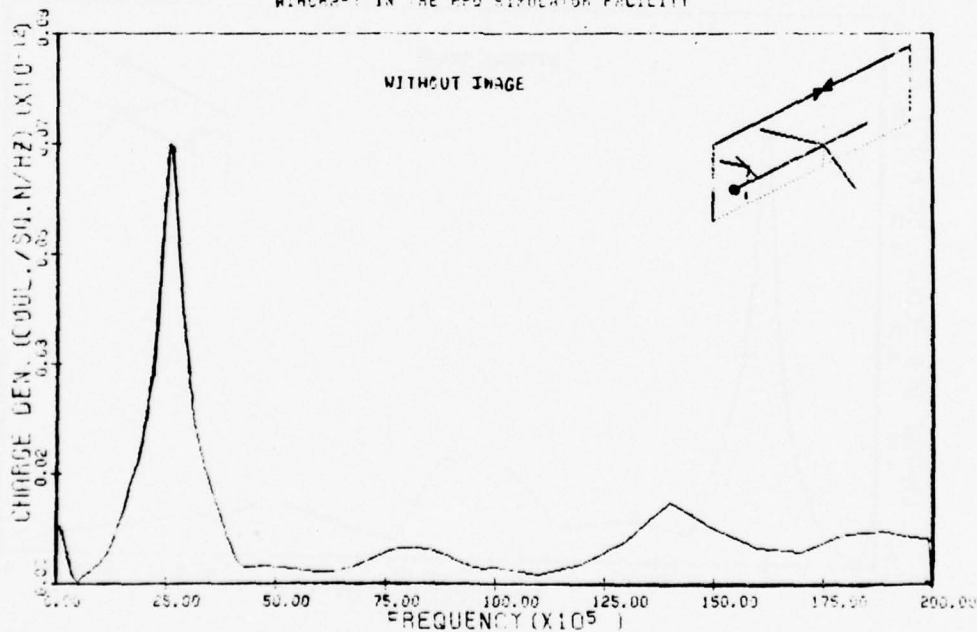


Figure 109:

CHARGE DENSITY AT POSITION 54 ON THE EC-135  
AIRCRAFT IN THE WPD SIMULATOR FACILITY

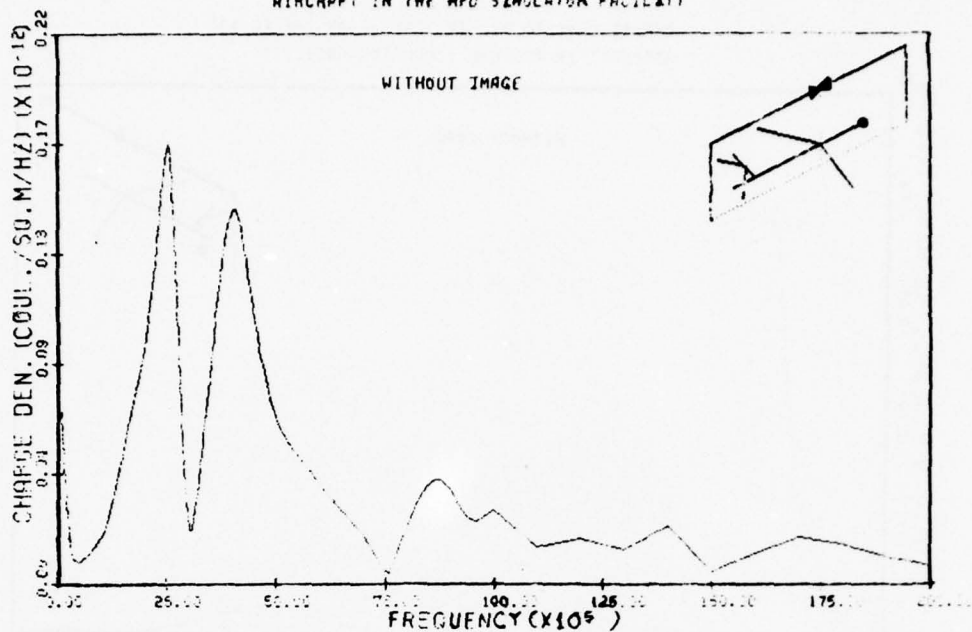


Figure 110:

CHARGE DENSITY AT POSITION 59 ON THE EC-135  
AIRCRAFT IN THE WPD SIMULATOR FACILITY

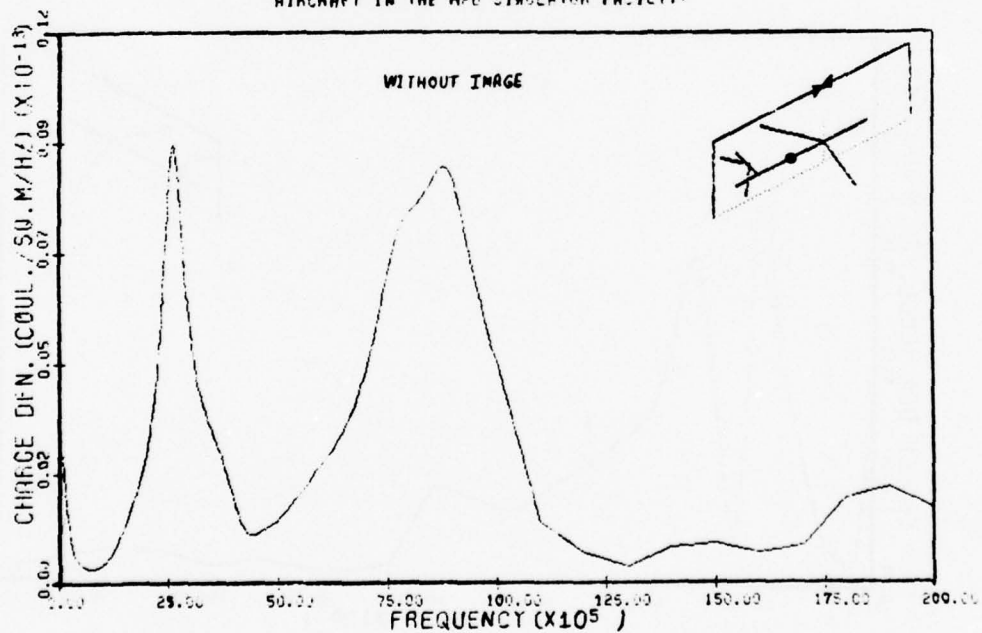


Figure 111:

CHARGE DENSITY AT POSITION 03 ON THE EC-135  
AIRCRAFT IN THE HPD SIMULATOR FACILITY

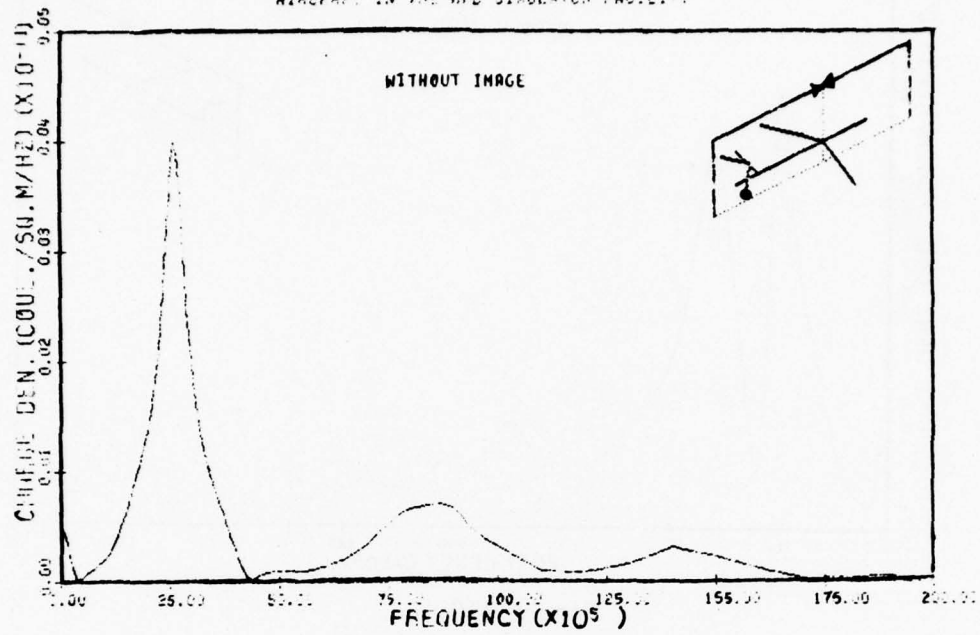


Figure 112:

CHARGE DENSITY AT POSITION 06 ON THE EC-135  
AIRCRAFT IN THE HPD SIMULATOR FACILITY

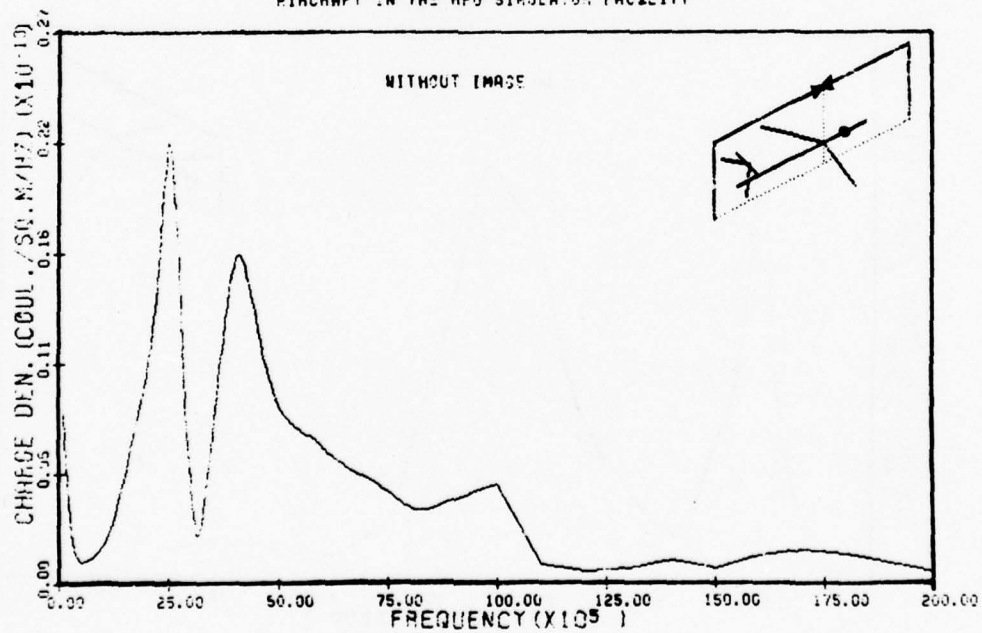


Figure 113:

CHARGE DENSITY AT POSITION 10 ON THE EC-135  
AIRCRAFT IN THE HPD SIMULATOR FACILITY

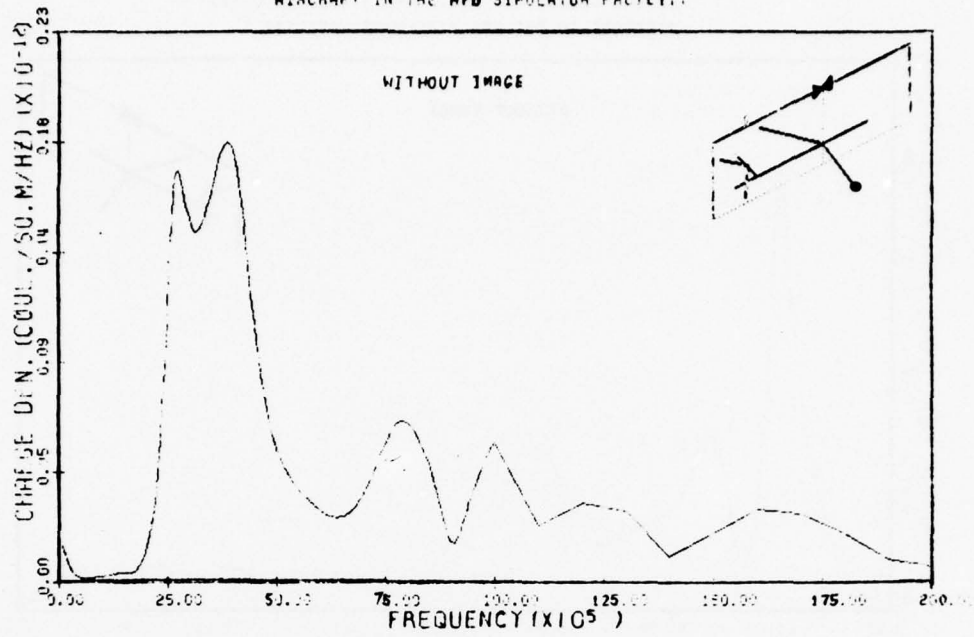


Figure 114:

CHARGE DENSITY AT POSITION 27 ON THE EC-135  
AIRCRAFT IN THE HPD SIMULATOR FACILITY

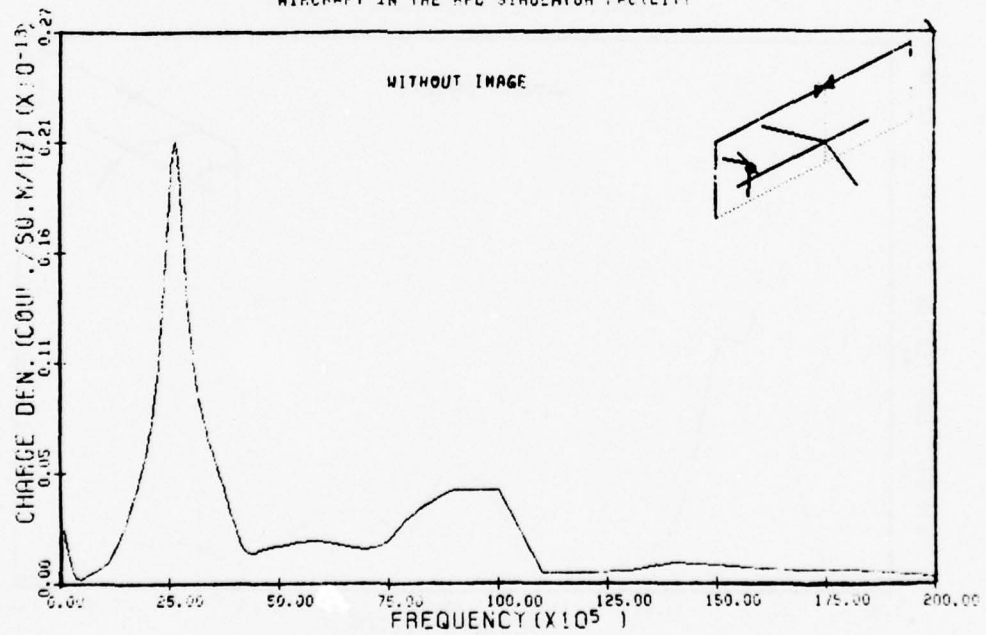


Figure 115:



CHARGE DENSITY AT POSITION 1 ON THE EC-135  
AIRCRAFT IN THE WPD SIMULATOR FACILITY

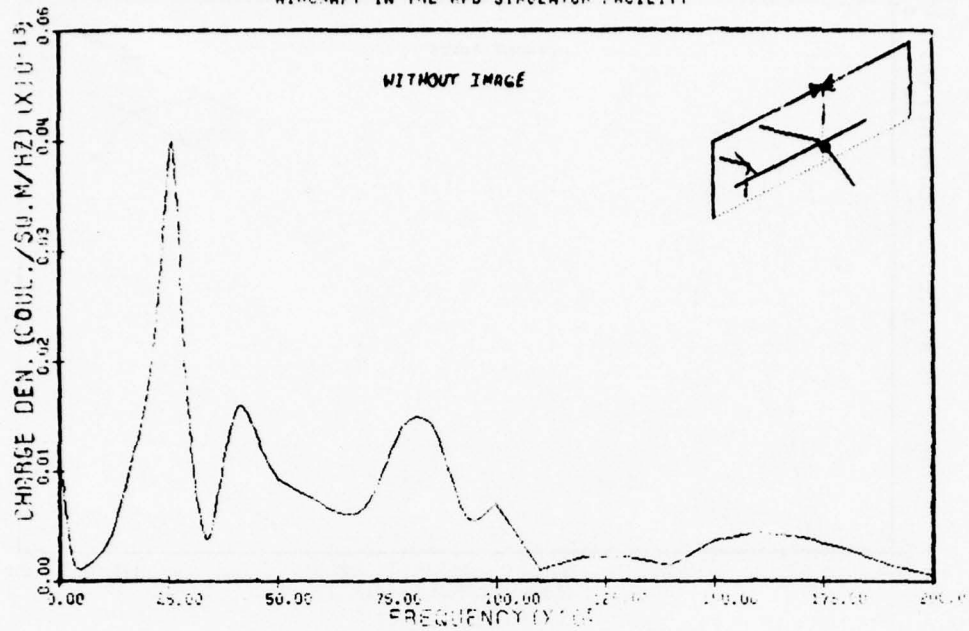


Figure 116:

CHARGE DENSITY AT POSITION 7 ON THE EC-135  
AIRCRAFT IN THE WPD SIMULATOR FACILITY

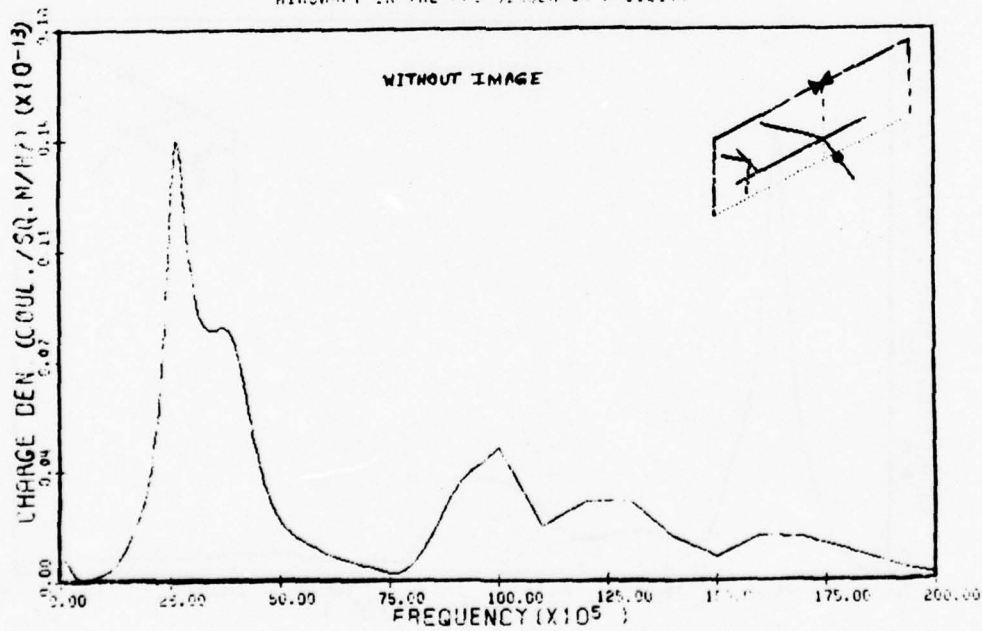


Figure 117:

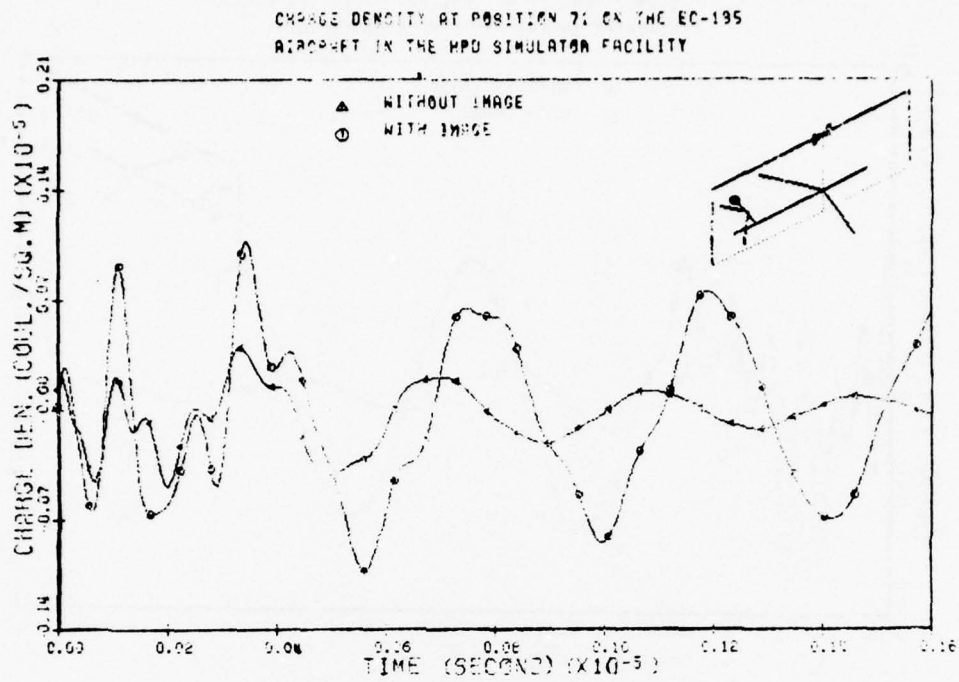


Figure 118:

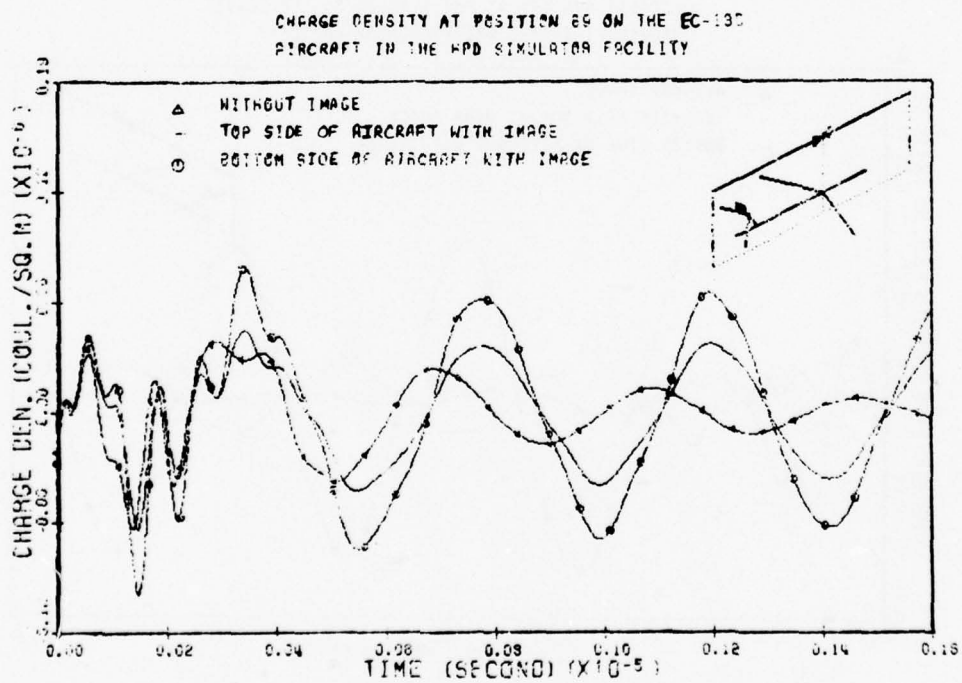


Figure 119:

CHARGE DENSITY AT POSITION 67 ON THE EC-135  
AIRCRAFT IN THE HPD SIMULATOR FACILITY

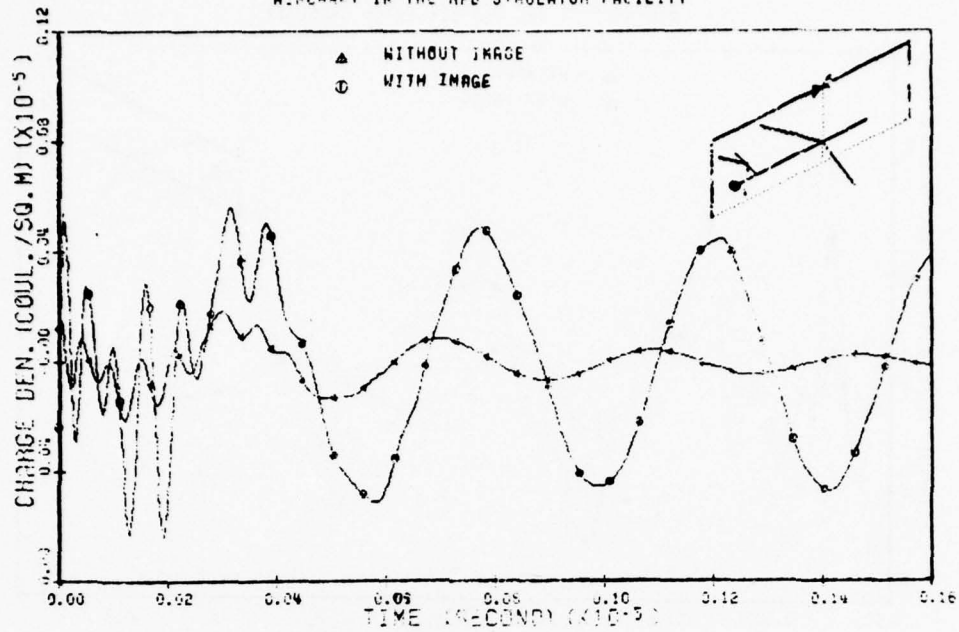


Figure 120:

CHARGE DENSITY AT POSITION 83 ON THE EC-135  
AIRCRAFT IN THE HPD SIMULATOR FACILITY

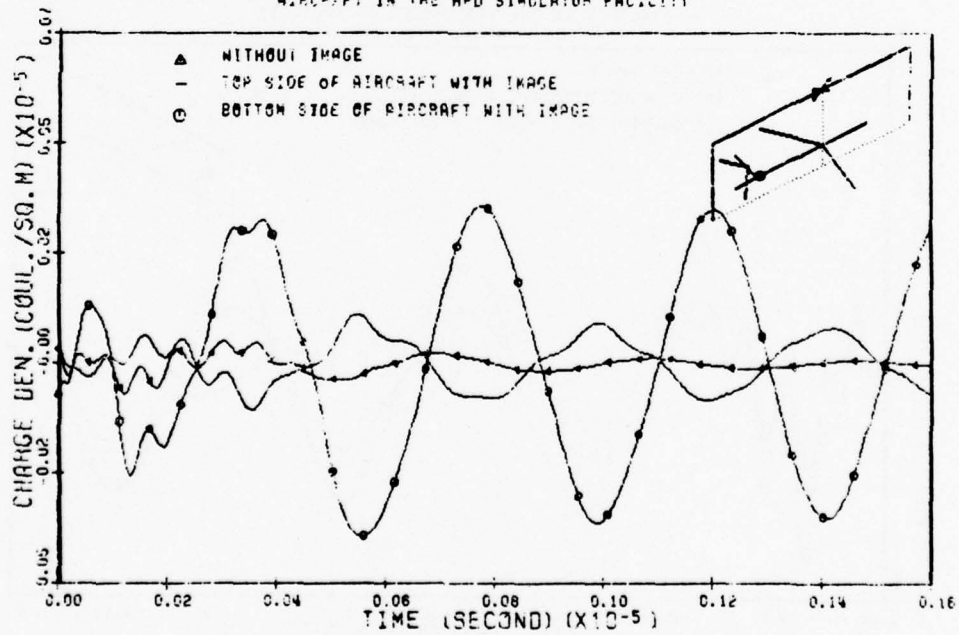


Figure 121:

CHARGE DENSITY AT POSITION 1 ON THE EC-195  
AIRCRAFT IN THE HPD SIMULATOR FACILITY

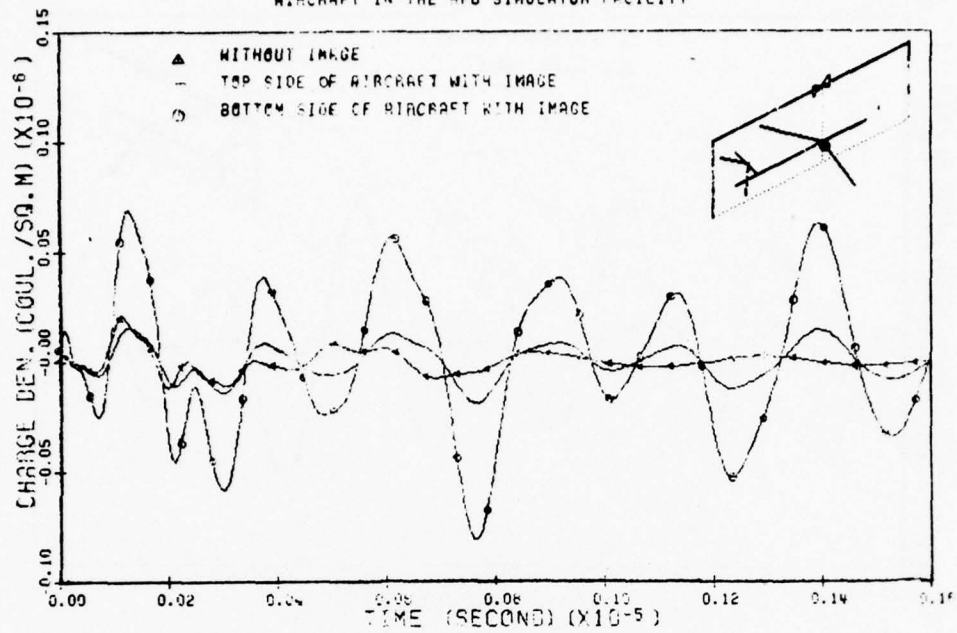


Figure 122:

CHARGE DENSITY AT POSITION 7 ON THE EC-195  
AIRCRAFT IN THE HPD SIMULATOR FACILITY

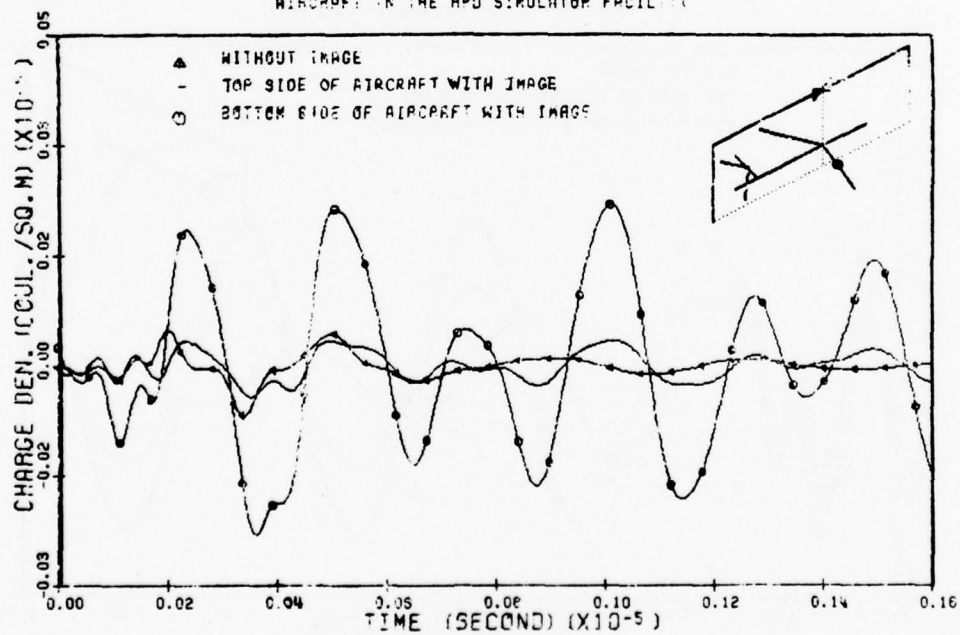


Figure 123:

CHARGE DENSITY AT POSITION 13 ON THE EC-135  
AIRCRAFT IN THE HPD SIMULATOR FACILITY

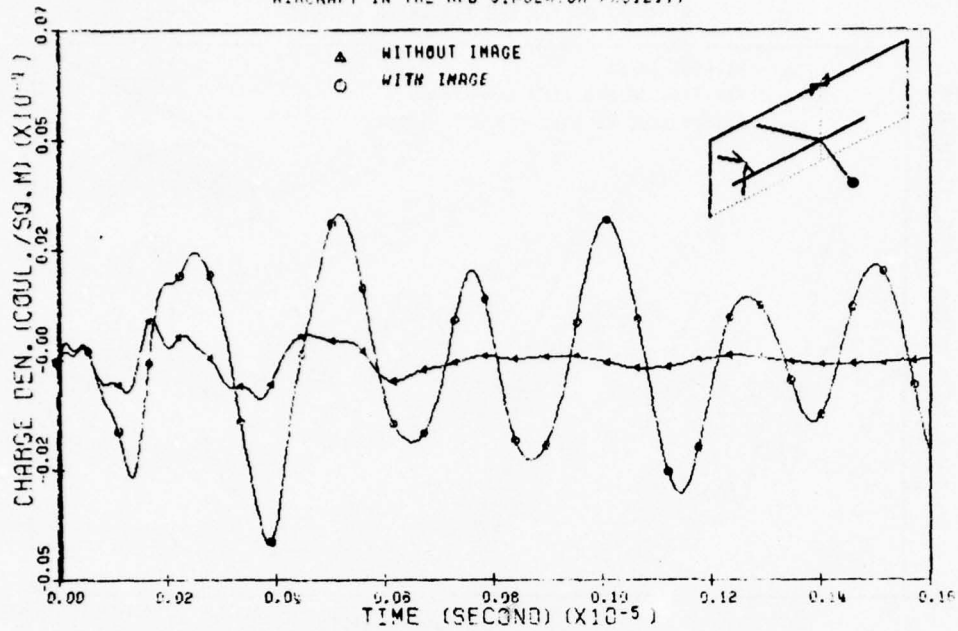


Figure 124:

CHARGE DENSITY AT POSITION 27 ON THE EC-135  
AIRCRAFT IN THE HPD SIMULATOR FACILITY

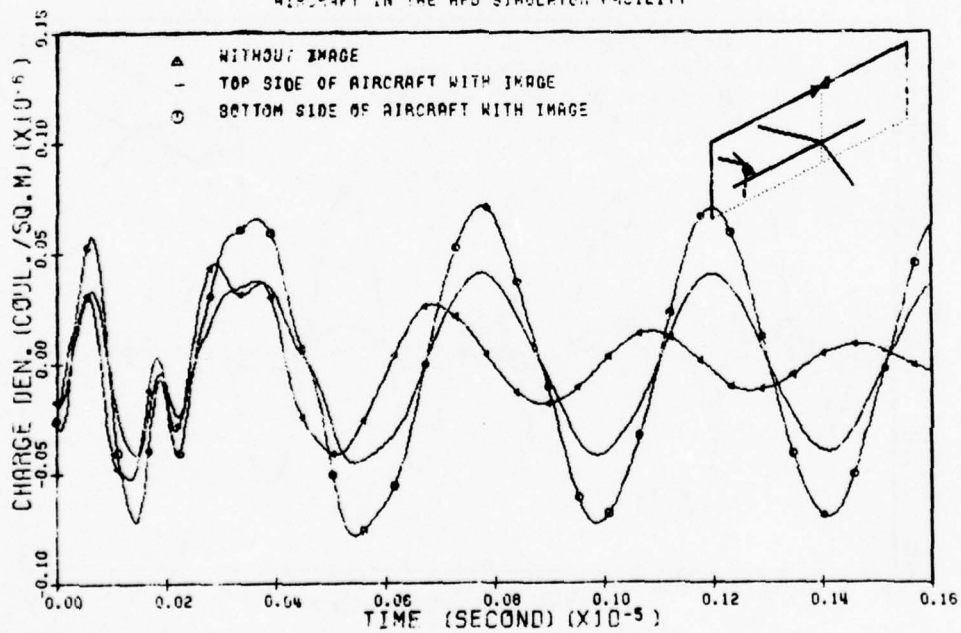


Figure 125:



CHARGE DENSITY AT POSITION 33 ON THE EC-135  
AIRCRAFT IN THE HPD SIMULATOR FACILITY

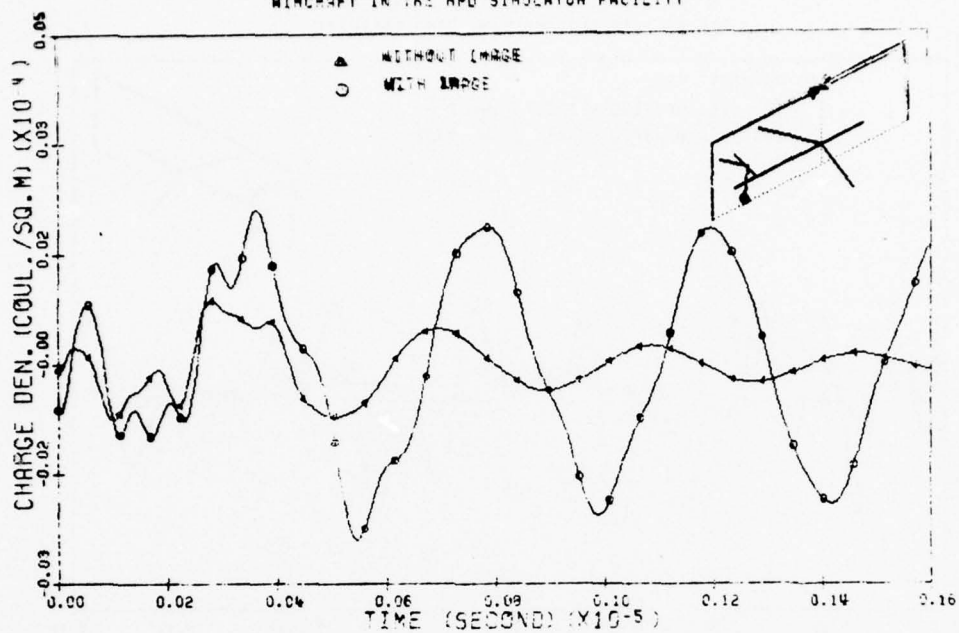


Figure 126:

CHARGE DENSITY AT POSITION 40 ON THE EC-135  
AIRCRAFT IN THE HPD SIMULATOR FACILITY

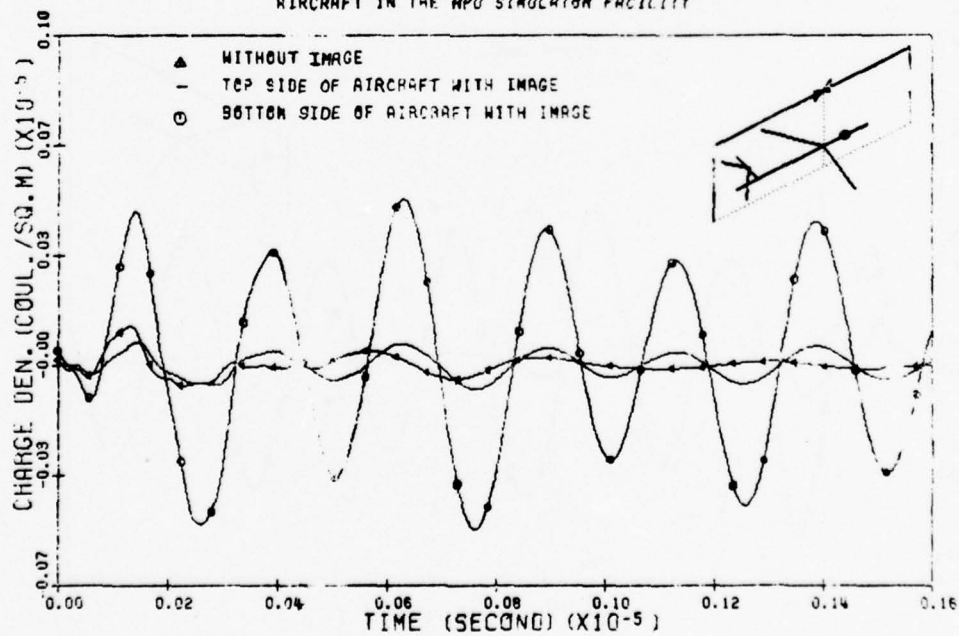


Figure 127:

CHARGE DENSITY AT POSITION 59 ON THE EC-135  
AIRCRAFT IN THE HPD SIMULATOR FACILITY

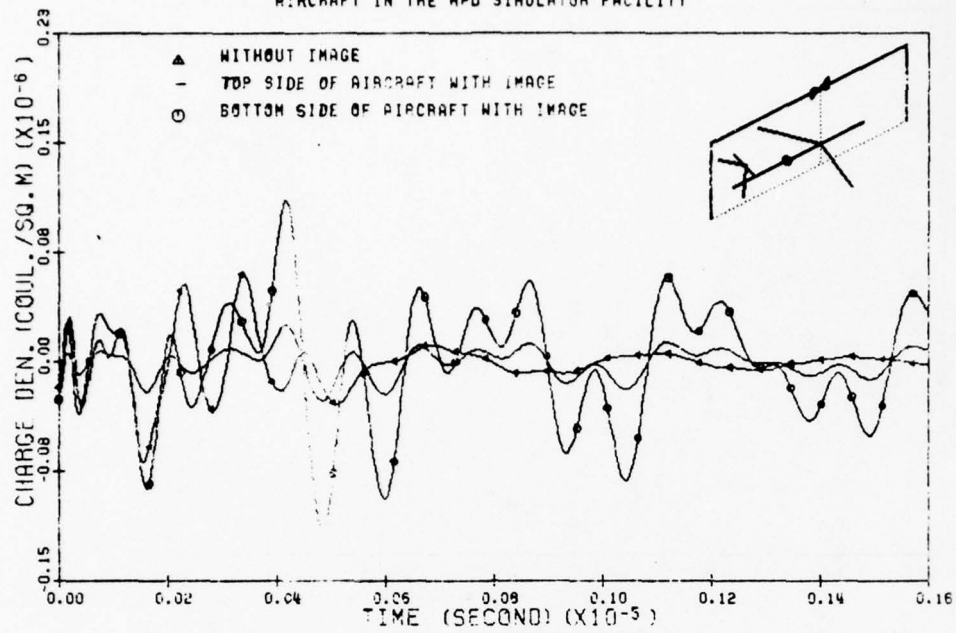


Figure 128:

CHARGE DENSITY AT POSITION 54 ON THE EC-135  
AIRCRAFT IN THE HPD SIMULATOR FACILITY

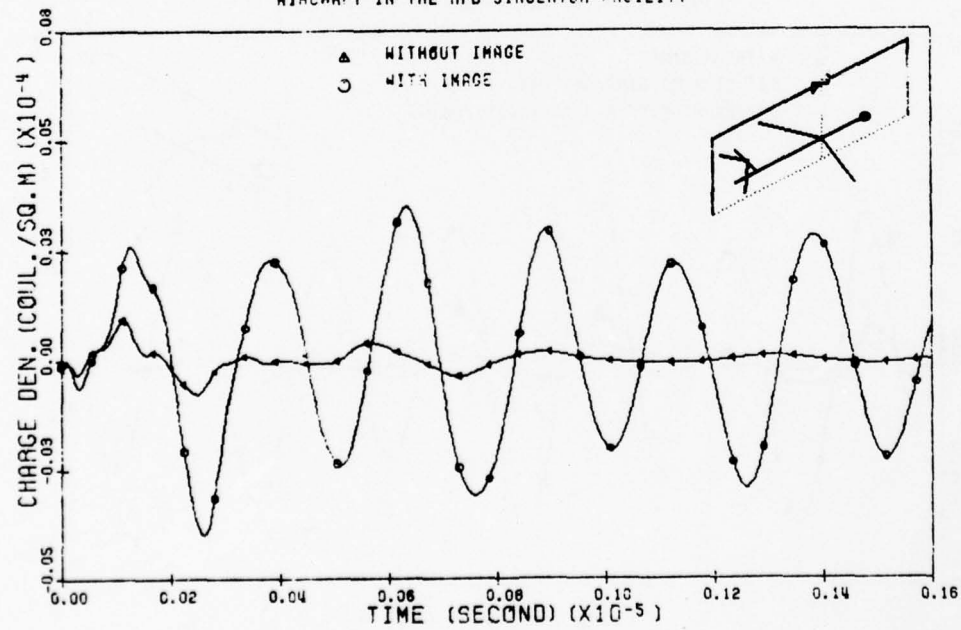


Figure 129:

CURRENT DENSITY (INCLUDING HINC FIELD) AT POSITION 1 ON THE EC-135  
AIRCRAFT FOR TOPSIDE INCIDENCE DOUBLE EXPONENTIAL PLANE WAVE

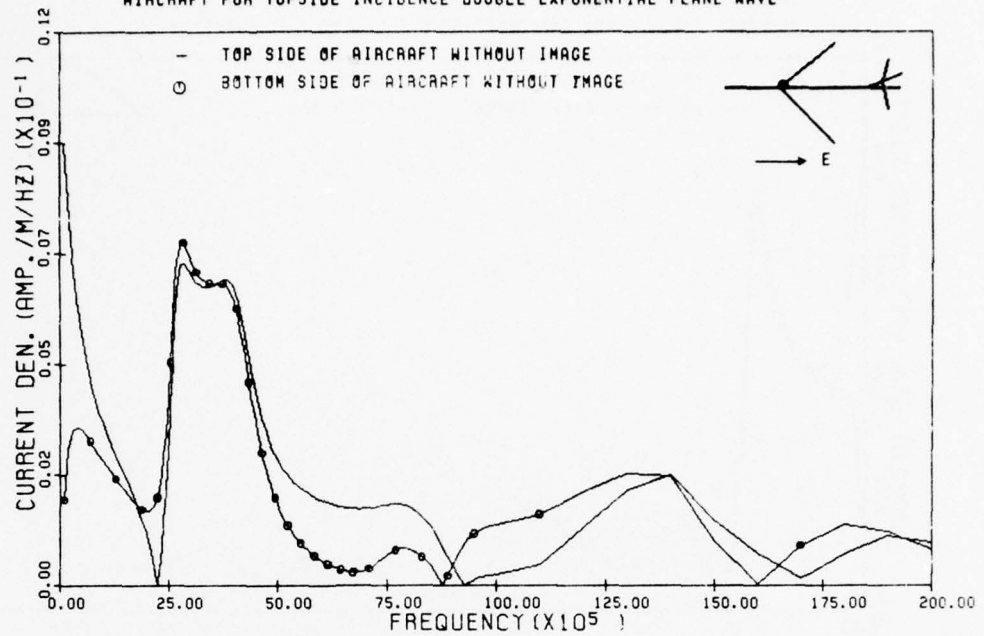


Figure 130:

CURRENT DENSITY (INCLUDING HINC FIELD) AT POSITION 7 ON THE EC-135  
AIRCRAFT FOR TOPSIDE INCIDENCE DOUBLE EXPONENTIAL PLANE WAVE

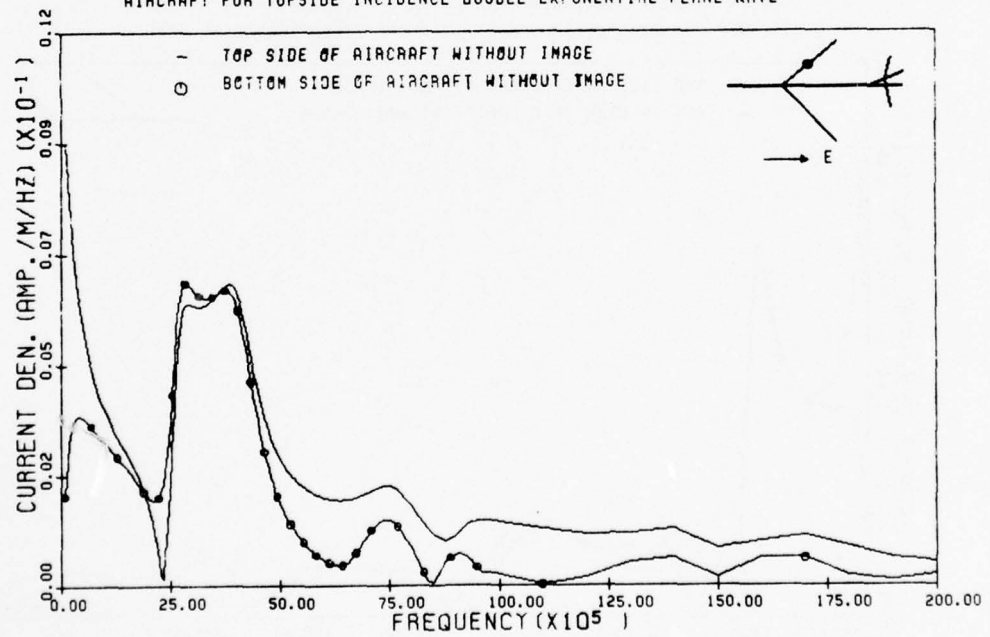


Figure 131:

CURRENT DENSITY (INCLUDING HINC FIELD) AT POSITION 27 ON THE EC-135  
AIRCRAFT FOR TOPSIDE INCIDENCE DOUBLE EXPONENTIAL PLANE WAVE

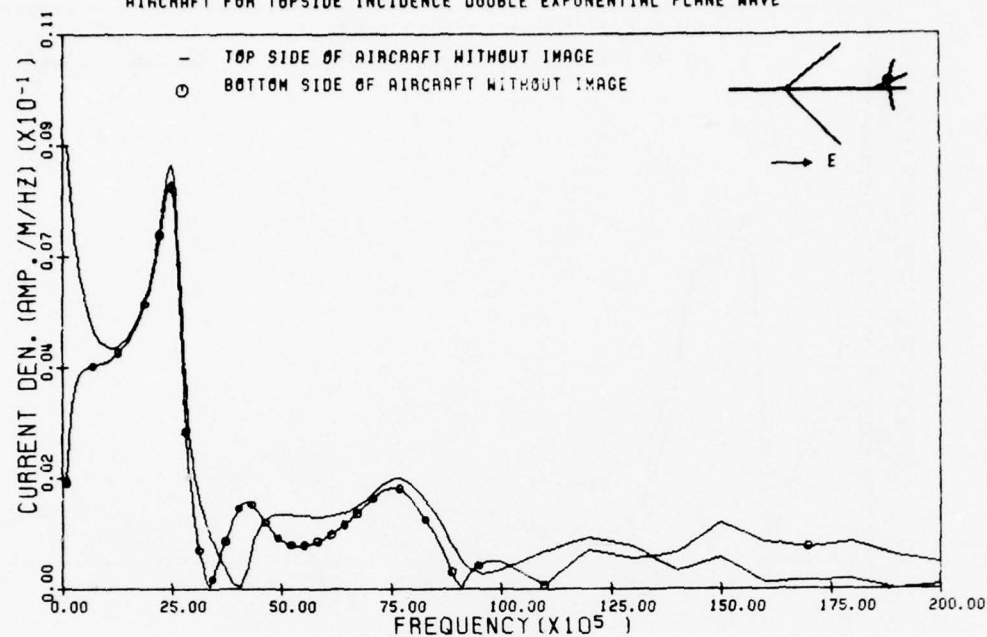


Figure 132:

CURRENT DENSITY (INCLUDING HINC FIELD) AT POSITION 30 ON THE EC-135  
AIRCRAFT FOR TOPSIDE INCIDENCE DOUBLE EXPONENTIAL PLANE WAVE

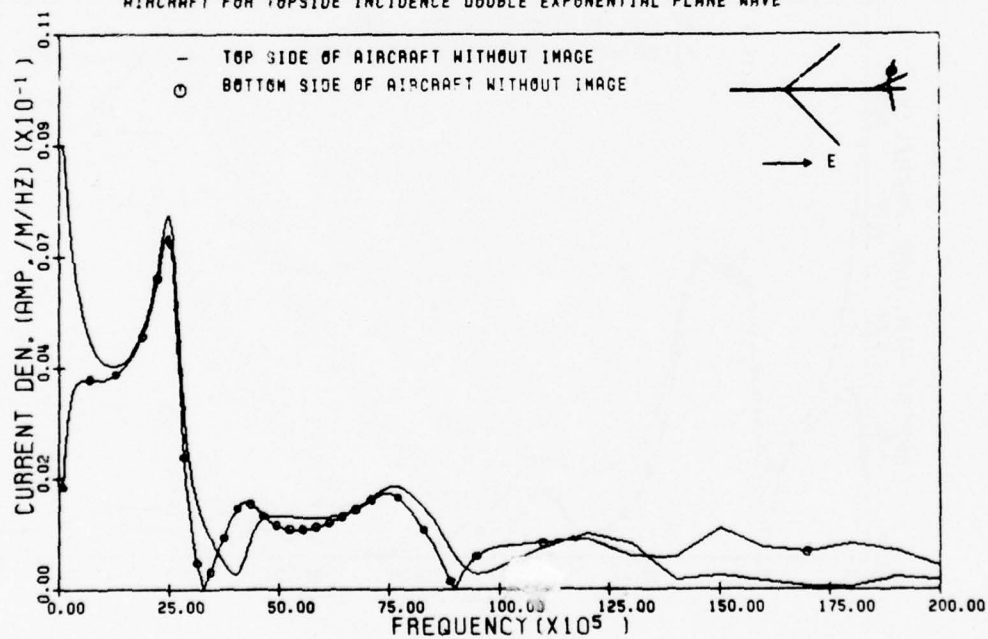


Figure 133:

CURRENT DENSITY (INCLUDING HINC FIELD) AT POSITION 59 ON THE EC-135  
AIRCRAFT FOR TOPSIDE INCIDENCE DOUBLE EXPONENTIAL PLANE WAVE

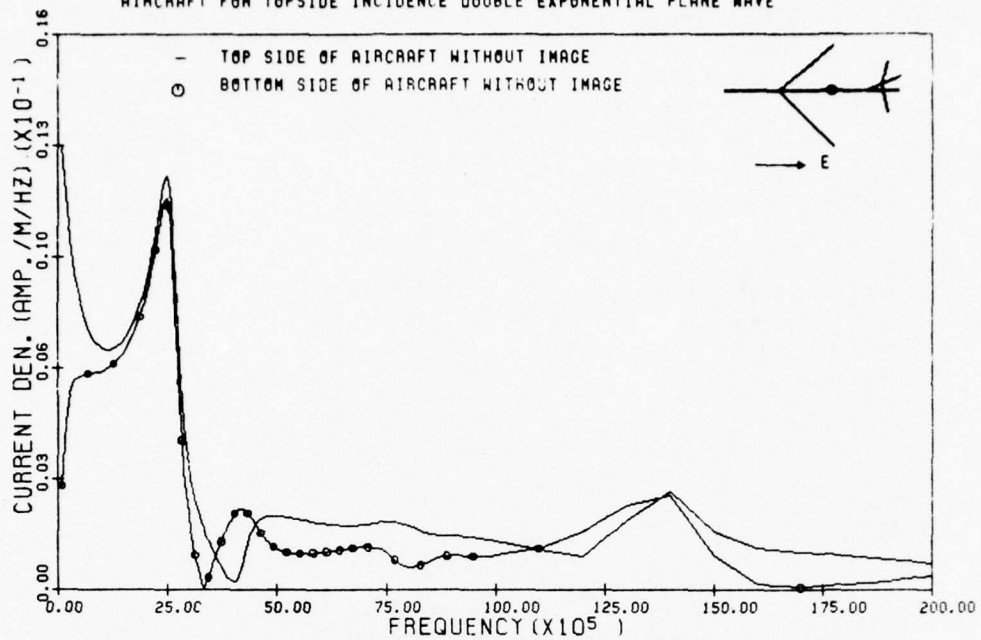


Figure 134:

CURRENT DENSITY (INCLUDING HINC FIELD) AT POSITION 49 ON THE EC-135  
AIRCRAFT FOR TOPSIDE INCIDENCE DOUBLE EXPONENTIAL PLANE WAVE

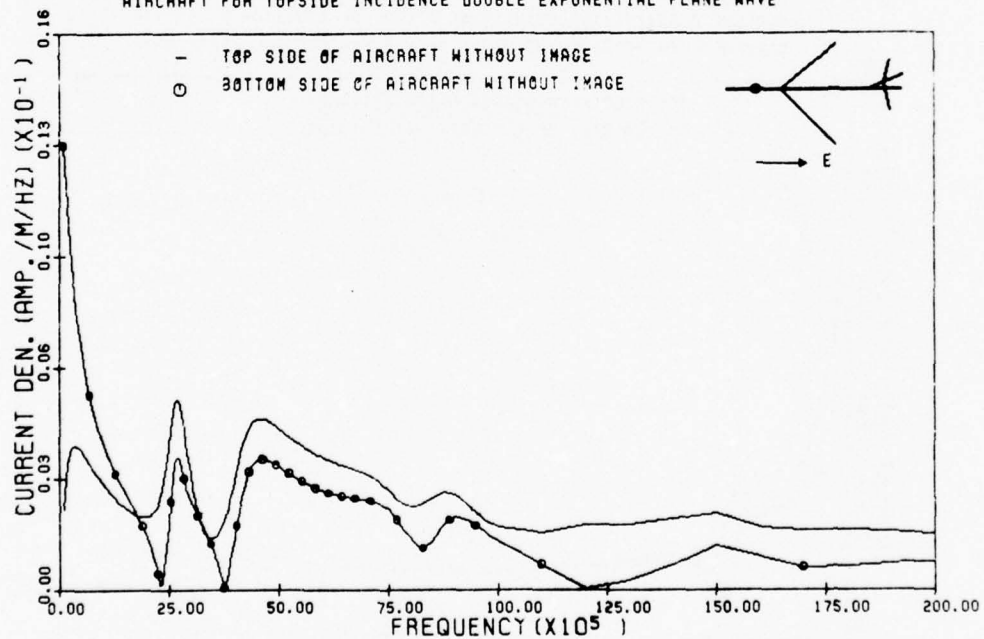


Figure 135:



CURRENT DENSITY (INCLUDING HINC FIELD) AT POSITION 82 ON THE EC-135  
AIRCRAFT FOR TOPSIDE INCIDENCE DOUBLE EXPONENTIAL PLANE WAVE

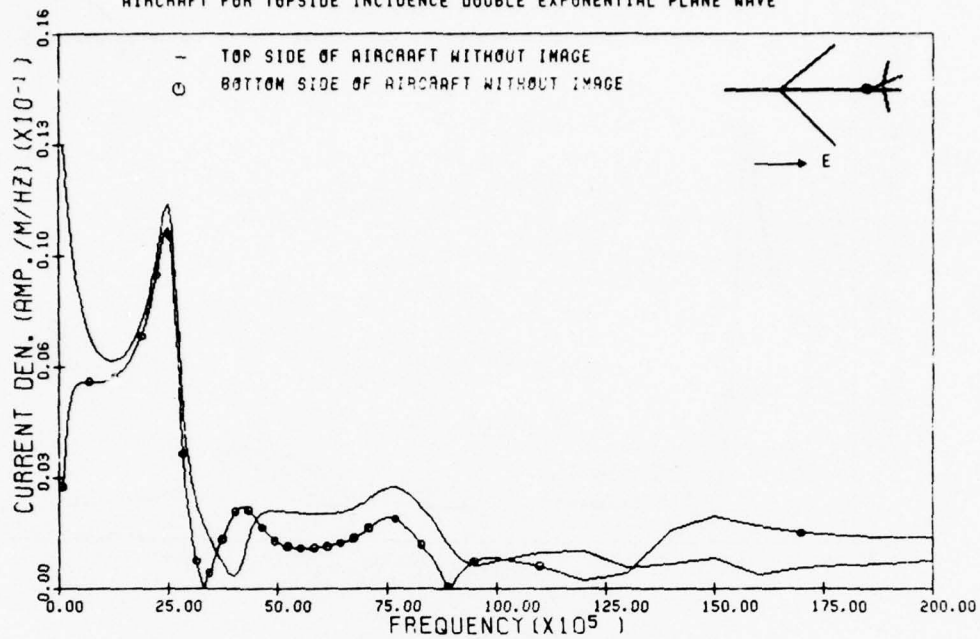


Figure 136:

CURRENT DENSITY (INCLUDING HINC FIELD) AT POSITION 65 ON THE EC-135  
AIRCRAFT FOR TOPSIDE INCIDENCE DOUBLE EXPONENTIAL PLANE WAVE

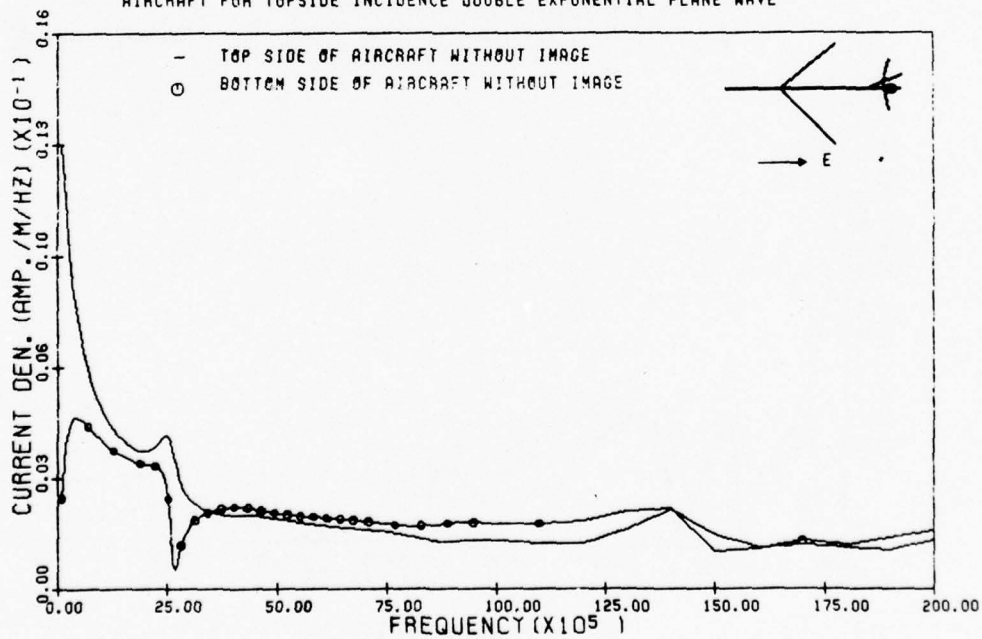


Figure 137:

CURRENT DENSITY (INCLUDING RING FIELD) AT POSITION 44 ON THE EC-135  
AIRCRAFT FOR TOPSIDE INCIDENCE DOUBLE EXPONENTIAL PLANE WAVE

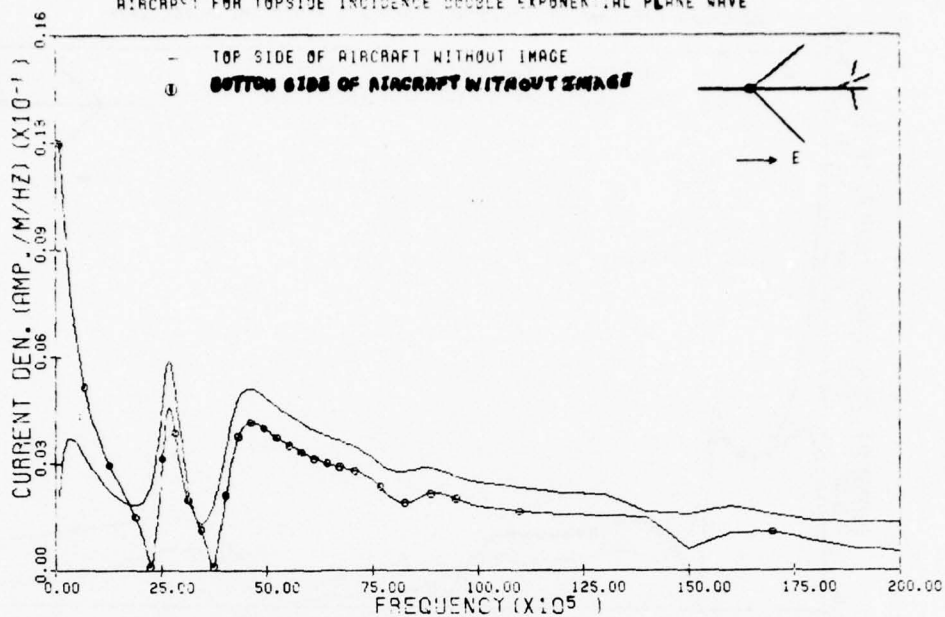


Figure 138:

CURRENT DENSITY (INCLUDING RING FIELD) AT POSITION 42 ON THE EC-135  
AIRCRAFT FOR TOPSIDE INCIDENCE DOUBLE EXPONENTIAL PLANE WAVE

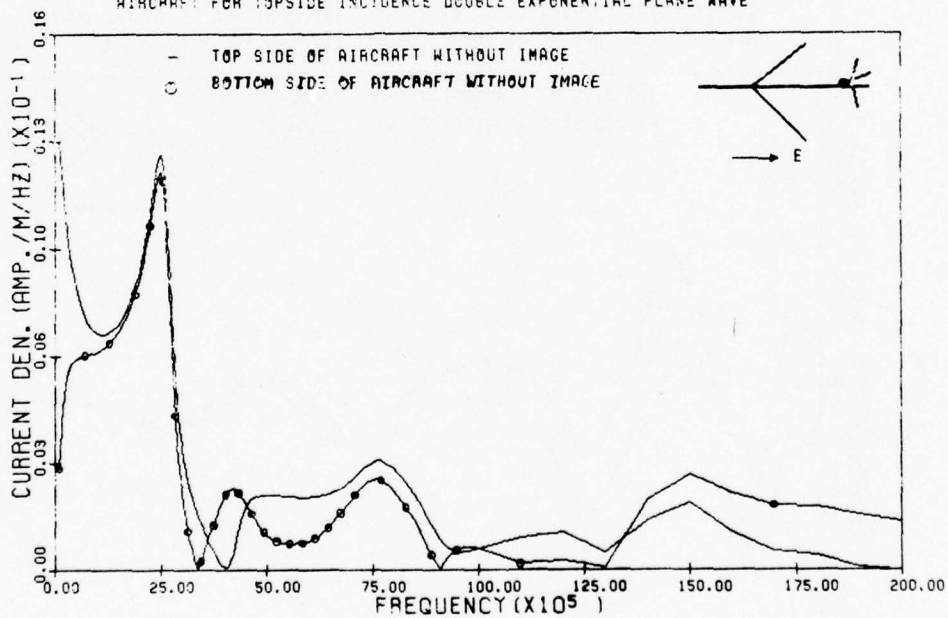


Figure 139:

CURRENT DENSITY (INCLUDING HINC FIELD) AT POSITION 69 ON THE EC-135  
AIRCRAFT FOR TOPSIDE INCIDENCE DOUBLE EXPONENTIAL PLANE WAVE

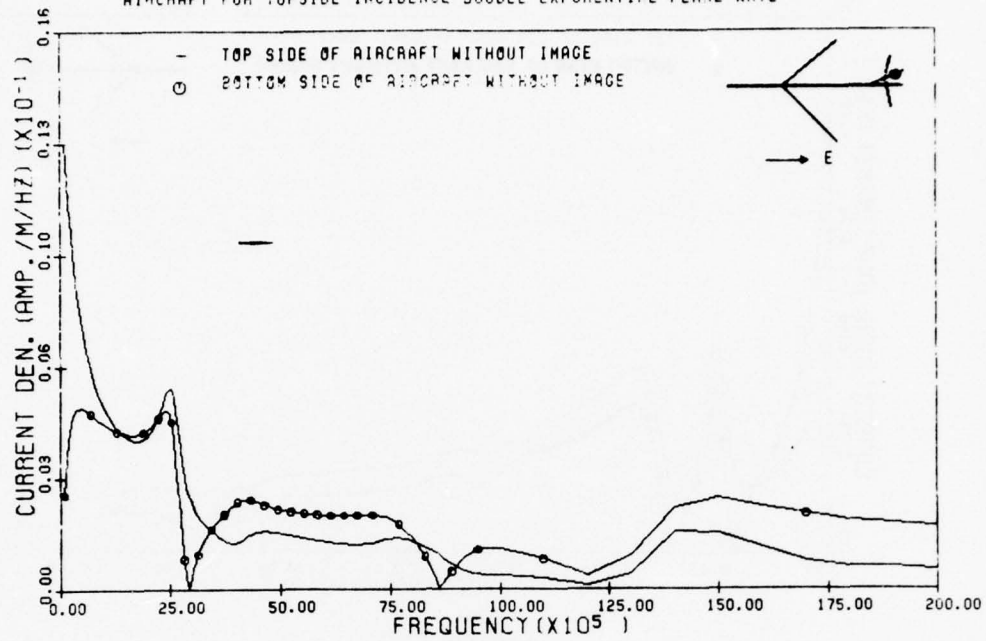


Figure 140:

CURRENT DENSITY (INCLUDING HINC FIELD) AT POSITION 1 ON THE EC-135  
AIRCRAFT FOR TOPSIDE INCIDENCE DOUBLE EXPONENTIAL PLANE WAVE

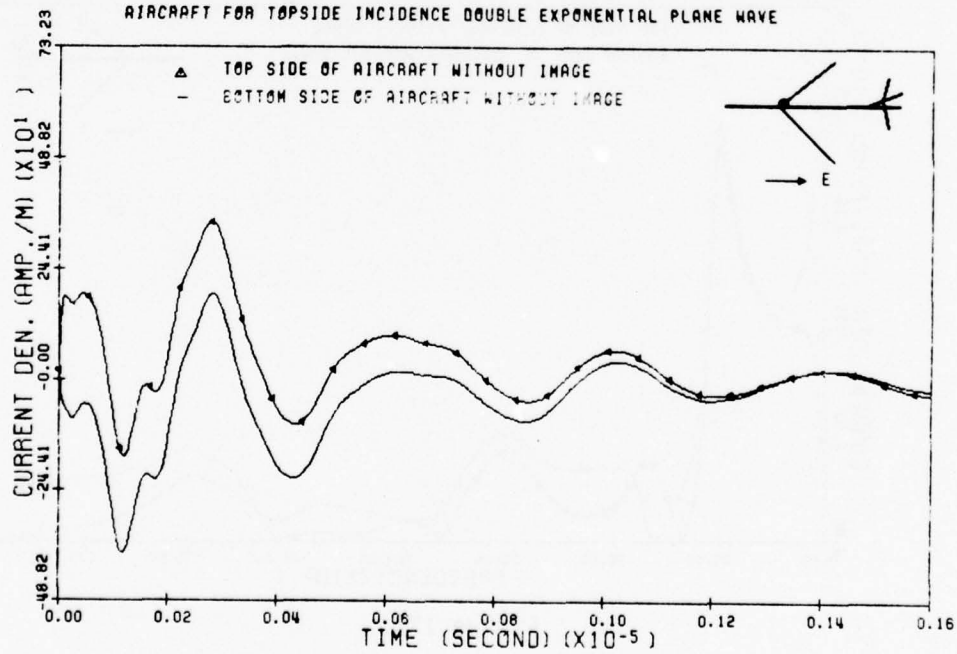


Figure 141:

CURRENT DENSITY (INCLUDING HINC FIELD) AT POSITION 69 ON THE EC-135  
AIRCRAFT FOR TOPSIDE INCIDENCE DOUBLE EXPONENTIAL PLANE WAVE

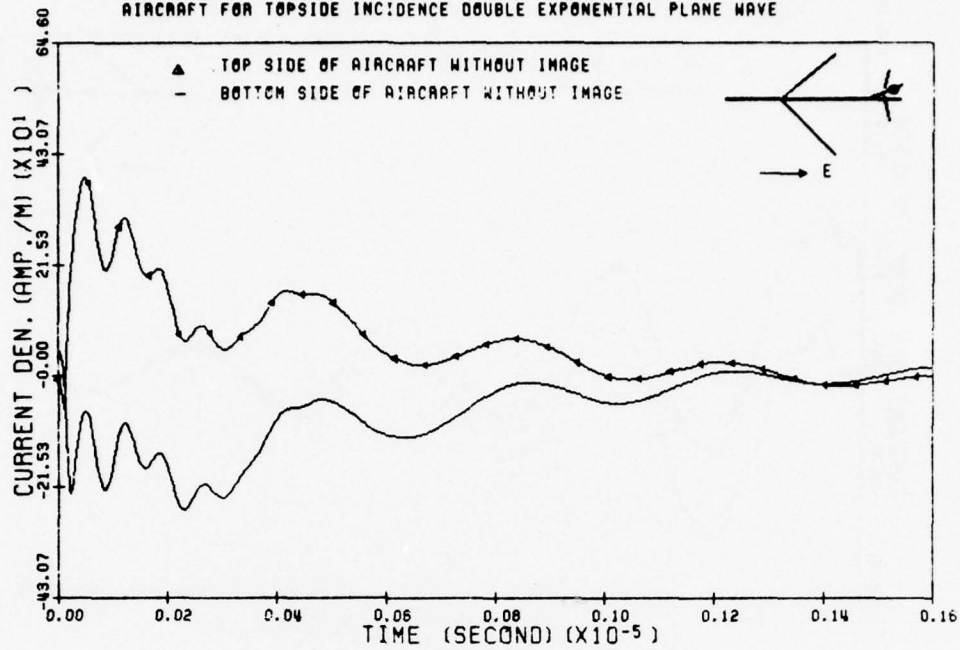


Figure 142:

CURRENT DENSITY (INCLUDING HINC FIELD) AT POSITION 65 ON THE EC-135  
AIRCRAFT FOR TOPSIDE INCIDENCE DOUBLE EXPONENTIAL PLANE WAVE

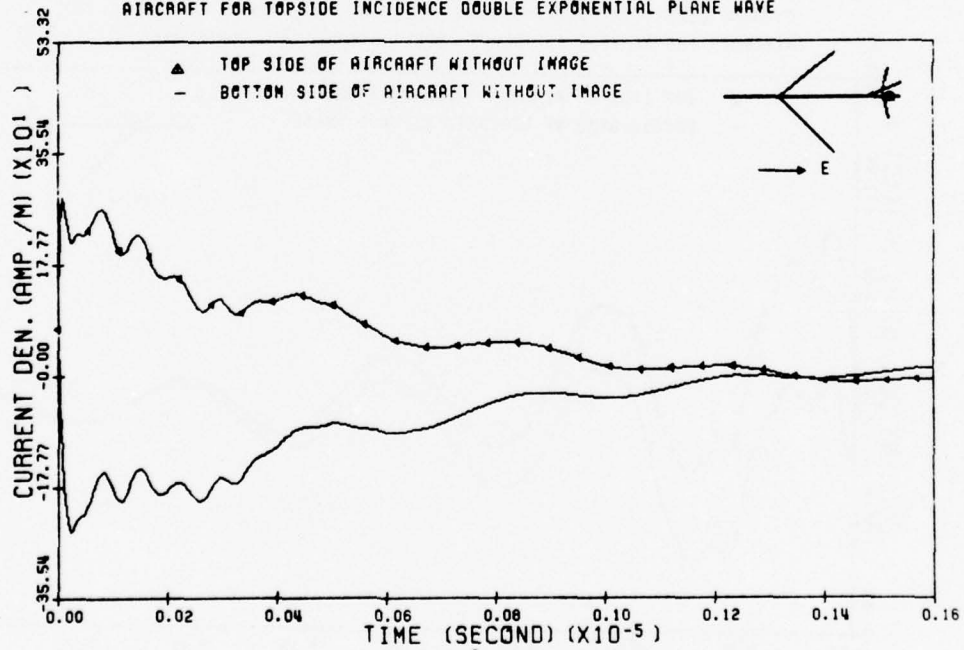


Figure 143:

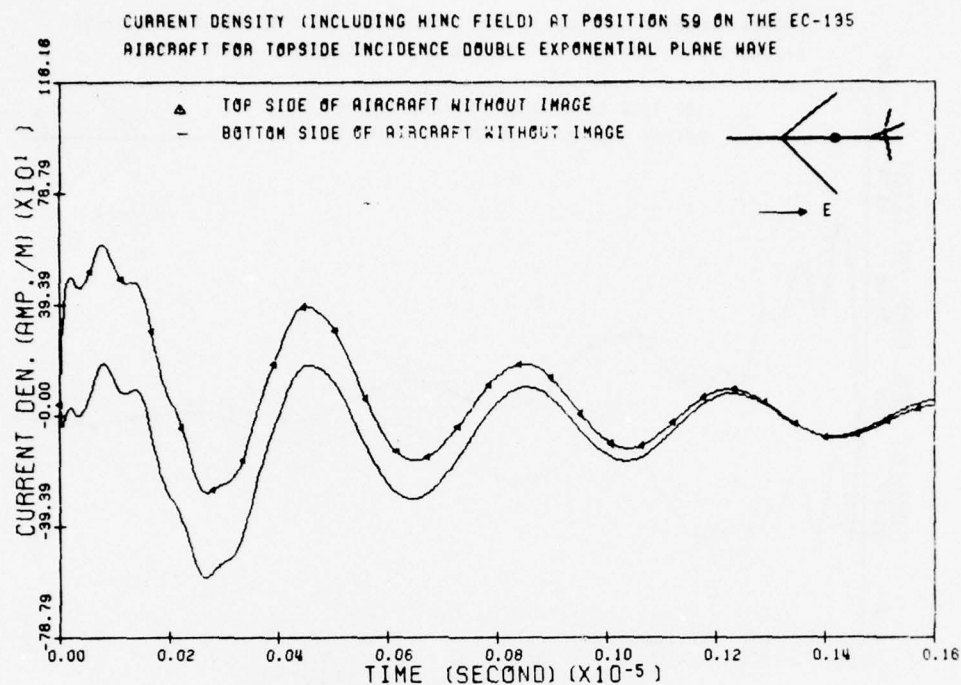


Figure 144:

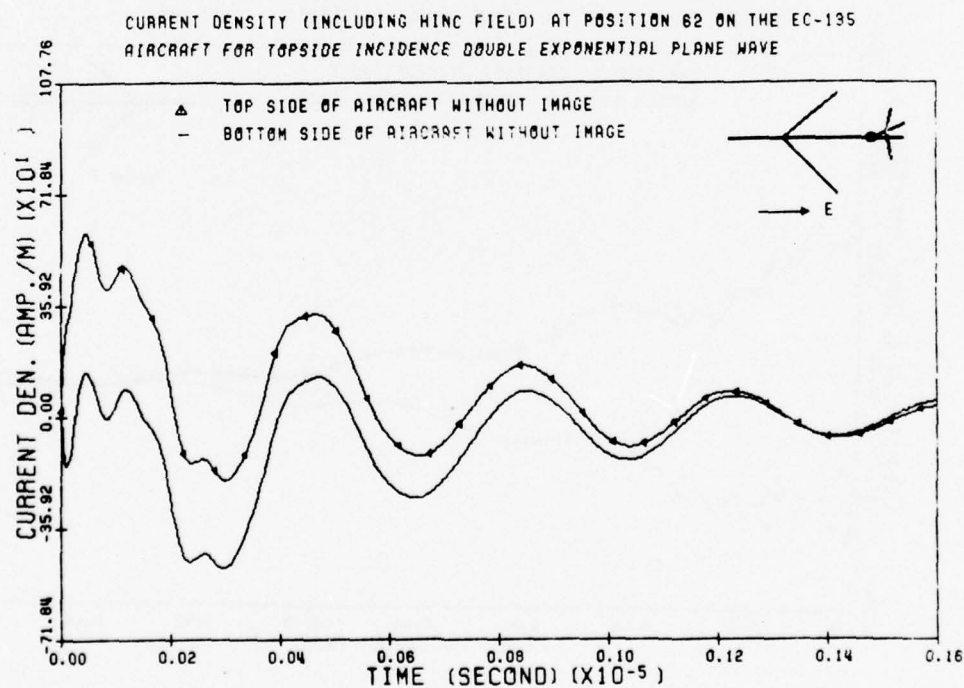


Figure 145:



CURRENT DENSITY (INCLUDING HINC FIELD) AT POSITION 44 ON THE EC-135  
AIRCRAFT FOR TOPSIDE INCIDENCE DOUBLE EXPONENTIAL PLANE WAVE

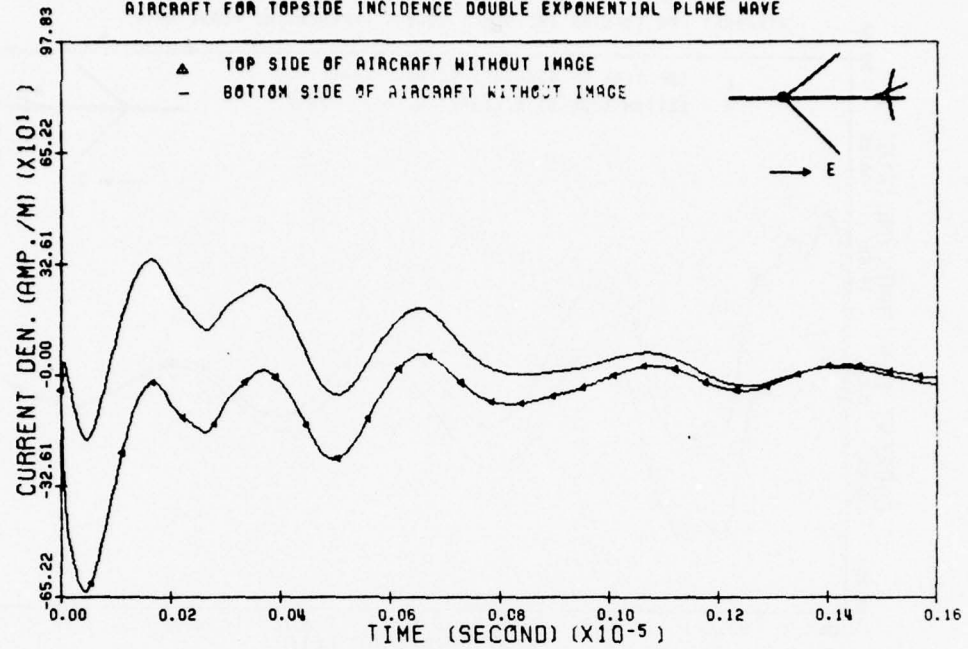


Figure 146:

CURRENT DENSITY (INCLUDING HINC FIELD) AT POSITION 49 ON THE EC-135  
AIRCRAFT FOR TOPSIDE INCIDENCE DOUBLE EXPONENTIAL PLANE WAVE

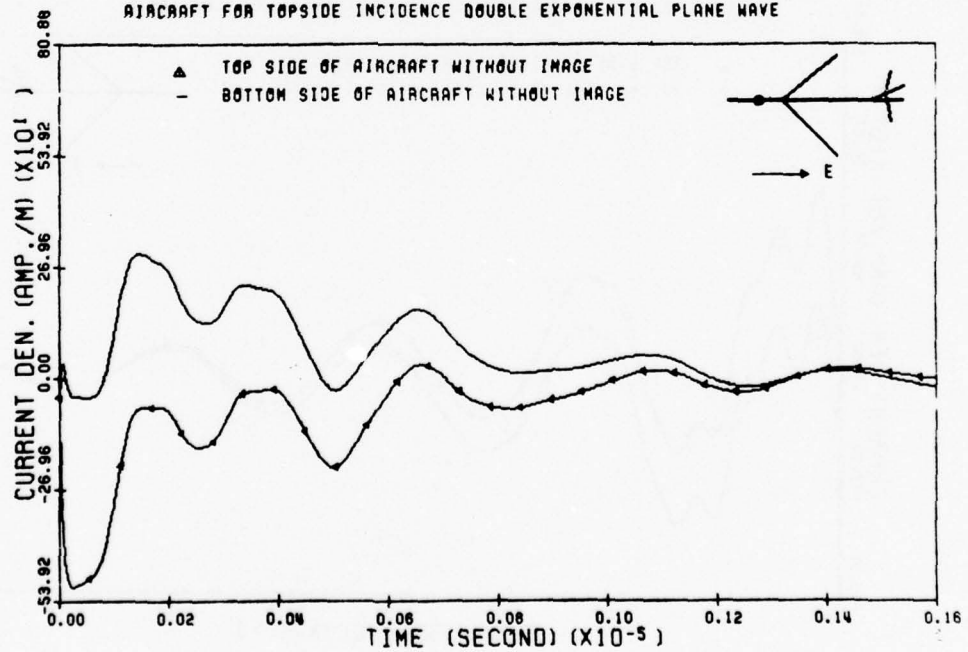


Figure 147:

CURRENT DENSITY (INCLUDING HINC FIELD) AT POSITION 90 ON THE EC-195  
AIRCRAFT FOR TOPSIDE INCIDENCE DOUBLE EXPONENTIAL PLANE WAVE

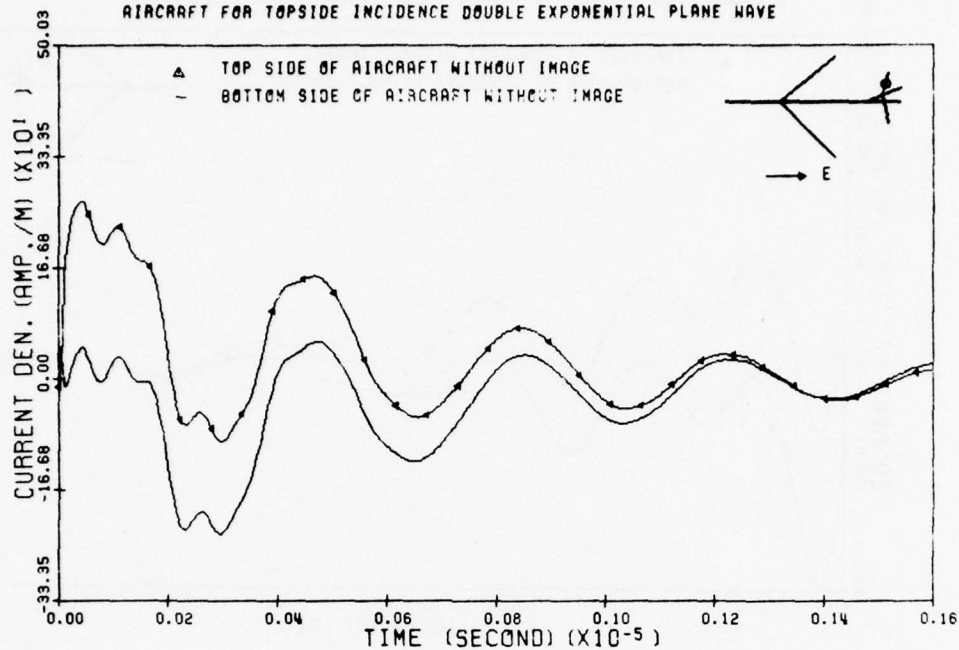


Figure 148:

CURRENT DENSITY (INCLUDING HINC FIELD) AT POSITION 42 ON THE EC-195  
AIRCRAFT FOR TOPSIDE INCIDENCE DOUBLE EXPONENTIAL PLANE WAVE

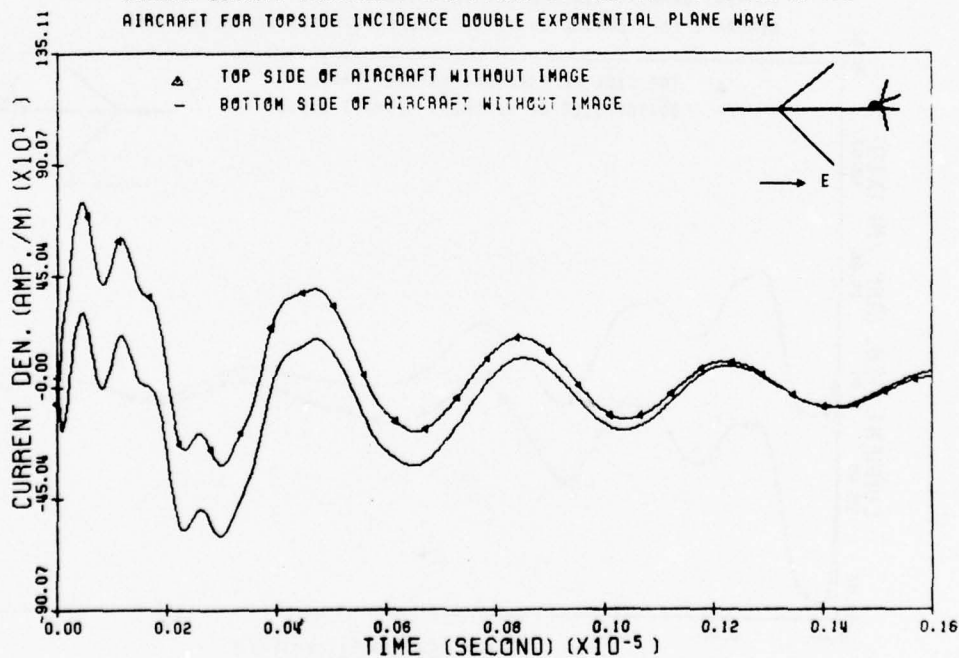


Figure 149:

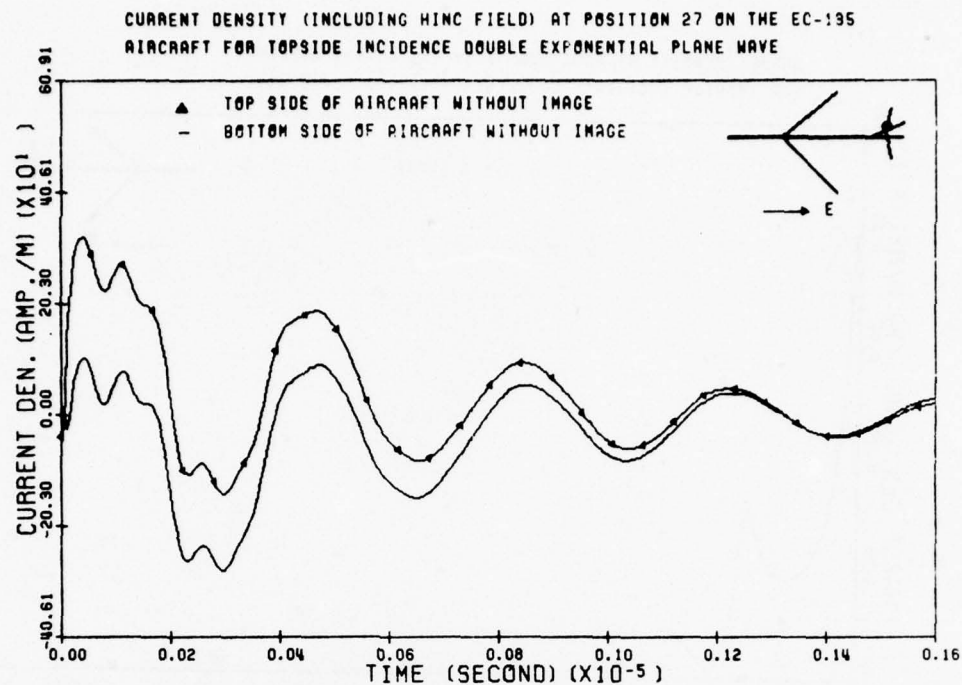


Figure 150:

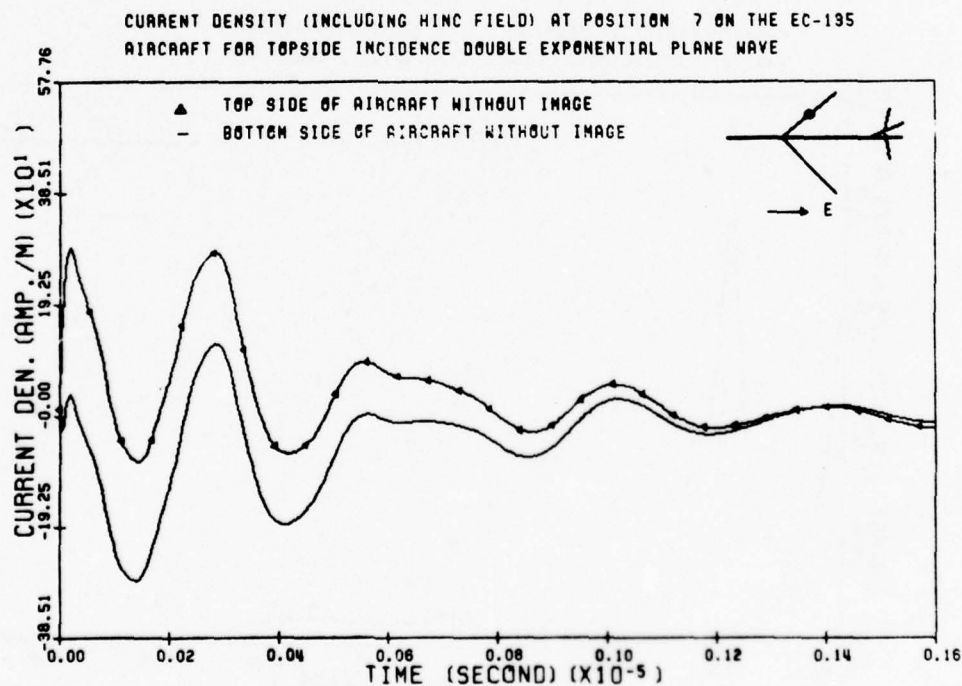


Figure 151:

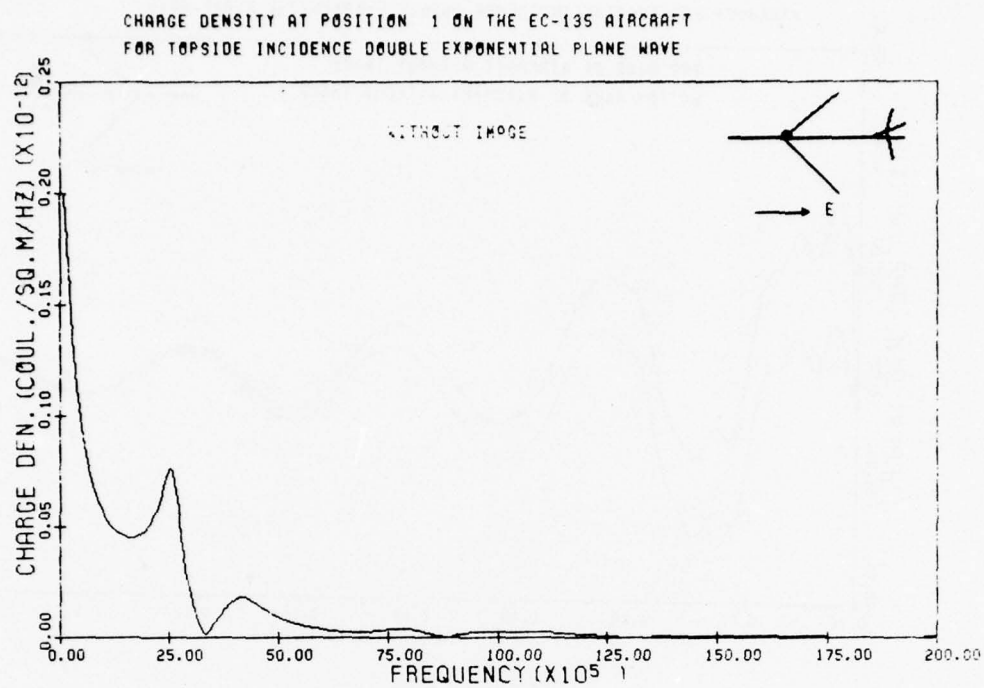


Figure 152:

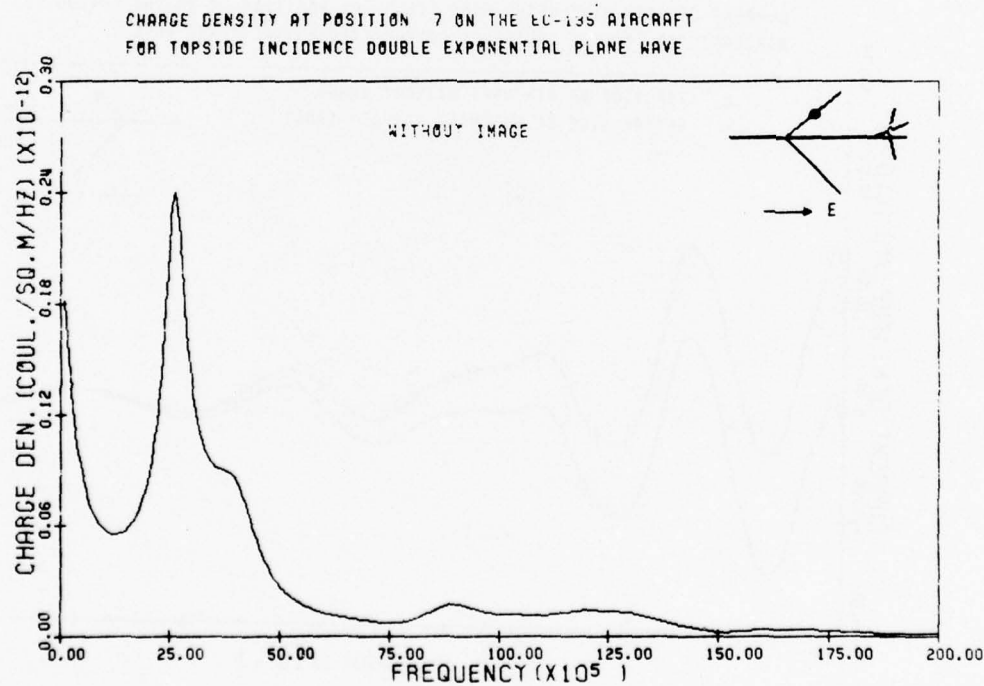


Figure 153:

CHARGE DENSITY AT POSITION 13 ON THE EC-135 AIRCRAFT  
FOR TOPSIDE INCIDENCE DOUBLE EXPONENTIAL PLANE WAVE

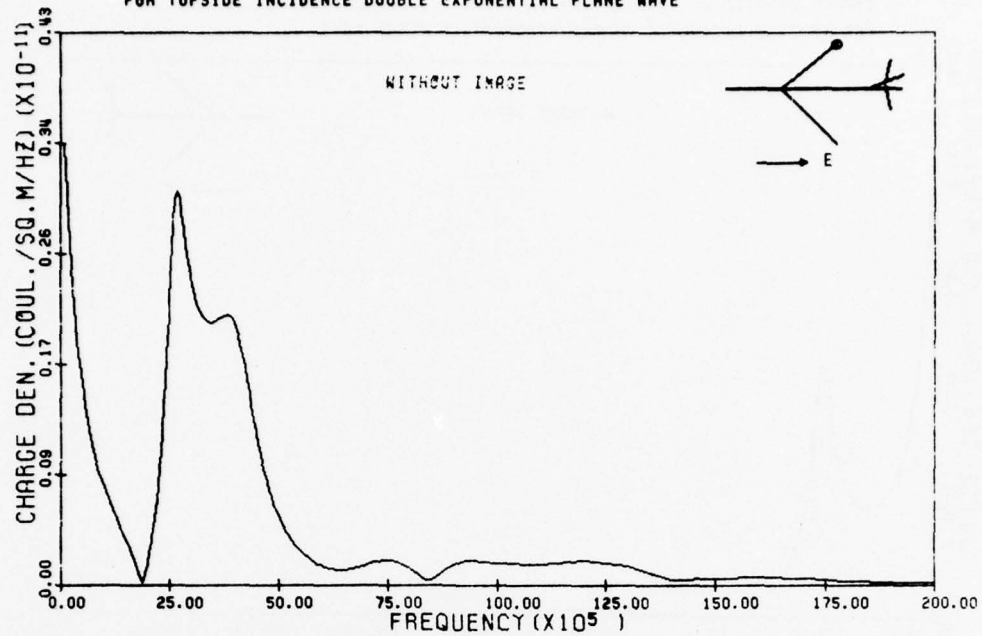


Figure 154:

CHARGE DENSITY AT POSITION 27 ON THE EC-135 AIRCRAFT  
FOR TOPSIDE INCIDENCE DOUBLE EXPONENTIAL PLANE WAVE

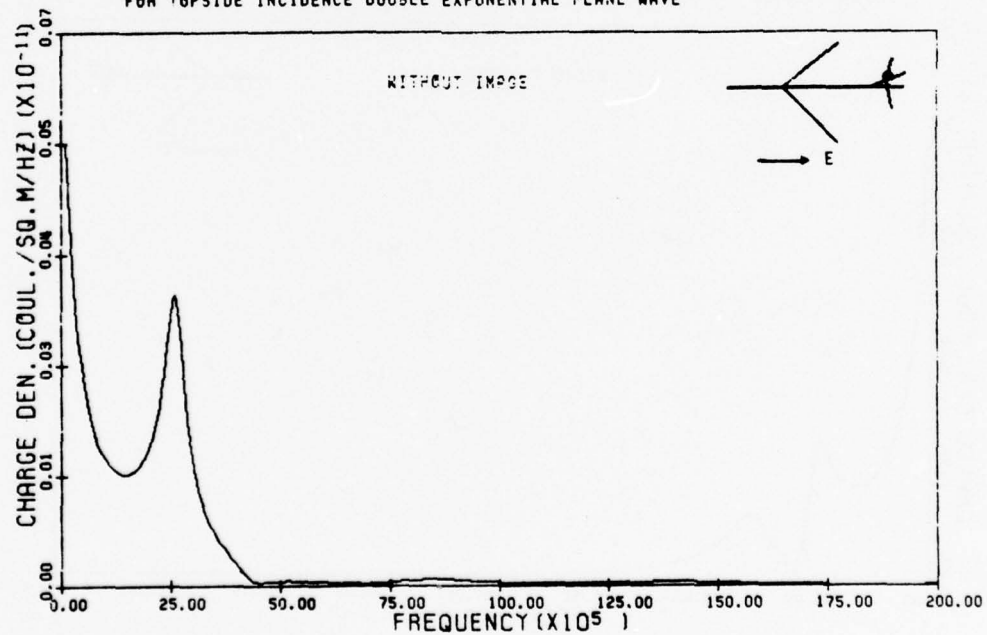


Figure 155:



CHARGE DENSITY AT POSITION 93 ON THE EC-135 AIRCRAFT  
FOR TOPSIDE INCIDENCE DOUBLE EXPONENTIAL PLANE WAVE

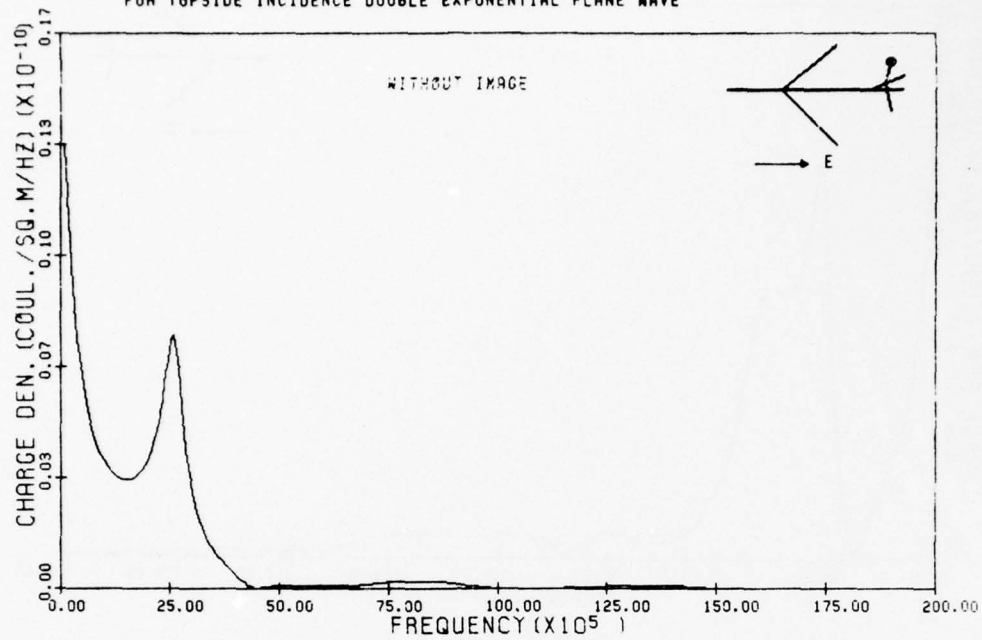


Figure 156:

CHARGE DENSITY AT POSITION 49 ON THE EC-135 AIRCRAFT  
FOR TOPSIDE INCIDENCE DOUBLE EXPONENTIAL PLANE WAVE

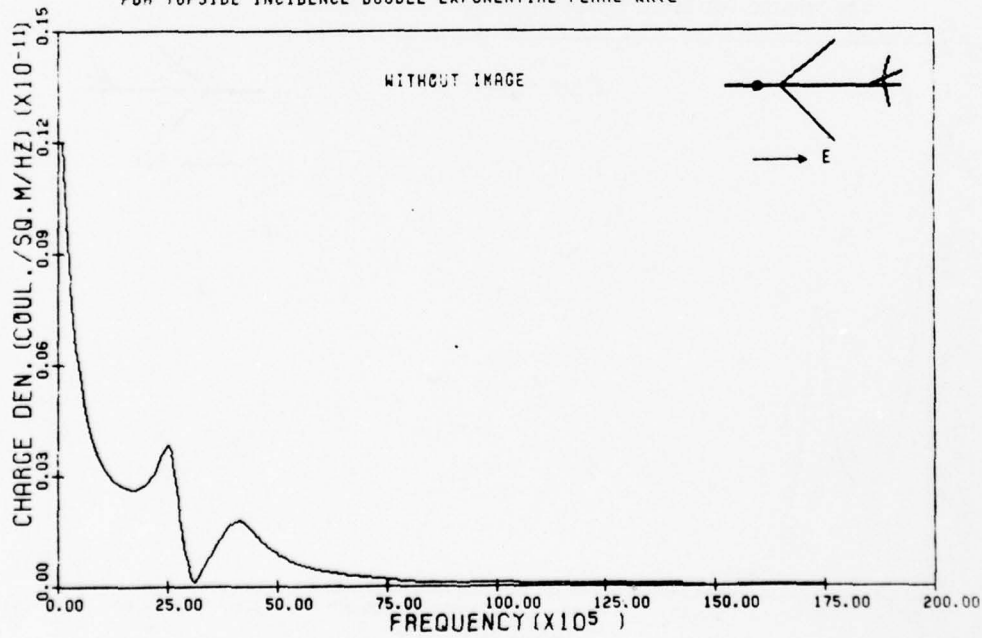


Figure 157:

CHARGE DENSITY AT POSITION 54 ON THE EC-195 AIRCRAFT  
FOR TOPSIDE INCIDENCE DOUBLE EXPONENTIAL PLANE WAVE

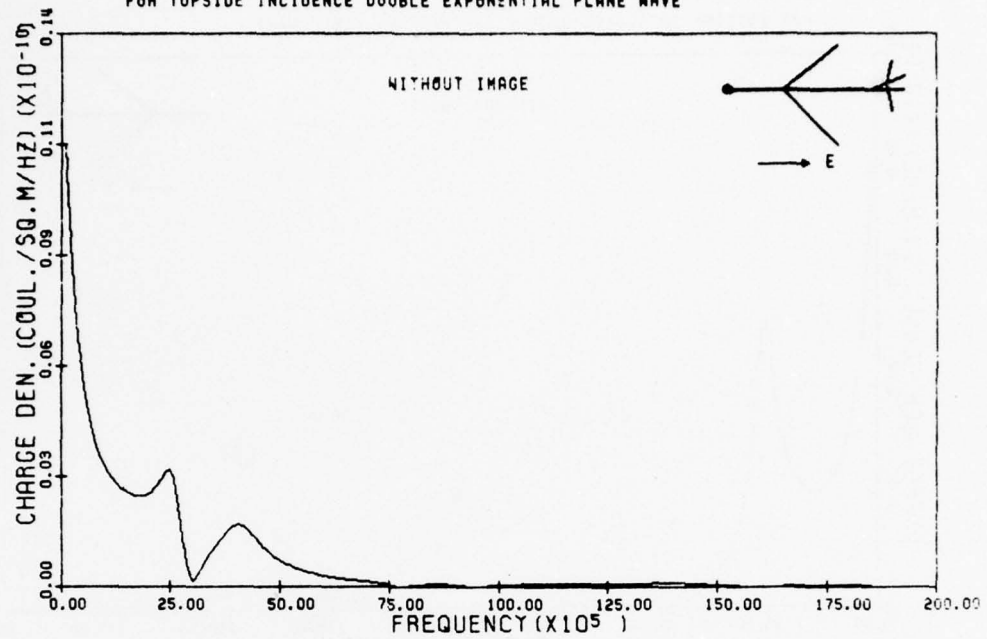


Figure 158:

CHARGE DENSITY AT POSITION 59 ON THE EC-195 AIRCRAFT  
FOR TOPSIDE INCIDENCE DOUBLE EXPONENTIAL PLANE WAVE

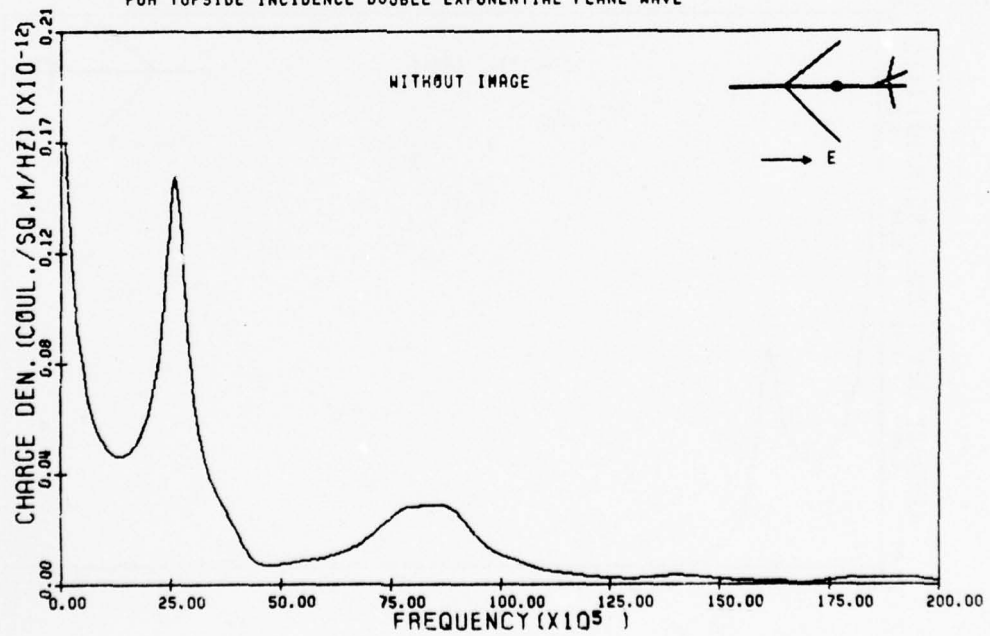


Figure 159:

CHARGE DENSITY AT POSITION 62 ON THE EC-135 AIRCRAFT  
FOR TOPSIDE INCIDENCE DOUBLE EXPONENTIAL PLANE WAVE

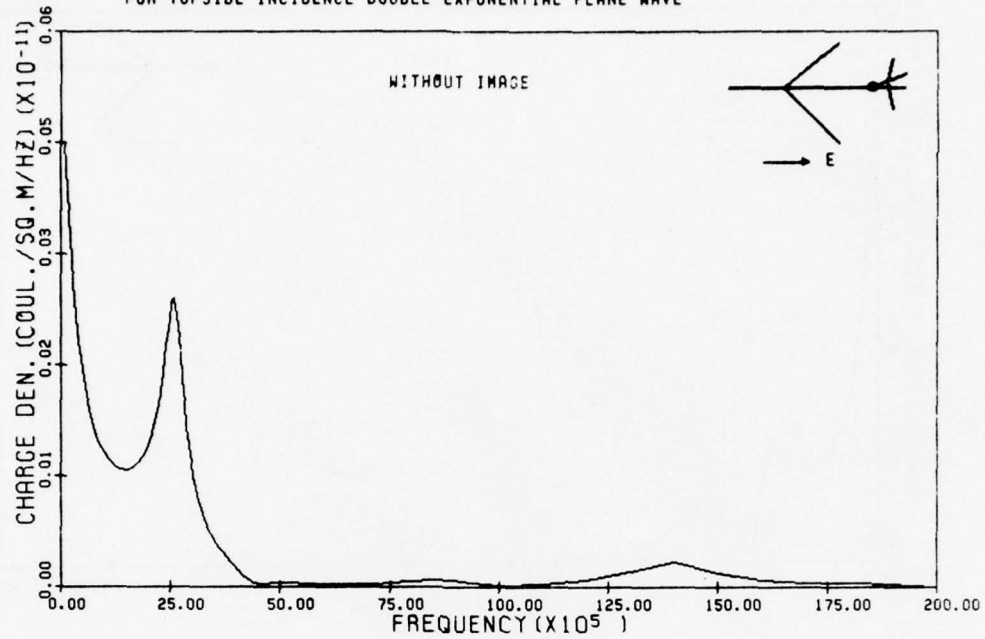


Figure 160:

CHARGE DENSITY AT POSITION 67 ON THE EC-135 AIRCRAFT  
FOR TOPSIDE INCIDENCE DOUBLE EXPONENTIAL PLANE WAVE

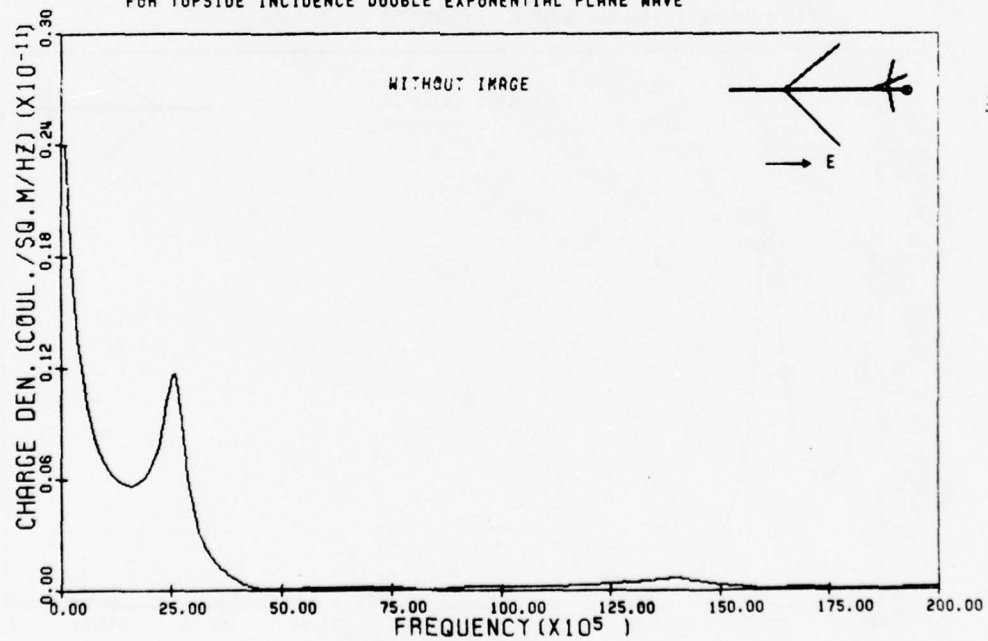


Figure 161:

CHARGE DENSITY AT POSITION 69 ON THE EC-135 AIRCRAFT  
FOR TOPSIDE INCIDENCE DOUBLE EXPONENTIAL PLANE WAVE

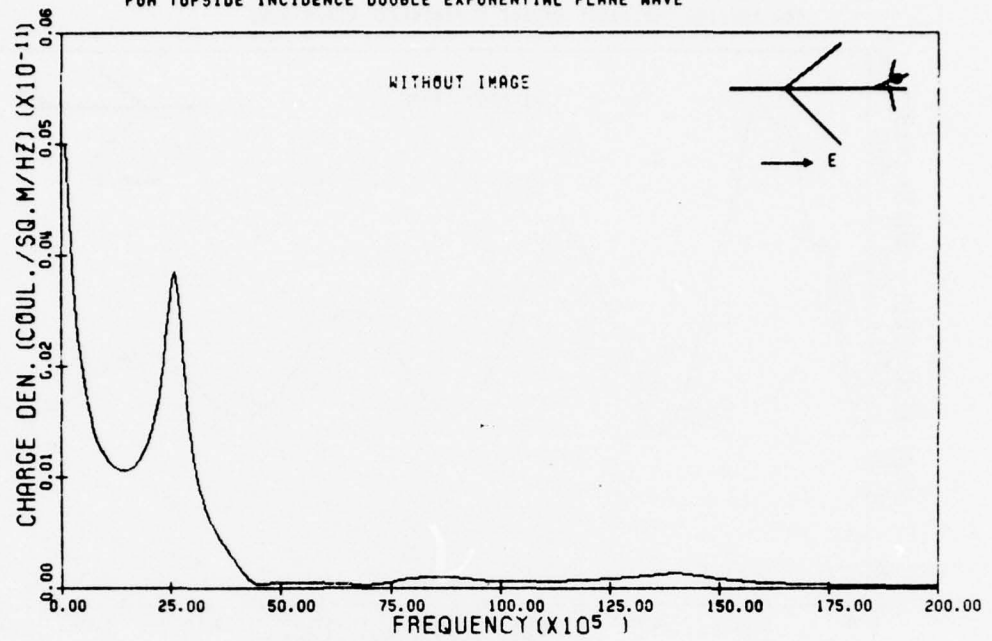


Figure 162:

CHARGE DENSITY AT POSITION 71 ON THE EC-135 AIRCRAFT  
FOR TOPSIDE INCIDENCE DOUBLE EXPONENTIAL PLANE WAVE

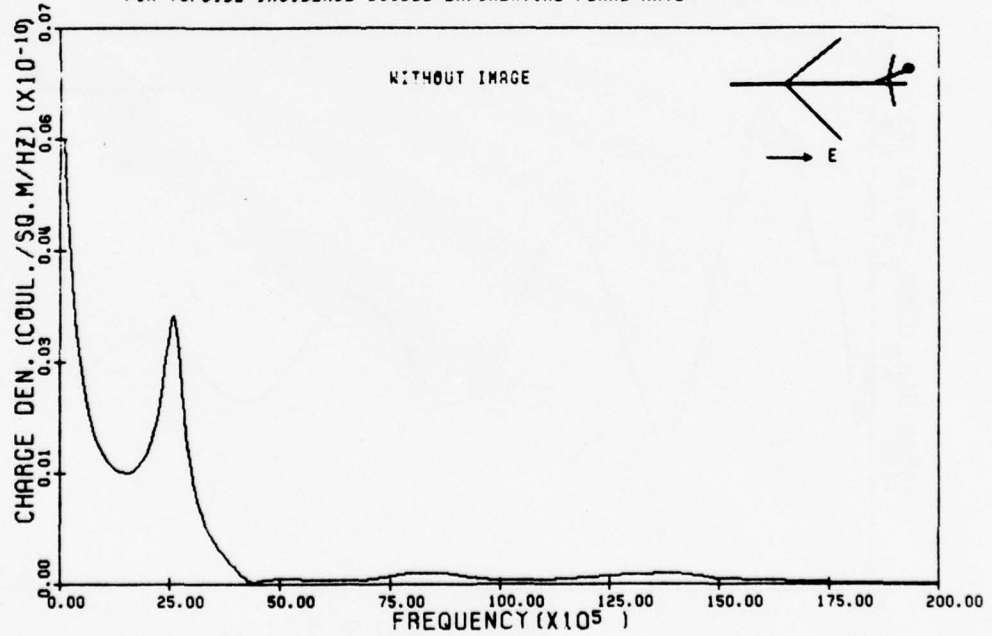


Figure 163:

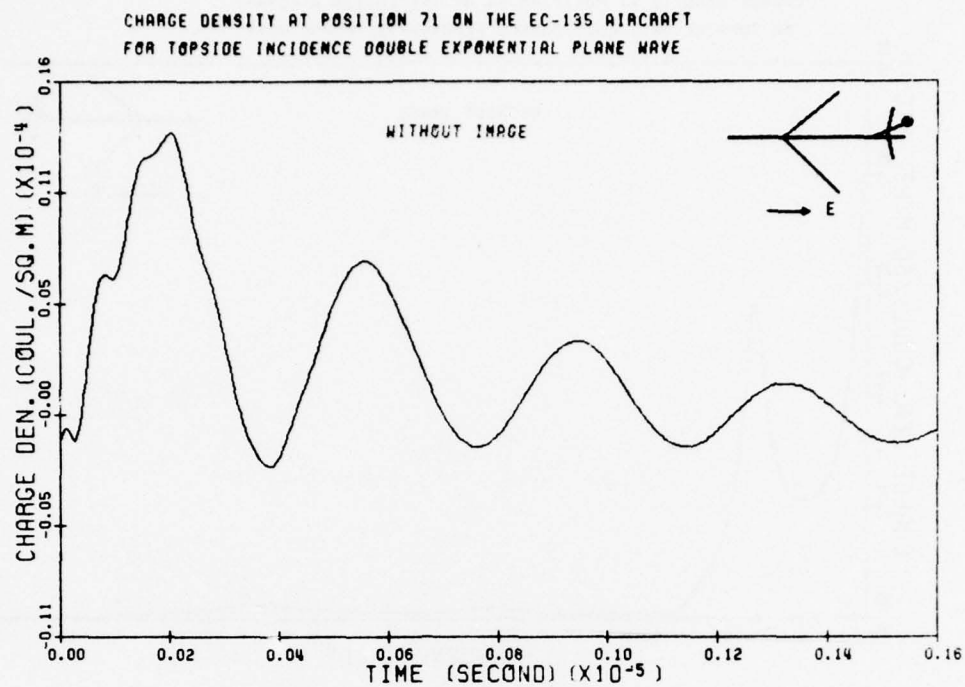


Figure 164:

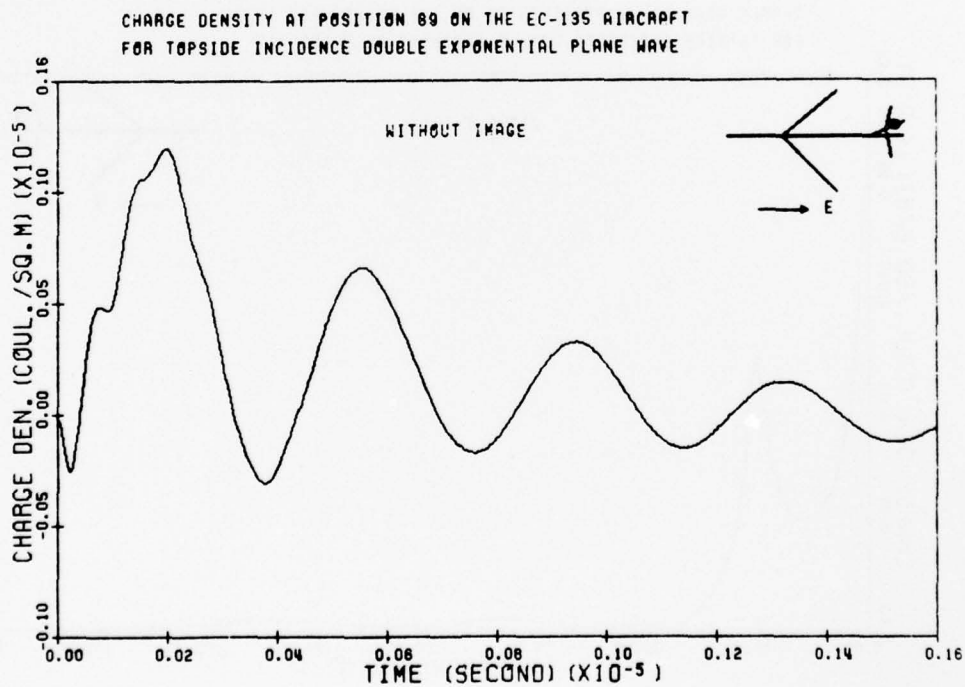


Figure 165:



CHARGE DENSITY AT POSITION 62 ON THE EC-135 AIRCRAFT  
FOR TOPSIDE INCIDENCE DOUBLE EXPONENTIAL PLANE WAVE

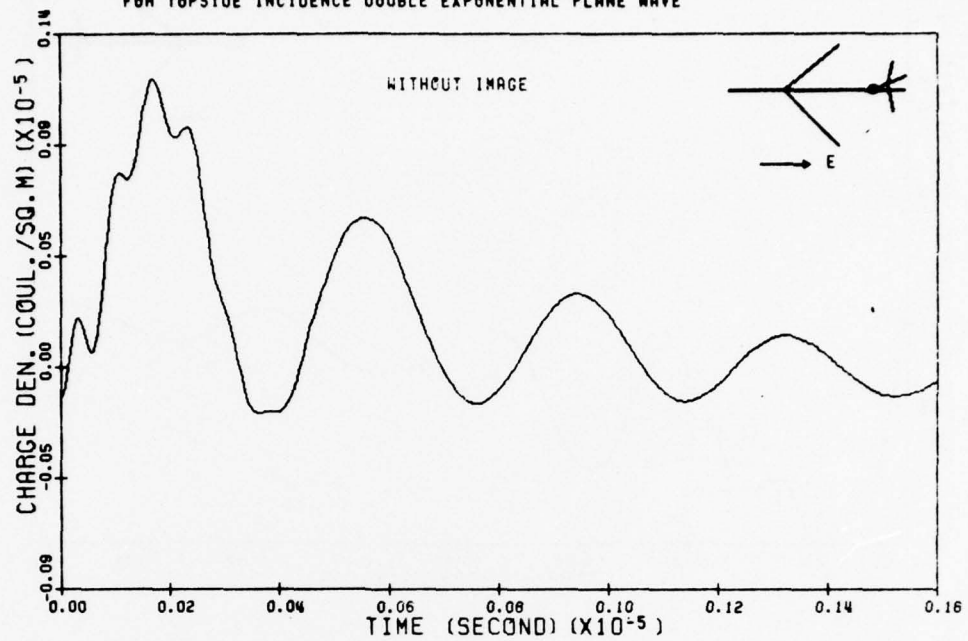


Figure 166:

CHARGE DENSITY AT POSITION 67 ON THE EC-135 AIRCRAFT  
FOR TOPSIDE INCIDENCE DOUBLE EXPONENTIAL PLANE WAVE

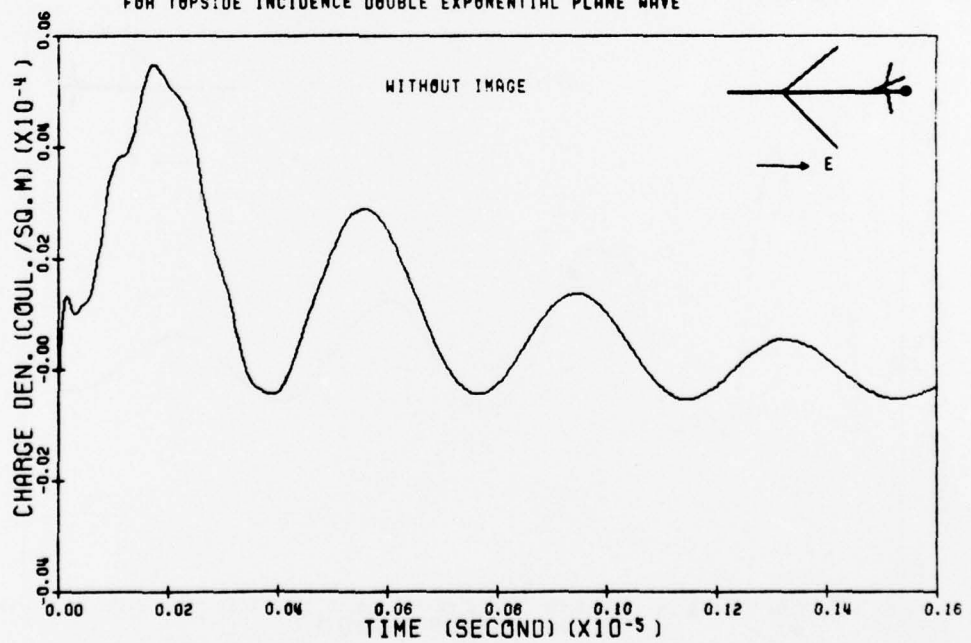


Figure 167:

CHARGE DENSITY AT POSITION 54 ON THE EC-135 AIRCRAFT  
FOR TOPSIDE INCIDENCE DOUBLE EXPONENTIAL PLANE WAVE

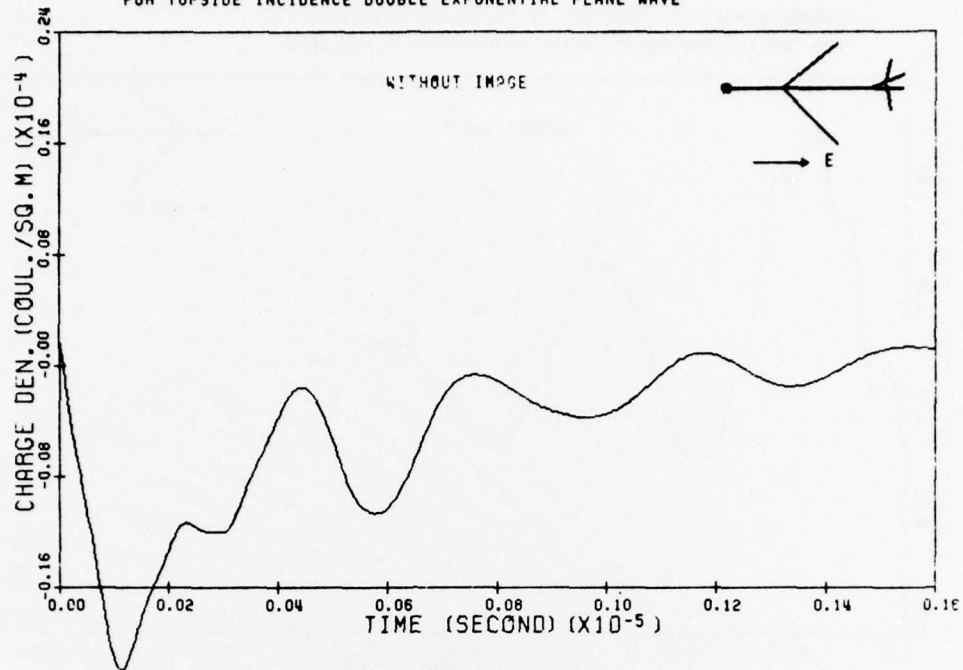


Figure 168:

CHARGE DENSITY AT POSITION 59 ON THE EC-135 AIRCRAFT  
FOR TOPSIDE INCIDENCE DOUBLE EXPONENTIAL PLANE WAVE

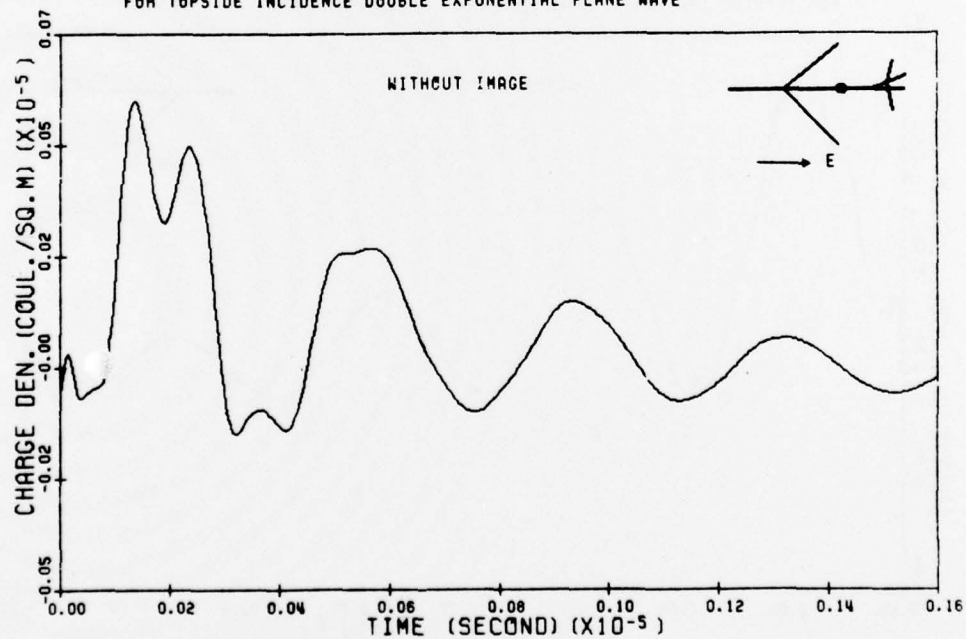


Figure 169:

CHARGE DENSITY AT POSITION 39 ON THE EC-195 AIRCRAFT  
FOR TOPSIDE INCIDENCE DOUBLE EXPONENTIAL PLANE WAVE

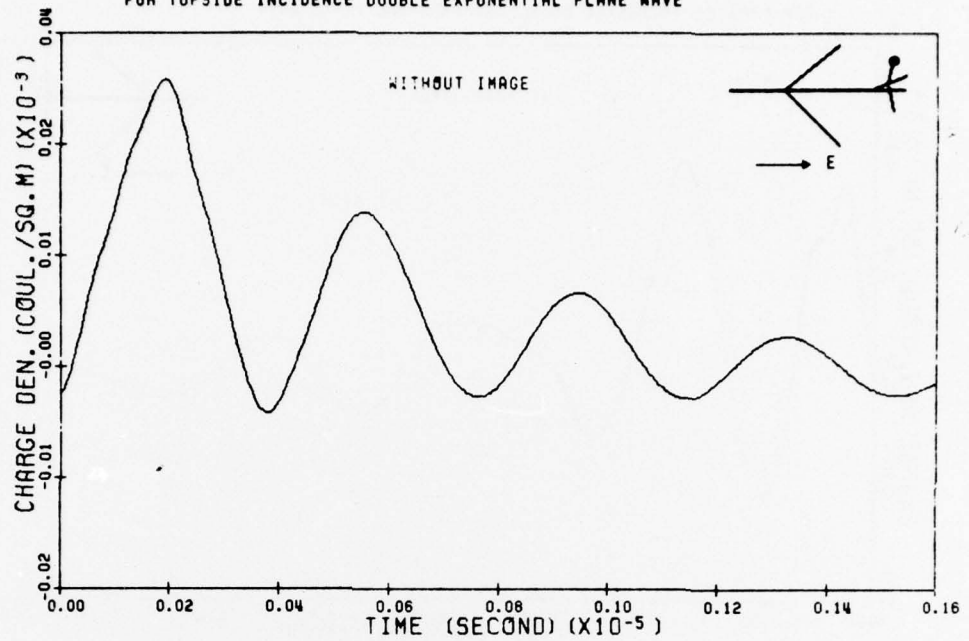


Figure 170:

CHARGE DENSITY AT POSITION 49 ON THE EC-195 AIRCRAFT  
FOR TOPSIDE INCIDENCE DOUBLE EXPONENTIAL PLANE WAVE

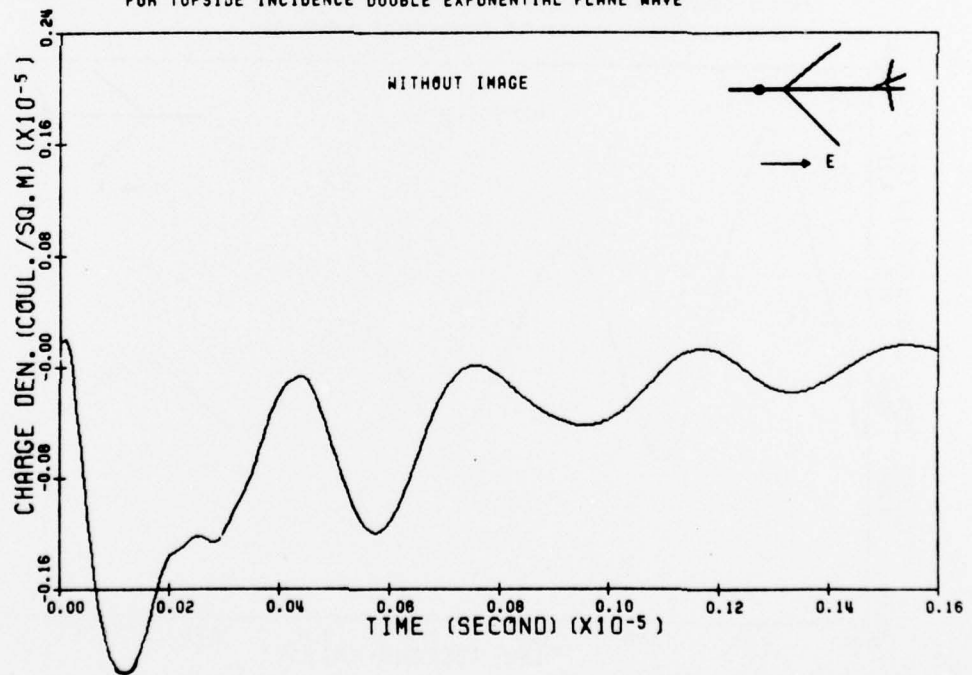


Figure 171:

CHARGE DENSITY AT POSITION 13 ON THE EC-135 AIRCRAFT  
FOR TOPSIDE INCIDENCE DOUBLE EXPONENTIAL PLANE WAVE

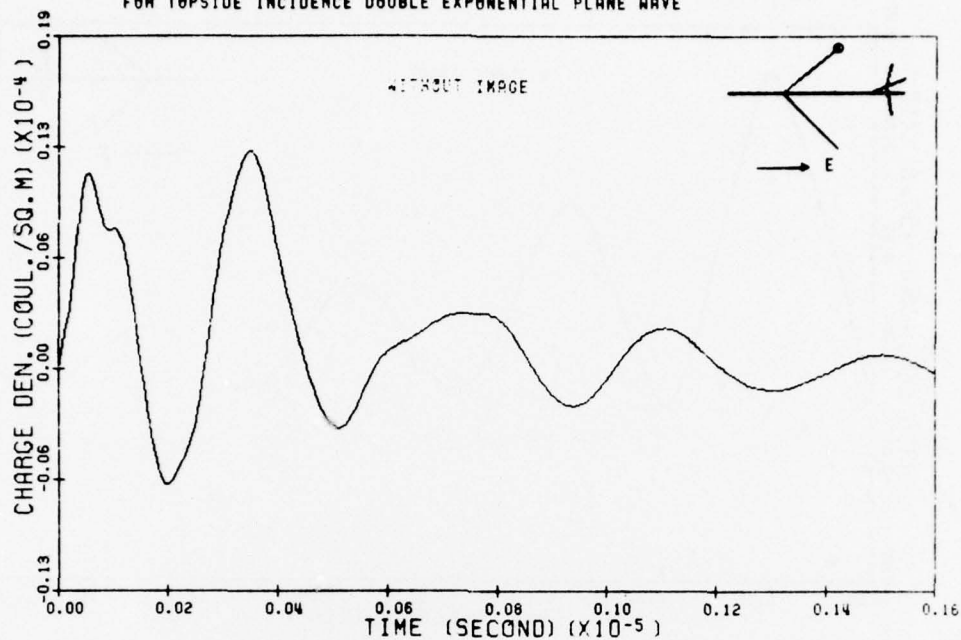


Figure 172:

CHARGE DENSITY AT POSITION 27 ON THE EC-135 AIRCRAFT  
FOR TOPSIDE INCIDENCE DOUBLE EXPONENTIAL PLANE WAVE

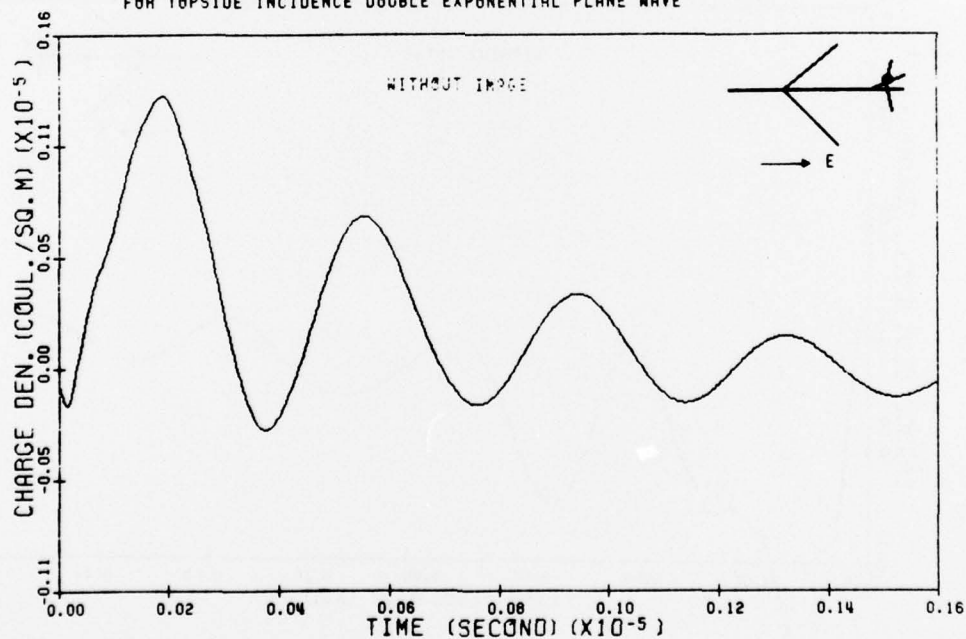


Figure 173:

CHARGE DENSITY AT POSITION 1 ON THE EC-195 AIRCRAFT  
FOR TOPSIDE INCIDENCE DOUBLE EXPONENTIAL PLANE WAVE

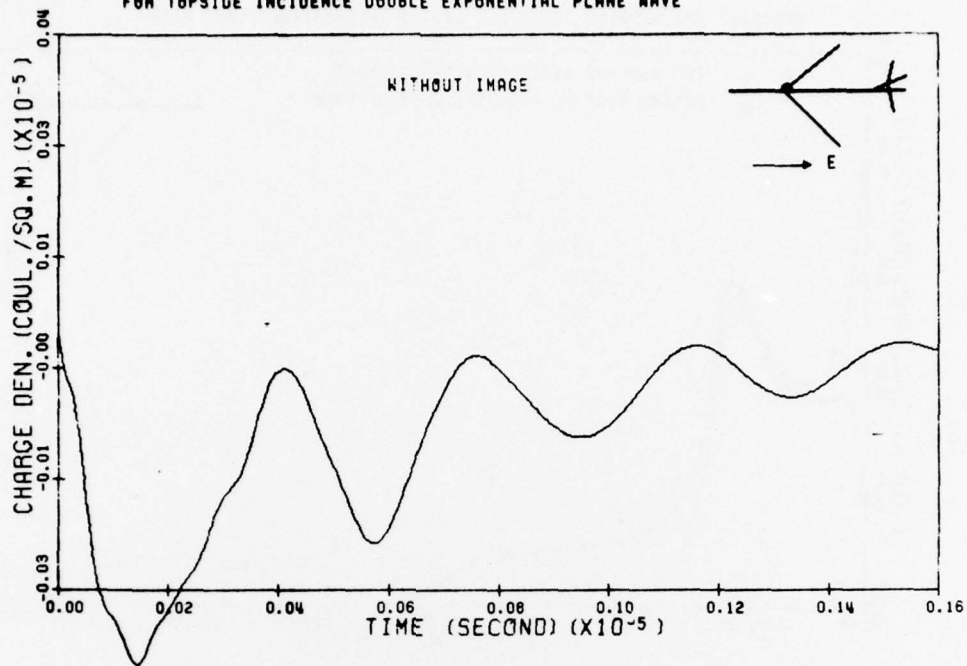


Figure 174:

CHARGE DENSITY AT POSITION 7 ON THE EC-195 AIRCRAFT  
FOR TOPSIDE INCIDENCE DOUBLE EXPONENTIAL PLANE WAVE

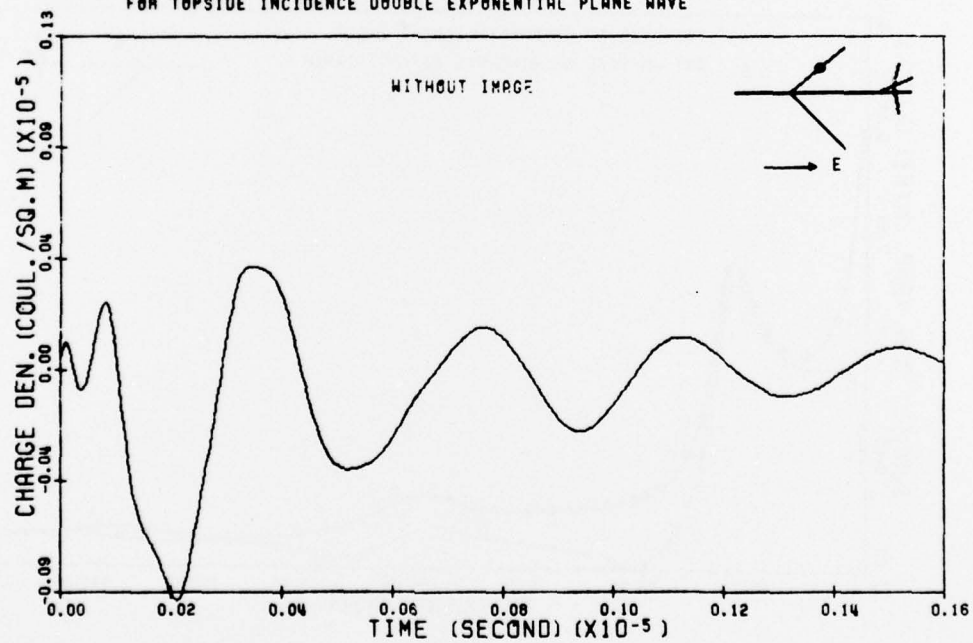


Figure 175:



CURRENT DENSITY (INCLUDING HINC FIELD) AT POSITION 1 ON THE EC-135  
AIRCRAFT FOR TOPSIDE INCIDENCE DOUBLE EXPONENTIAL PLANE WAVE

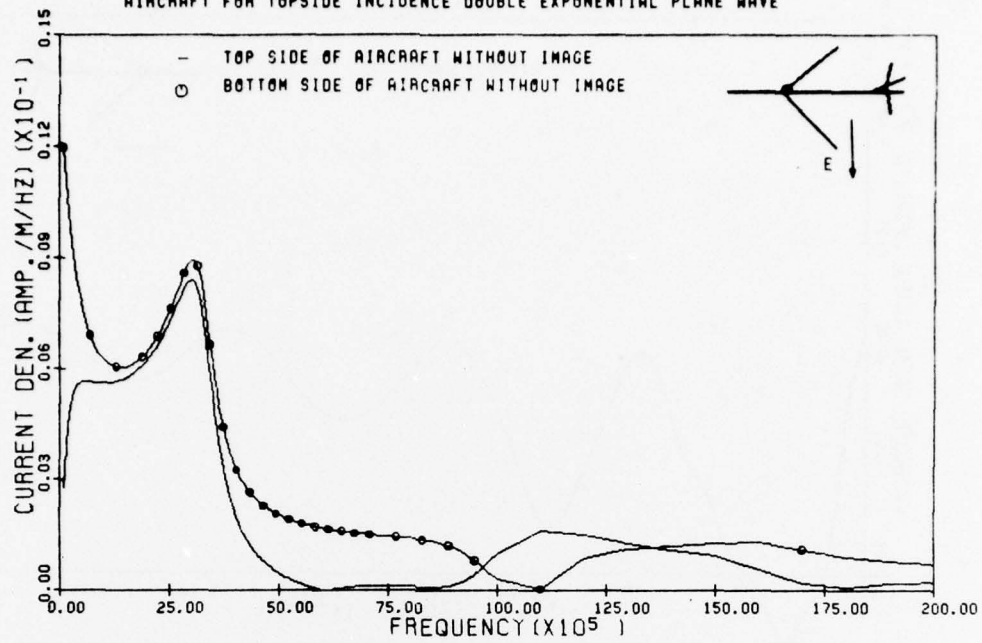


Figure 176:

CURRENT DENSITY (INCLUDING HINC FIELD) AT POSITION 7 ON THE EC-135  
AIRCRAFT FOR TOPSIDE INCIDENCE DOUBLE EXPONENTIAL PLANE WAVE

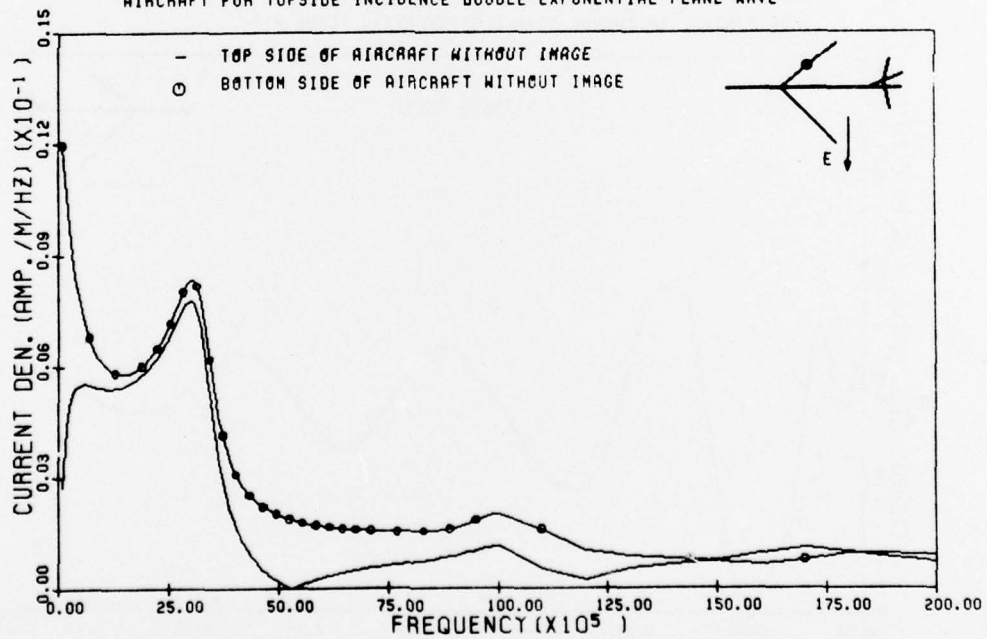


Figure 177:

CURRENT DENSITY (INCLUDING HINC FIELD) AT POSITION 27 ON THE EC-135  
AIRCRAFT FOR TOPSIDE INCIDENCE DOUBLE EXPONENTIAL PLANE WAVE

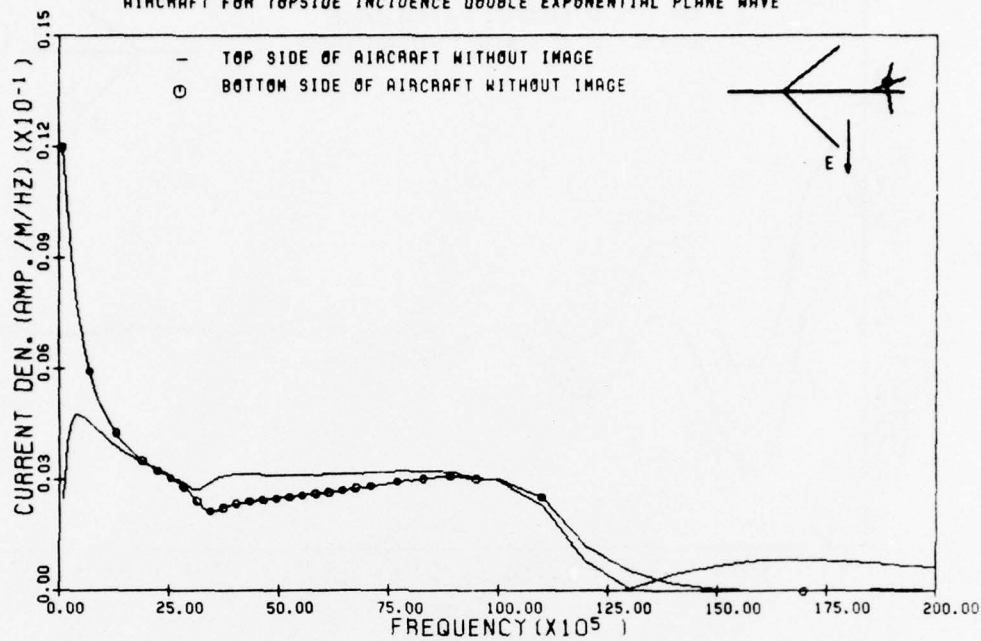


Figure 178:

CURRENT DENSITY (INCLUDING HINC FIELD) AT POSITION 30 ON THE EC-135  
AIRCRAFT FOR TOPSIDE INCIDENCE DOUBLE EXPONENTIAL PLANE WAVE

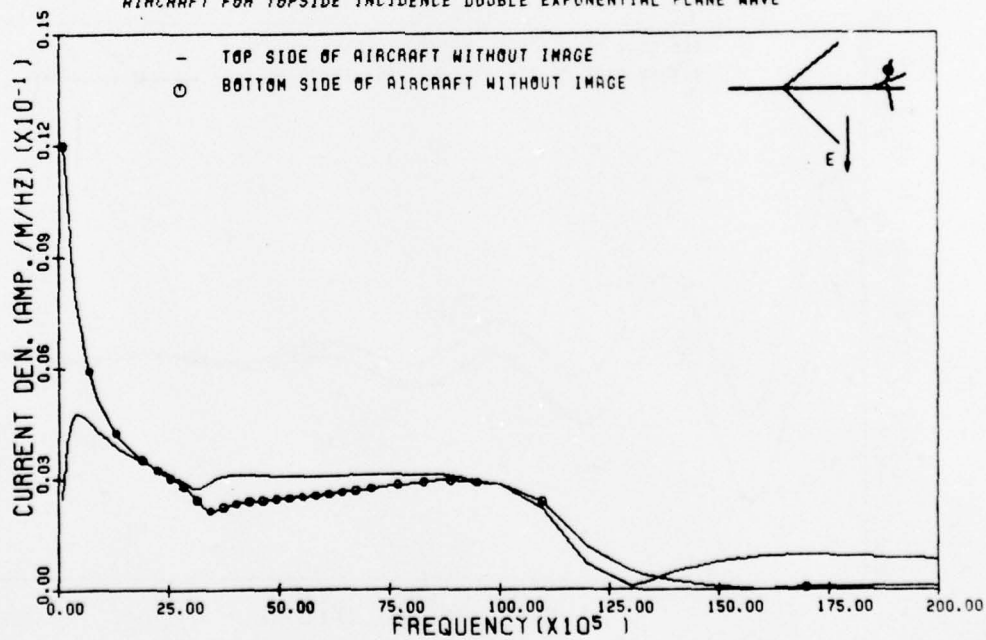


Figure 179:

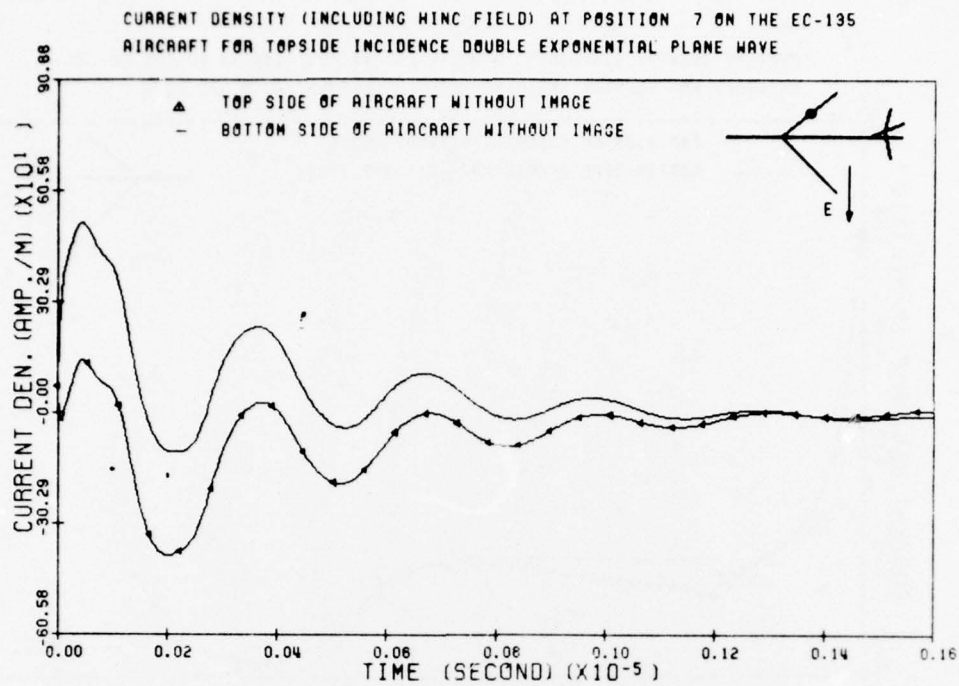


Figure 180:

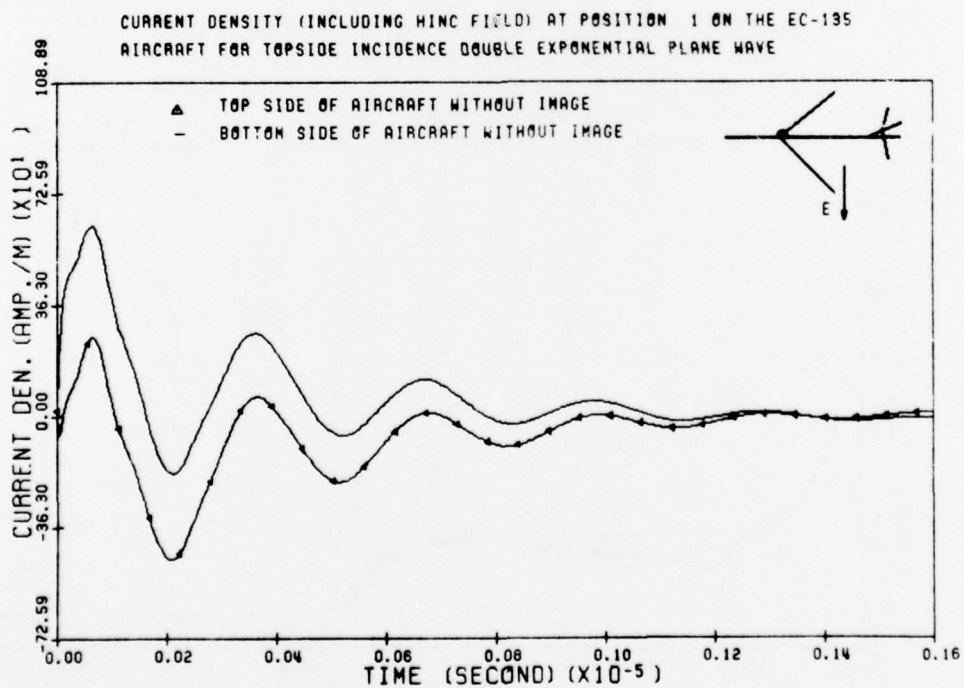


Figure 181:

CURRENT DENSITY (INCLUDING HINC FIELD) AT POSITION 30 ON THE EC-135  
AIRCRAFT FOR TOPSIDE INCIDENCE DOUBLE EXPONENTIAL PLANE WAVE

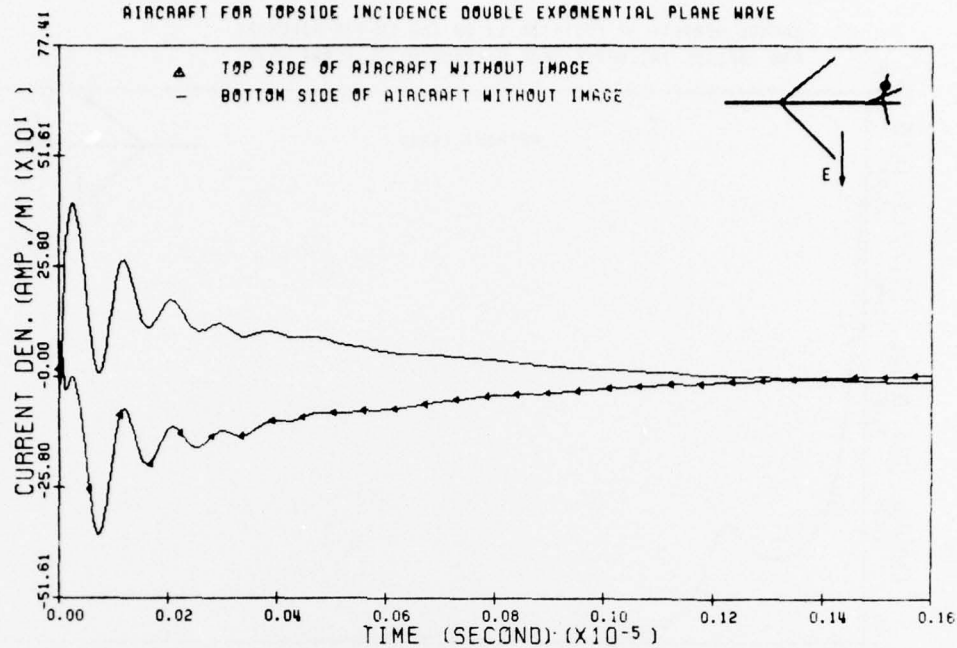


Figure 182:

CURRENT DENSITY (INCLUDING HINC FIELD) AT POSITION 27 ON THE EC-135  
AIRCRAFT FOR TOPSIDE INCIDENCE DOUBLE EXPONENTIAL PLANE WAVE

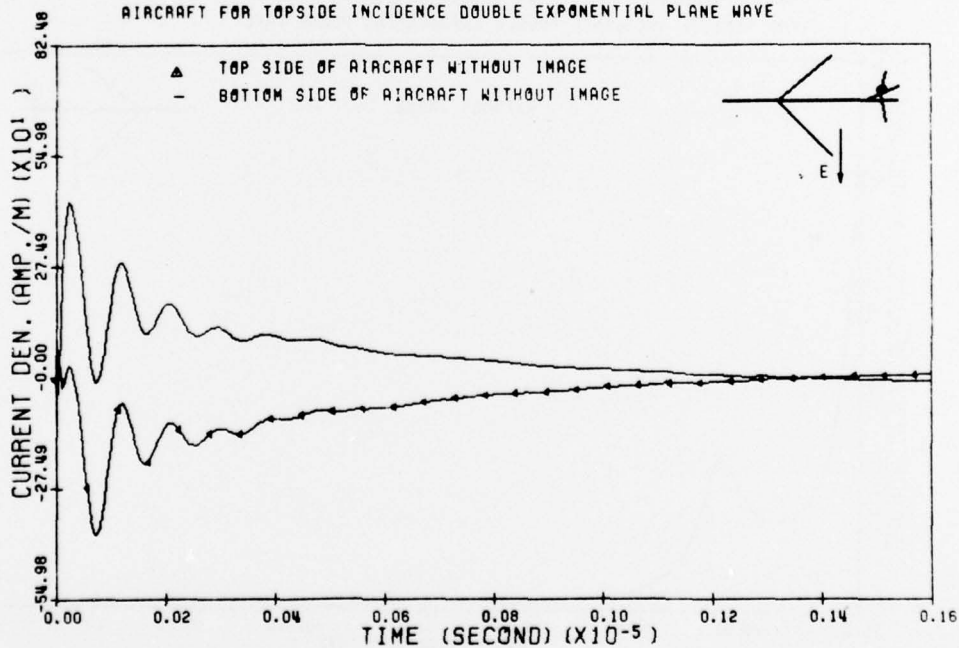


Figure 183:

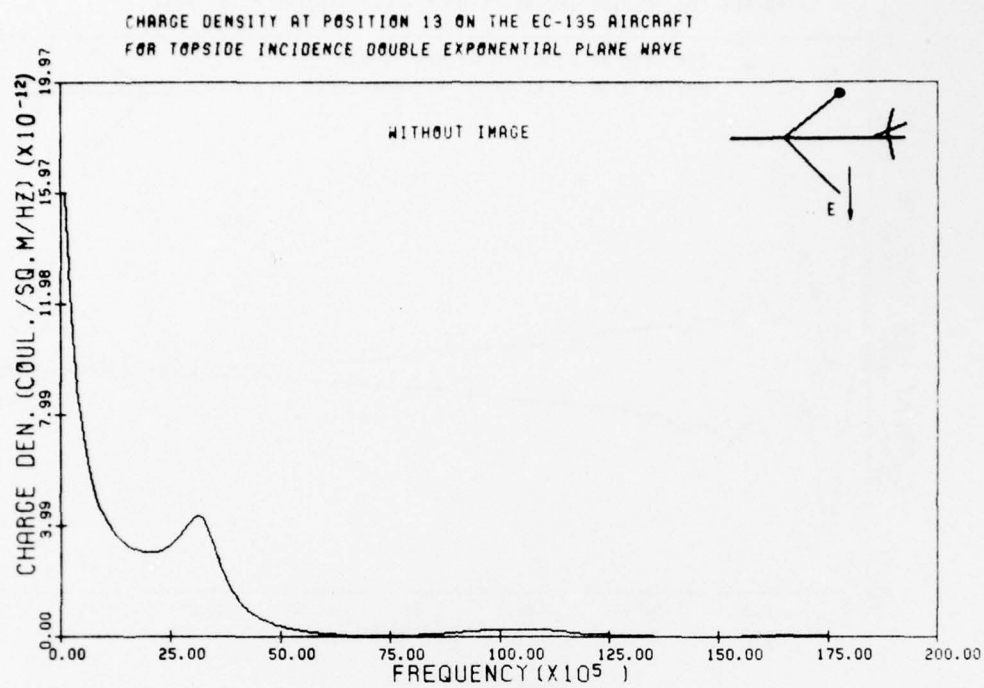


Figure 184:

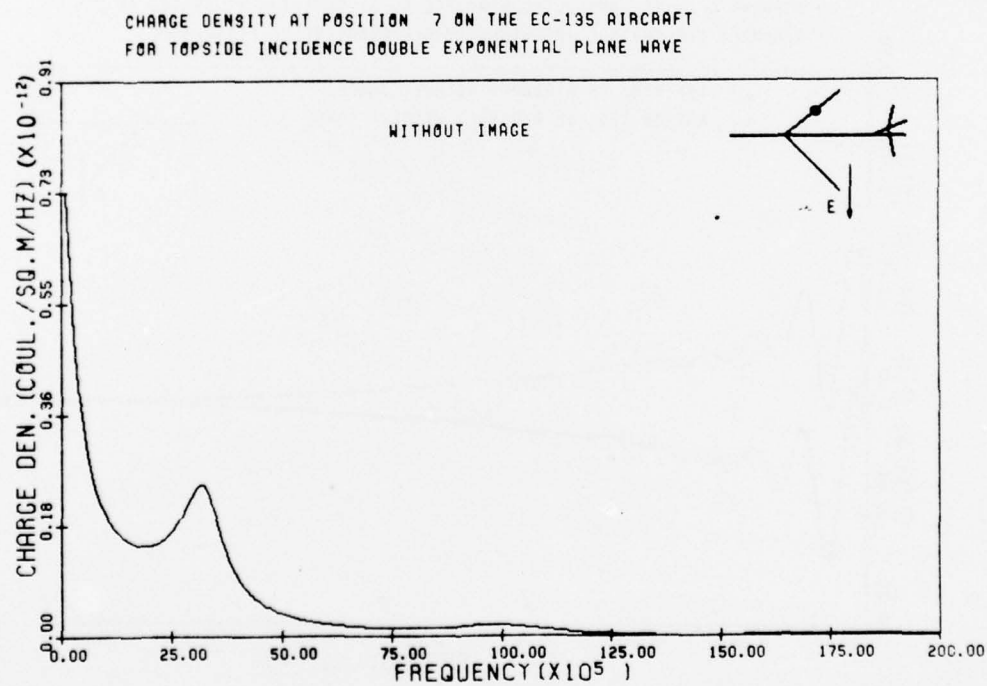


Figure 185:



CHARGE DENSITY AT POSITION 33 ON THE EC-135 AIRCRAFT  
FOR TOPSIDE INCIDENCE DOUBLE EXPONENTIAL PLANE WAVE

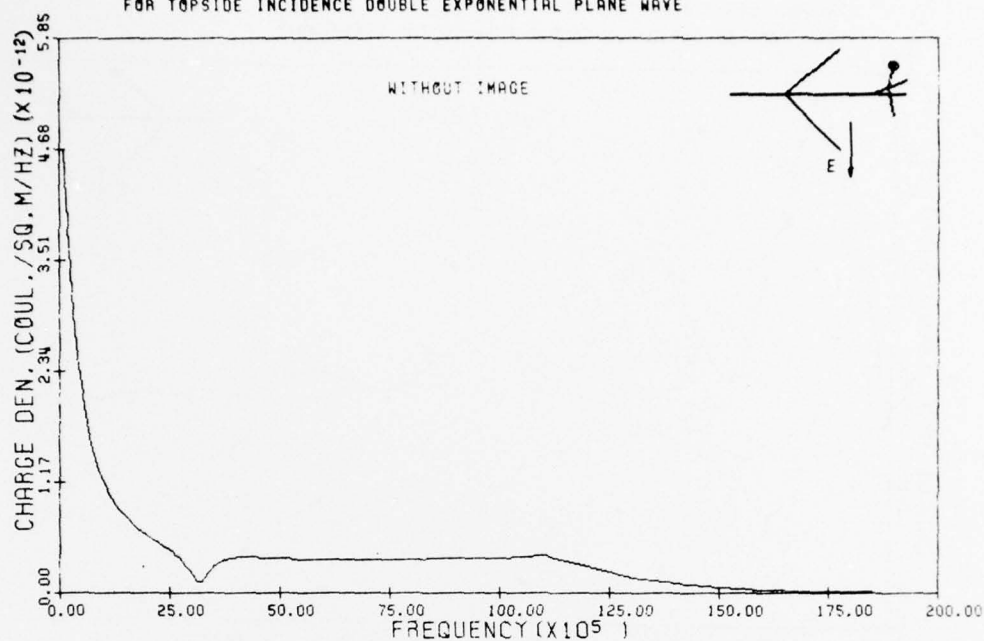


Figure 186:

CHARGE DENSITY AT POSITION 33 ON THE EC-135 AIRCRAFT  
FOR TOPSIDE INCIDENCE DOUBLE EXPONENTIAL PLANE WAVE

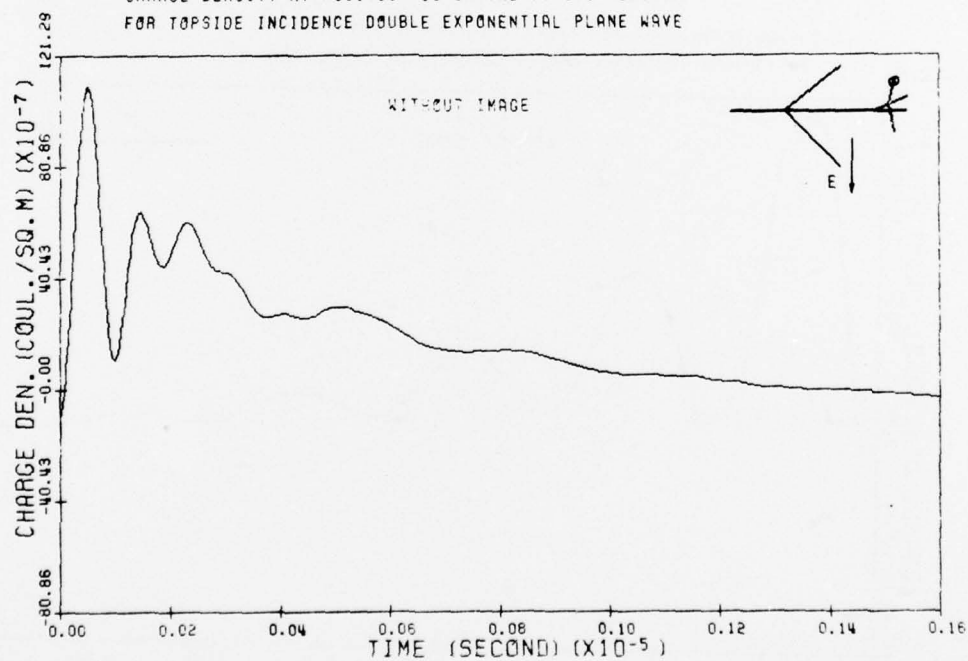


Figure 187:

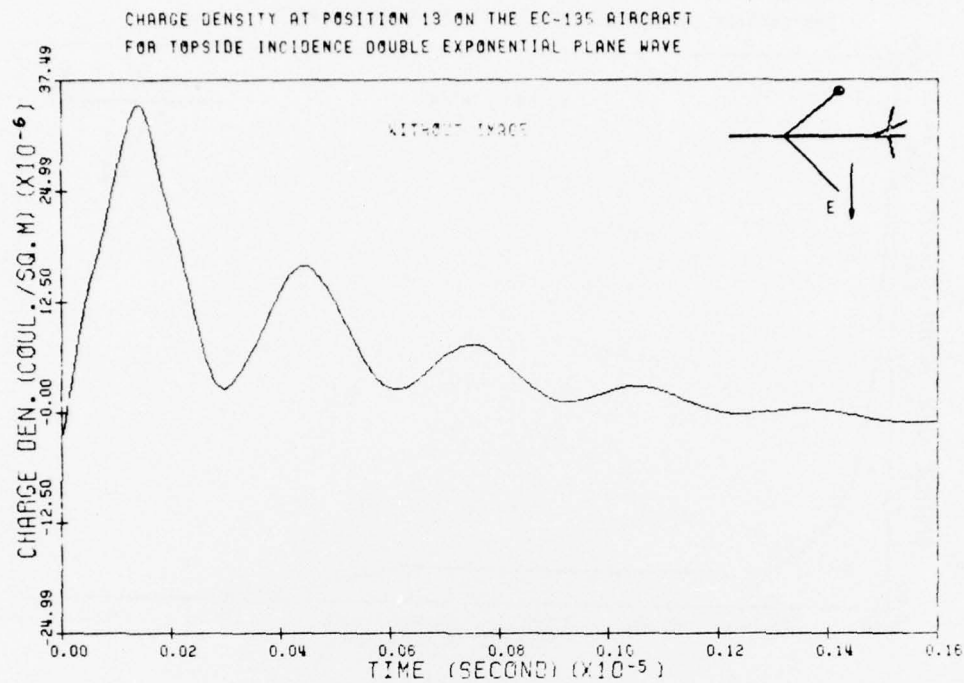


Figure 188:

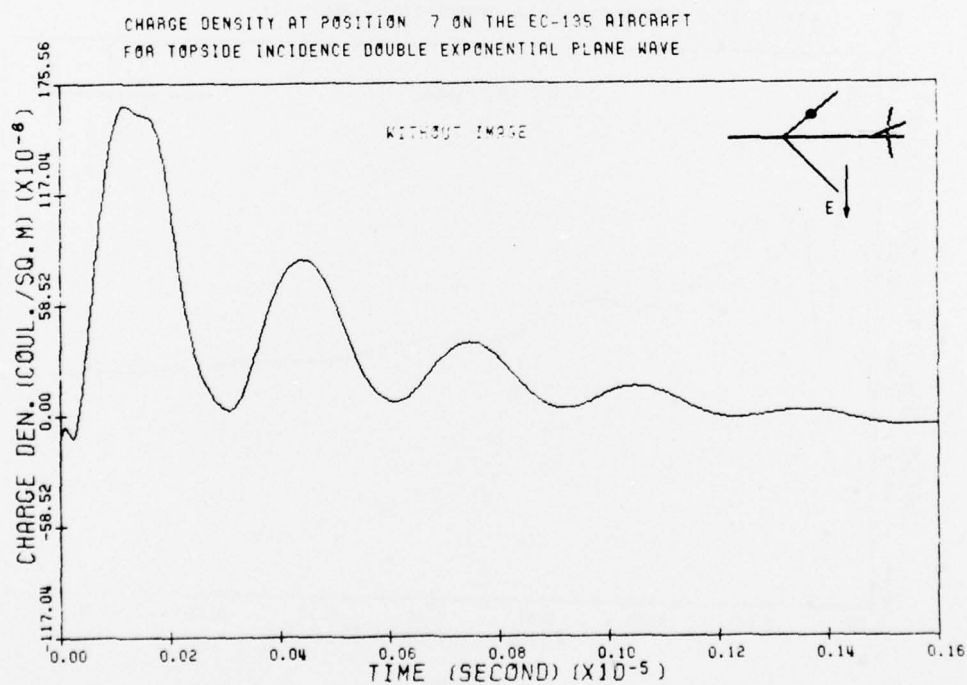


Figure 189:

REPORT DOCUMENTATION PAGE		READ INSTRUCTIONS BEFORE COMPLETING FORM
1. AFOSR - TR - 77 - 0636	2. GOVT ACCESSION NO.	3. RECIPIENT'S CATALOG NUMBER
4. TITLE (and Subtitle) A STUDY OF THE CHARGE AND CURRENT INDUCED ON AN AIRCRAFT IN AN EMP SIMULATOR FACILITY PART I: THE FORMULATION, PART II: THE SINGULARITY EXPANSION METHOD, PART III: THE NUMERICAL RESULTS		5. TYPE OF REPORT & PERIOD COVERED Scientific - Final
		6. PERFORMING ORG. REPORT NUMBER
7. AUTHOR(s) Clayborne D. Taylor Keh-Tong Chen Terry T. Crow		8. CONTRACT OR GRANT NUMBER(s) AFOSR 76-2961 <i>new</i>
9. PERFORMING ORGANIZATION NAME AND ADDRESS Department of Electrical Engineering Mississippi State University Mississippi State MS 39762		10. PROGRAM ELEMENT, PROJECT, TASK AREA & WORK UNIT NUMBERS 9751-05 61102F
11. CONTROLLING OFFICE NAME AND ADDRESS AFOSR/NP Bolling AFB, Bldg.#410 Wash DC 20332		12. REPORT DATE December 1976
		13. NUMBER OF PAGES 127
14. MONITORING AGENCY NAME & ADDRESS (if different from Controlling Office)		15. SECURITY CLASS. (of this report) Unclassified
		15a. DECLASSIFICATION/DOWNGRADING SCHEDULE
16. DISTRIBUTION STATEMENT (of this Report)  <b>Approved for public release; distribution unlimited.</b>		
17. DISTRIBUTION STATEMENT (of the abstract entered in Block 20, if different from Report)		
18. SUPPLEMENTARY NOTES  TECH, OTHER		
19. KEY WORDS (Continue on reverse side if necessary and identify by block number) Electricity and Magnetism Electromagnetic fields Waves Planar Transient		
20. ABSTRACT (Continue on reverse side if necessary and identify by block number) <i>Part I</i> A study of the aircraft skin current and charge is made for an aircraft under the illumination of the electromagnetic field produced by a nuclear EMP simulator. This work is motivated by the need to relate the response of an aircraft in the EMP illumination. The analysis is directed toward a specific EMP simulator at Kirtland AFB, New Mexico, however, the methodology presented is applicable to other types of simulator facilities.		

Part II - For an aircraft under the illumination of the electromagnetic field produced by a nuclear EMP simulator the natural resonant frequencies are significantly affected by the presence of the concrete pad supporting the aircraft. In order to determine this effect the singularity expansion method has been applied to a system consisting of two perpendicular crossed conducting thin cylinders oriented parallel to a perfectly conducting ground plane.

Part III - A theoretical-numerical solution technique is used to determine the current and charge densities induced on an aircraft by an electromagnetic pulse. To represent the aircraft the formulation uses an electromagnetic model formed with axial segments of bodies of revolution. Verification of the theoretical model is accomplished by extensive comparisons with measured data obtained by using scale models. Measured and calculated data are also presented for an EC-135 aircraft in the ATHAMAS I (also called HPD) simulator at Kirtland AFB, New Mexico. In addition the EC-135 is considered to be illuminated in flight by a typical estimate of the nuclear EMP. Comparison of the in flight data with corresponding simulator data is made to investigate the possibility of general trends.

1.0000000000000000  
0.0000000000000000